



TECHNISCHE
UNIVERSITÄT
WIEN

DISSERTATION

ULTRACOLD ATOMS ON SUPERCONDUCTING ATOMCHIPS

ausgeführt zum Zwecke der Erlangung des akademischen Grades eines Doktors der
Naturwissenschaften unter der Leitung von

UNIV. PROF. DIPL. ING. DR. TECHN. HANNES-JÖRG SCHMIEDMAYER

E141
Atominstitut

eingereicht an der Technischen Universität Wien
Fakultät für Physik

von

DIPL. ING. STEFAN MINNIBERGER

Matrikelnummer: 0255637
Schönau 18, 4701 Bad Schallerbach

Wien, im Dezember 2017

Diese Dissertation haben begutachtet:

Jörg Schmiedmayer

Oriol Romero-Isart

Hartmut Häffner

Abstract

Ultracold atoms on superconducting atomchips are a promising tool in atom optics, quantum information and quantum simulation. Combining the experimental techniques for ultracold atoms and superconductors is a very challenging task. This thesis describes the development of a complex experimental setup to transport ultracold atoms into a cryogenic environment where they are transferred to a superconducting atomchip. It also presents the properties of the superconducting atomchip trap and discusses approaches towards the creation of a hybrid quantum system. The transport of ultracold atoms from a room temperature MOT chamber to a cryogenic science chamber is realized with a magnetic conveyor belt. The cryogenic environment comes with technical advantages, like long atom lifetime because of the extremely low background pressure and rapid reconfigurability due to effective cryopumping, allowing to replace the atomchip in a matter of days rather than months. Magnetic microtraps realized by superconducting atomchips show some particularities as compared to their normal conducting counterparts. A detailed understanding of the current distribution in superconducting atomchips is necessary to make full use of their potential. I show how the current distribution in a type-II superconductor strongly depends on the history of applied fields and currents. It can therefore be tailored to a certain extent, allowing to reduce the effective wire width and to reach very small distances between the wire and the atom cloud. The magnetization of type-II superconductors also provides the possibility to create self-sufficient traps without any external connections, therefore being free from technical noise. This will allow future measurements of the reduced Johnson-Nyquist noise in the vicinity of superconducting surfaces. The primary goal of this project is however the creation of a hybrid quantum system with the long-lived hyperfine states of ultracold Rubidium 87 atoms and the excitations in a superconducting microwave cavity. I investigate the feasibility and present first steps towards the experimental realization of such a system using coplanar lambda-half and lumped element resonators. Finally, I discuss the prospect of superconducting vortex lattice traps for quantum simulation of Bose-Hubbard Hamiltonians. Vortices penetrating type-II superconductors can be used to create almost arbitrary arrays of magnetic microtraps. The lattice constant of these trap arrays can be significantly smaller than that of optical lattices, thus allowing to study a parameter range not accessible to the latter.

Kurzfassung

Supraleitende Atomchips sind ein vielversprechendes Werkzeug in der Teilchenoptik, der Quanteninformation und Quantensimulation. Die Kombination der experimentellen Techniken für die Erzeugung und Manipulation von ultrakalten Atomen und für Supraleiter stellt eine beträchtliche Herausforderung dar. Diese Arbeit beschreibt die Entwicklung eines komplexen experimentellen Aufbaus mit dem ultrakalte Atome in eine kryogene Umgebung transportiert werden und dort auf einen supraleitenden Atomchip geladen werden. Weiters werden die Eigenschaften der supraleitenden Chipfalle beschrieben sowie unsere Ansätze zur Erzeugung eines hybriden Quanten-Systems diskutiert. Die ultrakalten Atome werden mit einem magnetischen Förderband von der Raumtemperatur MOT Kammer in die kryogene Kammer transportiert, wo sich auch der supraleitende Atomchip befindet. Die kryogene Umgebung bringt einige technische Vorteile mit sich. Zum einen eine sehr lange Lebenszeit der Atome durch den geringen Hintergrunddruck. Zum anderen ermöglicht das effiziente Pumpen der kalten Oberflächen eine schnelle Rekonfiguration, womit der Atomchip innerhalb von Tagen gewechselt werden kann und nicht wie üblich in Monaten. Magnetische Mikrofallen auf supraleitenden Atomchips weisen einige Eigenheiten im Vergleich zu normalleitenden Atomchips auf. Ein genaues Verständnis der Stromverteilung im supraleitenden Atomchip ist notwendig um deren Potential ausnutzen zu können. Wir zeigen wie die Stromverteilung in einem Typ-II Supraleiter von der Geschichte der angelegten Felder und Ströme abhängt und zu einem gewissen Grad kontrolliert werden kann. Damit kann man die effektive Drahtbreite verringern und sehr kleine Abstände zwischen der Atomwolke und dem Atomchip realisieren. Magnetisierte Typ-II Supraleiter ermöglichen es Fallen ohne äußere Stromzufuhr zu erzeugen, diese sind daher frei von technischem Rauschen. Das sollte es ermöglichen, das reduzierte Johnson-Nyquist Rauschen in der Nähe supraleitender Oberflächen zu untersuchen. Das eigentliche Ziel dieses Projekts ist ein hybrides Quanten-System aus den langlebigen Hyperfeinzuständen in ultrakalten Rubidium 87 Atomen und den Anregungen eines supraleitenden Mikrowellen-Resonators. Die Realisierbarkeit eines solchen Systems und die ersten experimentellen Schritte mit verschiedenen koplanaren Wellenleiter-Resonatoren werden diskutiert. Zuguterletzt wird die Möglichkeit erörtert, magnetische Fallengitter mit Hilfe von Flussschläuchen in Typ-II Supraleitern zu erzeugen. Mit Hilfe von künstlichen Pinningzentren lassen sich beinahe beliebige Geometrien erzeugen. Die erreichbaren Gitterkonstanten sind wesentlich kleiner als bei optischen Gittern, wodurch neue Parameterbereiche für Quantensimulatoren erschlossen werden können.

Contents

Abstract	3
Kurzfassung	4
1. Introduction	9
1.1. Motivation	9
1.1.1. State of the art	10
1.2. Outline of the Thesis	11
1.3. Contributions	11
I. Theoretical background	13
2. Ultracold atoms	15
2.1. Introduction	15
2.2. Laser cooling	16
2.3. Polarization gradient cooling	17
2.4. The magneto-optical trap	18
2.5. Magnetic trapping	19
2.5.1. The effect of gravity	20
2.5.2. Types of traps	20
2.5.3. Atomchips	21
2.5.4. Optical pumping	21
2.6. Loss mechanisms	22
2.7. Evaporative cooling	23
2.8. Bose-Einstein condensation	23
3. Superconductivity	25
3.1. Introduction	25
3.2. The London equations	26
3.3. BCS theory	27
3.4. Ginzburg-Landau theory	28
3.5. Type II superconductors	29
3.6. The Bean critical state model (CSM)	31
II. Experimental realization	35
4. Setup overview	37

5. Vacuum system	41
5.1. The MOT chamber	41
5.2. Rubidium dispenser	42
5.3. Transport section and cryo chamber	43
5.4. Upgrades to the vacuum system	45
6. Cryogenic setup	47
6.1. Closed cycle cryocooler	47
6.2. Thermal shielding	51
6.3. Cryostat wiring and soldering	52
6.4. Experimental stage	53
6.5. High frequency setup	55
6.6. Chip mounting	58
6.7. Atomchip design and fabrication	59
6.8. Future upgrades	60
7. Magnetic coils and current control	61
7.1. normal conducting transport coils	61
7.1.1. High current electronics	62
7.1.2. Monitoring and safety	64
7.1.3. Upgrades	65
7.2. Bias coils	66
7.3. Superconducting coils	68
7.3.1. Current control	68
7.3.2. Upgrades	71
7.4. Atomchip current control	71
8. Transport current calculation	75
8.1. Horizontal transport	75
8.2. Vertical transport	78
8.3. Magnetic field simulations	80
9. Optical setup	83
9.1. Lasers	83
9.1.1. External cavity diode lasers	83
9.1.2. Distributed feedback laser diodes	84
9.1.3. Tapered amplifier	85
9.1.4. Temperature stabilization	85
9.1.5. Laser locking	85
9.1.6. Our lasers	86
9.2. Beam preparation	87
9.3. Imaging	88
9.3.1. MOT imaging	90
9.3.2. Main cryo imaging	91
9.3.3. Ioffe direction imaging	92
9.4. The quenching setup	93

10. Experimental control	97
10.1. The ADWIN system	97
10.2. MATLAB control program	97
10.3. QiController	99
10.4. Data acquisition	101
10.5. Auxiliary programs	101
10.5.1. Temperature and pressure measurement	101
10.5.2. Message collection program	103
10.5.3. RF sources	103
10.5.4. DC power supplies	103
10.5.5. NI DAQ	103
10.6. Upgrades to the IT	104
III. Results, discussion and outlook	107
11. Transport of ultracold atoms in a cryogenic environment	109
11.1. Laser cooling and magnetic trapping	109
11.2. Magnetic transport	110
11.3. The quadrupole Ioffe configuration (QUIC) trap	111
11.4. Transfer to the chip trap	114
12. The superconducting Z trap	117
12.1. Magnetic field microscopy	121
12.2. Current distribution in superconducting atomchips	127
12.2.1. Numerical simulation of supercurrent distributions	132
13. Towards trap recombination	135
14. Towards a hybrid quantum system	139
14.1. Introduction	139
14.1.1. The cavity	141
14.1.2. The atoms	142
14.1.3. System requirements	144
14.2. Lambda half resonators	145
14.3. Lumped element resonators	146
14.4. Three dimensional resonators	148
15. Towards superconducting vortex trap lattices	151
16. Conclusion and outlook	155
Bibliography	157
Appendices	167
A. Properties of Rubidium 87	169

B. Electronics	173
B.1. The switchbox	173
B.2. The Heidelberg current source	176
B.3. The Bilateral Current Source	178
B.4. Coil configurations	181
B.5. Breakout box	183
Acknowledgments	185

1. Introduction

1.1. Motivation

Magnetic trapping of ultracold atoms with microscopic wire structures, so called atomchips, continues to be an extremely versatile tool to explore the rich physics of Bose-Einstein condensates. Some of these include tunneling dynamics, dimensionality effects, unexpected thermodynamics and non-equilibrium physics in quantum many body systems [1, 2, 3].

In the quickly evolving field of quantum information processing, information is contained as the superposition of quantum states in so called "qubits" [4]. The coherence time of system has always been one of the major concerns [5]. The combination of different quantum systems to utilize long coherence times in one system as a qubit and perform operations in another system with faster interaction time is an approach to overcome the problems associated with decoherence. Those called "hybrid quantum systems" (HQS) have been realized using different physical systems as the qubit, for example Nitrogen-vacancy centers in diamond [6] or semiconductor quantum dots [7]. The quantum information is usually read out using photons, in the above example microwave photons. To ensure efficient coupling of the qubit system to the electromagnetic field, cavities are used. It is important to be aware of the timescales that govern the dynamics in different systems. Excitations in room-temperature solid state systems have coherence times below nanoseconds, at cryogenic temperatures at best microseconds. For information processing, solid-state electronics are the method of choice. For storage however, slower, more isolated systems are preferable, such as atoms or ions.

The motivation behind the experiment described in this thesis is the coupling of an ensemble of ultracold atoms to a superconducting microwave resonator [8]. The coherence time of a hyperfine state in such an ensemble can be very long, up to seconds, orders of magnitude above any solid state system. Superconducting microwave resonators are used in many experiments around the world, they are the workhorse for circuit quantum electrodynamics. The challenge lies in the combination of the very different technologies involved in superconducting electronics on one hand and the production and manipulation of ultracold atoms on the other hand, the steps made towards this goal are the main part of this thesis.

In our experiment, Rubidium 87 atoms are first trapped in a standard magneto-optical trap (MOT). The cold cloud is then transported into a cryogenic environment using a magnetic conveyor belt, where the atoms are transferred to a magnetic microtrap created by a superconducting atomchip [9]. This system can not only be used to create a hybrid quantum system by integrating a microwave resonator on the atomchip, it has also several other promising prospects. Ultracold atoms can be used as sensitive magnetic field sensors, thus allowing to study microscopic behavior of superconductors such as the flux creep and the Johnson noise produced.

Superconducting atomchips can also be used to probe properties of the superconductor.

1. Introduction

For instance, the current distribution in such a wire can be programmed by previously applied magnetic fields and currents. This can then be probed by the atomic cloud. Additionally, we are trying to create an array of magnetic microtraps for ultracold atoms by using the remnant magnetization of type-II superconductors. These trap arrays can be scaled down to a range where we are able to compete with optical lattices, with the ultimate goal being a trap array formed by the vortex lattice of a fully magnetized superconductor. A new loading scheme is under development right now, which should allow to increase the atom number in the atomchip trap by at least one order of magnitude. This increased atom number is a major progress on the path towards a hybrid quantum system. Throughout the project, many technical challenges have been overcome, the focus now lies in the design and integration of a microwave resonator on the atomchip as well as acquiring detailed understanding of the particularities of superconducting atomchips.

1.1.1. State of the art

To our knowledge, there are several other groups around the world that use superconducting atomchips or at least ultracold atoms in a cryogenic environment. Some of them pursue the exact same goal as we do, though strong coupling has not been reached in any experiment. Reviewing the current progress in the field will highlight again the experimental challenge this project signifies.

The Paris group (Serge Haroche) has successfully implemented a superconducting atomchip [10] and produced a BEC with it [11]. This group has performed first measurements of the trapping lifetime enhancement [12] and is focusing their attention on using the superconducting atomchip to manipulate Rydberg atoms [13, 14]. The setup features six superconducting bias coils, one quadrupole coil and a gold covered Niobium atomchip. Atoms enter the cryostat as a slow atomic beam from a room-temperature 2D-MOT. They are further cooled by a mirror-MOT created on the atomchip and transferred to the microtrap, where evaporative cooling takes place.

The Tübingen group (Jozsef Fortagh) uses a setup where only the atomchip is connected to the cold finger of a liquid Helium cryostat. Atoms from a room-temperature 3D-MOT are transported to the superconducting atomchip with a optical dipole trap [15]. Inductively coupled $\lambda/4$ resonators are integrated on the atomchip, which can be used to drive Rabi oscillations of the atoms [16]. The group is also pursuing an approach similar to ours, with a magnetic conveyor belt to transport the atoms into a dilution refrigerator [17].

The Stanford group (Benjamin Lev) employs a normal conducting atomchip in a cryostat. Between the atomic cloud and the trapping wires, a thin, thermally isolated sample can be placed to perform magnetic field microscopy from room temperature down to 4 K [18].

The group in Singapore (Rainer Dumke) uses high-temperature superconducting atomchips to study the magnetization of type-II superconductors [19, 20] and is also working towards a hybrid quantum system. They will use a Zeeman slower and a vertical magnetic transport to bring ultracold atoms into a dilution refrigerator.

The group in Japan (Tetsuya Mukai) uses moving room-temperature quadrupole coils to transport trapped atoms to their superconducting MgB₂ atomchip. The chip is operated

with a persistent current, thus no connections from the cold stage to the outside are required [21, 22].

To our knowledge, a group at the south china normal university recently also started an experiment that tries to create a hybrid quantum system.

1.2. Outline of the Thesis

The thesis is organized in three parts:

Part I will give an overview on the theoretical background of ultracold atoms and superconductivity, this part is by no means exhaustive.

Part II is the main part of this thesis and presents a comprehensive description of the experiment and all its subsystems. Upon request of those continuing the development of the setup, I designate a section on future upgrades at the end of each chapter.

Part III shows the results obtained with the superconducting atomchip and describes several ongoing projects such as the recombination of magnetic traps, the integration of a microwave resonator in our setup and the creation of superconducting trap arrays.

1.3. Contributions

An experiment like the one presented here is always a team effort. We have to thank our predecessors Stefan Haslinger, Christoph Hufnagl and Nils Lippok for their groundbreaking work on the magnetic transport. My colleague Fritz Diorico and I started our PhD thesis on the same day and most things presented here were done in close collaboration with him. Throughout the years, we supervised many Project- and Bachelor students, who helped us with small projects. Our Master students, Christian Novotny, Benedikt Gerstenecker, Naz Shokrani, Thomas Weigner, Zaneta Kurpias and Lukas Cvitkovich were indispensable for the development of this complex setup.

Part I.

Theoretical background

2. Ultracold atoms

2.1. Introduction

The history of ultracold atoms is closely linked to the revolutionary discoveries made more than a century ago. Radiation pressure, the force that light exerts on matter, has been proposed as early as 1619 by Johannes Kepler to explain why the tails of comets always point away from the sun. This pressure can be derived from Maxwell's equations. However, many phenomena such as the photoelectric effect can not be explained within the theory of electromagnetism. In 1900, Max Planck postulated that electromagnetic radiation could only be emitted in quantized form [23]. Albert Einstein developed his quantum theory of light in 1916 [24], where he predicted the momentum of a single photon to be $\hbar\vec{k}$. This prediction was experimentally confirmed by Arthur Compton in 1923 by X-ray scattering [25] and by Otto Frisch in 1933, who measured the recoil atoms experience when emitting or absorbing photons [26].

The new quantum theory was also successfully applied in atomic physics. In 1924, Louis de Broglie suggested that particles with momentum p behave like a wave with wavelength $\lambda = \hbar/p$ [27]. This mind-boggling matter-wave duality was experimentally verified for electrons in 1927 [28]. With Erwin Schrödinger's famous equation and its subsequent refinement, more complex atomic spectra could be explained and the quantum mechanical wave function was born [29].

The next key ingredient for ultracold atoms was the invention of the Laser in 1960. It relied on the concept of stimulated emission, which was introduced by Einstein in 1916 [30]. The first Laser was built by Theodore Maiman using a synthetic ruby pumped by flash lamps [31]. This new technology progressed quickly, more and more wavelengths became available and continuous-wave (cw) operation became possible.

With these intense monochromatic light sources available, Hänsch and Schawlow realized that radiation pressure can be used to cool atomic gases to very low temperatures [32]. Within a few years, several groups achieved to slow down and even stop neutral atoms by means of laser cooling [33]. These slow atoms could now be magnetically trapped, which for the first time was achieved in 1985 [34].

With matter at previously unreachable low temperatures, another prediction of quantum mechanics was within reach: the Bose-Einstein condensate (BEC). Satyendra Nath Bose derived the thermodynamic properties (i. e. Planck's radiation law) of light without any reference to classical physics in 1924 [35]. Einstein expanded his ideas to atoms and realized that at low enough temperatures, atoms would condense in the lowest available quantum state [36]. Such a BEC was first achieved in 1995 [37].

After this short historic outline, this chapter will review the most important concepts in the field of ultracold atoms which are relevant for this thesis. More comprehensive descriptions can be found in many textbooks, for example [38]. All numerical values in this chapter are

given for Rubidium 87.

2.2. Laser cooling

The probability to find an atom of an ideal gas at a certain velocity v is given by the Maxwell-Boltzmann distribution function

$$p(v) = \sqrt{\left(\frac{m}{2\pi k_B T}\right)^3} 4\pi v^2 e^{-\frac{mv^2}{2k_B T}}, \quad (2.1)$$

where m is the atomic mass, T the temperature and k_B the Boltzmann constant. The *rms* velocity is

$$\bar{v} = \sqrt{\frac{3k_B T}{m}}, \quad (2.2)$$

which at room temperature means 293 m/s for ^{87}Rb atoms (8.5% more than the mean velocity). The natural line width of the D2 line of ^{87}Rb is $\Gamma = 2\pi \times 6$ MHz [39]. The thermal motion results in a Doppler broadening

$$\Delta f_{FWHM} = \sqrt{\frac{8k_B T \ln 2}{mc^2}} f_0 \quad (2.3)$$

of this line by around 510 MHz. When an atom absorbs a photon, its momentum changes by $\Delta\vec{p} = \hbar\vec{k}$, causing a velocity change of 0.5 cm/s. This absorption is followed by spontaneous emission in a random direction. Is the frequency of the radiation red detuned from the atomic resonance, atoms moving towards the beam have a larger scattering cross section than others. Since the momentum kick by the spontaneous emissions averages to zero over many scattering events, the atomic motion opposing the laser beam will slow down. Applying beams in all 6 Cartesian coordinate directions results in an overall deceleration of the gas. The force on an atom by one beam

$$F_{scatt} = \hbar\vec{k} \cdot R_{scatt} = \hbar\vec{k} \cdot \frac{\Gamma}{2} \frac{I/I_S}{1 + I/I_S + 4\Delta^2/\Gamma^2} \quad (2.4)$$

is given by the momentum change per scattering event times the scattering rate. It depends on the spontaneous emission rate Γ , the intensity I and saturation intensity I_{sat} (the saturation intensity will be discussed further in section 9.3). The Doppler shift introduces a velocity dependence of the laser detuning $\Delta = \omega - \omega_0 - \vec{k}\vec{v}$ and therefore of the force, as is shown in figure 2.1. The similarity to viscous friction or stickiness has led to the term *optical molasses* for such a configuration [40]. Of course laser cooling can not remove all the energy from the atoms. The random nature of the absorption and emission events is equivalent to a heating process. At the lowest reachable temperature the heating- and cooling rate are in equilibrium. It becomes minimal when the detuning is set to $\Delta = \omega - \omega_0 = -\Gamma/2$. This so called Doppler temperature

$$T_D = \frac{\hbar\Gamma}{2k_B} \quad (2.5)$$

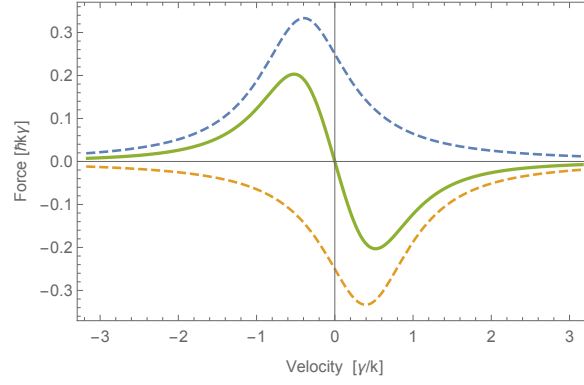


Figure 2.1.: Scattering force on an atom in a one-dimensional optical molasses. The dashed curves show the force from each beam, the solid curve is their sum. The saturation parameter $s = I/I_S$ is set to 2 and the detuning $\Delta = \Gamma/2$. The asymmetry in the scattering rates leads to a net force slowing down the atoms.

is $152 \mu\text{K}$ for ^{87}Rb and corresponds to an *rms* velocity of 20 cm/s .

For the mechanism above to work, each atom has to scatter many thousand photons. It is required that spontaneous emission from the excited state always leads to the same ground state, otherwise the atom is transparent for the cooling laser. ^{87}Rb has an almost closed cooling cycle between $|F = 2\rangle$ and $|F' = 3\rangle$. However, atoms have a small probability to decay to the $|F = 1\rangle$ ground state. Therefore a weak laser, the so called repumper, resonant with the $|F = 1\rangle$ to $|F' = 2\rangle$ transition is mixed to the cooling light to lift atoms out of the dark state, as shown in figure A.3.

2.3. Polarization gradient cooling

However, temperatures much lower than T_D are achieved by laser cooling. So far the theory does not include the polarization of the light field or the multilevel structure of the atomic transitions. Both are necessary for an explanation of this sub-Doppler cooling mechanism. Let us consider two counter-propagating beams with σ^+ and σ^- polarizations, the configuration used in this work. Their interference results in a continuous linear polarization which rotates by 180° over a distance of $\lambda/2$ as is depicted in figure 2.2. Atoms at rest in such a light field would mainly occupy the $m_f = 0$ substate. The quantization axis for moving atoms rotates and they must be optically pumped in order to follow the local polarization direction. Since optical pumping requires finite time, the ground state population of moving atoms always lags behind the steady state distribution. Dalibard and Cohen-Tannoudji showed in [41] that atoms moving towards the laser beam with σ^+ polarization are preferentially occupying the $m_f = +1$ state (and vice versa for atoms moving towards the beam with σ^-). In this state the atoms scatter σ^+ (or σ^-) light much more efficiently than the other polarization due to the different Clebsch-Gordan coefficients. The cooling effect relies on the preferential scattering of the opposing laser beam, this time not caused by the Doppler shift but by a population imbalance due to the rotating quantization axis. The lower limit for laser cooling is the recoil temperature, associated with the energy change of the absorption or emission of a single photon:

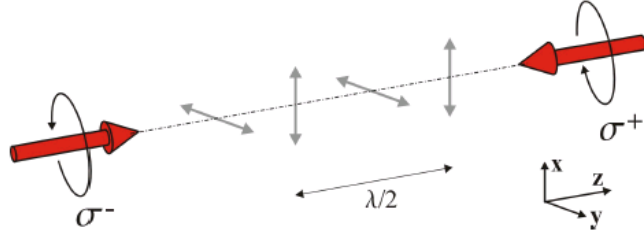


Figure 2.2.: Rotating linear polarization of a standing wave in the σ^+ - σ^- configuration. Drawing taken from [42].

$$T_r = \frac{\hbar^2 k^2}{2k_B m}, \quad (2.6)$$

in the case of ^{87}Rb 350 nK or $v_{rms} = 0.5$ cm/s. In reality, this polarization gradient cooling mechanism described above reaches temperatures as low as $2 \mu\text{K}$, about 5 times above the recoil limit. There are cooling schemes beating the recoil limit, but they will not be discussed here.

2.4. The magneto-optical trap

So far the atoms feel a velocity dependent friction force that slows down their thermal motion, but there is no trapping because they can just diffuse out of the molasses region. In [43] it was proven that there can be no stable trap using only the scattering force, this is referred to as the *optical Earnshaw theorem*. In order to create a trap for the atoms, a position dependent restoring force is required. This can be achieved by adding a magnetic quadrupole field to the intersecting laser beams and is called *magneto-optical trap (MOT)* [44]. The working principle of this configuration can be easily understood by considering a hypothetical atom with a spin $S = 0$ ground state and a $S = 1$ excited state in a one-dimensional field, as illustrated in Figure 2.3. The magnetic field is zero in the center and increases linearly with distance from the trap, $B_z(z) = b \cdot z$. This field leads to a splitting of the Zeeman sub-levels according to $\Delta E = \mu m_s B = \mu m_s b z$. The $m_s = 1$ level will be shifted upwards at positive z and downwards at negative z (and vice versa for the $m_s = -1$ state). Adding red-detuned, counter-propagating laser beams with σ^+ polarization in the $+z$ direction and σ^- in the $-z$ direction makes atoms at $z > 0$ ($z < 0$) preferentially absorb σ^- (σ^+) photons, which results in a net force towards the center. In reality, the energy level scheme is slightly more complicated, but the principle is the same. The force on the atoms in a MOT can be calculated similarly to equation 2.4, where the detuning contains an additional position dependent term $\Delta = \omega - \omega_0 - k\vec{v} + \mu' B(z)/\hbar$, where $\mu' = (g_e M_e - g_g M_g)\mu_B$ is the change of magnetic moment for the used transition. The velocity range of atoms that can be captured with a MOT lies on the order of 30 m/s, assuming beams with a diameter of 2 cm. According to equation 2.1, about $1.5 \cdot 10^{-4}$ of all atoms in a room temperature vapor lie below this velocity. Under typical conditions, is possible to load a MOT with several 10^8 atoms in a few seconds [38].

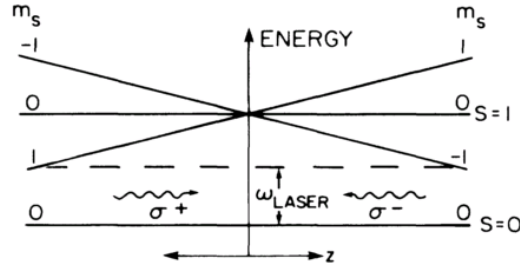


Figure 2.3.: Energy levels and laser beams in a 1D MOT for a hypothetical atom and beams with orthogonal circular polarization and frequency ω_L below the $B = 0$ resonance. At either side, the beam directed toward the center gets into resonance with the atoms. Drawing taken from [44].

2.5. Magnetic trapping

Magnetic trapping of neutral atoms relies on the Zeeman effect. The coupling of the nuclear magnetic moment of $3/2$ and the spin $\pm 1/2$ of the s-electron results in a ^{87}Rb ground state with total spin $F = 1$ or $F = 2$. The detailed level schemes and the hyperfine splittings are reproduced in appendix A. In the low field limit, the magnetic moment associated with each individual state is given by

$$\mu = \mu_B g_F m_F, \quad (2.7)$$

where μ is the magnetic moment, $\mu_B = e\hbar/2m_e$ the Bohr magneton, g_F the Landé g-factor and m_F the projection of the total spin on the quantization axis. The potential energy of a magnetic moment in an external field \vec{B} is

$$E = -\vec{\mu} \cdot \vec{B} = \mu_B g_F m_F |B|. \quad (2.8)$$

This assumes that the atom can follow any change of the external field adiabatically, thus not changing the m_F sublevel. An inhomogeneous field results in a force

$$\vec{F} = \mu_B g_F m_F \nabla |B|. \quad (2.9)$$

According to Earnshaw's theorem [45, 46], there can be no local magnetic field maximum in free space. Therefore only atomic states where $g_F m_F > 0$ are trappable by local magnetic minima. These so called *low field seeking states* are $|F, m_F\rangle = |1, -1\rangle$, $|2, 1\rangle$ and $|2, 2\rangle$ for the ^{87}Rb ground state¹. The small scale of this interaction shows that atoms need to be cooled significantly to be trappable. A field of $|\vec{B}| = 1 \text{ G}$ relates to a potential energy of $k_B \cdot 67 \mu\text{K}$ for the $|2, 2\rangle$ state. In order to keep a real cloud of that temperature, also the Boltzmann tail needs to be trapped, thus a much lower temperature is required.

A thermal atom cloud in a harmonic trap shows a Gaussian distribution in all directions. The width of the gaussian is given by the trapping frequency ω and the cloud temperature T :

¹High-field seeking states may be trapped in orbits around wires, [47].

$$x_0 = \frac{1}{\omega_x} \sqrt{\frac{2k_B T}{m}} \quad (2.10)$$

2.5.1. The effect of gravity

Of course atoms in magnetic traps are also subject to gravitation. The trap is modified in vertical direction, equal to an additional vertical magnetic field gradient of

$$B'_z = \frac{m \cdot g}{m_f g_f \mu_B} = 15.57 \text{ G/cm} \quad (2.11)$$

for the $m_F = 2$ sub-state. Gravity also shifts the position of the trap center downwards. The weak direction of a trap should therefore not be along the vertical direction, as the gravitational sag would be significant.

2.5.2. Types of traps

Magnetic traps are characterized by the shape of the potential landscape around the trap center (=field minimum). Some important parameters are:

- The trap bottom $|B(\vec{r} = 0)|$ is the field at the trap center. If it vanishes the atoms are subject to Majorana spin flip losses, as will be discussed in section 2.6.
- The trap depth, usually given as a temperature, is the energy an atom needs to escape the trap.
- The gradients $\partial B / \partial r_i$ define the volume to which the atoms are restricted
- The curvature of the field landscape. For many traps it is convenient to assume a harmonic potential around the minimum.
- The *trapping frequencies* $\omega_{x,y,z}$ are the oscillation frequencies of a trapped particle in different directions, assuming a harmonic potential.
- The aspect ratio describes the shape of the trap and can range from spherical or oblate to very elongated, quasi-1D traps.

There are many configurations of magnetic coils, current carrying wires and other magnetic structures to form traps. The most simple one is the *quadrupole trap*, created by a pair of coils in anti-Helmholtz configuration. The potential is linear around the center, with twice the slope in the axial direction and zero trap bottom. One possibility to raise the trap bottom of a quadrupole trap is to use a third, perpendicular coil pointing at the quadrupole center, it is called *Quadrupole-Ioffe-Configuration (QUIC)* trap [48] and features a harmonic trap bottom. More details on the QUIC trap are given in section 11.3.

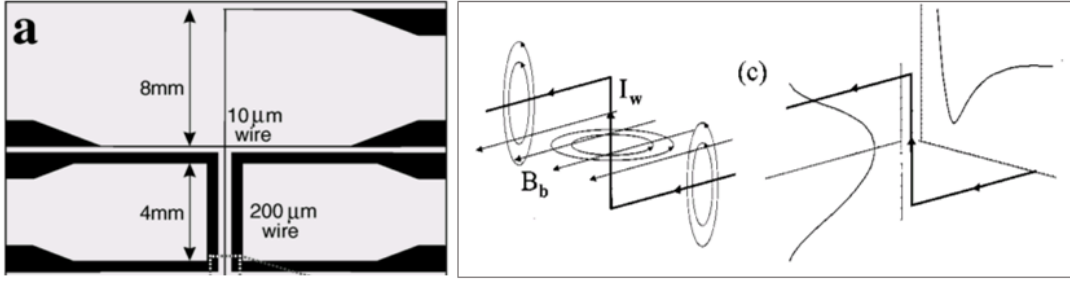


Figure 2.4.: Left: Microscope image of one of the first atomchips [50]. Right: Schematic of the trapping potential produced by a Z-shaped wire with current I_w along with a homogeneous bias field B_b , taken from [49]

2.5.3. Atomchips

Steeper gradients and higher trapping frequencies are possible with traps very close to microscopic wire structures. These so called *atomchips* (see figure 2.4) have become an extremely important tool in the field of ultracold atoms and also form the basis for this thesis [49].

The principle of a magnetic microtrap is the creation of a trap by superimposing the field of a wire with a homogeneous bias field as shown on the right in figure 2.4. The magnetic field around a long current carrying wire is given by

$$B(r) = \frac{\mu_0 I}{2\pi r} \quad (2.12)$$

with the derivative

$$\frac{dB(r)}{dr} = -\frac{\mu_0 I}{2\pi r^2}. \quad (2.13)$$

The smallest achievable distance between the atoms and a magnetic coil is obviously limited, so in order to increase the field gradient one has to decrease the distance r to the current I . A current of 1 A at a distance of 0.1 mm results in a magnetic field gradient of 2 kG/cm, a value hard to reach with macroscopic coils.

2.5.4. Optical pumping

From equation 2.8, it is clear that it is desirable to have all atoms in the most tightly trapped state, where $g_F \cdot m_F$ has a maximum, which is $|2, 2\rangle$ for ^{87}Rb . By shining σ^+ polarized light resonant with the $F = 2$ to $F' = 2$ transition through the cloud, with a weak, homogeneous magnetic field to provide a quantization axis, the atoms can climb the m_F ladder and end up in $|2, 2\rangle$. This mechanism is called optical pumping.

Experiments towards the creation of a hybrid quantum system use the clock state microwave transition $|F, m_F\rangle = |1, -1\rangle$ to $|2, 1\rangle$, as will be discussed in chapter 14. To prepare the atoms in the $|1, -1\rangle$ state, an alternative optical pumping scheme uses σ^- polarized light set to the $F = 1$ to $F' = 1$ transition.

2.6. Loss mechanisms

Ultracold atoms in magnetic traps are subject to different loss mechanisms. The most important are:

Majorana losses: A moving atom in a magnetic trap will experience a changing magnetic field in its rest frame. The rate of change of the quantization axis must be slower than the Larmor frequency $\omega_L = \mu|B|/\hbar$. If this condition is violated, spin-flips to untrapped states cause losses. For traps with vanishing trap bottom, these Majorana spin flips [51, 52] are the dominant loss source, while even a rather small (10 mG) offset field can suppress them efficiently.

Background gas collisions: Even at UHV conditions with pressures typically smaller than 10×10^{-10} mbar, the number density of the background gas is around 2×10^6 cm $^{-3}$. Apart from Rubidium itself, the most abundant background gas particles are Nitrogen, Oxygen, Hydrogen and water. Each elastic collision between a fast background gas particle and a slow ^{87}Rb atom transfers enough energy to kick it out of the trap. This process leads to an exponential decay with a time constant proportional to the number density n_i , the scattering cross sections σ_i and the thermal velocity v_i of the background gas species present. The loss rate is given by the sum over all relevant gas species i :

$$\Gamma_{bg} \approx \sum_i n_i \langle \sigma_i \cdot v_i \rangle, \quad (2.14)$$

Typical loss rates lie on the order of 3×10^7 mbar $^{-1}$ s $^{-1}$, for details refer to Table I in [53]. A background gas pressure of 1×10^{-9} mbar would then result in a lifetime of about 25 s.

Two body collisions: The rate of elastic two body collisions between trapped ^{87}Rb atoms determines the time scale on which rethermalization of the cloud happens, as will be discussed in section 2.7. *Inelastic* two body collisions are suppressed by selection rules in fully spin-polarized clouds where all atoms are in the $|2, 2\rangle$ state and therefore play no significant role in our experiments [54].

Three body losses allow the formation of Rb_2 molecules, where the third atom takes away the binding energy. This loss rate is proportional to the square of the ensemble density and becomes only relevant in very cold samples. For BECs however, this is usually the dominant loss mechanism. Since these three body collisions happen in regions of high density, where the potential energy is low, the atoms lost from the trap carry away less than their share of the thermal energy and the ensemble heats up [55], somehow the reverse process of evaporative cooling.

Current noise in the trapping wire or the coils causes magnetic field fluctuations at the location of the cold cloud. The mechanism how this noise causes atom loss is determined by the frequency range. For frequencies on the order of any of the trapping frequencies or its harmonics, typically from 10 Hz to several kHz, atoms are lost through parametric heating. In the range above ~ 100 kHz, spin-flips to untrapped m_f sublevels occur [56, 57, 58]. The source of this noise is technical, either from electronics involved in producing the current or

through interference or cross-talk between wires in a noisy lab environment. A quantitative approach to this loss mechanism is presented in chapter 3 in reference [57].

Johnson-Nyquist noise from thermal fluctuations in the trapping wires also causes atom loss through spin-flips. In contrast to technical current noise, it can only be reduced by lowering the temperature of the conductor. For superconducting surfaces however, there are theoretical predictions that they provide an extremely low noise environment with spin-flip lifetimes on the order of thousands of seconds [59].

2.7. Evaporative cooling

The limits of laser cooling were discussed in section 2.2. In order to achieve even colder temperatures, a different method is used: *evaporative cooling*. Much like blowing on hot tea, atoms on the high velocity tail of the Boltzmann distribution get removed by RF induced spin-flips to untrapped states. The remaining ensemble will then again thermalize through elastic collisions and equilibrate at a new, colder temperature. For this process to work efficiently, the ensemble lifetime needs to be long compared to the thermalization time. This means the ratio of "good" elastic collisions $n\sigma v$ (σ is the s-wave scattering cross section, n the particle density and v their velocity) to "bad" background gas collisions must be large, at least a few hundred. The most important parameter characterizing the evaporation process is the increase in phase space density $D = n\lambda_{dB}^3$, where $\lambda_{dB} = \sqrt{2\pi\hbar^2/mk_B T}$ is the thermal de-Broglie wavelength [55, 60]. With the right parameters, D can increase by more than seven orders of magnitude. Without considering loss processes, there is no fundamental limit for evaporative cooling.

2.8. Bose-Einstein condensation

All particles can be categorized according to their spin. Half-integer spin particles are called fermions and have an antisymmetric wavefunction. This gives rise to the Pauli exclusion principle, which forbids identical fermions from occupying the same quantum state. Systems of many fermions (for example electrons) are described by the Fermi-Dirac statistics. On the other hand, bosons are particles with integer spin and a symmetric wavefunction, which means many bosons can occupy the same quantum state. This has an important effect on the statistical properties of bosonic systems. The occupation numbers $\langle n_k \rangle$ in a non-interacting Bose gas are distributed according to the Bose-Einstein distribution

$$\langle n_k \rangle_{Bose} = \frac{1}{e^{\beta(\epsilon_k - \mu)} - 1}, \quad (2.15)$$

where $\beta = 1/k_B T$, ϵ_k is the single particle energy and μ is the chemical potential. The total particle number is given by the sum over all states k :

$$\begin{aligned}
 N_{T,V,\mu} &= \sum_{k=0}^{\infty} \langle n_k \rangle = \sum_{k=0}^{\infty} \frac{1}{e^{\beta(\epsilon_k - \mu)} - 1} \\
 &= \frac{e^{\beta\mu}}{1 - e^{\beta\mu}} + \sum_{k=1}^{\infty} \frac{1}{e^{-\beta\mu} e^{\beta\epsilon_k} - 1} \\
 &= \frac{z}{1 - z} + \frac{1}{h^3} \int_0^{\infty} \frac{\sqrt{\epsilon}}{z^{-1} e^{\beta\epsilon} - 1} d^3 p d^3 q \\
 &= \frac{z}{1 - z} + \frac{2\pi V (2m)^{3/2}}{h^3} \int_0^{\infty} \frac{\sqrt{\epsilon}}{z^{-1} e^{\beta\epsilon} - 1} d\epsilon.
 \end{aligned} \tag{2.16}$$

For large N , the discrete sum can be written as an integral over the entire phase space $d^3 q d^3 p$ or over all eigenenergies ϵ , respectively. For a three dimensional potential, the density of states is proportional to $\sqrt{\epsilon}$. The first term, where $k = 0$, contains the ground state population N_0 and has to be treated separately since $\epsilon_0 = 0$. The chemical potential for such a bosonic gas is negative and approaches 0 for small temperatures [61], therefore the so called fugacity $z = e^{\beta\mu} \rightarrow 1$. The integral in equation 2.16 can be solved by using the generalized Riemann zeta function $\zeta_{3/2}(z)$ for $0 < z < 1$:

$$N(N, V, z) = N_0(z) + \frac{V}{\lambda_{dB}^3} \zeta_{3/2}(z). \tag{2.17}$$

The excited state population reaches its maximum when the phase space density $n\lambda_{dB}^3 = \zeta_{3/2}(1) = 2.612$. After this point, all additional particles will be accommodated in the ground state and a Bose-Einstein condensate (BEC) starts to form. The critical temperature for this process is

$$T_C = \frac{2\pi\hbar^2}{mk_B} \frac{n}{\zeta_{3/2}(1)}. \tag{2.18}$$

At this temperature, the thermal de-Broglie wavelength becomes comparable to the inter-atomic distance and the individual wavefunctions start to overlap. For atoms trapped in a harmonic trap, the calculation is slightly modified and the transition temperature becomes

$$T_C = \frac{\hbar\omega_{ho}}{k_B} \frac{N}{\zeta_{3/2}(1)}, \tag{2.19}$$

where $\omega_{ho} = \sqrt[3]{\omega_x\omega_y\omega_z}$ is the mean trapping frequency [62].

3. Superconductivity

3.1. Introduction

This chapter will start with an overview of the history of superconductivity, after which I will discuss some important theoretical and experimental results. The emphasis lies in the modeling of the current distribution through superconducting thin films as well as their remnant magnetization and the distribution of vortices.

The history of superconductivity is somewhat reverse to that of ultracold atoms, where theory was more than half a century ahead of experiments. The first satisfying microscopic theory for superconductivity was proposed in 1957, 46 years after the first experimental observation. Even today, some aspects of superconductivity, especially high-temperature superconductors, remain unclear.

The first liquefaction of Helium in 1908 by Heike Kamerlingh Onnes opened a new chapter in low-temperature physics. Previously, electrical resistivity and other material properties were studied down to 14 Kelvin, the temperature at which solid hydrogen sublimates. At this temperature, the resistivity of platinum and other metals falls linearly with temperature. It was known that the decreasing electrical resistance is due to weaker scattering of the conduction electrons on the metal ions and the question was how this would evolve when approaching absolute zero. Lord Kelvin assumed that the mobility of electrons would also vanish, resulting in infinite resistivity, while others predicted zero resistivity at zero temperature. Kelvins assumption was disproven in late 1910, when measurements on platinum in liquid helium showed no further decrease of the electrical resistivity. The ratio of the room temperature resistivity and this value is called the residual resistance ratio (RRR) and depends on the purity of the metal. In early 1911, Kamerlingh Onnes noted that the resistivity of mercury, a metal that could be easily purified, was “near enough zero” when cooled to liquid Helium temperatures [63]. Subsequent, more accurate measurements revealed a sudden jump in resistivity (Figure 3.1) at what is known today as the critical temperature T_C . Kamerlingh Onnes also demonstrated the existence of persistent currents that flow without a voltage applied. Soon lead and tin were also shown to become superconducting and it was proven that a completely new phenomenon has been discovered.

The next important discovery was made by Walther Meißner and Robert Ochsenfeld in 1933. They showed that superconductors expel magnetic fields from their interior [64], up to a critical field H_C at which superconductivity breaks down.

A first phenomenological theory was presented by the brothers Fritz and Heinz London in 1935 [65]. Their equations predict a rapid decay of the magnetic field inside the superconductor through shielding surface currents.

Lew W. Shubnikov and coworkers discovered what is today known as type-II superconductors in 1936 [66]. These materials do not exhibit a complete field expulsion, but let flux penetrate above a certain field H_{C1} , an effect not covered by the London equations.

3. Superconductivity

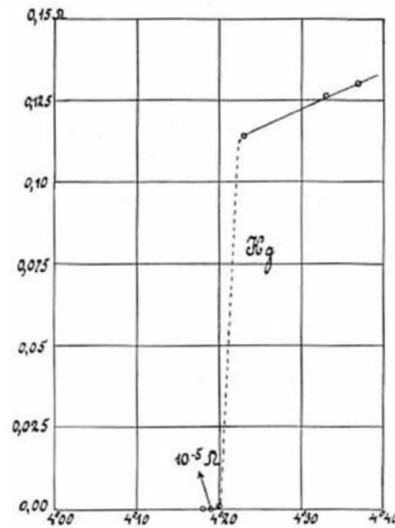


Figure 3.1.: Historic plot of resistance versus temperature for mercury. Plot taken from [63].

Vitaly Ginzburg and Lev Landau formulated a macroscopic theory based on second-order phase transitions in 1950 [67]. This theory was employed by A. A. Abrikosov in 1957 to explain how the magnetic field penetrates type-II superconductors [68].

A complete microscopic theory was developed by John Bardeen, Leon Cooper and John R. Schrieffer in 1957 [69], explaining superconductivity through the superfluidity of cooper pairs, electrons forming a bound state through the exchange of phonons. As shown by Lev Gor'kov, the Ginzburg-Landau equations could be derived from the BCS theory [70].

The last major breakthrough was the discovery of high-temperature superconductors (HTCs) in 1986 [71]. Complex ceramic materials with copper oxide planes show superconductivity at temperatures above 77 K, the boiling point of liquid nitrogen. Up to now, there is no complete microscopic theory for these unconventional superconductors.

3.2. The London equations

The equation of motion for an electron in an electric field \mathbf{E} and a magnetic field \mathbf{B} is given by $\mathbf{F} = e\mathbf{E} + e\mathbf{v} \times \mathbf{B}$. In contrast to the classical Drude theory of electric transport, there is no damping term in a superconductor. This assumption results in the first London equation

$$\frac{\partial \mathbf{j}_s}{\partial t} = \frac{n_s e^2}{m} \mathbf{E}, \quad (3.1)$$

which essentially states loss-free current transport. Here is $\mathbf{j}_s = n_s e \mathbf{v}$ the superconducting current density, e the elementary charge and n_s the density and m the mass of superconducting charge carriers. An equation describing the behavior of the magnetic field in a superconductor can be found by taking the curl of the first London equation and then applying Faraday's law $\nabla \times \mathbf{E} = -\frac{\partial \mathbf{B}}{\partial t}$ to it:

$$\nabla \times \mathbf{j}_s = -\frac{n_s e^2}{m} \mathbf{B} \quad (3.2)$$

This is the second London equation. Using Ampere's law $\nabla \times \mathbf{B} = \mu_0 \mathbf{j}$ gives

$$\nabla^2 \mathbf{B} = \frac{1}{\lambda_L^2} \mathbf{B}. \quad (3.3)$$

with the one dimensional solution $B(x) = B_0 e^{-x/\lambda_L}$, which means that the magnetic field inside the superconductor decays on a length scale of λ_L , in accordance with the Meißner-Ochsenfeld effect. The characteristic length

$$\lambda_L = \sqrt{\frac{m}{\mu_0 n_s e^2}} \quad (3.4)$$

is called the *London penetration depth*. λ_L is on the order of 50 nm for many superconductors. The energy it costs to expel the field provides a simple explanation that superconductivity breaks down for high enough magnetic fields.

3.3. BCS theory

As mentioned in the introduction, the BCS theory provides a microscopic understanding for superconductivity. A short overview over this theory is given here for the sake of completeness. The key ingredient for the BCS theory is the formation of cooper pairs [72], bound states of conduction electrons with opposing spin and momentum. The origin of the attractive interaction can be qualitatively understood by considering the deformation of the crystal lattice caused by an electron moving through it. The polarization of the lattice can overcompensate the coulomb repulsion and attract another electron as shown in figure 3.2.

This electron-electron interaction through the exchange of phonons happens on a distance of 100–1000 nm, which is much larger than the lattice spacing, therefore many cooper pairs overlap. This length ξ_0 is called the BCS-coherence length and is not to be confused with ξ_{GL} .

The typical binding energy of a cooper pair is on the order of 1 meV, hence the pair formation is a low temperature phenomenon. The BCS theory predicts a maximum critical temperature on the order of 30–40 K, depending on the Debye temperature of the metal and the coupling of the electrons.

Since a cooper pair is formed by two fermions, it possesses an integer spin and is not bound by the Pauli exclusion principle. This means that all cooper pairs will occupy the same ground state and move coherently through the lattice as a macroscopic matter wave [69].

The pair formation results in an energy gap Δ between the ground state occupied by the cooper pairs and the excited states. The energy gap is larger than the highest possible phonon energy, so the cooper pairs can not exchange energy with the lattice and move without dissipation.

Another important consequence of the macroscopic wave function is the flux quantization. The magnetic flux through a superconducting ring can only be integer multiples of the magnetic flux quantum Φ_0 , since the wave function must reproduce itself during one turn around the ring.

Many experiments confirmed the predictions of the BCS theory. Gor'kov derived the Ginzburg-Landau equations (see next section) from the BCS theory [70] and allowed to

3. Superconductivity

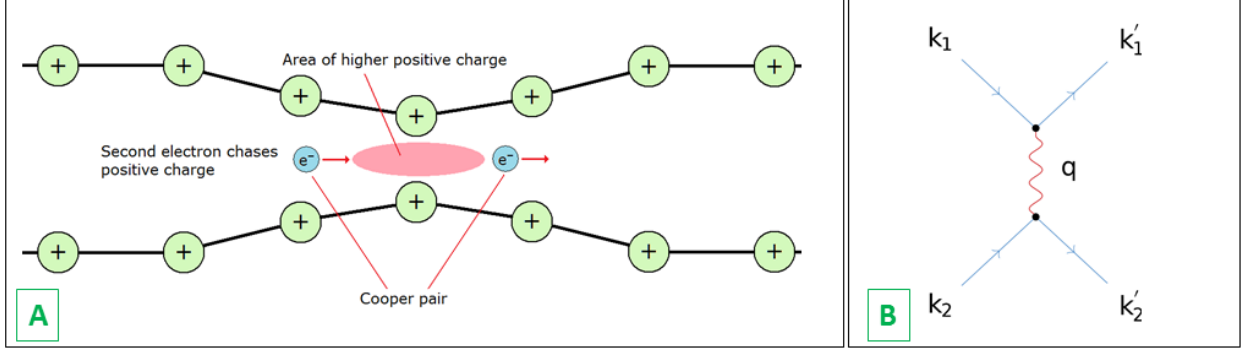


Figure 3.2.: A: Illustration how the lattice deformation can lead to an attractive force between electrons, from [73]. B: Feynman diagram of the phonon exchange. Two electrons with opposing wave vectors k_1 and k_2 interact through the exchange of a phonon q . From [74].

identify the order parameter Ψ in the Ginzburg-Landau theory with the Cooper pair wave function.

3.4. Ginzburg-Landau theory

Even without any knowledge about the microscopic origin of superconductivity, thermodynamic considerations have provided a very successful theoretical framework. The experimental observation that the heat capacity for many superconductors jumps at the critical temperature indicates a second order phase transition, for which Lev Landau has elaborated his famous theory. It is based on the construction of the free energy as a sum of the high-temperature case and a function of an order parameter Ψ . This function is a power series in Ψ which can be found by considering the symmetry of the ordered state [75]. By minimizing the Landau free energy for a given set of external parameters such as temperature and pressure, the stable state can be found. Ginzburg and Landau applied this theory to the superconducting phase transition, where $|\Psi|^2$ was identified as the density of the superconducting charges. The free energy in the Ginzburg-Landau theory is

$$F = F_n + \alpha|\Psi|^2 + \frac{\beta}{2}|\Psi|^4 + \frac{1}{2m^*} \left| \left(\frac{\hbar}{i} \nabla + e^* \mathbf{A} \right) \Psi \right|^2 + \frac{|\mathbf{B}|^2}{2\mu_0} \quad (3.5)$$

with the free energy in the normal state F_n , the effective mass of the charge carriers m^* , phenomenological parameters α and β , the vector potential \mathbf{A} and the magnetic induction \mathbf{B} . The last term describes the energy required to expel the external field \mathbf{B} and the penultimate term takes local variations of Ψ into account, which is of particular importance for the understanding of type II superconductors in section 3.5. As shown in the BCS theory (section 3.3), the effective charge e^* corresponds to the charge $2e$ of paired electrons. Above the critical temperature T_C , the complex order parameter Ψ is zero and the material is in its normal state. Minimizing the free energy leads to the two Ginzburg-Landau equations

$$\alpha\Psi + \beta|\Psi|^2\Psi + \frac{1}{2m^*} \left(\frac{\hbar}{i} \nabla + e^* \mathbf{A} \right)^2 \Psi = 0 \quad (3.6)$$

and

$$\mathbf{j} = -\frac{2e}{m^*} \text{Re} \left\{ \Psi^* \left(\frac{\hbar}{i} \nabla + e^* \mathbf{A} \right) \Psi \right\} \quad (3.7)$$

where \mathbf{j} is the current density, Re the real part and Ψ^* the complex conjugate of Ψ . Without an external field, equation 3.6 simplifies to

$$\alpha\psi + \beta|\psi|^2\psi = 0 \quad (3.8)$$

with the non-trivial solution

$$n_s = |\Psi|^2 = -\frac{\alpha}{\beta} \quad (3.9)$$

Using this relation between the order parameter and the superconducting carrier density n_s , we can write the London penetration depth (eq. 3.4) as a function of Ψ :

$$\lambda_L = \sqrt{\frac{m^*}{4\mu_0 e^2 |\psi|^2}} \quad (3.10)$$

With this, the the second London equation (eq. 3.2) can be recovered from the second Ginzburg-Landau equation 3.7 by assuming a spatially constant Ψ . From the first Ginzburg-Landau equation 3.6, another characteristic length, the Ginzburg-Landau coherence length ξ_{GL} , can be found. It is given by

$$\xi_{GL} = \sqrt{\frac{\hbar^2}{2m^*|\alpha|}}. \quad (3.11)$$

Both of these characteristic lengths vary with temperature according to

$$\lambda_L(T) = \frac{\lambda_L(0)}{\sqrt{1 - T/T_C}} \quad \text{and} \quad \xi_{GL}(T) = \frac{\xi_{GL}(0)}{\sqrt{1 - T/T_C}}. \quad (3.12)$$

At $T = T_C$, both quantities approach infinity. Another important quantity is the thermodynamic critical field B_{cth} which is defined as the energy difference between the superconducting and the normal conducting case

$$F_n - F = -\alpha|\psi|^2 - \frac{1}{2}\beta|\Psi|^4 = \frac{1}{2\mu_0} B_{cth}^2 \quad (3.13)$$

For a detailed derivation and discussion of these equations, refer to [76].

3.5. Type II superconductors

All superconductors can be categorized in two types, according to their behavior under an applied field as is illustrated in figure 3.3. Type I superconductors expel an external field completely from their interior. They are perfect diamagnets and they remain in this so called Meissner phase until superconductivity breaks down at B_c . Type II superconductors go from the Meissner phase to the mixed phase at the first critical field B_{c1} , then the field can partially penetrate the material up to B_{c2} .

3. Superconductivity

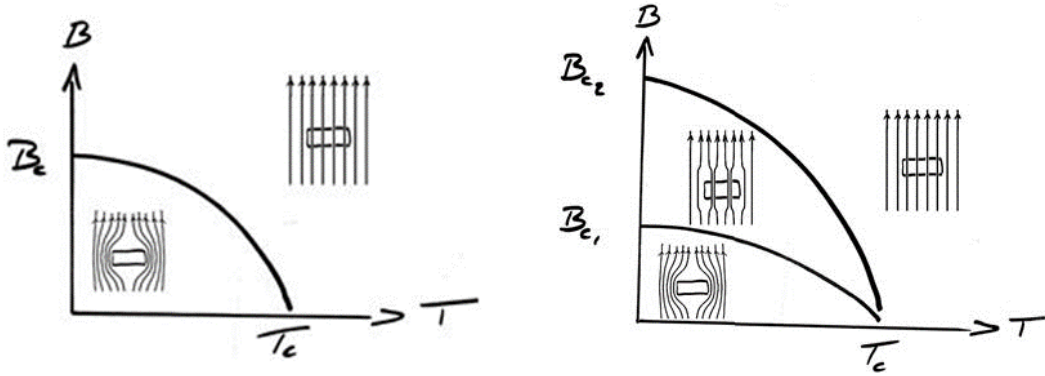


Figure 3.3.: The phase diagram for a Type I superconductor (left) and a type II superconductor (right). In type I superconductors, the magnetic field is completely expelled until superconductivity breaks down. In type II superconductors, a mixed phase, the so called Shubnikov phase appears and lets the magnetic field partially penetrate the sample in form of vortices. From [77].

This behaviour is not covered by the BCS theory. From the Ginzburg-Landau theory however, the nature of this flux penetration can be derived. The ratio

$$\kappa = \frac{\lambda_L}{\xi_{GL}} \quad (3.14)$$

between the penetration depth and the coherence length is called the *Ginzburg-Landau parameter* and plays an important role in the classification of superconductors. The surface energy σ_{ns} between the superconducting and normal conducting phase lowers with increasing κ and vanishes at $\kappa = 1/\sqrt{2}$. Materials with $\kappa < 1/\sqrt{2}$ are type-I superconductors. They show perfect diamagnetism until the external field exceeds the critical field, where superconductivity breaks down. Type-II superconductors on the other hand have a larger Ginzburg-Landau parameter $\kappa > 1/\sqrt{2}$, which results in a negative surface energy σ_{ns} . It is thus energetically favorable to establish superconducting-normal conducting boundaries. Most superconducting materials other than pure elemental superconductors actually fall in this category.

Beyond a first critical field H_{C1} , type-II superconductors let an external field penetrate the sample in the form of quantized flux lines. Superconducting vortices consist of a normal conducting core surrounded by circular supercurrents, see figure 3.4 B. The vortices arrange in a triangular lattice, the Abrikosov vortex lattice, which was derived from the Ginzburg-Landau theory [68]. An image of the vortex lattice is shown in figure 3.4 A. The lattice constant decreases up to the second critical field H_{C2} , where the material stops being superconducting. The partial penetration of the magnetic field in this so called mixed state (or Shubnikov phase) means that less expulsion energy is required, which allows much higher critical fields than in type-I superconductors. Each vortex contains a magnetic flux of

$$\Phi_0 = \frac{h}{2e} = 2.068 \times 10^{-15} \text{ Wb}, \quad (3.15)$$

as the cooper pair wavefunction has to reproduce itself after one turn around the vortex.

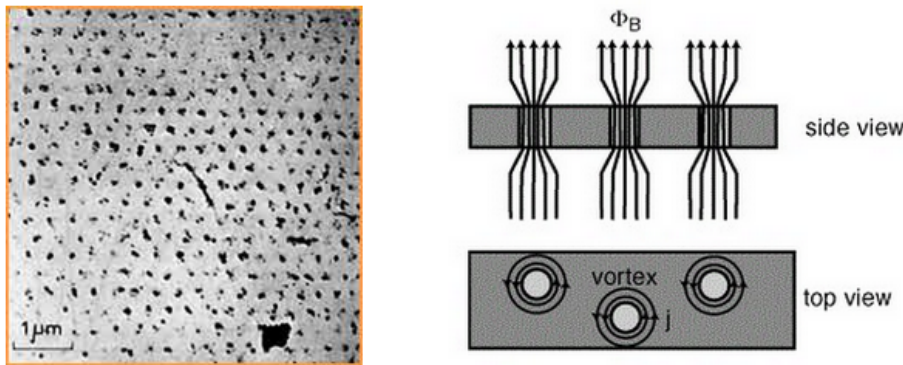


Figure 3.4.: Left: First image of the Vortex lattice in lead at 1.1 K and 195 G, imaged with bitter decoration [78]. Right: Schematic view of the field of superconducting vortices with circular supercurrents around a normal conducting area of radius ξ_{GL} . From [79].

The Lorentz force acts on the vortices and moves them through the superconductor. This is a dissipative process and causes a finite resistance. The flux lines can be pinned to sites in the material, either to natural lattice defects or artificial pinning sites such as dots or antidots. The strength of this flux pinning determines the strength of the Lorentz force (due to a field and/or a current) at which the vortices get depinned and start to move. Superconductors with very strong flux pinning are called hard superconductors and show particularly high critical fields and currents.

3.6. The Bean critical state model (CSM)

The penetration of flux lines and their pinning causes irreversible magnetic behavior in type II superconductors. The difference between the magnetization of type I and II superconductors as well as a typical hysteresis loop for a hard type II superconductor are shown in figure 3.5.

Charles Bean has developed a macroscopic model that describes the magnetization of

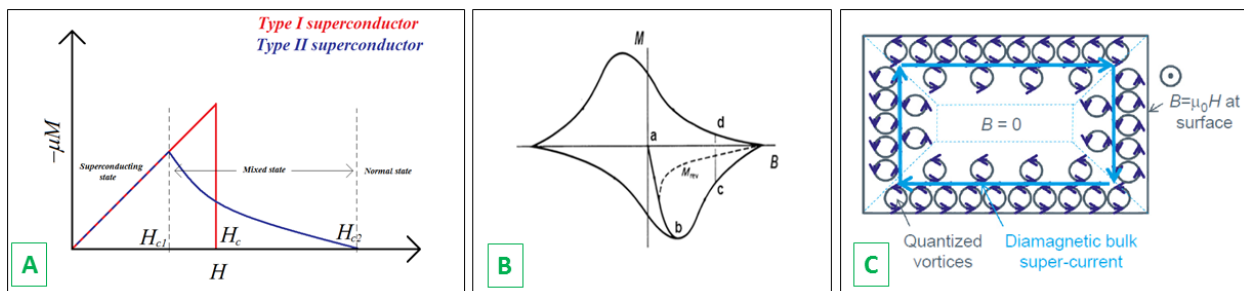


Figure 3.5.: A: Magnetization of a type I and a type II superconductor [80]. B: Hysteresis loop of a type II superconductor. Once the external field has exceeded the first critical field, a remnant magnetization of the sample remains (from [81]). C: The gradient in the vortex density towards the center of the sample corresponds to a macroscopic current loop. From [82].

3. Superconductivity

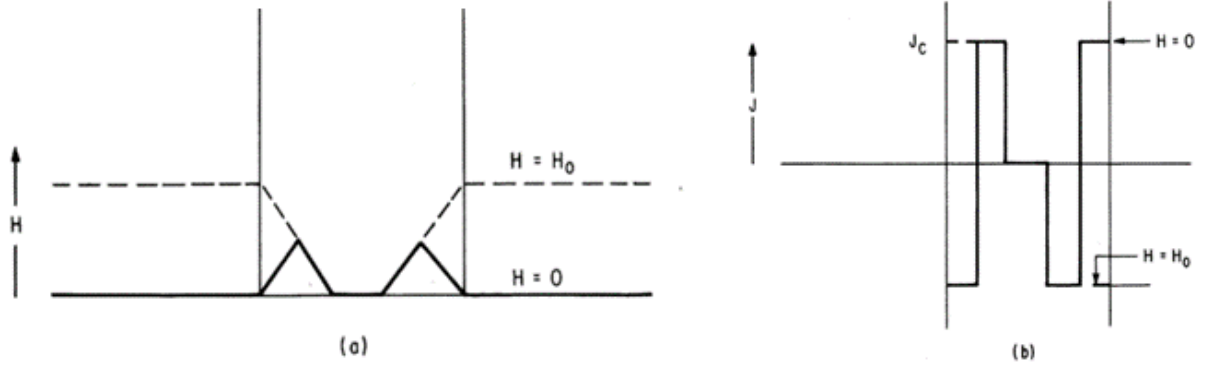


Figure 3.6.: The magnetic field (a) and the current distribution (b) in a slab after applying and removing an external field H_0 , from [84]. The case of a thin film will be discussed in chapter 12.

superconductors [83, 84]. When a field (or equivalently a transport current) is applied to a type II superconductor, vortices nucleate at the surface and a magnetic flux of magnitude $B = n\Phi_0$ (averaged over several intervortex spacings) starts to penetrate the sample, where n is the local area density of vortices. The vortex distribution gives rise to a macroscopic current density $\mathbf{j} = \nabla \times \mathbf{H}$. Whenever the Lorentz force density $\mathbf{F} = \mathbf{j} \times \mathbf{B}$ exceeds the pinning force density, the vortices move in the direction of the force. This process results in a constant field gradient $\mu_0 J_c$, or equivalently, in the current density J_c flowing from the surface up to a certain depth [85]. When the external field is removed, vortices are expelled from the sample such that the field on the surface equals zero. The reversed slope in the magnetic field is equivalent to a macroscopic current density of opposite direction, as shown in figure 3.6. The current density remaining after removing all external fields gives rise to the remnant magnetization of a type II superconductor.

The CSM can be solved analytically for some geometries. The geometry relevant for this thesis is the infinitely long, thin strip. The approximations made to get to the solution are detailed in [85] and the references therein. It should be noted that the field expulsion leads to a deformation of the applied magnetic field as it is wrapped around the sample. Its magnitude is significantly changed, especially at the sample edges. This is of course geometry dependent and described by the demagnetization factor N_m [86]. For a long strip of width $2W$ and thickness d , where $W \gg d$ holds, the field at the edge of a sample is given by[85]:

$$B_{edge} \approx \sqrt{W/d} B_{applied}. \quad (3.16)$$

Typical values for W and d in our chips lead to a field enhancement factor of 20. For non-ideal geometries such as our Z-shaped atomchip, numerical methods are used to find the current distribution, as is described in detail in chapter 12. An important consequence of the CSM is that the current distribution in a superconducting atomchip depends not only on the applied transport current and the perpendicular field, but also on the history of applied fields and currents. This greatly affects the trapping potential and needs to be taken into account, especially for traps closer than the width of the wire. More details of how the atomchip traps are affected by the magnetization currents are given in chapter 12.

The CSM assumes a vanishing first critical field H_{c1} . This condition is fulfilled for hard superconductors such as YBCO¹. Our atomchips are fabricated from Niobium, a superconductor with a critical temperature of $T_c = 9.2$ K, the highest of all elements. The Ginzburg-Landau parameter κ is ≈ 0.81 , close to $1/\sqrt{2} = 0.707$. Even the purest available samples of Niobium $\kappa > 1/\sqrt{2}$. Niobium is therefore a type II superconductor, but its properties vary significantly from those of ideal type II superconductors [87]. The exact values depend strongly on the purity and fabrication of the film and are not easily experimentally accessible. A summary of the properties of bulk Niobium is given in table 3.1. The upper critical field in thin film Niobium can be much larger than in bulk Niobium, because of the enhancement of the Ginzburg-Landau parameter due to film imperfections that act as pinning sites and increase κ [88]. The relatively high first critical field of Niobium limits the applicability of the CSM.

Table 3.1.: Properties of bulk Niobium, from [89, 87, 76, 90]. As mentioned in the text, the exact values can vary significantly from sample to sample, depending on the purity of the material, the growth method and other factors.

Critical Temperature	T_c	9.20	K
Lower critical field (T=0)	H_{c1}	≈ 1400	G
Upper critical field (T=0)	H_{c2}	≈ 4000	G
Energy gap (T=0)	2Δ	2.98	meV
GL coherence length	ξ_{GL}	39-40	nm
Penetration depth	λ_L	32-44	nm
GL Parameter	κ	0.8	
Critical current density	\mathbf{j}_c	5	MA/cm ²

¹Yttrium-Barium-Copper-Oxide

Part II.
Experimental realization

4. Setup overview

This chapter provides an overview on the experimental setup and explains fundamental design decisions that have been made during construction. The starting point for this experiment was the proposal to trap ultracold Rubidium atoms with a superconducting atomchip and to integrate a superconducting microwave resonator on that atomchip [8]. The production of ultracold atoms is done routinely in many labs around the world. All components and techniques necessary for laser cooling and trapping of ^{87}Rb atoms have already been described in textbooks and our group in Vienna is amongst the most experienced atomchip groups. However, the need for a cryostat is a massive complication and there are only a handful of similar experiments around the world [17, 10, 20, 22], none of which has succeeded in creating a hybrid quantum system yet. Our approach to this problem is a separated MOT and cryogenic chamber, and a magnetic conveyor belt transport connecting those two. Transporting ultracold atoms over large distances can be achieved either magnetically [91] or optically [92]. The main reasons for the spatial separation of the MOT and the cryogenic science chamber and the magnetic transport are:

- **Dispenser:** The heat dissipation of an alkali metal dispenser is on the order of 20 Watts, which is way above the cooling power provided by usual cryostats. An initial attempt to design an electron beam driven Rubidium source to use directly inside the cryostat did not produce sufficient atom numbers, even though the energy dissipation was greatly reduced compared to conventional alkali metal dispensers [93].
- **Rapid reconfigurability:** It is possible to work on the cryogenic part of the setup without breaking the vacuum in the MOT chamber. The pumping effect provided by the cold surfaces allows to reach a vacuum level suitable for ultracold atoms within a few days, without any further effort.
- **Vacuum:** The vacuum in the cold science chamber is not affected by the far away Rubidium source. Pressure can be several orders of magnitude below the vacuum in the MOT chamber. This minimizes background gas collisions and allows exceptionally long atom lifetimes.
- **Stray light:** Generally the biggest problem of an optical transport scheme, where atoms are transported along with the moving focus of a laser beam, is the unavoidable stray light. This is irrelevant in a room-temperature experiment, however in a cryostat with limited cooling power and exposed superconductors one has to be very careful. A magnetic transport scheme allows, in contrast, to upgrade the cryostat to a dilution refrigerator, which has a much lower cooling power. Also it is possible to realize non-straight geometries as in [17], where there is no line-of sight between the superconducting surface of the atomchip and any room-temperature element.

4. Setup overview

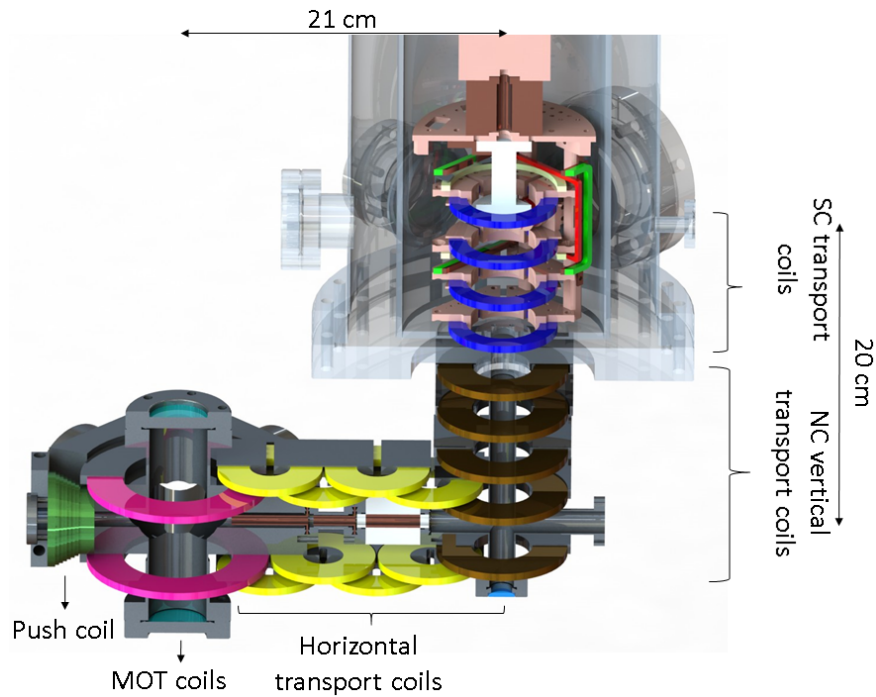


Figure 4.1.: Rendering of the experimental setup. The MOT chamber on the is lower left and the (semi-transparent) cryo chamber on the top right. The transport coils are shown in different colors for clarity. All coils inside the cryostat are superconducting.

Figure 4.1 shows the principal design of our experiment, the vacuum chamber, parts of the cryogenic setup and most of the magnetic coils. In the following chapters I will elaborate on the design of all relevant subsystems. Over time, the complexity of the setup grew and some smaller and larger design flaws became apparent. In every chapter, I will discuss possible future upgrades to the subsystem, many of which are already underway. At the time of writing, the experiment was about to move to another room, which poses an opportunity to actually implement many of these upgrades. The setup is built on a vibration damped optical table, the electronics are located above and below the table. This part of the thesis is structured as follows:

- Chapter 5: the vacuum chamber including pumps, gauges and the dispenser.
- Chapter 6 describes the cryogenic setup with the cryostat, the thermal shields and the "cold stage". This also includes the design and fabrication of our superconducting atomchips and the radiofrequency- and microwave setup.
- All magnetic coils to transport and manipulate the atoms as well as the electronics to produce the required currents for the coils and the atomchip in chapter 7.
- Chapter 8 explains the calculation of the current sequence to move the atoms from the MOT chamber to the cryostat and the simulation tools that were developed to visualize the magnetic trap throughout different current sequences.

- The optical setup for laser cooling, the imaging systems and the optical quenching system are described in chapter 9. This chapter also includes some basics about the frequency stabilization of diode lasers and the imaging of cold atomic clouds.
- The control software, the data acquisition programs and the monitoring systems, which contain probably more working hours than all other systems combined are described in chapter 10.

Overall, this experiment is significantly more complex than other cold atom or atomchip experiments, simply because the number of devices and tools that need to work simultaneously is much larger. Another factor is that much of the know-how had to be acquired, especially the cryogenic engineering and the fabrication of superconducting atomchip.

Just to give one example: One of the superconducting transport coils, for example V6, involves two analog channels, two digital channels, two isolation amplifiers, two current sources including their two power supplies, two switches and one current sensor, plus the associated number of wires, resulting in a setup as shown in figure 4.2. Each additional device and cable is a possible error source. There are important lessons learned during the construction of this experiment, often through painful and time consuming mistakes:

- Keep it simple - wherever possible reduce the number of devices, cables, connections etc.
- Monitor and record as many signals, currents, voltages, light powers etc. as possible. This helps tremendously to find the reason for a given problem, or at least to exclude some factors.
- Build things sturdy.
- Write down everything. In a lab with many people working on different projects, it is important to keep track and document all changes.

4. Setup overview

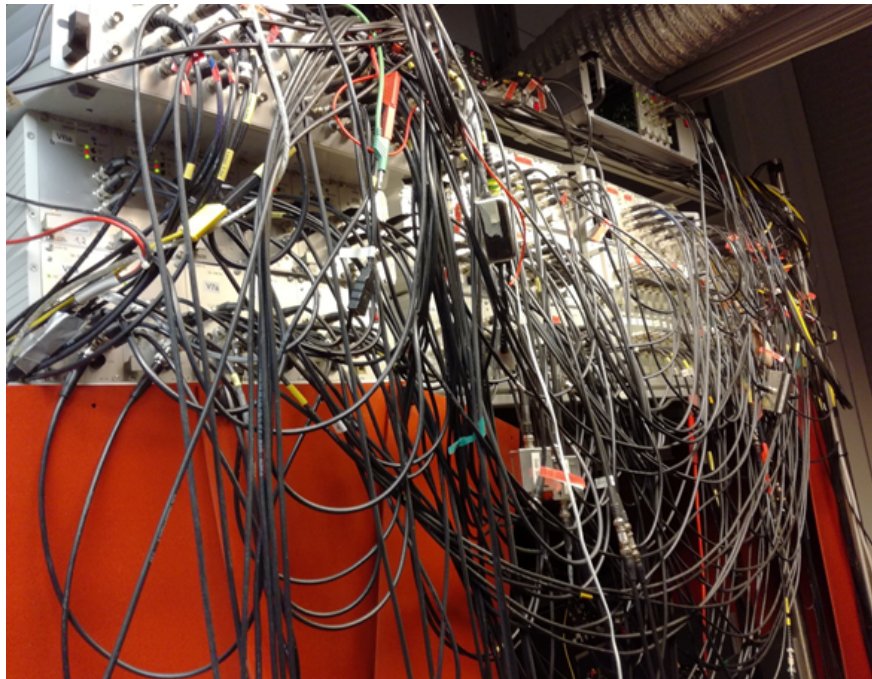


Figure 4.2.: The reality compared to the rendering in figure above. This picture shows a small part of the total wiring, mostly for the superconducting coils.

5. Vacuum system

The vacuum system forms the basis for any experiment dealing with ultracold atoms. As discussed in chapter 2, collisions with background gas particles will kick atoms out of the magnetic trap. From equation 2.14, it can be estimated that the pressure should be on the order of or below 1×10^{-9} mbar for a MOT. To reach this ultra-high vacuum (UHV) conditions means a careful selection of materials, to ensure clean assembly and patience to pump down and bake out the chamber after evacuation. Residual gas consists of remaining air molecules (O_2 , N_2 , CO_2 , Ar), water adsorbed on the chamber walls, organic residues from finger prints or polymer materials and even outgassing from the surface of untreated metals such as aluminum or copper.

Our vacuum system consists of three parts: the MOT chamber, which is constantly kept under UHV conditions, the transport section and the cryochamber. This configuration has the main advantage that it allows frequent upgrades to the cryochamber without the need to pump down the MOT chamber repeatedly.

5.1. The MOT chamber

Ultracold atoms are produced and captured in the MOT chamber. It is a flat stainless steel octagon with optical access for the cooling beams. This chamber connects to a CF-63¹ cross where a 50 l/s ion pump and a pressure gauge are mounted. Another flange is connected to a T-piece which holds the dispenser and an angle valve where a turbo pump can be attached. The MOT chamber and the vacuum assembly around it is shown in figure 5.1.

After assembly, the chamber is connected to a turbo pump with a CF-flange and wrapped with heat tape. The heating significantly speeds up the pump down process as it facilitates desorption of water molecules from the chamber walls. At pressures below 1×10^{-6} mbar, the ion getter pump can be turned on. A typical pump down time with moderate heating at about 150 °C is two weeks to reach 1×10^{-10} mbar.

¹Conflat (=CF) flanges are standard for UHV vacuum connections according to ISO 3669:2017, where stainless steel blades are pressed into a copper gasket

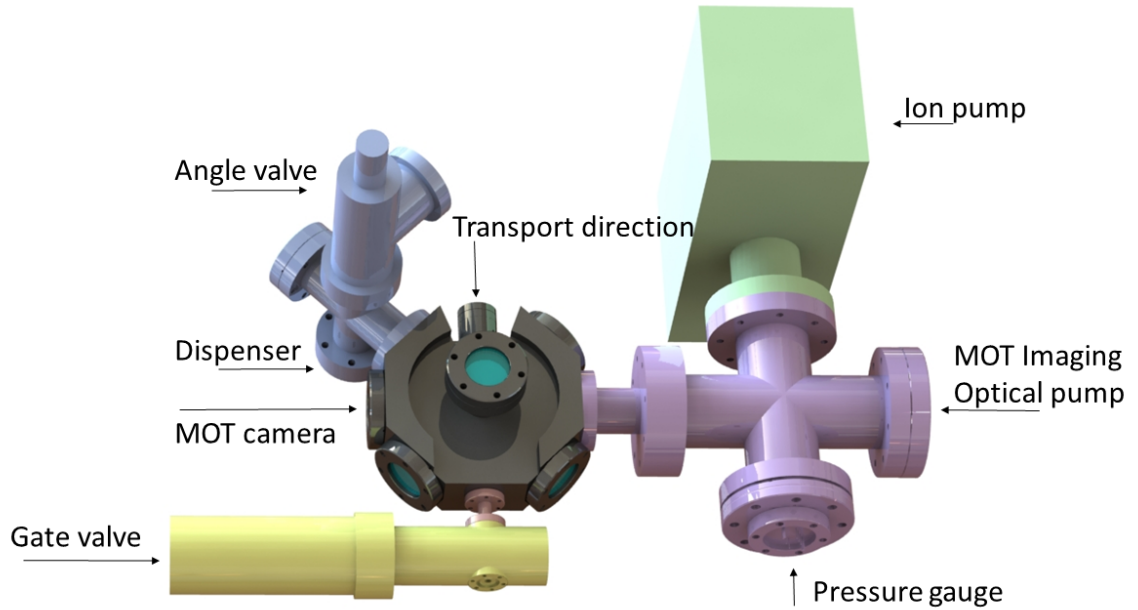


Figure 5.1.: Rendering of the vacuum assembly around the MOT chamber (Top view).

5.2. Rubidium dispenser

As a source for Rubidium vapor alkali metal dispensers from SEAS Getters are used². The dispenser contains Rb_2CrO_4 powder as a Rubidium source and a mixture of 84% Zr and 15% Al as a reducing agent. Upon heating, the Chromate gets reduced and gaseous Rubidium can leave the dispenser through a thin slit at the top of the metal enclosure. The nominal Rb content for this dispenser type is 9.4 mg. We use six dispensers in total, where two times three are connected in parallel, a picture of the electrical feedthrough with the mounted dispensers is shown in figure 5.2. A typical operating current is 12.1 A, which results in ≈ 4 A per dispenser. This is well below their nominal emission onset current of 5.3 A, ensuring a long lifetime of several years. This is desired since a dispenser change means opening the MOT chamber and a time consuming bake out. We operate the dispensers continuously from morning to evening, an optimal Rubidium background is achieved within one hour.

²www.saesgetters.com, RB/NF/14/25 FT10+10

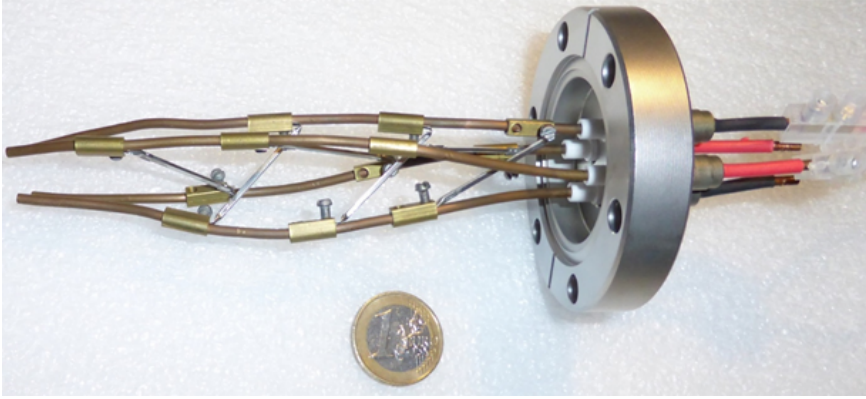


Figure 5.2.: Picture of the vacuum flange with electrical feedthroughs and the attached Ruthenium dispensers. The dispensers can be bent (minimum bending radius 40 mm) to accommodate them between the copper contacts.

5.3. Transport section and cryo chamber

The room temperature part of the magnetic transport is shown in figure 5.4. A 31 mm short tube with an inner diameter of 7 mm connected to the MOT chamber is the starting point for the magnetic transport. This tube is required for the connection of the gate valve. Also, without that tube, one of the mirrors for the MOT would not fit.

In order to maintain a high pressure gradient between the MOT chamber and the transport section, two differential pumping stages were constructed. Instead of using regular copper gaskets between the MOT chamber and the short tube and between the tube and the gate valve, copper inlays were designed to reduce the inner diameter of the tube from 7 mm to 5 mm. The first one reaches 5 cm into the MOT chamber, the second with 2.75 cm almost fills the full length of the tube. The molecular pipe conductivity for a straight tube of length l and diameter d is $\propto d^3/l$, therefore reduced by almost a factor of 3. A pressure gradient of at least two orders of magnitude between the MOT chamber and the cryo chamber can be achieved. However, this very narrow region in the horizontal transport causes significant atom loss.

The UHV gate valve³ separates the MOT chamber from the rest of the setup, which allows us to maintain ultra-high vacuum in the MOT chamber during upgrades on the cryogenic setup. The valve has to be closed whenever the cryostat is not at low temperature, as the pressure increases drastically within minutes after turning off the cryostat. To protect the UHV in the MOT chamber, we built a system to automatically close the valve in case of an unexpected pressure rise in the cryo chamber. This motorized valve operation also minimizes the risk of misaligning the optics when opening or closing the valve manually. The system, shown in figure 5.3, allows carefree overnight operation of the experiment. Details on the design of this motorized valve are given in [94] and [95].

It should be noted that the pressure readings of the two vacuum gauges show quite unexpected behavior in some circumstance. When opening the valve, with a pressure difference of 2 orders of magnitude (typical pressure in the MOT chamber 5×10^{-11} mbar, cryo chamber 5×10^{-9} mbar), the pressure in the MOT chamber actually *decreases* by a factor of 2-3.

³VAT 48124-CE01

5. Vacuum system

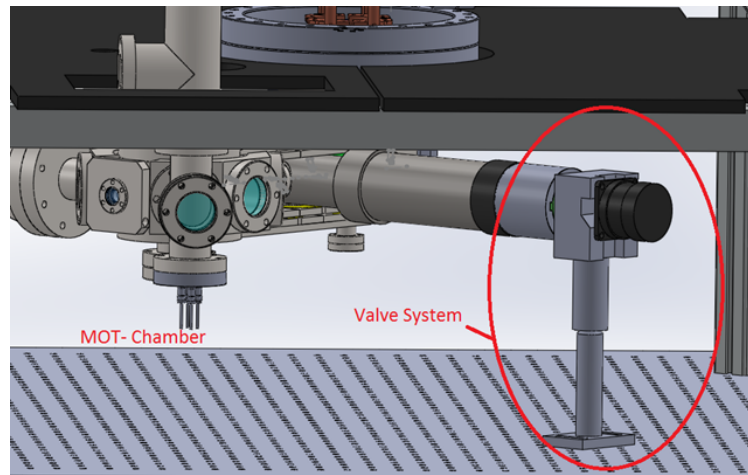


Figure 5.3.: CAD drawing of the motorized valve using a stepper motor. A stepper motor is connected to the gate valve with a torque limiting mechanism. From [95].

A possible explanation for this strange behavior is the location of the cryo pressure gauge, which does not indicate the pressure in the transport tube as it is located far up the cryo chamber.

The transition from horizontal to vertical transport happens in a CF-16 4-way cross after the gate valve. This cross also provides optical access to the chip from below. The baseplate of the cryochamber is directly attached to the top flange of this cross. The 201/s ion pump responsible for the transport section is connected via a short welded bellow in order to minimize any torque on the setup, which could cause vacuum leaks though uneven pressure on the copper gaskets. Since this part of the setup is exposed to atmosphere whenever the cryo is opened, it is permanently wrapped with heat tape. However, it remains the hardest part to evacuate and it takes several days of pumping and cryo-operation before the pressure in this region, and therefore the atomic lifetime throughout transport, reach sufficient values.

The cryogenic part of the experiment rests in a CF-200 chamber which is connected on top of the transport cross by means of a CF-16 to CF-200 adapter flange. This chamber provides optical access to the experimental stage through four windows and it holds a pressure gauge. For pumping, a turbo pump is directly connected to a full-metal angle valve at the top of this chamber. The performance of this turbo pump is crucial for the time required to start experimenting after the cryostat has been switched off. The pressure gauge is located about 20 cm above the windows. The space between the 50 K shield and the outer chamber is very narrow, the pressure indicated by the vacuum gauge is certainly not valid in the transport tube and only serves as a reference. The pressure within the thermal shields is probably orders of magnitude below the value indicated by the gauge.

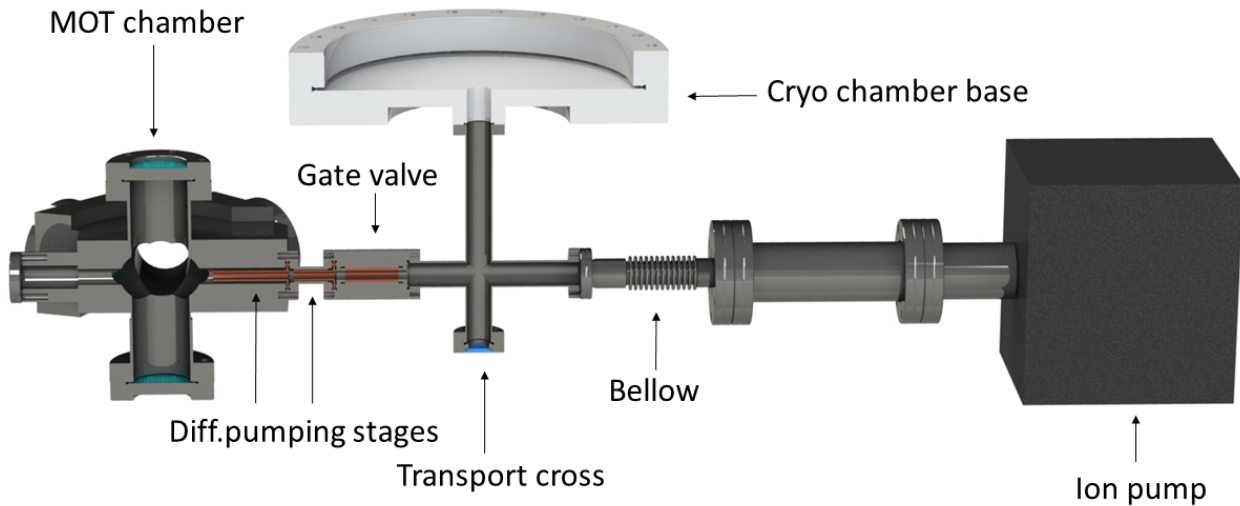


Figure 5.4.: Cut through the horizontal transport section without coils, just vacuum components. From left to right: the flange holding the push coil, the MOT chamber, the short tube with the copper inlay, the gate valve, the CF-16 cross and the corner ion pump. At the top, the CF-16 cross is connected to the baseplate of the CF-200 cryo chamber.

5.4. Upgrades to the vacuum system

The current setup has several drawbacks which should be resolved in the next overall upgrade. Some bigger and smaller suggestions:

- Removal of the differential pumping stage to avoid unnecessary atom loss. The copper inlays reducing the diameter of the transport tube are not necessary to maintain a pressure gradient.
- A flat UHV gate valve⁴ between the cross and the cryo chamber would drastically reduce the time required after any operation on the cryogenic setup and therefore allow a truly rapid reconfigurability which would essentially just be limited by the cool down time of the cryostat. Right now the evacuation time of the transport line is the limiting factor. It takes at least two weeks after closing the chamber before proper transport efficiencies are reached. The positions of some vertical transport coils might change a bit when installing this valve, but can be quickly implemented in the sequence with the new controller (see section 10.3). Even if this valve contains magnetizable steel components, we expect a negligible magnetization as the fields in vertical transport point both ways and the distance to the atomchip is still significant.
- Improve the heater tape installation in the transport section to reach higher temperatures for a faster pump down. Given the massive obstructions around our MOT chamber, a permanent heater solution could also be installed there during the next dispenser replacement, to save time in the future.

⁴For example the VAT Series 010 with the "insert" option.

5. *Vacuum system*

- An additional T-piece before the ion pump in the corner to install a pressure gauge at this critical section.
- Upgrade the 20 l/s ion pump. It has been exposed to atmosphere every time the cryo was open and has been operated under high load. A new and more powerful ion pump would certainly benefit the setup and reduce transport losses.

6. Cryogenic setup

For a complex cryogenic setup with superconducting coils, a large number of current carrying cables and optical access from several directions, many aspects need to be considered, from the choice of materials to proper assembly and operation. Numerous details of the setup seem very mundane at this point, but required significant trial and error, especially the thermal anchoring of the wires. The first decision to be made is of course wet cryostat versus a closed-cycle cryocooler. Despite the higher cooling power of wet cryostats and their inherent vibration free operation, closed-cycle cryocoolers are far more practical in daily use as they are essentially turn-on devices. There is no need for manipulating dewars or a dependence on a steady liquid helium supply. In this chapter, I will first describe our cryocooler and provide some important details for its operation and maintenance, after which the specifics of all components within the cryo chamber are presented.

6.1. Closed cycle cryocooler

The cryostat used in this experiment is a Gifford-McMahon (GM) closed cycle cryocooler¹. In a GM cryocooler, a mechanical piston moves up and down, forcing Helium through a regenerator material. A rotary valve connects the cold head alternately to the high- and low pressure side of a Helium compressor. First, high pressure Helium is pushed through the regenerator down to the expansion volume, now the low pressure side is connected and the expansion leads to cooling. The cold gas is then pushed through the regenerator upwards and the cycle starts over. The cooling power of the cold finger is 800 mW at 4.2 K and 8 W at 10 K. Our system consist of four components:

- A water cooled **Helium compressor** with an electric power of 7.7 kW. It supplies about 100 m³/h at a pressure of around 22 bar, the return pressure is 6 bar. Since it is a bulky and loud machine, it is located on the attic two floors above the lab². The compressor can be switched on and off from the lab via a relay. The compressor is constantly water cooled, if the water supply is interrupted it turns off withing a few minutes.
- **Helium lines** from the compressor down to the lab. The first part is done with copper tubes, the last few meters with flex lines such that the cold head can be moved without disconnecting the Helium lines.

¹ARS DE210S cold finger with GMX20-B vibration isolation interface, Advanced Research Systems Inc., Macungie, PA - USA

²We measure a considerable potential difference (>100 mV) between the attic electrical ground, brought to the lab by the helium lines, and the optical table. To avoid interference, we made sure to isolate the helium lines and the cold head completely from our lab ground.

6. Cryogenic setup

- The actual **cold head** with an electric motor for the rotary valve and the Helium supply and return connectors. The piston is actuated pneumatically. The current for the electric motor is supplied by an inverter in the compressor. The cold head is mechanically isolated from the UHV setup.
- The **vibration isolation interface** connects to the CF-200 flange at the top of the cryo chamber and is part of the UHV vacuum setup. For work on the cryogenic setup, the vibration isolation interface and the actual cold head are connected with metal plates and can then be pulled out of the cryo chamber together. During operation, cold head and vibration isolation interface are connected only with a rubber bellow. Four flanges on the vibration isolation interface hold the electrical feedthroughs for the cryogenic setup.

Gifford-McMahon cryocoolers produce significant vibrations due to the moving piston. The vibrations have an amplitude on the order of millimeters, therefore efficient damping is required. This is achieved through a Helium filled heat exchange volume between the actual cold head and the vibration isolation interface, which is part of the vacuum setup. The vibrating cold finger has no mechanical contact to the experimental stage, while heat can still flow through a thin layer of Helium. This reduces the vibration amplitude below 5 nm. At the tip of the cold finger, a copper spiral increases contact surface with the Helium to facilitate heat transfer. The cold head and the vibration isolation interface are shown in figure 6.1.

Another problem are contaminations in the working gas. Any gaseous contamination will be solid at 4.2K and block the porous regenerator material (a polymer powder with very uniform size distribution), thus reducing the cooling power.

While this cryostat can be turned off and on by just pressing a button, it still requires quite some maintenance in order to provide a low base temperature. The most important issue is to keep the Helium in the system very clean and at the correct pressure level. When refilling Helium into the system, great care has to be taken not to displace oil in the compressor. This can also happen when moving or tilting the compressor. If oil gets displaced and enters the Helium lines and subsequently the cold head, the porous regenerator material will get contaminated. This requires the entire system to be sent to the factory, pretty much the worst case scenario. The following list of maintenance measures is our standard procedure when the base temperature is too high, in order of complexity, cost and time:

- The mechanical alignment between cold head and vibration damping interface has to be within specifications. If the cold head is not parallel to the table or the distance is too large, either vibrations will be transmitted to the experiment or the heat transfer does not work efficiently. When the top of the vibration isolation interface gets cold or even shows water condensation, the alignment has to be checked.
- After an extended period of operation, a brief (30 min) switch off helps to remove any frozen contaminants from the regenerator, such as Hydrogen, Oxygen, Nitrogen or Argon.
- Helium is lost from the system and needs to be refilled regularly. It is very important to refill the gas very slowly in order not to displace any oil in the compressor, which might contaminate the flex lines and the cold head.

- A full gas cleanup, which means to release and refill all Helium from the system several times, can help if contamination of the gas is suspected. After this procedure, the system should rest for 24 hours and then the compressor should be operated for another 24 hours without the Helium lines connected. The internal overpressure valve allows the gas to circulate inside the compressor, eventually returning all oil to its reservoir. This measure is not described in the manual but has been suggested by an ARS technician.
- The vibration isolation interface is filled with Helium at a slight overpressure of 80 mbar, so no ambient air should be able to enter. However, we notice significant corrosion on the copper surfaces in there and also found water drops at several instances. Such oxidized surfaces can reduce the heat transfer efficiency. This can be cleaned by using an acidic detergent solution³.
- The adsorber within the compressor can be replaced. This device is intended to keep the Helium gas clean. However, we never saw a noticeable improvement.
- A factory service of the cold head is suggested every 12000 operating hours, due to mechanical wear of the seals and the rotary valve inside the cold head. ARS has no service center in Europa, making this a very time consuming undertaking. A clear indication that it is time for such a service are abnormal sounds from the rotary valve.

³Extran with phosphoric acid, pH 2

6. Cryogenic setup

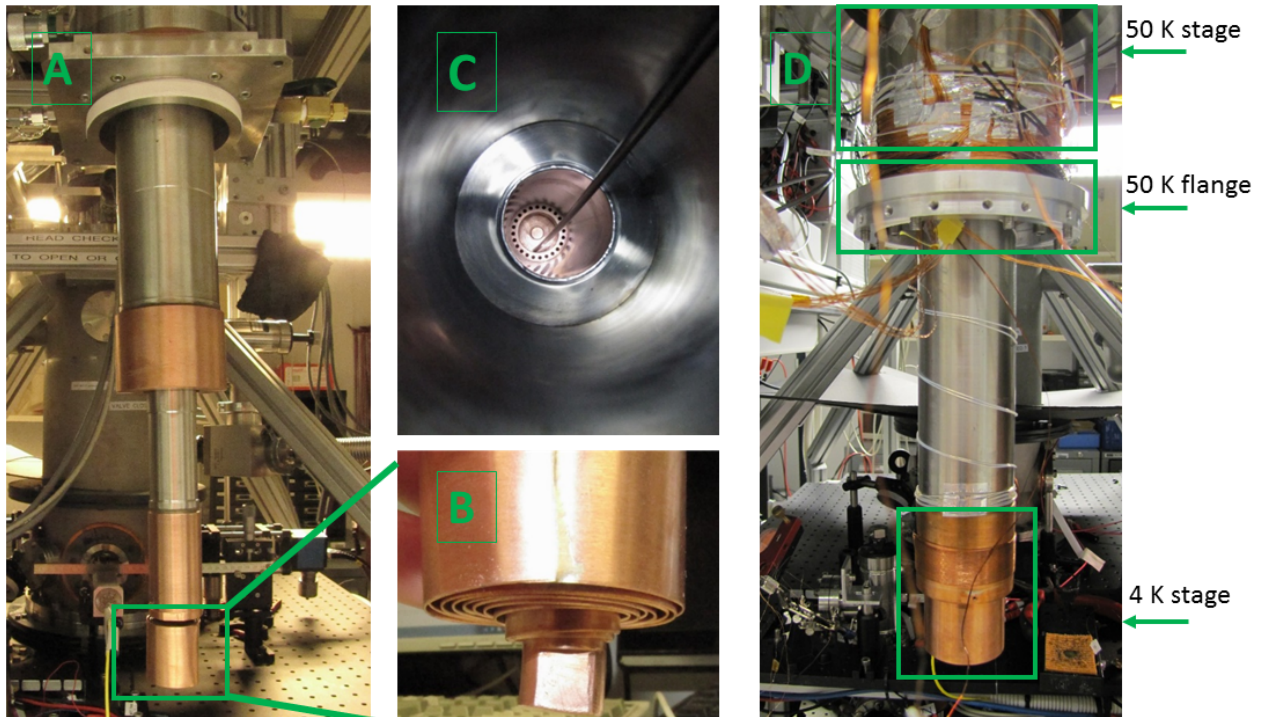


Figure 6.1.: A: The bare cold head. B: The copper spiral at the tip of the cold head. C: The Helium side of the vibration isolation interface where the cold head rests. The holes in the bottom increase the contact surface for better heat conduction. D: The vacuum side of the vibration isolation interface, with the 50 K stage on top, the mounting ring for the 50 K shield and the 4 K stage with the adapter for the baseplate.

6.2. Thermal shielding

To achieve a low base temperature it is necessary to shield the setup against thermal radiation. This is done in two stages, at 50 K and at 4 K. The cold finger provides a connection at the upper stage of the cryostat, which is at around 50 K. The first shield is a cylinder made of pure Aluminum for its better heat conduction. It should exhibit a low temperature gradient between the upper and the lower side, while maintaining a very high temperature gradient between inside and outside. To achieve this, several alternating layers of a plastic net (actually a mosquito net) and mylar⁴ foil are wrapped around the aluminum cylinder. The net acts as a spacer, while the mylar reflects thermal radiation. With this technique, we achieve a very large temperature gradient. The measured temperature on the outside is on the order of 180 K, while the aluminum body is at 50 K. Four anti reflection coated windows are mounted with steel rings. They are made from SF57 glass which exhibits low stress induced birefringence. The complete 50 K shield is shown in figure 6.2.

The 4 K shield is mounted directly at the baseplate of the experimental stage. It is a 3D printed cylinder, the material is polylactic acid (PLA) with unknown thermal properties but good performance so far, since we did not experience any deformations or cracks after many thermal cycles. We assume that the material has a very low thermal conductivity at 4 K, like most non-conducting materials. It is also wrapped with mylar and mosquito net in several layers. The windows for optical access are mounted with aluminum tape. In the Ioffe imaging direction, we use a lens instead of a window, for details refer to subsection 9.3.3. At the bottom there is only one layer of mylar, with a hole where the atoms get transported through. The complete 4K shield is shown in figure 6.2.

Apart from shielding thermal radiation from the respective outer layer, the shields also create almost closed volumes with only one opening, namely the hole in the bottom where the atoms get transported through. At UHV conditions, this means that significant pressure gradients between the inside and outside of the shields can be achieved. Pressure measurement at the cryo chamber happens necessarily between the outer chamber and the 50 K shield. We therefore assume that the pressure inside the 4 K shield is several orders of magnitude below the measured value of typically 1×10^{-10} mbar, given the strong cryopumping effect of the cold surfaces.

⁴aluminized and stretched PET foil

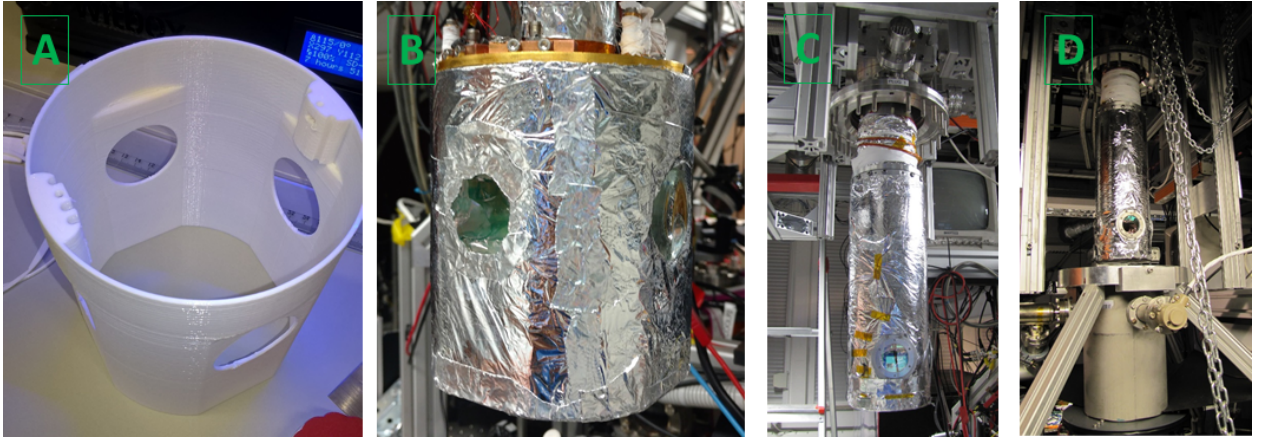


Figure 6.2.: A: The 3D printed 4K shield. B: The 4K shield with mylar isolation and windows mounted on the experimental stage. C: The mounted 50K shield. D: The full assembly before being lowered into the cryo chamber.

6.3. Cryostat wiring and soldering

The superconducting coils and the atomchip require 26 electrical connections at the 4 K stage and each of our four temperature sensor also needs four wires. We have two 20 pin connectors and one 10 pin connector⁵ installed, leaving several spare wires for future upgrades.

Having a large number of wires connecting the room temperature feedthroughs and the 4 K stage means that there is a significant heat load on the cryostat. In order to minimize this, and therefore reach a lower base temperature, careful thermal anchoring is necessary. There is a trade-off between thick and short wires, which means lower heat dissipation when operational, and long, thin wires to reduce the heat transport along the wires.

Our wiring scheme uses 4 m long enamelled copper wire with a diameter of 0.4 mm. These wires are twisted in pairs and soldered to the inside of the feedthroughs with UHV suitable solder. The wire pairs are wound around the upper stage of the cold finger. For the first windings, nylon screws act as spacers between the warm wires and the cold cryostat surface, in order to acquire some cable length between the electrical feedthrough and the first thermal anchoring. Then the wire pairs are carefully anchored on the cold head, ensuring maximum contact between the wires and the cold metal at around 50 K, this is shown in figure 6.3 A. All wires are fed through a small slit in the first stage to the second stage. Here, the cold finger has a temperature of around 20 K, figure 6.3 B. Again, the same method is used for anchoring: one round with nylon spacers and then one round of proper thermal contact.

Direct soldering of the copper wires to the superconducting Niobium-Titanium⁶ wires has proven to be very unpredictable in terms of critical current, despite all efforts. To overcome this, we use a commercial high-temperature superconductor (HTc) tape⁷ in between the low temperature superconductor and the copper wires. The HTc tape has a critical temperature of around 90 K, meaning that the heat transported or produced by the copper wires or the solder contacts will not quench the HTc superconductor. We electrically isolate the

⁵Amphenol Circular MIL Spec UHV feedthrough, wire size AWG16

⁶Type 54S43 copper stabilized multifilament NbTi wire, 127 μm diameter, Supercon Inc.

⁷SCS2050-AP Superpower Inc.

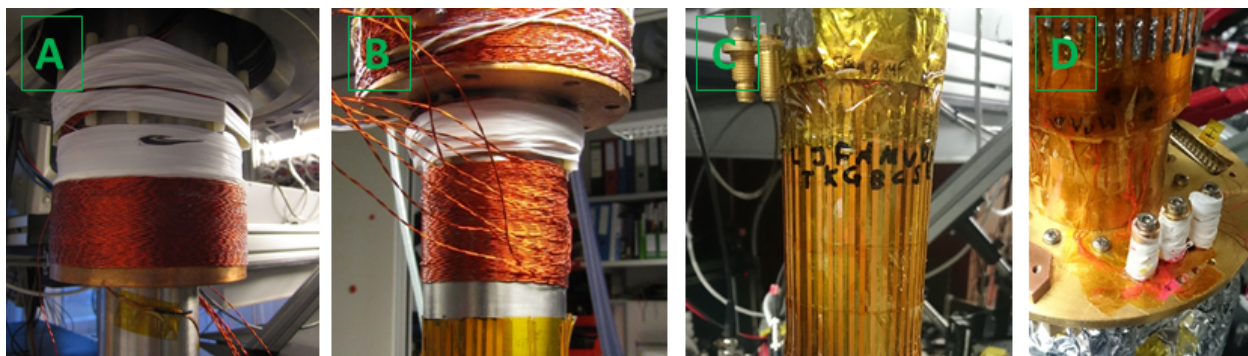


Figure 6.3.: A: The twisted pair wires are first wound around nylon spacers, before being carefully anchored to the 50 K stage. B: Copper wire anchoring at the 20 K stage. C: The HTc tapes going down the cold finger. D: The solder joints between the HTc tapes and the NbTi wires. The excess wire length is wound around copper bobbins and covered with Teflon tape.

cold finger with Kapton tape and fix the HTc to it, shown in figure 6.3 C. The tape with its flat shape is in very good thermal contact to the cold finger, despite the Kapton tape underneath. Since the HTc tape has a copper layer on top, it is very easy to solder on. Removing the isolation from the NbTi wires is however tricky, since the wires are too thin for any mechanical tools. We first scratch the isolation with a sharp blade and let the wire then soak in concentrated formic acid for around five minutes. The Polyimide isolation gets soft and can be wiped off the wire with a tissue.

With this method we achieve reproducible critical currents for all coils. The limiting factor is actually not any of the superconductors (which are all rated for very large currents, 50 A for the HTc and >10 A for the NbTi wires) or the normal conducting solder joints, but rather the copper wire itself. At currents of around 5 A, the wire heats up and the enamel burns off. This happens directly at the feedthrough, where the temperature and therefore the specific resistance is maximum.

6.4. Experimental stage

The main experimental stage is shown in figure 6.4. It holds all superconducting coils and the atomchip. It is made from oxygen-free copper to ensure maximum thermal conductivity and is gold plated to prevent oxidizing. This material is however very soft such that threads can be damaged easily. The circular baseplate is connected to the cold finger with a cylindrical adapter piece. Four massive copper rods mounted under the base plate make sure the temperature gradient between the base plate and the coil mountings remains small. The transport coil mountings for the four superconducting vertical transport coils V6-V9 are quadratic copper structures, which were cut in four quadrants and glued together with Stycast to minimize the formation of eddy currents. The designations for all superconducting coils are shown in figure 7.5.

The Ioffe coil mounting is fixed with elongated holes to allow a variation of the position, this is unfortunately not a very accurate procedure such that the exact value of the Ioffe current needed to produce a QUIC trap varies slightly whenever we open the cryostat, see

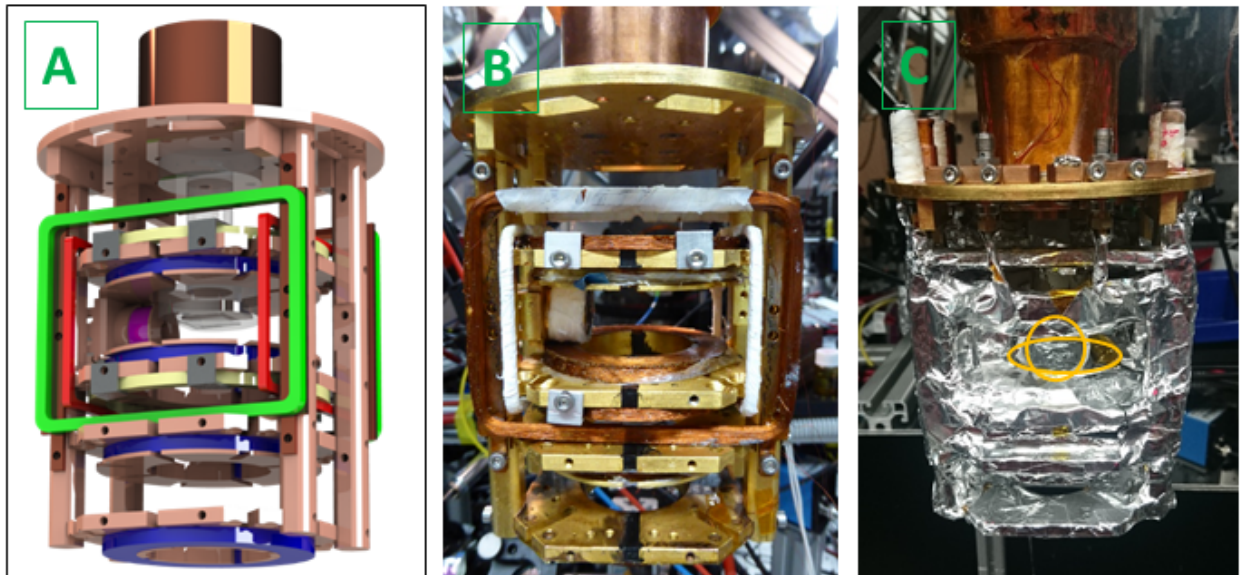


Figure 6.4.: A: Rendering of the experimental stage, showing the transport coils V6 - V9 (blue, from bottom to top), the Ioffe coil (pink), the bias coils for the main imaging direction (called "HBIM", green), the bias coils in Ioffe direction ("HBIO", red) and the vertical bias coils ("BV8" and "BV9", yellow). The chip mounting is semi-transparent. B: A picture of the experimental stage with all coils mounted, without chip mounting. C: Before the 4K shield is mounted, all coils are covered with aluminum tape. The orange circles mark the two RF coils.

section 11.3. The vertical bias coils are placed on the mountings of V8 and V9, held by small aluminum clamps. The rectangular bias coils in the Ioffe direction (HBIO) are just anchored on their vertical sides, the horizontal part of these coils is free standing. The horizontal bias coils for the main imaging direction (HBIM) have an additional mounting frame underneath. Both, HBIO and HBIM, are connected in series to form Helmholtz coil pairs. The solder joints between the NbTi wires are realized using a short piece of HTC tape, anchored on the base plate. The geometric and magnetic properties of all superconducting coils are given the next chapter.

All coils have around half a meter of excess wire on each side to allow several solder joint replacements. All the excess wires are wound around copper bobbins screwed into the baseplate for thermal anchoring. The coils are shielded with Teflon tape and aluminum tape, such that no NbTi wire is exposed to light, this proved to be a crucial point in achieving reproducibly high critical currents. Repeated rerouting of the cables eventually causes wear on the isolation of the NbTi wires which creates shorts to ground. Since all materials (the cage, the isolation, the wire) have very similar colors, these small defects are very hard to find. We use pink nail polish for cable repair, cf. figure 6.5. This material is very elastic at room temperature and forms contiguous layers. For the NbTi wires, this very simple and cheap solution turned out to work perfectly even after many thermal cycles. The semi-rigid coax lines on the other hand seem to have a different thermal expansion coefficient, making the nail polish fall off after the first thermal cycle.

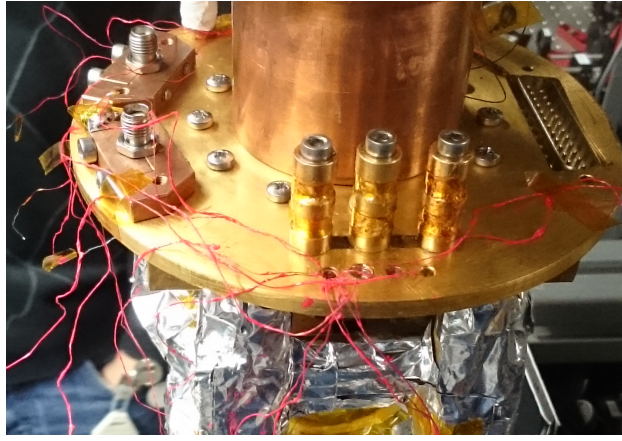


Figure 6.5.: The damaged isolation of the NbTi wires is repaired using pink nail polish.

6.5. High frequency setup

Evaporative cooling, the microwave antenna and the superconducting microwave resonators require several coaxial cables down to the 4K stage. The fourth flange on the vibration isolation interface holds four SMA feedthroughs⁸ for the radiofrequency and microwave signals. On the inside of the SMA feedthroughs, 1 m long, Kapton isolated UHV compatible coax cables⁹ are connected. These are only loosely wound around the upper stage, without thermal anchoring. The wires are then connected to semi-rigid coax cables¹⁰, which penetrate the mounting ring for the 50 K shield. To bridge temperature gradients, we use stainless steel cables because of their lower thermal conductivity and copper wires for connections within the same temperature. A 90 cm long zig-zag line leads from the 50 K stage down to the baseplate. The RF cables are thermally well anchored to the baseplate with copper clamps and 0 dB attenuators. Details of the RF setup are shown in figure 6.6. The purpose of the four coax wires is summarized in table 6.1.

The inner conductor of the coax lines is thermally isolated from the outside through its Teflon dielectric. This means that the inner conductor can be at a different temperature than the outside. An attenuator provides electrical and hence thermal contact between the inner and outer conductor. In dilution refrigerator systems, this technique is routinely used to equilibrate the temperature between inner- and outer conductor. We also built this in, but it turned out that with proper anchoring of the outer conductor and a sufficient cable length this is not required for our setup, no extra heating of the base was observed.

For evaporative cooling of the atoms after magnetic transport, we use two RF coils. They have 20 windings each and are made of NbTi wire like the superconducting coils. One is mounted vertically between V8 and V9, the other one is placed horizontally on the V8 mounting. The location of the two RF coils is marked in figure 6.4 C. At the time of writing, a new RF coil was installed, using just one winding around the top of the chip mounting. This is expected to result in stronger RF fields at the location of the atoms. Several RF frequency

⁸242-SMAD18G-C40-4, Allectra

⁹380-SMA-MM-1000, Allectra

¹⁰UT-85C

6. Cryogenic setup

generators can be connected to a single RF antenna using a cascade of RF switches¹¹ without signal distortion.

The third coax wire is connected at the lower end of the HTc wires connecting the atomchip Z wire. Since the chip current source is floating, the ground of this coax cable has to be isolated by using a DC block at the 50 K transition. This allows to measure the RF noise picked up by the chip directly and verify the effects of our noise reduction efforts. Additionally, this connection gives us the possibility to feed an RF signal directly to the chip wire and thus use the chip wire as an RF antenna for evaporative cooling. This has the advantage of producing stronger RF fields at the location of the atoms compared to the two RF antennas, thus allowing faster RF cooling ramps.

The fourth coax wire is connected to a microwave patch antenna. This will allow to probe the coherence of the atomic cloud. The antenna was designed for a frequency of ≈ 6.83 GHz, the hyperfine transition frequency between $|F = 1\rangle$ and $|F = 2\rangle$. A picture of the antenna is shown in figure 6.7 B. It is positioned between the mountings for V8 and V9, as close as possible to the location of the atoms. We will use this antenna to drive hyperfine transitions and probe the coherence time of our atoms.

Table 6.1.: Summary of the RF setup.

Connector	50 K feedthrough	4 K stage	Inside	Outside
A	0dB attenuator	0 dB att.	RF coil around chip	RF sources
B	-3dB attenuator	-3 dB att.	RF coil vertical	spare
C	-	-	Microwave antenna	Microwave source
D	DC block	-	Chip wire	Spectrum analyzer

¹¹Mini Circuits ZX80-DR230+

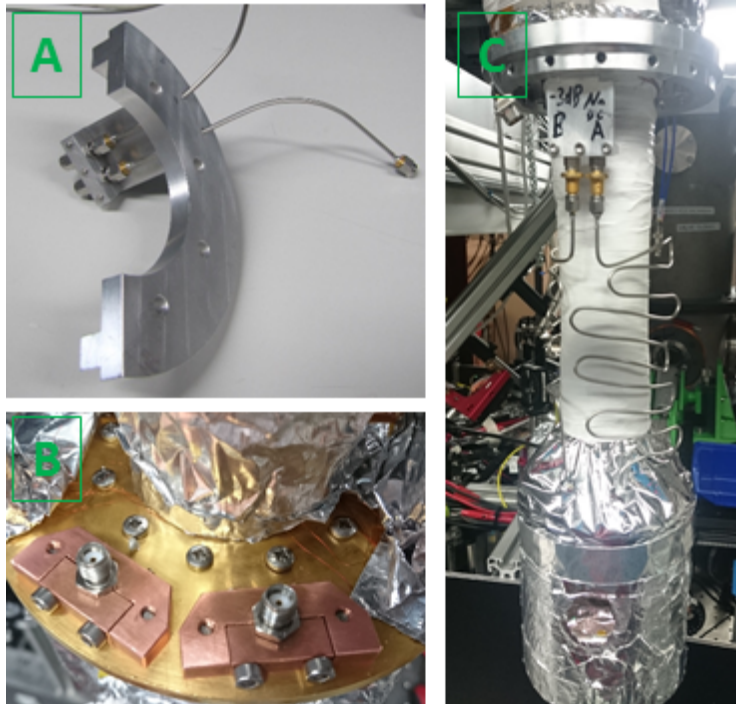


Figure 6.6.: A: Two semi-rigid cables are fed through on half of the 50 K shield mounting ring and are then thermally anchored using attenuators. The two other coax cables are fed through the other half ring, without attenuator anchoring. B: Two of the anchoring clamps at the baseplate. C: The zig-zag lines connect the 50 K stage with the baseplate.

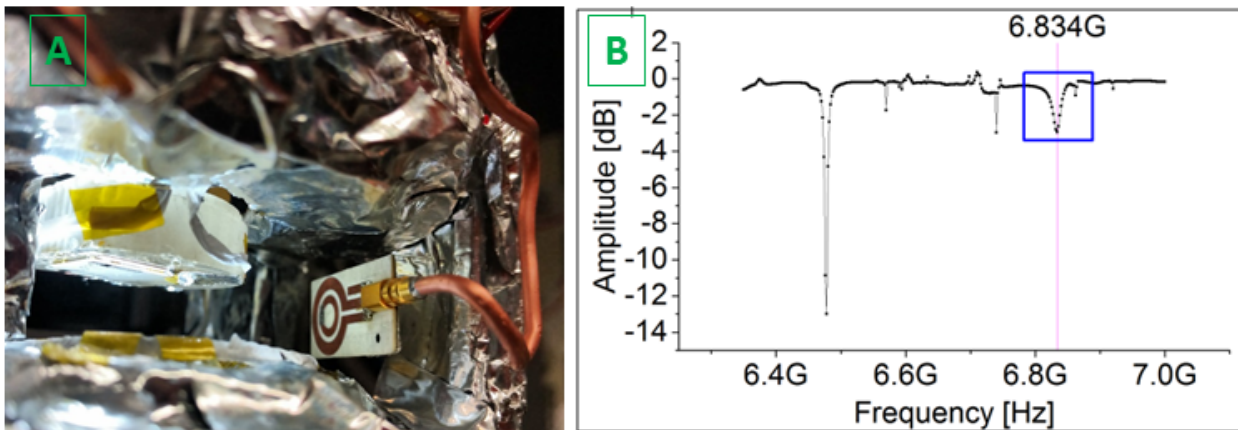


Figure 6.7.: A: The microwave antenna pointing directly at the chip. B: Simulation of the S11 parameter of the microwave patch antenna. The dip at 6.834 GHz means that the power is not reflected back into the microwave source but radiated into the chamber.

6.6. Chip mounting

The chip mounting, shown in figure 6.8 A, is made from a quartz single crystal. The material has to be non conductive to prevent eddy currents forming in close proximity to the chip trap, while still providing a high thermal conductivity. Quartz is extremely hard to machine, the first version of the chip mounting lost a part of the top while drilling. The second version does not have any holes in the top, as they turned out to be unnecessary. This makes machining less risky and significantly cheaper¹².

The atomchip is glued to the top using GE 7031 Varnish. This resin is the standard adhesive in cryogenic engineering. It has a relatively high thermal conductivity and can be diluted with ethanol to the desired viscosity. Short pieces of HTc tape are used as contact pads for the atomchip and the NbTi wires supplying the current.

Contacting the Niobium atomchip chip is not straightforward. Niobium forms a very hard oxide layer as soon as it is exposed to air. To achieve a reproducible critical current, several options were considered:

- Spring loaded contacts with flattened Niobium wires, as shown in figure 6.8 C, are very unpredictable in terms of critical current.
- Regular soldering does not work. The liquid solder does not wet the Niobium surface. Several types of solder, including Roses' metal, an alloy of bismuth, lead and tin, were tested.
- Ultrasound assisted soldering¹³ breaks the oxide layer and allows to wet the surface with solder. We used high lead content (80:20) solder, this alloy becomes superconducting and remains ductile at 4 K [96]. Unfortunately the solder joints were still mechanically unstable and no reproducible critical currents were achieved.
- Wire bonding with Niobium wire does not work because the filaments do not stick to the Niobium surface.
- The working solution is wire bonding with 25 μm thin Aluminum filaments. Since Aluminum does not become superconducting at 4 K, a large number of filaments is required to carry the chip current and prevent heating of the atomchip. The bonded chip is shown in figure 6.8 B.

¹²Machining done by Klein & Becker GmbH & Co. KG, Idar-Oberstein, Germany

¹³USS-9210, MBR ELECTRONICS GmbH, Switzerland

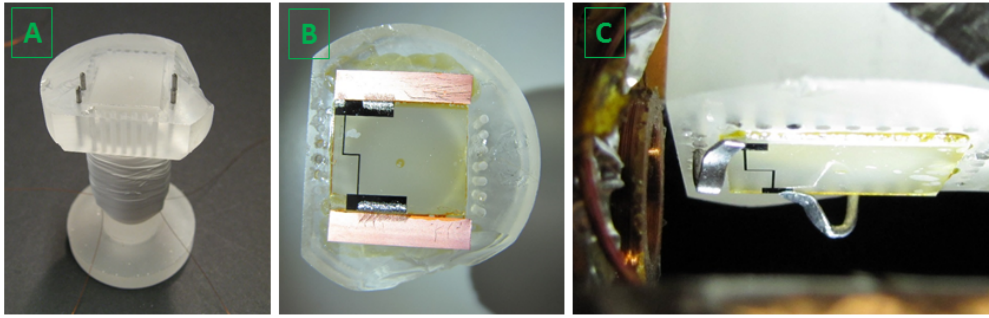


Figure 6.8.: A: The chip mounting. A piece of the head broke off during manufacturing. B: HTc stripes and atomchip are glued to the mounting and wire bonded with many aluminum filaments. C: Our historically first attempt to contact the chip with niobium wire hooks.

6.7. Atomchip design and fabrication

The fabrication of normal conducting atomchips has been optimized over the years, state-of-the-art chips are multilayer structures with many wires and features down to sub-micron size. Usually gold wires on silicon substrates are used [97]. Superconducting atomchips are fabricated on sapphire substrates. This material has a high thermal conductivity at cryogenic temperatures and a low loss tangent in the frequency range of the microwave transition. Niobium is the superconducting material of choice because it is the element with the highest critical temperature. This makes thin film deposition much easier compared to compounds such as MgB_2 and provides relatively high critical current densities and small high frequency losses.

The films with thickness between 200 nm and $1 \mu\text{m}$ are deposited using magnetron sputtering¹⁴. The film qualities depend strongly on the purity of the substrate and the conditions in the chamber [98]. The wafers are spin-coated with photoresist and the chip design is written using a laser writer¹⁵. Unexposed resist is removed and the structure is created with reactive ion etching, using a mixture of Argon and SF_6 . The last step is dicing the wafer into chips with a diamond saw. For details on the required file format for the laser writer and the fabrication recipes, refer to [98]. Atomchips with superconducting materials such as YBCO [99] and MgB_2 [100] are used in other labs. For our current applications, especially the microwave resonators, Niobium remains the material of choice for us. However, we are investigating other materials as well, a first YBCO chip has already been fabricated and the results are presented in [101].

The fabricated chips are tested in a liquid helium bath cryostat in collaboration with the low temperature physics group at the Atominstitut. A new sample stick for measuring the critical current of our chip wires and the properties of the superconducting microwave resonators was designed recently. This will allow to fully characterize the microwave resonators at different temperatures and magnetic fields, details about the sample stick and the

¹⁴Most wafers were coated at the AIT (www.ait.ac.at). The films created in-house were of poor quality and used only to establish fabrication recipes. High-quality films for resonator fabrication were purchased from Starcryo, www.starcryo.com

¹⁵Heidelberg DWL 66, www.himt.de

measurements are given in [102, 94] and [103].

6.8. Future upgrades

The main issue with our current experimental stage design is space. It is very hard to anchor and route such a large number of wires in an orderly fashion, preferably without the wires crossing each other to avoid capacitive coupling, which introduces electronic noise. A new version of the experimental stage provides designated routes for each wire pair and also allows the installation of new devices that will be needed in the future, most importantly a microwave amplifier. Electronic components for filtering and switching the currents have to be accommodated as well. Another important design goal is to facilitate microwave connections to- and replacement of the atomchip. A first mock-up model of this new experimental stage has been designed and 3D-printed, details are given in [95]. Furthermore, the fixation of the Ioffe coil mounting will be modified such that accurate and reproducible positioning is possible. With the current mounting, the optimal Ioffe current ratio has to be found after each opening of the cryostat. The new Ioffe coil mounting also has a larger inner diameter for better optical access. Finally, we are considering a superconducting shield for the experimental stage¹⁶. Such a shield could be fabricated using lead foil, the implications for the magnetic transport have to be carefully considered before.

¹⁶This was strongly suggested to us by Michel Brune from the Paris group.

7. Magnetic coils and current control

Trapping and transporting of ultracold atoms requires precise control over the magnetic fields. This is realized with a large number of coils, 39 in total. The coils are divided into three categories:

- Normal conducting coils for the magnetic transport, designed for high currents. (16 coils)
- Sets of bias coils mounted around the MOT chamber and the cryo chamber. (12 coils)
- The superconducting coils in the cryostat. (11 coils)

In this chapter I will summarize the geometric and magnetic properties of all coils for future reference and provide details about the electronic circuits for driving and switching the currents.

7.1. normal conducting transport coils

The transport coils are made out of rectangular enamelled copper wire with a cross section of $2.5 \times 1 \text{ mm}^2$. A trade off between wire cross-section and the achievable number of windings has to be made. The high currents required to achieve the desired trapping gradients result in a power dissipation of up to 2 kW per coil, which means all normal conducting transport coils have to be water cooled. The normal conducting transport coils are shown in figure 7.1.

- **MOT coils:** The MOT coils create the magnetic trap in the beginning of the experimental sequence. Their radius is larger compared to the other transport coils to allow the MOT beams to pass, as shown in figure 7.2 A.
- **Push coil:** The Push coil is responsible for the initial shift of the magnetic trap in the transport direction. It is conically wound around a mounting fixed on the flange opposite the transport tube. The winding scheme can be found in [104], figure G1. This coil receives particularly high currents, it is therefore very important to ensure proper water cooling. It should be noted that the materials used for the coil mounting and the water connection have to be compatible. In the first version, a brass water connector was screwed into the Aluminum mounting, which corroded and eventually blocked the water flow completely. Now the water connectors are from stainless steel.
- **Horizontal transport coils H1 - H4:** Horizontal transport is realized with four pairs of coils in anti-Helmholtz configuration. Each of them is glued in an Aluminum case, which are then screwed to a water cooled rail. The coils overlap, meaning that H1 and H3 have a larger distance than H2 and H4.

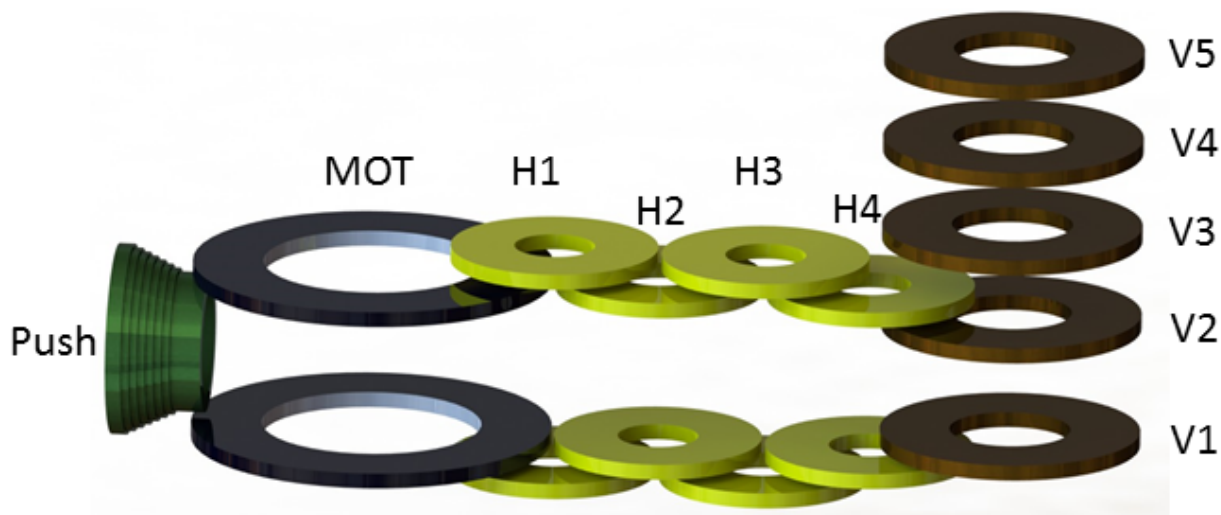


Figure 7.1.: Rendering of all normal conducting transport coils. The MOT coils and the horizontal transport coils H1-H4 are connected in anti-Helmholtz configuration.

- **Vertical transport coils V1 - V5:** The first five vertical transport coils are located outside the cryostat and therefore normal conducting. Each of these coils can be controlled individually, the coils V2-V5 can be operated bipolar because the atoms travel through their center. One of the vertical transport coils is shown in figure 7.2 B.

The following tables 7.1 and 7.2 summarize the geometric properties of the normal conducting transport coils. To get a feeling for the strength of a coil, the trapping gradient for a current of 1 A is given. The inductances are estimated for single coils, not coil pairs, using online tools¹.

7.1.1. High current electronics

The normal conducting transport involves 11 coils or coil pairs (Push, MOT, H1-H4 and V1-V5). The coils V2-V5 are operated bipolar, thus a total of 15 (unipolar) currents are required. Since no more than four coils or coil pairs are active at the same time during magnetic transport (see chapter 8 for details), there is no need to buy 15 expensive power supplies.

We use five DC power supplies from Delta Elektronika². They are operated in constant current mode and are controlled by analog input signals from the ADWIN control system. Each power supply is connected to a switchbox to switch between up to three coils, see table 7.3. Each switchbox contains an H-bridge which allows to change the polarity of one of the output currents. The switchboxes are controlled with digital signals from ADWIN.

This circuits have been operational for years. However, switchbox 4 kept dying in irregular intervals. Replacing the entire switchbox did not solve the problem. As the damage seems

¹<http://www.66pacific.com/calculators/coil-inductance-calculator.aspx>

and <https://www.eeweb.com/toolbox/rectangle-loop-inductance>

²www.delta-elektronika.nl

Table 7.1.: Normal conducting coils/coil pairs for horizontal transport.

Coil name	Push	MOT	H1	H2	H3	H4
Inner radius [mm]	34	36.2	13.3	13.3	13.3	13.3
Outer radius [mm]	52-72 (conical)	59.5	34.3	34.3	34.3	34.3
Height [mm]	30.6	5.1	5.1	5.1	5.1	5.1
Distance of coil pair [mm]	-	55.1	71.5	55.1	71.5	55.1
x Position of coil center [mm]	-56.6	0	60.5	95	129.5	164
Number of axial windings	12	2	2	2	2	2
Number of radial windings	6-13 (conical)	23	23	23	23	23
Total windings	107	46	46	46	46	46
Trap gradient Gauss/(cm A)	-	2.19	2.24	3.93	2.24	3.93
Inductance (mH)	-	0.270	0.094	0.094	0.094	0.094

Table 7.2.: Normal conducting coils for vertical transport. The trap gradient is given for the combination with each previous coil (e. g. V2 with V1) at their geometric center.

Coil name	V1	V2	V3	V4	V5
Inner radius [mm]	20	20	20	20	20
Outer radius [mm]	43	43	43	43	43
Height [mm]	5.1	5.1	5.1	5.1	5.1
x Position of coil center [mm]	210.4	210.4	210.4	210.4	210.4
z Position of coil center [mm]	-20	20	50	80	110
Number of axial windings	2	2	2	2	2
Number of radial windings	20	20	20	20	20
Total windings	40	40	40	40	40
Trap gradient Gauss/(cm A)	-	4.28	4.78	4.78	4.78
Inductance (mH)	0.108	0.108	0.108	0.108	0.108

Table 7.3.: The assignment power supply - switchbox - coils for the normal conducting part of the magnetic transport.

Power Supply	Type	Current range	Switchbox	Coils
Delta 1	SM 15-200D	0-200A	Switchbox 1	Push coil, V1
Delta 2	SM 30-100D	0-100A	Switchbox 2	MOT, H4, V4
Delta 3	SM 30-100D	0-100A	Switchbox 3	H1, V2
Delta 4	SM 15-200D	0-200A	Switchbox 4	H2, V3
Delta 5	SM 30-100	0-100A	Switchbox 5	H3, V5

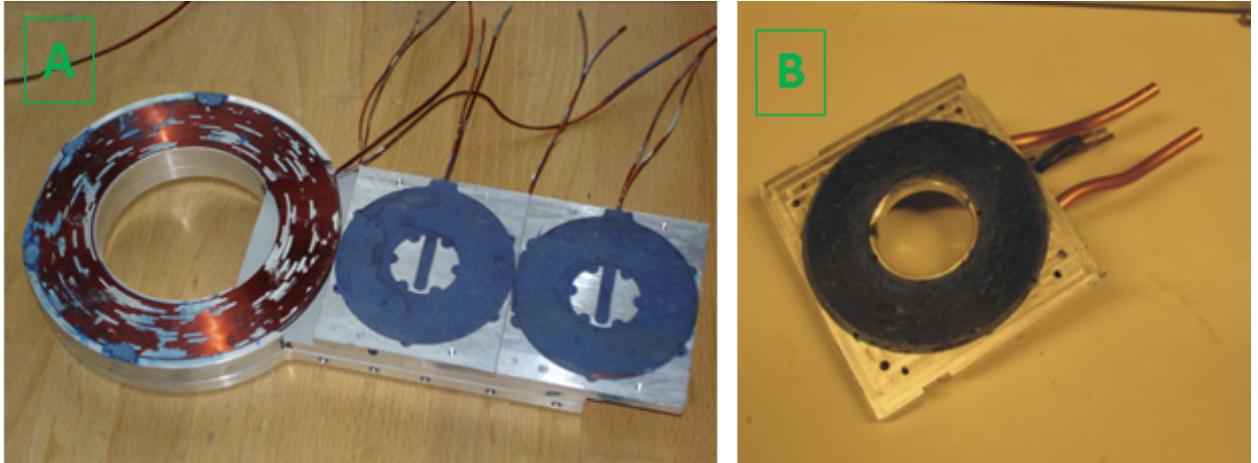


Figure 7.2.: A: The coil rail with the MOT coil and the horizontal transport coils H1-H4. The water cooling pipe is not yet mounted on the back. B: One of the vertical transport coils in its mounting.

to happen randomly, we were never able to identify it. Possible suspects are voltage/current spikes from the power supply or the analog control signal, a spurious ground connection of the coil, or occasional (and fast) drops in the digital signal, causing rapid switching of the inductive load. In order to mitigate this problem, we use four solid state relays (SSR)³ instead of the two half-bridge drivers. Two relays share one floating power supply (one for the two low side SSRs, one for the two high side SSRs), which directly switch the MOSFET banks. This improvised construction seems to be immune to the unknown defect.

The current switchbox design has several issues, from the mechanical assembly of the high current rails and cables as well as the operational safety in case of power loss and the reliability (see previous paragraph). A new version of the switchbox was designed to overcome these problems and make operation and debugging significantly easier, see [105] for details. It features magnetoresistive current senses⁴ for all outputs, has high current plugs instead of cable lugs, more powerful MOSFETS⁵ and a separate power supply board ensuring safe shutdown in case of power loss. A detailed explanation of the design is given in section B.1.

For time-of-flight (TOF) measurements, the MOT current needs to be switched off abruptly. This is not done using a switchbox, but an additional TTL controlled switch with the appropriate protective circuits.

7.1.2. Monitoring and safety

The delta power supplies have analog monitoring outputs. Their output voltages are proportional to the current and the voltage delivered. We monitor these voltages continuously on a computer with a NI DAQ card⁶. The power delivered by each power supply is also calculated. An increase in the power necessary to drive a given current is a sign for heating

³Crydom CS380D5R

⁴Sensitec CMS2050

⁵Infineon IRFP4004

⁶NI DAQ6229 BNC

up of a coil. This monitoring system has no automatism, should anything go wrong the cycle still has to be stopped manually.

In operation, the normal conducting coils dissipate up to 2 kW for a short time. The power supplies are designed for 3 kW continuous load. Each coil needs to be water cooled to maintain an acceptable temperature. Should the water cooling fail or the current be turned on for too long or the current be too high, the coils would overheat immediately, causing the wire enamel to burn. Changing a transport coil means almost a complete disassembly of the setup. As a safety measure we use bimetal switches glued to each coil mount. They open at 80 °C and are all connected in series. The main power supply for all 5 deltas runs through a industrial relay which cuts the power if one of the bimetal switches open. Additionally, the cable is routed to the control room, for manual shutdown, cf. figure 7.3 B.

7.1.3. Upgrades

The biggest issue with our normal conducting transport coils is the mechanical alignment. In the current setup, the coil rail can rotate several degrees around the axis defined by the MOT coil pair. Furthermore, the entire assembly sags downwards toward the corner. These small deviations result in heavy atom loss through the narrow transport tube. As of now, optical translation stages are used to adjust the position of the coils. The vertical transport coils are also not as rigid as necessary, however transport is more robust to deviations as there is no narrow section. A rigid mounting that keeps all coils perfectly oriented with respect to the vacuum chamber and to each other would be a major improvement and prevent time-consuming debugging.

We also plan to upgrade the safety system. Right now, the coils are the weakest link in terms of current carrying capacity, meaning they burn first. The first step towards a more reliable and redundant safety system are slow fuses rated just above the maximum desired current for each coil. As a second measure, a digital temperature measurement system for the coil mountings is under preparation, which will trigger a remote shutdown signal for the power supplies. The temperature sensors must be resilient against magnetic field transients, as they will be screwed to the coil mountings. An old version of this system using I^2C sensors produced random measurements during transport and were unusable.

Another upgrade concerns the water cooling. At the moment, we have only one flow meter measuring the total water flow to the experiment, around 10 l/s, before it is split into the four cooling water cycles for the different coils. We are implementing a new system, measuring the water flow in each of these four cycles and sending it to a computer which triggers a shutdown in case one or more of the flows is too low. For details on the cooling water monitoring, refer to [94].

Switching off the Delta power supplies is happening now using the circuit breaker box that directly cuts the 400 V mains supply. As a more "soft" approach, the power supplies feature a TTL input for remote shutdown⁷. This pin will be connected to one of the GPIO ports of a Raspberry Pi single-board computer and triggered by the water- and coil temperature sensor programs.

Furthermore, all electronics for the normal conducting transport coils will be put in a 19 inch rack. This will free some room below the optical table for other components, as the

⁷Pin 5 of the Programming connector.

experiment is continuously growing and space is precious. Having everything in one rack also makes things easier to service, as the back side of the current sources and switchboxes is not accessible now.

7.2. Bias coils

In addition to the MOT coils which produce a magnetic quadrupole trap in the middle of the MOT chamber, homogeneous bias fields can be applied in all three directions through three pairs of coils. The coil pairs in horizontal direction are realized with flat ribbon cables wound to rectangular coils, the vertical coils are made from a normal copper cable and rest in a round plastic mounting. Their properties are summarized in table 7.4. A picture showing the coil assembly around the MOT chamber is shown in figure 7.3.

Table 7.4.: MOT bias coils.

Direction	Vertical	Transport direction	Optical pumping
Shape	round, 21 cm diameter	21 x 15 cm	22 x 19 cm
Distance	15 cm	11.5 cm	9.5 cm
Windings	83	8 wires, 6 layers	8 wires, 10 layers
Resistance	4.7 Ohm	15.7 Ohm	27.2 Ohm

The coil pairs for vertical direction and for the transport direction are connected to a DC power supply⁸ and the current can be set through the control software, but remains fixed during the cycle, see section 10.5 for details. The bias field in the optical pumping direction is supplied with a chip driver current source (see section B.2). The current can be controlled with an analog signal, which allows to apply a short current pulse during the optical pumping phase.

For precise control of the magnetic field at the location of the atomchip, additional three pairs of coils are also mounted on the outside of the cryochamber. The properties of these coils are given in table 7.5. These coils could be used to induce persistent currents in the superconducting bias coils. The cryo bias coils are the first coils where the new bilateral current source will be tested, see section B.3.

⁸Agilent 6623A

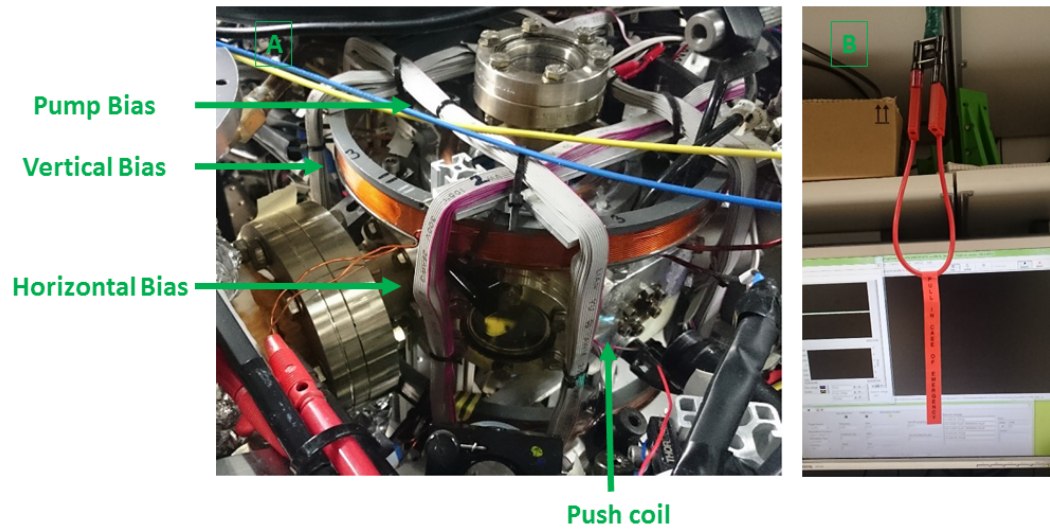


Figure 7.3.: A: The biascoils around the MOT chamber. The location of the push coil is indicated for orientation. B: Pulling this emergency cable switches off all high current power supplies. This wire has prevented fire on several occasions.

Table 7.5.: The coils mounted on the outside of the cryo chamber.

Direction	Vertical	Ioffe	Imaging
Inner diameter [mm]	150	60	60
Distance [mm]	190	205	205
Height [mm]	3	10	10
Windings	50	100	100
Resistance [Ohm]	13.4	10.4	10.4
Field constant [G/A]	2.47	2.81	2.81

7.3. Superconducting coils

The setup uses eleven superconducting coils:

- **Transport coils V6 - V9:** The last four coils of the vertical transport have 3000 windings each. The coils are mounted on copper mountings for good thermal anchoring. The mountings are divided in four sections isolated with stycast, this prevents large circular eddy currents to form, see figure 7.4 A.
- **Ioffe coil:** The Ioffe coil (small pink coil in fig. 7.5) is used to transform the quadrupole trap formed by V8 and V9 into a harmonic QUIC trap. It has 1800 windings with a small radius to fit between V8 and V9. The axis of the Ioffe coil points horizontally to the center of V8 and V9 and is rotated 45° with respect to the horizontal transport axis. The Ioffe coil is shown on its mounting in figure 7.4 B.
- **Bias coils:** Three additional coil pairs are used for producing homogeneous bias fields in all directions. They are called **HBIO** (Horizontal Bias Ioffe direction) (red in fig. 7.5), **HBIM** (Horizontal Bias Imaging direction, green in fig. 7.5) and **BV** (Bias Vertical)(yellow in fig. 7.5). HBIO and HBIM are directly soldered in series at the 4K stage, while BV can be switched from Helmholtz- to anti-Helmholtz configuration with external SSRs. This is used during the buffer trap, where atoms are held by the BV coils while V8 and V9 are switched in series. HBIO and HBIM are not circular but rectangular in shape. However, at the central region where the QUIC trap or chip trap are located, their field can be regarded as homogeneous.

All coils are made of commercial Niobium-Titanium wire⁹. The wire contains 54 NbTi filaments embedded a copper matrix and is isolated with Formvar. All coils are wound using GE 7031 Varnish and baked at 100°C . For thermal anchoring and soldering refer to sections 6.3 and 6.4. The full cryogenic setup is shown in figure 6.4. The properties of all superconducting coils are summarized in table 7.6 and 7.7.

7.3.1. Current control

The long copper wires for all coils and the chip in the cryostat are twisted in pairs to minimize noise pick up (as described in the wiring section 6.3). Outside the vacuum feedthroughs, a bundle of shielded cables lead to a breakout box. All wires entering the cryo chamber are connected here, except the coaxial high frequency lines. The breakout box contains a magnetoresistive current sensor for each coil¹⁰, solid state relays for switching the coil configurations and two mechanical relays for the chip wire. The breakout box provides isolated BNC connectors at the front panel. Depending on the device connected, the BNC shield can be grounded in the breakout box or at the device output.

Each superconducting coil is connected to one or more current sources through electronic switches. The switches were modified to account for the high inductance of the superconducting coils, for details on this circuit refer to [104], appendix B. As current source, all

⁹Type 54S43 copper stabilized multifilament NbTi wire, $127\ \mu\text{m}$ diameter, Supercon Inc.

¹⁰Sensitec CMS2005

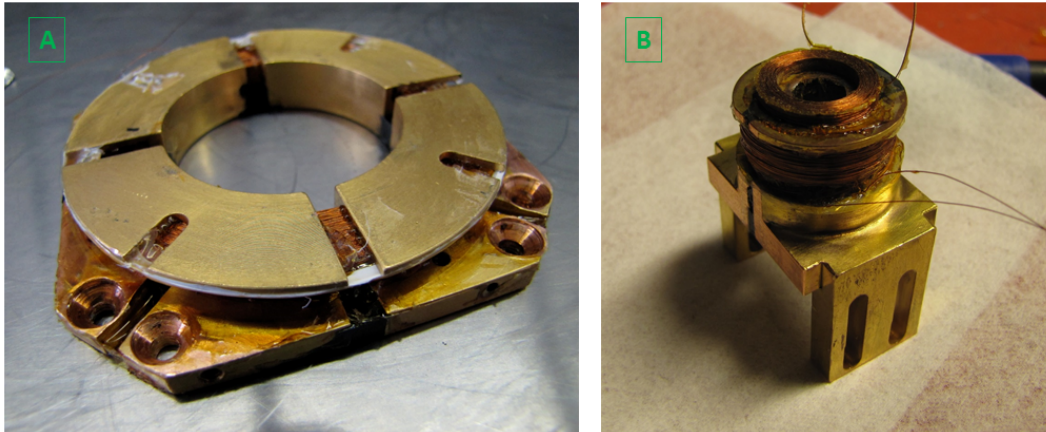


Figure 7.4.: A: One of the transport coils in its mounting. B: The Ioffe coil on its mounting. The long holes allow to shift the position of the coil. The small coil on top is not present in the setup as of now.

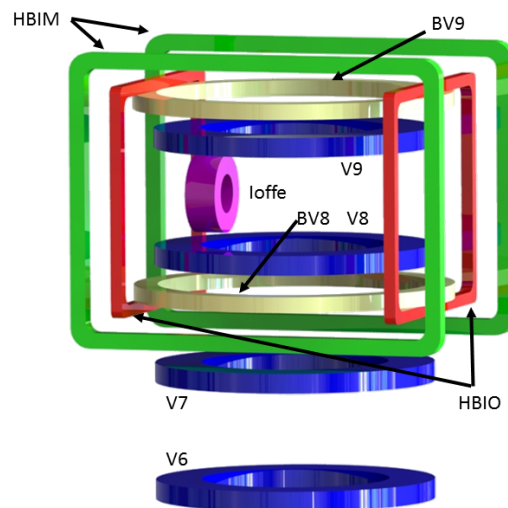


Figure 7.5.: Rendering of all superconducting coils and their names. Four transport coils V6-V9, six bias coils (HBIM, HBIO, BV8+BV9) and the Ioffe coil.

7. Magnetic coils and current control

Table 7.6.: Properties of all round superconducting coils. All but the Ioffe coil are concentric around the vertical transport axis. The x position of the Ioffe coil is given with respect to the vertical transport axis. The trap gradient is given for the combination with each previous coil (e. g. V9 with V8) at their geometric center.

Coil name	V6	V7	V8	V9	BV8	BV9	Ioffe
Inner radius [mm]	24	24	24	24	35	35	5
Outer radius [mm]	35	35	35	35	41	41	10
Height [mm]	5	5	5	5	4	4	8
x Position of coil center [mm]	210.4	210.4	210.4	210.4	210.4	210.4	-22.4*
z Position of coil center [mm]	140	170	200	230	190.5	239.5	215
Number of axial windings	36	36	36	36	29	29	33
Number of radial windings	84	84	84	84	43	43	55
Total windings	3000	3000	3000	3000	1240	1240	1800
Resistance at 300 K [Ohm]	2064	2142	2027	2117	1082	1087	341
Trap gradient Gauss/(cm A)	-	381	381	381	-	88	-
Inductance (mH)	829	829	829	829	215	215	34

Table 7.7.: Properties of the rectangular bias coils HBIO and HBIM. The resistance is given for the full coil pair, while the inductance is calculated for individual coils. The field constant is also given for the round vertical bias coils BV8 and BV9 in Helmholtz configuration.

Coil name	HBIO	HBIM	BV (Helmholtz)
Width [mm]	62	90.9	-
Height [mm]	53	67.4	-
Coil center position[mm]	35	28	-
Cross section axial x radial [mm ²]	3 x 3	4 x 4	-
Number of axial windings	21	28	-
Number of radial windings	22	29	-
Total windings	462	812	-
Resistance at 300 K [Ohm]	793	1935	-
Inductance per coil (mH)	61.5	274	-
Field constant (G/A)	55	127,2	245

coils use the chip driver current source designed in Heidelberg. The circuitry of this device is discussed in detail in B.2.

To switch the polarity of a coil during magnetic transport, two current sources and two switches are required. For the QUIC trap, V8 and V9 are put in series to minimize the effect of low frequency noise. Initially it was planned to include the Ioffe coil in this circuit as well, such that the QUIC trap is powered by only one current source as in [48]. However, this requires "luck" in the placement of the Ioffe coil due to some play in our mechanical design. One could also use an additional "Super-Ioffe" coil as a compensation, however this coil is not installed and we drive the QUIC trap with an independent Ioffe current source. This circuit is shown in figure B.7.

The vertical bias coils BV8 and BV9 have two purposes: while switching V8 and V9 in series, the atoms are stored in a trap formed by BV8 and BV9 in anti-Helmholtz configuration. Afterwards, BV8 and BV9 are switched in Helmholtz configuration to provide a vertical bias field. The connection diagram including is shown in figure B.8.

7.3.2. Upgrades

As mentioned in the section 6.4, a better routing of the wires in the cryostat can help to reduce interference and noise pick-up. For the setup outside the cryostat, a new breakout box is currently under construction, see section B.5. There will be a dedicated box just for the current carrying wires, independent of the temperature sensors. The new box routes the input currents from the BNC plugs through a PCB board, where the current sensors are mounted and effective noise-reduction measures are in place. Each line features optional capacitors and inductors to reduce all high frequency components. Car batteries instead of switching power supplies for the current sensors and relays will be used. The solid state relays used to switch between the current configurations will be placed in separate, shielded boxes to maintain full flexibility. Lastly, the new bipolar current source (see section B.3) will help to make the whole setup less complex as fewer components and signals will be required.

7.4. Atomchip current control

The superconducting atomchip is supplied through the chip driver current source described in B.2. The complete connection diagram is shown in figure 7.6. An optional second current source (not shown in the figure) allows to apply a current pulse in reverse direction for current distribution programming as described in section 12.2.

Atoms in a chip trap are very sensitive to current noise in the chip wire because of the proximity. The low impedance of the wire readily transmits frequencies in the MHz range. The superconducting coils reject current noise very efficiently, as the AC resistance Z of a high-inductance coil $Z = \omega L$ rises with frequency. Any given current noise amplitude at the chip wire on the other hand translates directly into magnetic field noise. Depending on the frequency range of the noise signals, this causes either parametric heating of the cloud through trap oscillations or induces unwanted spin-flips between Zeeman sublevels.

The reasons for noise are manifold. The 50 Hz power line frequency and its harmonics are virtually omnipresent, as are high frequencies around 2–5 MHz from switching power supplies. Other noise sources are digital electronics, electric motors in fans and pumps.

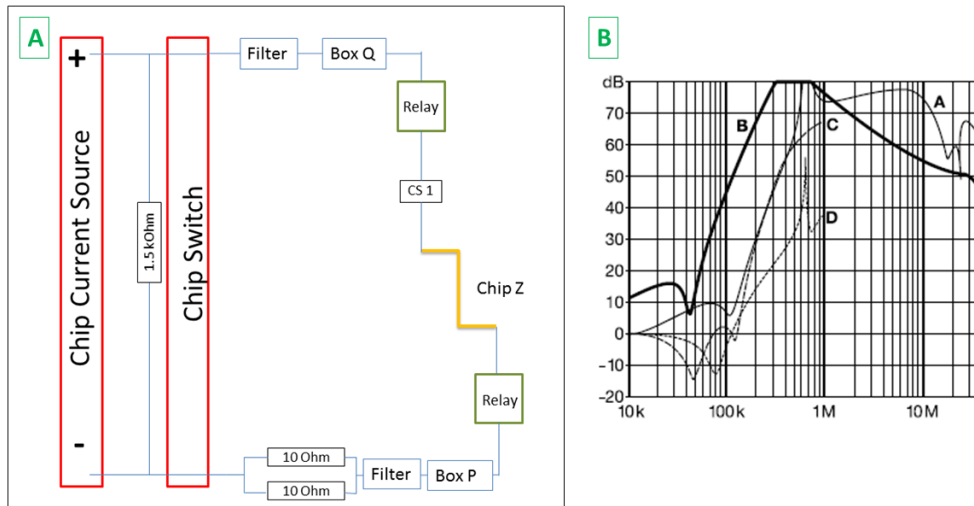


Figure 7.6.: A: Connection diagram for the chip wire. The atomchip is powered by the standard chip driver current source N142. The current source is supplied by car batteries, the 15 and 12 V terminals are both connected to an 18 V voltage regulator. This higher voltage allows to exceed the nominal 2 A maximum current. A 5 Ohm series resistor in the circuit prevents the current to oscillate, since the chip has practically no impedance. A parallel 1.5 kOhm resistor across the current source output prevents current spikes when closing the mechanical relays. Both wires are filtered using a line filter (Schaffner FN2060-10-06) before entering the breakout-box. B: The characteristics of the line filter, frequencies above 100 kHz are very efficiently absorbed.

Furthermore, in a setup with hundreds of cables, ground loops are particularly hard to avoid and even harder to find, they predominantly introduce sub-kHz noise [106].

To avoid noise on the chip wire, the low noise chip driver current source is used. The cryo chamber and the 50K shield provide very efficient shielding against RF radiation. However, even if all the outside wiring for the chip wire is optimal, noise can still be introduced through capacitive coupling to other wires. Avoiding capacitive coupling means keeping large distance between the wires or having a ground plane between them, both can not be done in our cryostat, as all wires have to be thermally anchored. Therefore noise present on any of the wires leading to the superconducting coils translates into current noise in the chip rather than in the coil. This coupling becomes more efficient with frequency given by $Z = 1/(\omega C)$.

To measure the noise spectrum directly on the chip wire, a floating coaxial cable is connected at the HTc-NbTi solder joint. Noise filtering directly at the chip is difficult because of the limited space at the cold stage, however ceramic capacitors can be installed between the wires and the baseplate. The other option is to filter all wires before entering the cryostat. This way, coupling between the wires will not introduce more noise on the chip wire. Filtering of all current carrying wires entering the cryostat is done in the new breakout box, explained in section B.5.

8. Transport current calculation

The principle behind the magnetic conveyor belt transport is straightforward. The magnetic minimum forming the trap is shifted by varying the current through a series of coils. With the known geometry of the transport coils, the currents required can be calculated analytically. The general expression for the field of a single current loop is given in [107]. It is a complex equation containing elliptic integrals, but in the end it is just a geometric factor and the field components are linear in the loop current. We can therefore make a system of linear equations and solve it for the currents in the individual coils. The calculation is done with Mathematica, a detailed explanation can be found in [108]. At the end of this chapter, I present our 3D simulation tool we use to optimize current ramps and visualize the exact shape of the magnetic traps.

8.1. Horizontal transport

The horizontal transport scheme using overlapping quadrupole coil pairs has been first described in [91]. Up to three coils are used at the same time. The field is calculated only on the transport axis (=x-axis), therefore the y- and z-component are zero. The three conditions required to solve the equation system are:

- The magnetic field at the location of the trap x_0 has to be zero. As $B_y = B_z = 0$ on the transport axis, this can be written as:

$$|\vec{B}|_{(x=x_0)} = B_{x(x=x_0)} = 0 \quad (8.1)$$

- The gradient of the trap in vertical direction is set to be 130 G/cm:

$$\frac{\partial B}{\partial z} = 130 \text{ G/cm} \quad (8.2)$$

- To avoid parametric heating of the atoms due to trap oscillations, the aspect ratio (the ratio of the gradients for a linear trap) has to remain constant during transport. This particular value of A is chosen such that only unipolar currents have to be applied.

$$A = \frac{\partial B_y / \partial y}{\partial B_x / \partial x} = 1.715 \quad (8.3)$$

The magnetic trap before transport has an aspect ratio of 1. This means that in the beginning of transport, the aspect ratio is set to increase smoothly from 1.0 to 1.715, as is shown in figure 8.1 A. As the magnetic trap approaches the end of the horizontal transport, only two coil pairs are active and the aspect ratio is returning to 1. The third condition

8. Transport current calculation

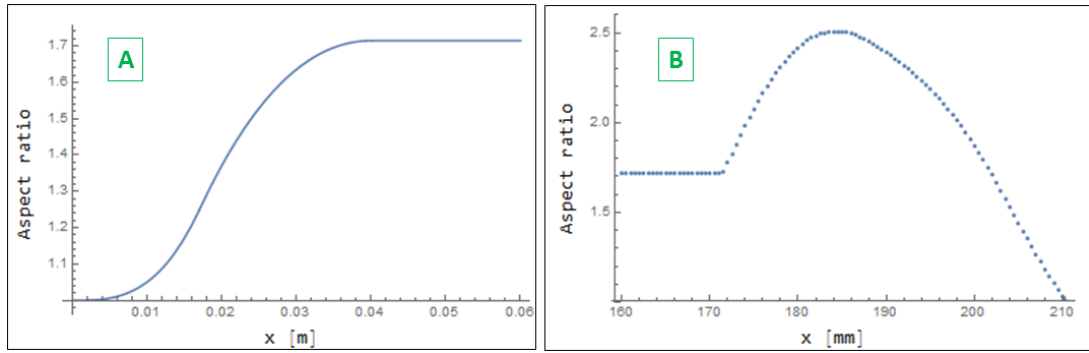


Figure 8.1.: A: In the beginning of the horizontal transport, the aspect ratio is varied smoothly from 1 to 1.715. B: Towards the corner, the aspect ratio becomes a dependent variable, approaching 1 at the end.

is therefore dropped from the equation system and the aspect ratio becomes a dependent variable. This is shown in figure 8.1 B.

The resulting currents are shown in figure 8.2. The calculation is done in different sections. A new section starts when in the previous section the current for the farthest coil would change polarity.

The calculation described above yields a position dependent current $I(x)$ for each coil. This has to be translated into a time dependent current $I(t)$. The function $x(t)$ is calculated by defining a total transport time and the time of maximum velocity and assuming a fourth order polynomial for $x(t)$. The resulting acceleration, velocity and position are shown in figure 8.3. In the experiment, we find that the currents for H4 need to be increased by around 40% to achieve optimal transport efficiencies.

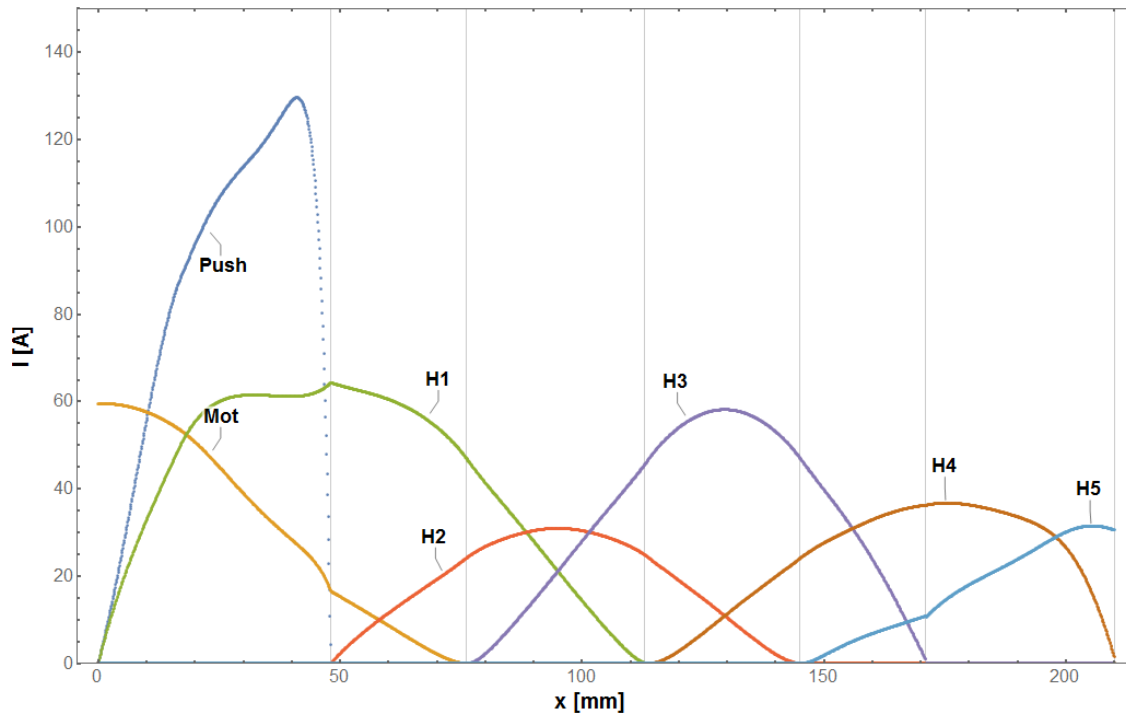


Figure 8.2.: Calculated horizontal transport currents. The black vertical lines indicate the six different sections. The push coil receives particularly high currents and drops very sharply to zero. The currents in H1 and H3 are higher because their distance is larger. The coil pair H5 consists of the (individually controlled) coils V1 and V2. The current for H4 has to be increased by 40% for optimal transport efficiency.

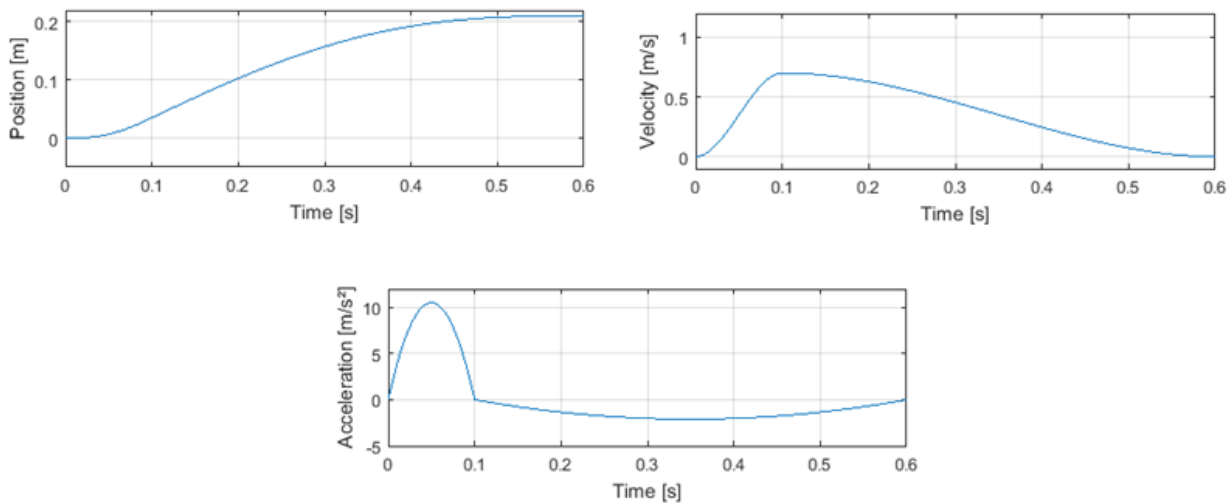


Figure 8.3.: Position, velocity and acceleration during horizontal transport. The two independent variables to calculate the x-t diagram are the total time, typically 600 ms, and the time when the maximum velocity is reached, here 100 ms. This high initial acceleration minimizes the time the atoms spend in the narrow transport tube.

8.2. Vertical transport

In vertical transport all coils share the same axis. The x- and y-component are zero on the axis, therefore $B = B_z$. As the atoms move through the center of a coil, the polarity of this current needs to change. Using up to four coils at the same time results in smooth transport currents. The four conditions for solving the equation system are:

- The magnetic field at the location z_0 of the trap has to be zero. $B_x = B_y = 0$ on the transport axis, so this condition becomes:

$$|\vec{B}|_{(z=z_0)} = B_{z(z=z_0)} = 0. \quad (8.4)$$

- Also for vertical transport we chose a trap gradient in transport direction of 130 G/cm:

$$\frac{\partial |\vec{B}|_{(z=z_0)}}{\partial z} = \frac{\partial B_{z(z=z_0)}}{\partial z} = 130 \text{ G/cm}. \quad (8.5)$$

- In vertical transport, the aspect ratio stays constant. Instead, as a third condition, we demand the second derivative of the field to be zero at the location of the trap. This makes sure the trapping gradient has a maximum at the trap,

$$\frac{\partial^2 B_{(z=z_0)}}{\partial z^2} = 0. \quad (8.6)$$

- The fourth condition requires the sum of all current loops to be zero. This condition results in smooth currents, it can be understood as a minimizing the total magnetic field produced by all active coils,

$$\sum_{i=1}^4 N_i I_i = 0. \quad (8.7)$$

The resulting currents for the vertical transport are shown in figure 8.4. Like in horizontal transport, the calculation has to be done in segments, as indicated by the black vertical lines. In the first two and also in the last segment, only three coils are active and the fourth condition is dropped. The red lines mark points with high symmetry, where no unique solution can be found and where the currents are interpolated between neighboring points. At the transition from the normal- to the superconducting coils, the fourth condition (equation 8.7) needs to be modified to

$$\sum_{i=1}^4 N_i I_i R_i^k, \quad (8.8)$$

where R_i is the mean radius of the i^{th} coil and $k = -1.02$ is an exponent chosen to produce smooth currents.

Again, the currents $I_{(z)}$ need to be transformed into time dependent currents $I_{(t)}$. The velocity profile chosen for the horizontal transport does not work for vertical transport, almost all atoms are lost. Instead, a symmetric acceleration profile is chosen, somehow similar to an elevator. The velocity is quickly brought to its maximum value where it remains, until the same deceleration happens at the end of transport. The profiles are shown in figure 8.5. Typical values for the maximum acceleration are 4 m/s^2 and for the final velocity 0.15 m/s .

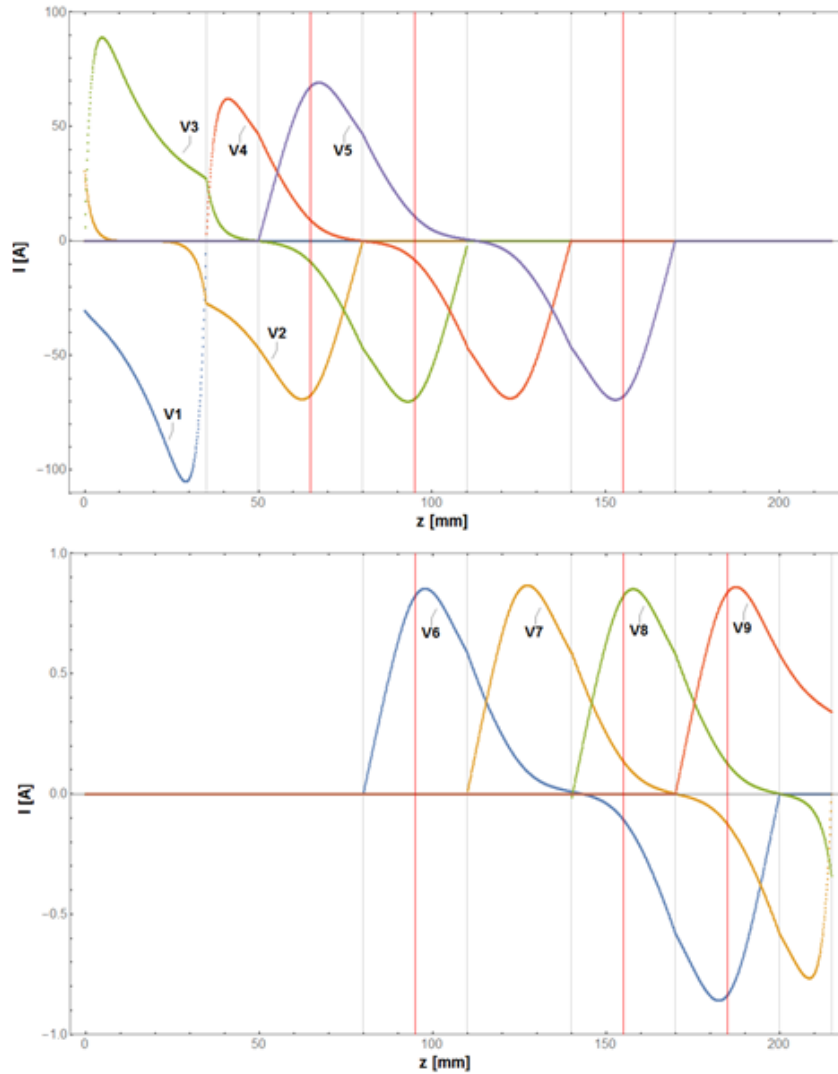


Figure 8.4.: Vertical transport currents for the normal conducting coils V1-V5 (top) and the superconducting coils V6-V9 (bottom). The currents for the superconducting coils V6-V9 are much lower, since they have many more windings. The vertical lines are explained in the text.

8. Transport current calculation

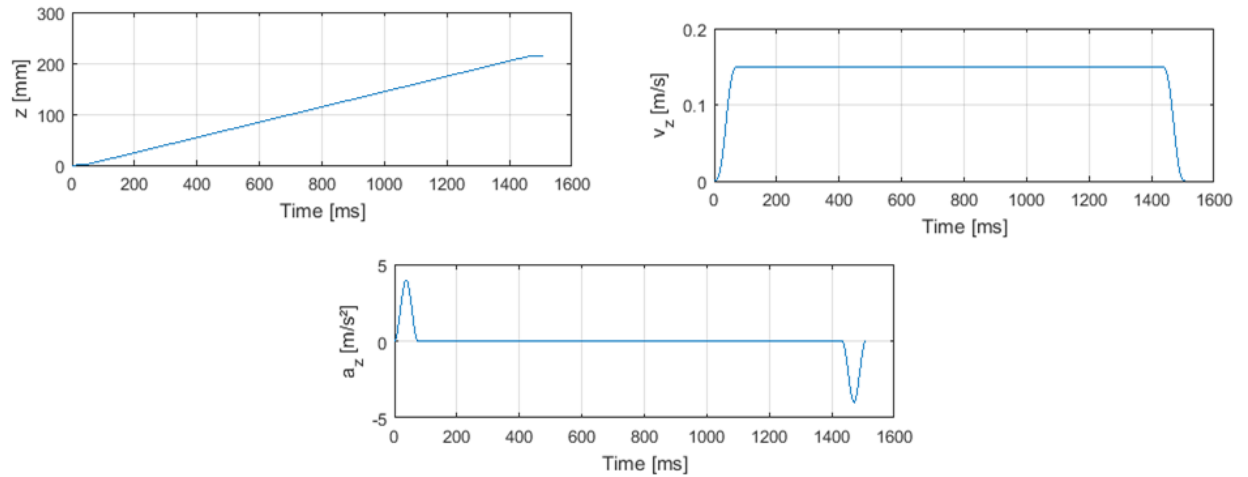


Figure 8.5.: Position, velocity and acceleration throughout vertical transport. The independent variables here are the maximum acceleration and the maximum velocity.

8.3. Magnetic field simulations

The transport current calculation described above only takes the magnetic field and its derivatives at points on the transport axis into account. For the reloading procedure in section 8.3, our efforts towards the recombination of atomic clouds in chapter 13 and for a better understanding of all our magnetic traps, a full 3D simulation tool was developed. All coils are taken into account with their real dimensions and all windings, the chip wire can be structured into many segments to account for a complex current distribution. This section is supposed to act as a short manual for this tool and make it reusable by others.

The first step in a simulation procedure are the "define*.m" files, in which the geometry of the coils and the chip is defined and where the region of interest (ROI) and the spatial resolution can be selected. The "model.m" allows to display the created geometry.

The basis for the simulations are the analytical solutions for the magnetic field of a circular current loop from [107] and those of a filamentary wire segment from [109]. Since the magnetic field is strictly linear in the applied currents, the computationally intense calculations need to be done for each coil only once for unit current. The calculated arrays are saved to files. For a region of interest with around 20 million points, the individual arrays are on the order of 250 MB in size and require around 2 hours of calculation time.

For each coil and the chip (or each filament of the chip, respectively), arbitrary current sequences can be created and saved to a file. For visualization, the "plottrap.m" script reads the current sequence file step by step and adds the field of all coils. This script also takes gravity into account by adding/subtracting a field gradient according to equation 2.11 above/below the relevant field minimum. The figures are automatically saved, allowing to easily create very detailed movies. The workflow to create a movie is as follows:

- Define and name a region of interest in `defineroi.m`
- Define geometries in `definecoils.m`, `definebigcoils.m`, `definebiascoils.m` and `definechip.m`

- Verify the model, save the parameters, exclude specific coils if wanted and generate a figure of the model using `model.m`
- Run `simulatecoils.m`, `simulatebiascoils.m`, `simulatebigcoils.m`
- Run `simulate_z.m` for an arbitrary current distribution in the Z wire or `simulate_chip.m` for one of the "standard" current distributions
- Define or import the time dependens currents using `currentsequence.m`
- display the resulting trap with `plottrap.m`
- the resulting images are stored in a folder "name-of-sequence-name-of-simulation"
- animate the picture sequence

9. Optical setup

This chapter describes the optical systems used in the setup. I will start with some basics about narrow linewidth laser diodes, discuss frequency locking and describe the lasers we have in use. Furthermore I will briefly explain the MOT optics, our imaging systems and the quenching setup.

9.1. Lasers

Doppler- and sub-Doppler cooling requires lasers with narrow bandwidth, smaller than the natural linewidth of the cooling transition, which is 6.1 MHz for the ^{87}Rb D2 line. It should also be small compared to the Doppler broadening of the ensemble at the desired temperatures. Sub-Doppler cooling reaches far below 100 μK , which in ^{87}Rb corresponds to a Doppler broadening of 300 kHz.

For laser cooling and absorption imaging, several laser lines are needed. The main laser drives the $F = 2$ to $F' = 3$ cooling transition. The weaker, so called repump laser recovers atoms that got lost from the cooling cycle and decayed to the $F = 1$ ground state. Optical pumping to the $|F, m_F\rangle = |2, 2\rangle$ sublevel uses the $F = 2$ to $F' = 2$ transition. These lines are summarized in figure 9.1 and in more detail in figures A.1 and A.3.

9.1.1. External cavity diode lasers

At the cooling transition of 780 nm, laser diodes are readily available. However, their linewidths can be as broad as nanometers and they typically operate on several longitudinal modes. A method to reduce their linewidth is to use an external cavity with a wavelength selective element, i. e. a grating. This so called external cavity diode lasers (ECDL) are a cheap alternative to Titanium-Sapphire ring lasers and are widely used in laser cooling experiments. Very cheap laser diodes similar to those in CD drives can be used, but it is more convenient to purchase pre-selected and anti-reflection coated laser diodes. The working principle of an ECDL is illustrated in figure 9.2 A. The output beam of the laser diode is directed at a diffraction grating and the first diffraction order is reflected back into the laser diode, providing extra feedback for a narrow frequency range. The extra cavity length of around 2 cm reduces the resonator bandwidth according to equation 9.1.

$$\Delta\nu_r = \Delta\nu_{\text{FSR}} \cdot \frac{1 - R}{\sqrt{R}\pi} = \frac{c}{n_g L} \cdot \frac{1 - R}{\sqrt{R}\pi} \quad (9.1)$$

Here, $\Delta\nu_{\text{FSR}}$ is the free spectral range for a cavity with length L , refractive index n_g and reflectivity R . This resonator bandwidth enters quadratically in the Schawlow-Townes-Formula which describes the linewidth limit of a laser, thus reducing the ECDL linewidth, in our case well below 1 MHz. Details of the theory of semiconductor laser linewidths are

9. Optical setup

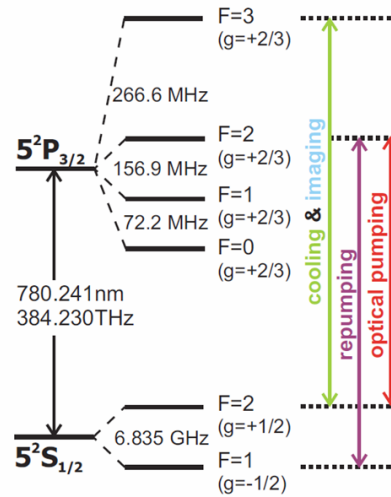


Figure 9.1.: The laser lines for cooling, repumping and optical pumping. The applied detunings from the exact transition frequency is not shown here. From [104].

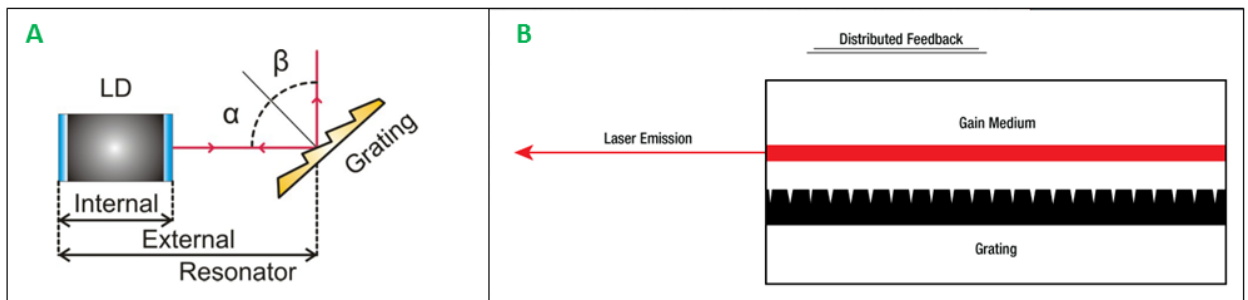


Figure 9.2.: A: The principle of an ECDL. The first diffraction order of a grating is fed back into the laser diode, thus extending the cavity length and providing wavelength dependent feedback. Taken from [112]. B: In a DFB laser diode, a periodic structure acts as a diffraction grating and generates wavelength dependent feedback. Illustration taken [113].

given in [110, 111], numerical values for our laser systems can be found in [112]. By tilting the angle of the grating, the laser frequency can be tuned over several nanometers. The length of the external cavity and therefore the laser frequency can be modulated using a piezo element, which is used in frequency stabilization.

9.1.2. Distributed feedback laser diodes

In distributed feedback (DFB) laser diodes, the active region is periodically structured as shown in figure 9.2 B. This acts as a diffraction grating which provides wavelength selective feedback distributed over the entire resonator length. Compared to normal laser diodes, where the facets of the chip form the mirrors, DFB laser diodes operate on a single longitudinal mode. Their linewidth is typically a few MHz, far better than normal laser diodes but worse than an ECDL. The main advantage of DFB laser diodes is the simple installation.

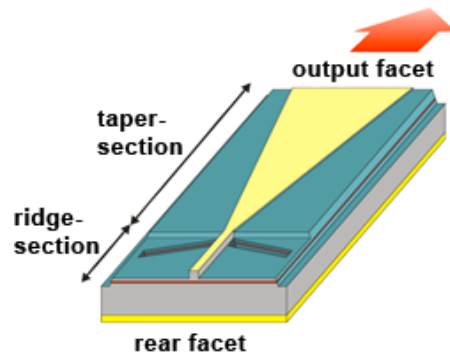


Figure 9.3.: Illustration of a tapered amplifier chip. The narrow input channel serves as a spatial mode filter. Taken from [114].

9.1.3. Tapered amplifier

A tapered amplifier (TA) chip is a specially shaped laser diode. The gain medium starts with a width of a few μm and widens to several hundred μm , as illustrated in figure 9.3. A seed laser is coupled into the narrow side and is amplified in a single pass through the TA diode. The entrance channel can be compared to a single mode fiber and serves as a spatial mode filter. Typical input powers of 10–50 mW result in an output power of up to several Watts.

9.1.4. Temperature stabilization

The output frequency of a laser diode depends strongly on temperature. This is mostly due to the change of the optical path length and a shift in the gain curve. The dependence on the output current can, up to a certain frequency, also be explained by the change of temperature. This temperature dependence can be used to tune the output frequency over several nm. For reliable long term operation on the same laser mode and frequency, active temperature stabilization is required. A PID regulator circuit with a temperature sensor like a NTC thermistor close to the laser diode and a cooling or heating element (we use Peltier elements) can achieve a temperature stability of around 1 mK [115]. This however requires stabilized environmental temperature (around 0.1°C) and proper isolation of the laser box.

9.1.5. Laser locking

The frequency of a laser can be stabilized by comparing it to a frequency reference, in our case a hyperfine transition in ^{87}Rb . As mentioned before, the linewidth of a hyperfine transition is on the order of MHz, while the Doppler broadening at room temperature amounts to ≈ 500 MHz. This is overcome by using **Doppler-free absorption spectroscopy**. The laser beam is retroreflected through a Rubidium vapour cell. Atoms with zero velocity in the direction of the two beams will be resonant with both counterpropagating beams. If the incoming beam intensity suffices to saturate the transition, the reflected beam will experience less absorption and the hyperfine transitions show as dips in the absorption profile. The laser frequency can be scanned around the desired atomic transitions by slowly (≈ 100 Hz) varying

9. Optical setup

the laser diode current. The signal from a photodiode then shows the hyperfine transitions. This is used for manual adjustment of the current and the temperature.

With **frequency modulation** (FM) locking, the laser can be actively locked to a certain transition. In this technique, the laser frequency is modulated with a high frequency component (21 MHz in our case), either through modulating the current or, for an ECDL, the external cavity length. The spectroscopic signal recorded with a fast avalanche photo diode (APD) is used to generate an error signal for a PID regulator, which controls the laser diode current or grating angle.

To adjust the detuning of a laser relative to a hyperfine transition, **frequency offset** (FO) locking is used. Overlaying the laser with a locked reference beam on an APD generates a beating signal at the frequency difference. Comparing this signal to that of a voltage controlled oscillator (VCO) produces an error signal for a PID regulator. With the reference laser locked to a fixed transition, the detuning can simply be adjusted by controlling the VCO.

9.1.6. Our lasers

All the lasers are located in an isolated wooden box on the optical table. Temperature stability is achieved through air conditioning of the room (1 °C) and independent air conditioning of the table (0.1 °C). Apart from temperature, the most sensitive part in the setup are the cables going in- and out of the laserbox. They transmit vibrations which can massively distort the spectra and locking performance. In the near future, each laser will get its own laser box with specially designed cable holders. For details on the upgraded laser setup refer to [116]. Also, the lasers will be moved on another optical table, this way mechanical work on the setup, especially the cryostat, will cause less disturbance to the sensitive lasers.

The choice of the lock point for each laser has to be such that the desired frequency can be reached with the AOMs (acousto-optic modulators, see next section) and that the slope of the error function is as large as possible to keep the lock stable. Furthermore, it is useful to lock to a strong transition for easy identification in the spectroscopy. The relevant laser lines are shown in figure 9.1 and A.3.

- **Reference laser:** This is a self built ECDL, the operating current is set around 50 mA, guaranteeing a long lifetime, since the diode is rated for 150 mA. This laser is FM locked to the cross-over transition [117], $F = 2 \rightarrow COF' = 1, 3$, as this transition shows a large error signal slope. The estimated linewidth is a few hundred kHz and the output power is around 10 mW.
- **Cooler laser:** The main laser is a commercial Toptica TA 100 system. This laser is used for cooling, optical pumping and absorption imaging. It contains a master ECDL for seeding and a TA diode for amplification, the output power is around 700 mW. A weak part of the master laser is overlaid with the reference laser on a APD. The beating signal is used to FO lock the master laser to the reference laser. The frequency offset can be tuned with an analog control voltage, the VCO has a tuning range of about 100 MHz.

- **Repumper laser:** The linewidth requirements for repumping are less stringent, therefore a DFB laser diode can be used without further linewidth reduction efforts. This laser is locked to the $F = 1 \rightarrow COF' = 1, 2$ crossover transition using a FM lock. We use an Eagleyard diode¹, operated around 100 mA. The output power is typically on the order of 20 mW.
- **Backup lasers:** Two additional laser systems are under construction, one DFB laser and one ECDL. These lasers serve as a backup should any of the main lasers break, which means reduced standstill time for the experiment. Also the ECDL laser can be used as an independently tunable imaging laser. This will result in more power in the cooler since no imaging light needs to be split off. Furthermore the new ECDL laser will be used for the alternative pumping scheme to bring the atoms to the $|F, m_F\rangle = |1, -1\rangle$ state.

The biggest issue with frequency stabilized lasers is electronic noise. To make the setup more immune against noisy power supplies, rapidly switching coils, slightly shifting ground potentials and other noise sources that prevent the lasers to stay in lock, several measures are currently underway:

- A metal enclosure, where the entire electronics are housed will help to prevent interference
- Massive filtering of all power lines
- Physical separation from known noise sources such as high current switches
- Careful, star-shaped grounding for all components
- The use of custom-made cables with the exact length required and the right plug on either side². The fewer adapters needed the better, as loose contacts are a major noise source.
- Careful cable arrangement, avoiding any mechanical stress. Using cable clamps blocks the transmission of vibrations along the cables. A flexible design for such a 3D printed cable holder is described in [95]. It can be easily adjusted for any number and diameter of cables and printed at very little cost [116].

9.2. Beam preparation

The precise optical paths of all beams are shown in [118], figure 3.12, a short description is given here for the sake of completeness. A detailed explanation of the chosen lock points, the required detunings and frequency shifts are also given in [118], subsection 3.3.1 and especially figure 3.10.

Beam preparation relies on acousto-optic modulators (AOMs). In these devices, a RF-voltage generates a sound wave in a transparent piezoelectric crystal which acts as a periodic

¹Eagleyard photonics, EYP-DFB-0780-00080-1500-TOC03-0005

²For example from www.coax24.de

9. Optical setup

modulation of the refractive index, scattering incoming light into different diffraction orders. AOMs are used for fast switching, frequency shifting and laser power control. We use our AOMs only in fixed frequency mode, thus avoiding changing diffraction angles. AOMs switch faster than μs , while mechanical shutters need several ms. Varying the RF power allows to vary the power between the diffraction orders. A comprehensive description of the laser park, the beam preparation and exact procedures for alignment and debugging is given in [118].

Cooler light: The output of the TA is sent through the cooler AOM, adding 62 MHz in the first diffraction order. After passing a mechanical shutter, the cooler light is expanded in a telescope to a diameter of 50 mm. The beam is split in six parts, each prepared to the correct circular polarization before entering the MOT chamber. From the (theoretical) 1 W output of the TA chip, about 15 mW of laser power enter in each window.

Repumper light: This is the output of the DFB laser. After passing an AOM with 78.5 MHz, this beam is overlaid with the cooler light and follows its exact path. The power needed for repumping is much lower than for laser cooling.

Imaging light: Absorption imaging uses the same beam as laser cooling, shifted to the right frequency with the FO lock. Before the telescope, a small fraction of the cooler light is split off and, after passing mechanical shutters, coupled into optical fibers leading to the corresponding imaging outcoupler for MOT imaging and the two cryo imaging systems. Each of the three imaging beams contains around 2 mW of power, which can be adjusted by varying the cooler AOM amplitude or the $\lambda/2$ waveplates in front of the corresponding beam splitters.

Optical pumping: This uses the zeroth order of the cooler AOM, which is sent through a 80 MHz AOM in double pass configuration, subtracting 160 MHz from the laser frequency. After applying the correct circular polarization, this beam enters the chamber at the same window as the MOT imaging beam.

Upgrades: The entire beam preparation could be done in a much more compact fashion, if there is ever the need for more space on the optical table. Better mechanical isolation of the shutters, for example by mounting them somewhere else than on the table, should help reducing spikes on the spectroscopy, which eventually unlock the lasers. Finally, a modified vacuum assembly would allow to place the quarter-wave plates directly in front of each window, avoiding distortions to the polarization from the Bragg mirrors. These measures would result in higher atom numbers and colder clouds.

9.3. Imaging

Light passing through a cloud of ultracold atoms experiences absorption, re-emission and a phase shift. These three effects can be used to optically detect the atomic density distribution $\rho(x, y, z)$ at the end of an experimental cycle. A detailed discussion of the available imaging methods can be found for example in [119]. In fluorescence imaging, only the re-emitted photons are collected. This method is especially useful for detecting very small signals down

to few atoms [120]. In the experiment presented here, fluorescence imaging is only used during the MOT phase, where it serves as a debugging tool for alignment. The fluorescence in this case is even visible to the eye.

The most commonly used method however is absorption imaging. It can be viewed as imaging the shadow cast by the atoms. This method is straightforward to implement and still provides high sensitivity. Light absorbed by the atoms is reemitted by spontaneous emission into a solid angle of 4π . Typical imaging systems have a low numerical aperture compared to that, therefore the fluorescence collected by the camera can usually be neglected. To extract useful data from the absorption images, a few theoretical considerations must be taken into account. The saturation intensity I_S for an ideal two-level atom in a resonant light field is defined as

$$I_S = \frac{\pi \hbar c}{3\lambda^3 \tau}. \quad (9.2)$$

This is the intensity where the Rabi frequency Ω of an atom in this light field equals $\Gamma/\sqrt{2}$. The scattering cross section σ is defined as the scattered power divided by the incident flux:

$$\sigma = \frac{\sigma_0}{1 + 4\Delta^2/\Gamma^2 + I/I_S} \quad (9.3)$$

with the weakly pumped limit σ_0 :

$$\sigma_0 = \frac{\hbar \omega \Gamma}{2I_S} = \frac{3\lambda^2}{2\pi}. \quad (9.4)$$

At $I = I_S$, σ drops to $1/2$ of σ_0 . In the above equations, Γ is the natural decay rate of the excited state with lifetime $\tau = 1/\Gamma$, ω is the frequency and λ the wavelength of the atomic transition and Δ the detuning from the resonance frequency [39, 38].

The intensity change dI of a resonant probe beam of intensity I traveling a distance of dz in a medium with a number density $\rho(x, y, z)$ is given by

$$dI = -\sigma I \rho dz = -\frac{\sigma_0}{1 + I/I_S} \cdot I \rho dz \quad (9.5)$$

which results in

$$\ln \frac{I_t}{I_0} + \frac{I_0 - I_t}{I_S} = \sigma_0 \int \rho(x, y, z) dz = \sigma_0 n(x, y) \quad (9.6)$$

through separation of variables and integration. For small (<0.1) saturation parameter $s = I/I_S$, the second term on the left hand side can be neglected and the column density $n(x, y)$ only depends on the ratio of the incident intensity I_0 and the transmitted intensity I_t . This allows quantitative measurements without knowing any absolute intensities:

$$n_{x,y} = -\frac{1}{\sigma_0} \ln \frac{I_t}{I_0}. \quad (9.7)$$

The optimal setting for absorption imaging would be at $I_t/I_0 = 0.5$. With this technique, the laser beams don't need to be homogeneous, even intensity fluctuations between the pulses can be accounted for by scaling the images. All surfaces in the imaging beam path should be anti-reflection coated to avoid interference fringes. To get the correct column density, the

magnification of the optical system and the pixel size of the camera have to be taken into account. The duration of the imaging pulse should be short enough such that the motion of the atoms can safely be ignored.

Trapped clouds can be optically dense with transmitted intensity $I_t = 0$ such that the variations of the atomic density can not be detected. Using far detuned light to reduce the optical density is difficult, as the cloud acts as a gradient index lens and the spatial resolution would degrade. Another way to image optically dense clouds is to use intensities far above saturation, where the scattering cross section is reduced. Details on strong saturation imaging and how to reduce the signal-to noise ratio are given in [121] and [122].

Typical absorption imaging involves more than 100 absorption and re-emission events per atom. The polarization of the imaging light is of importance because the atoms can be pumped between different Zeeman sublevels during the imaging process. This leads to a correction factor α of the scattering cross section σ_0 . For σ^+ polarized light and a quantization field parallel to the beam, $\alpha = 1$ [123].

An imaging sequence consists of three pictures: first an image with atoms present I_t , then a second image of the probe field I_0 where the atoms are gone after release from the trap and a third image I_{bg} to determine the background light level. The absorption image is calculated from these three images. An example for an imaging sequence is shown in figure 9.4. Many parameters can be calculated directly from the column density, such as the cloud size or its position. The total atom number is given by integrating the column density in both directions. By fitting a Gaussian to the integrated column density of the cloud and measuring its full width at half maximum (FWHM) $x_{(t)}$ at different time of flight (TOF) values t , the temperature of the expanding cloud can be calculated from the following equation [124]:

$$T = \frac{m_{Rb}}{k_B t^2} (x_{(t)}^2 - x_{t=0}^2). \quad (9.8)$$

The width of the atomic density distribution of a thermal cloud in a harmonic trap is given by equation 2.10. This allows us to infer the temperature in-situ, which can be useful when a rapid switch-off is impossible. It is given by

$$T = \frac{x^2 \omega_x^2 m}{2k_B}, \quad (9.9)$$

where x is again the FWHM of the Gaussian distribution in one direction and ω_x the trapping frequency in this direction. After these general remarks about the imaging of ultracold atomic clouds, the different imaging systems used in the experiment are described in the following subsections.

9.3.1. MOT imaging

At the beginning of each experimental cycle, atoms are cooled and trapped in the lower chamber. For optimizing laser cooling and the magnetic transport, we need to be able to image the atoms in the lower chamber. The fluorescence of the MOT is visible by eye, (as mentioned in the introduction to this section) it is collected by a small finger camera pointing along the transport axis. A screenshot of the MOT fluorescence is shown in figure 11.1. The MOT imaging direction is indicated in figure 5.1, 45 degrees to the transport direction. The

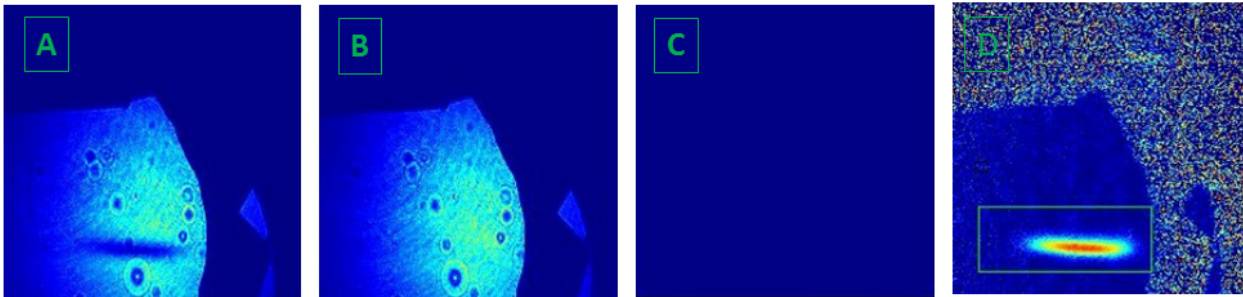


Figure 9.4.: Absorption imaging sequence. A is the image with the atoms present, the shadow is clearly visible. In B, the atoms are gone and only the laser beam is imaged. C is the light background. The absorption image in D is calculated from the three images. When imaging an atomic cloud in situ, i. e. with the trapping fields still present, each atom experiences a local detuning depending on the position. Quantitative measures of the atom number are therefore not possible in situ.

atom numbers at this stage of the experiment are huge and we do not need a high resolution. Therefore we use a commercial camera objective³ with f-number of 1.7 and minimal focal length 45 cm. An additional 4 diopters macro lens allows to position the camera 15 cm in front of the window, 25 cm away from the center of the MOT. We use an industrial CCD camera⁴ for imaging.

9.3.2. Main cryo imaging

The main imaging system in the cryostat shows the atoms in the x-z plane, the coordinate system is shown in figure 9.5. The main imaging system should be able to image the atoms in the quadrupole trap right after transport, during the transition to the QUIC trap and the transfer into the chip trap. And this imaging system should of course provide high resolution images of the atoms trapped on the atomchip.

The optical system is rather simple. It is a two lens setup, with the atoms in the focal plane of the objective lens with focal length $f_1 = 150 \text{ mm}$ ⁵. It is mounted on a motorized translation stage⁶ such that the focus can be optimized with the control software. The second lens focuses the collimated light on the camera. This lens has a focal length $f_2 = 300 \text{ mm}$, resulting in a magnification $|M| = f_2/f_1 = 2$. The camera is a Pixelfly qe⁷ with a pixel size of $6.45 \times 6.45 \mu\text{m}$ and an effective chip size of $9 \times 6.6 \text{ mm}$. This results in a field of view of $4.5 \times 3.3 \text{ mm}$. To image both the quadrupole and the QUIC trap, the magnification can be reduced by introducing an additional third lens in front of the camera using a magnetic mount. All lenses have a diameter of 50 mm, the numerical aperture of the system is about 0.26. The camera is mounted on an x-y-z translation stage to adjust the field of view. The outcoupler for the imaging light can be positioned parallel to the table for standard imaging

³Minolta MD Rokkor 50 mm

⁴Imaging Source, DMK 21BU04, USB connected, BNC trigger input

⁵Thorlabs AC508-150-B Achromatic Doublet, Anti reflection coating: 650-1050 nm

⁶Thorlabs MTS25-Z8

⁷PCO GmbH, www.pco.de. Quantum efficiency at 780 nm: 12% standard and 25% in high gain mode, 12 bit resolution, 1392 x 1024 pixels.

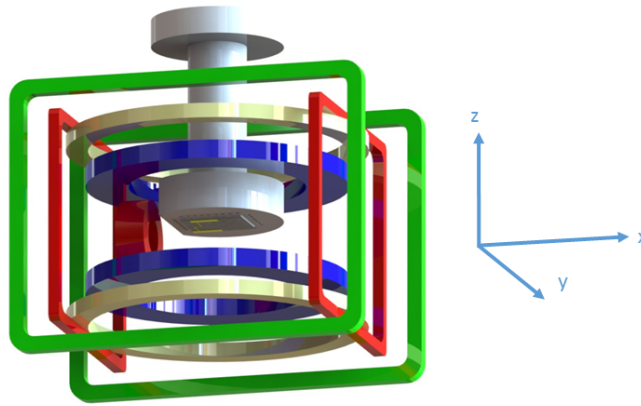


Figure 9.5.: The coils at the experimental stage in the cryostat including the chip mounting. The main imaging system looks along the y -axis. The Ioffe imaging system images the cloud through the opening of the ioffe coil along the x -axis. The center of the coordinate system is the exact middle of the last transport coil V8 and V9. The QUIC trap forms around 6 mm to the left, the chip is located roughly 2 mm above. Note that the perspective of this rendering might be misleading, the y -axis points into the page.

and at an inclined angle for reflection imaging, see figure 9.6.

9.3.3. Ioffe direction imaging

To image the transverse position of the atomcloud, a second imaging system is used. It is aligned perpendicular to the main imaging system, the light enters through the Ioffe coil mounting, therefore atoms are imaged in the y - z plane. We can use both imaging directions simultaneously without any distortion.

The objective lens for this system is a 50 mm lens mounted on the 4 K shield. To get a sharp image for both the quadrupole trap and the chip trap, we need a high depth of field, hence, a low numerical aperture. A 72 mm and a 50 mm lens outside the chamber focus the image on the camera. Details of this imaging system will be discussed in [126].

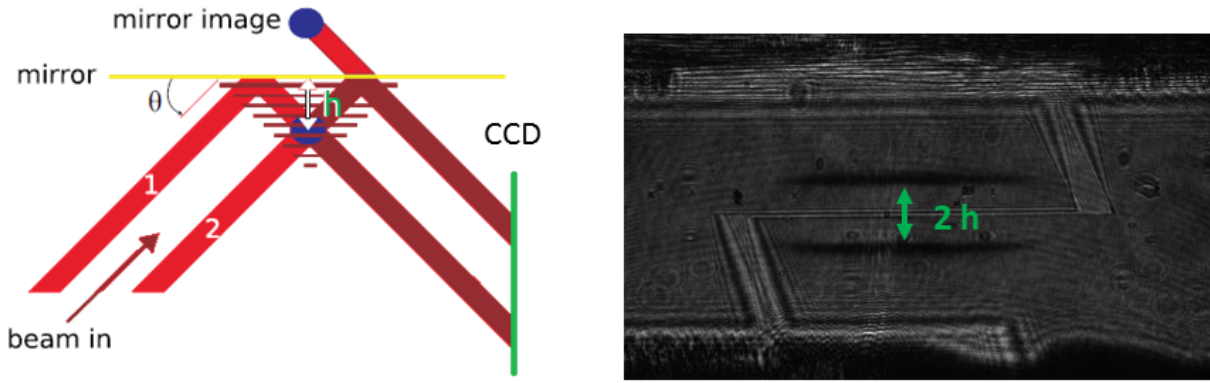


Figure 9.6.: A: Illustration of the reflection imaging adapted from [125]. The imaging beam is first reflected from the chip before passing the atom cloud or the other way round. The distance of the two images on the camera is twice the atom to chip distance. B shows a raw image with the shadow of an atom cloud. The Z-wire as well as the contact pads are clearly visible.

9.4. The quenching setup

As explained in section 3.6, type-II superconductors show irreversible magnetizations depending on the history of applied fields and currents. The only way to reinitialize the superconducting atomchip to its virgin, vortex-free state is to quench the material. This could be done by just turning off the cryostat and wait until the chip is above T_c . The disadvantage of this method is that, due to the comparatively low thermal conductivity of the chip mounting, the atomchip is the last element that quenches. It takes several minutes until the chip becomes normal conducting, during which pressure rises significantly. Until the setup is ready for the next experimental cycle it takes at least 20 minutes, much too long for any practical use. Also this can obviously not be done while atoms are present in the cryostat. Another method to quench the chip is to simply exceed the critical current I_c for a short time. This method produces a spike in the pressure, disturbing any atomcloud that might be in the vicinity. Also it is hard to make sure that no other coil quenches when the current pulse is too long. Our first atomchip was actually destroyed (figure 9.7) while quenching it with a moderate current after turning off the cryostat.

The best way to induce a quench is to use optical quenching with a high intensity laser pulse that locally heats up the thin superconducting layer. Such a quench can be detected by applying a small test current to the chip and measuring a voltage change across the chip. We use an infrared laser⁸, the beam is fed through the bottom window of the transport cross (cf. figure 5.4). This optical system is very hard to align, as the only indication to actually hit the chip wire is the change in resistance. Therefore, we designed a system to simultaneously image the chip wire while aligning the laser. As the camera is sensitive to infrared light, we can see the beam on the chip. The beampath is shown in figure 9.8. When the infrared laser is aligned to the Z-wire, the beamsplitter can be flipped out of the beam to get the maximum laser power on the chip. The imaging system has to take into account the different wavelengths for imaging and quenching by using achromat lenses. A detailed

⁸Innolight Mephisto 1000 NE, Wavelength 1064 nm

9. Optical setup

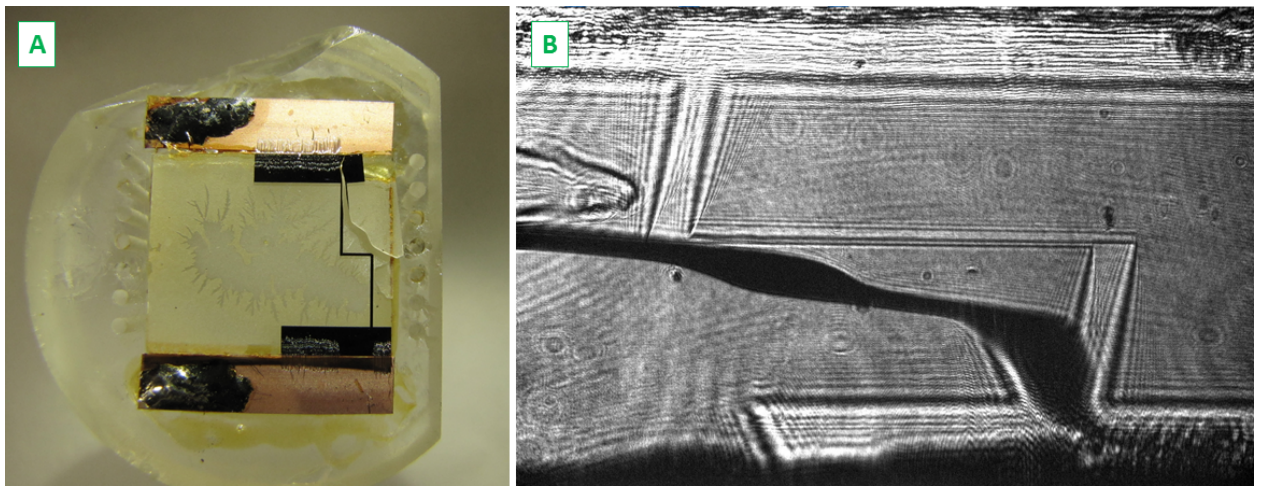


Figure 9.7.: A: The first atomchip broke during a quench. The sapphire substrate cracked due to thermal stress. B shows the broken chip still in the chamber, in reflection imaging.

description of the optical system is given in [127]. This system is able to reliably quench the chip wire within a few milliseconds, as shown in figure 9.9. After the laser is turned off, the wire will return to the superconducting state within 20 ms. This allows to perform the quench with atoms trapped in the vicinity, immediately before transferring them into the atomchip trap.

Future upgrades to the quench setup include a more reliable alignment and a better focusing of the laser. The long term goal is to selectively quench certain areas on the chip, for instance the microwave resonator, while keeping the trapping wire superconducting. This idea is further discussed in chapter 14. The quenching setup also makes a persistent current chip possible. A closed wire loop on the chip can be kept normal conducting while applying a strong vertical field. After turning off the quenching laser, the field is ramped down and a persistent current is induced in the loop, this technique has been successfully applied in [128].

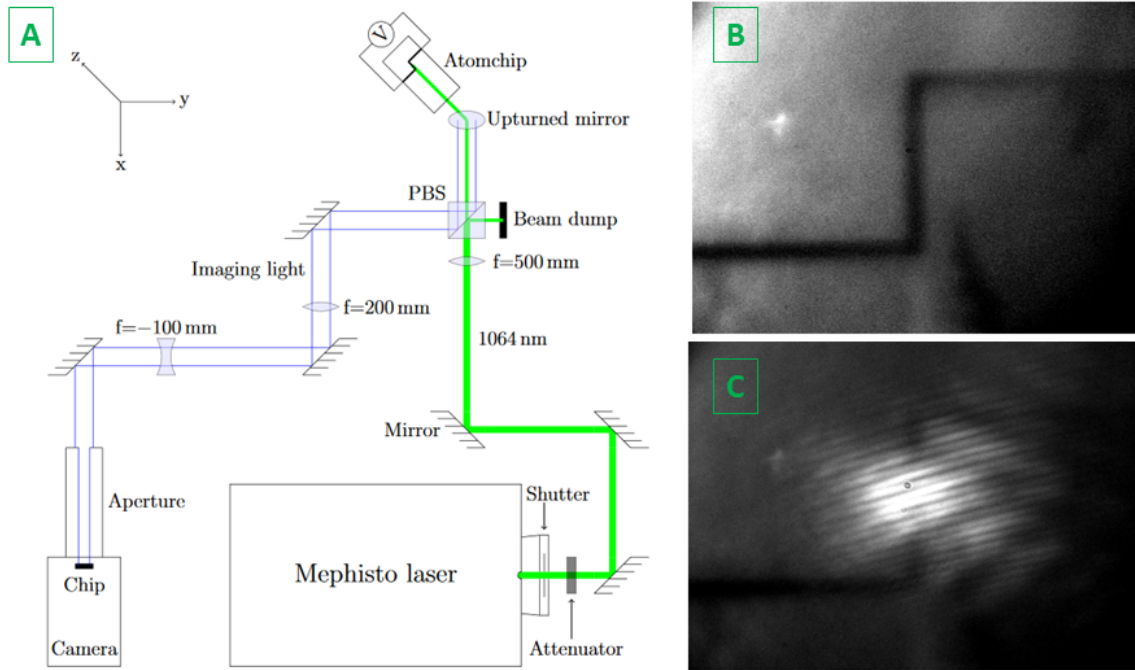


Figure 9.8.: A: Schematics of the quench setup and the vertical imaging. The chip is illuminated from the side through one of the cryo windows with white light to align the imaging optics. Once the Z-wire is in focus (B), the attenuated infrared laser can be aligned to the Z-wire (C).

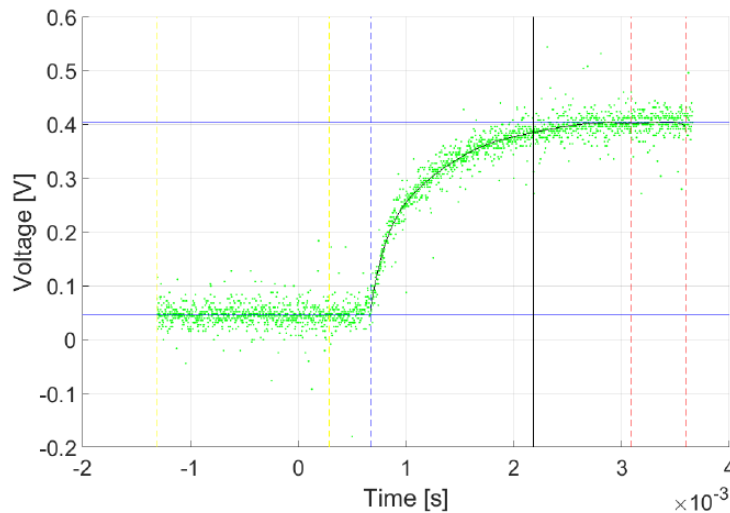


Figure 9.9.: The measured voltage across the outer chip terminals. A constant current of 20 mA is applied. Less than 1 ms after opening the the laser shutter $t=0$, the voltage jumps, indicating a sudden change in resistance. The voltage does not rise further afterwards, showing that the entire chip wire has quenched.

10. Experimental control

Around 100 electronic devices are involved in the setup. Most of these devices are subject to the control system. An experimental sequence involves time scales from a few tens of microseconds (e. g. for optical pumping) up to minutes (e. g. for RF-precooling). The majority of devices are controlled with analog input voltages and TTL trigger signals. Some instruments and devices are configured and controlled through their own software. The complexity of the experimental setup and even more the temporal sequence calls for an efficient software solution to control more than 1000 different parameters, all of which are crucial for a successful experimental run. This chapter presents the hard- and software we use to accomplish this task.

10.1. The ADWIN system

The heart of our control system is an ADWIN PRO real time system¹. There are four analog output modules with 32 analog channels and two digital input-output (DIO) cards with 64 digital channels. The analog channels output voltages in the range of $-10.. +10V$ with a resolution of 16 bit. The digital channels output TTL signals with $+5V$. At the moment, we are using the T10 processor module, with an 80 MHz CPU and 128 MB DRAM. This unit runs an ADbasic program, written in Jäger's own programming language. It runs independently of the control PC, thus undisturbed by the operating system or other processes, which allows to have a predictable and reliable execution time. The achievable time resolution depends on the complexity of the ADbasic program, in the best case around $10\ \mu s$ for the new controller (see section 10.3), and $25\ \mu s$ for the old system (section 10.2). All signals are connected to isolation amplifiers (analog) or optocouplers (digital) to ensure galvanic isolation between the devices and the ADWIN box, therefore avoiding ground loops.

10.2. MATLAB control program

The sequence ADWIN executes is programmed in a MATLAB graphical user interface (GUI). This program has first been described in [129] and significantly expanded in the years after. I will shortly review the concept here and outline its limitations. The experimental sequence is built up by blocks for the analog and digital channels as shown in figure 10.1. These blocks are arranged in matrices for the analog as well as for the digital channels.

An analog block consists of of three values - the duration of this block, the start value and the type (constant or ramp). Each channel is calibrated such that the values can be entered in natural units of the controlled device (MHz, mA, etc.). The analog blocks also know a third type, which is a 3rd order polynomial. These blocks can not be entered through the

¹Jäger Computergesteuerte Messtechnik, www.adwin.de

10. Experimental control

A							B							
Co AOM lev [V]	0	C	0	C	C_level_mot	C	C_level_mot	R						
6 calibrate	T_wait		T_startramp		9966		Tmedium_ram		10	push	L	10165.9	139.04	200
Rep AOM lev [V]	0	C	0	C	R_level_mot	C	R_level_mot	R	11	V1	L	10423.6	6	20
7 calibrate	T_wait		T_startramp		9966		Tmedium_ram		12	QUAD	H	10323.4	710.32	3
									13	unused	L	0	0	0

Figure 10.1.: A: Part of the analog matrix. Each channel consists of blocks, each block contains a value, the type (C=constant, R=ramp) and the duration of the block. Times and values can be entered as numbers or variables. B: Part of the digital matrix. Each block defines the time until the next state change. Each channel can be configured to start low (L) or high(H).

GUI but have to be added by a separate script. Each digital block simply contains the time until the next state change.

All times and values in the analog and digital matrices can be either numbers or variables. Variables can either be directly entered by the user or calculated in a separate script. The direct variables can be scanned from a start- to an end value, two- or more dimensional scans are possible, although the program tends to crash during very large scans.

The MATLAB program transforms the analog- and digital channel matrices into one vector containing 69632 values, which is transferred to the ADWIN system. All time values are converted to integer multiples of the ADWIN update time ($25 \mu\text{s}$), all values to numbers between 0 (= -10V) and 65536 (= $+10\text{V}$). The first 65536 values contain the analog data, 2048 points for each of the 32 channels. A block consists of 8 points, therefore each experimental sequence consists of 256 analog blocks per channel ($8 \cdot 256 \cdot 32 = 65536$). The remaining 4096 data points for the digital data are split in two, 2048 points for each of the two 32 channel DIO cards. An eight-point block is built as follows:

- Type (1=constant, 2=linear ramp, 4=3rd order polynomial)
- Time
- Offset
- Linear coefficient
- Quadratic coefficient
- Cubic coefficient
- Zero
- Zero

The blocks for the digital data are all of type constant. The state of all 32 channels of one DIO card is reflected by a single 32 bit number. The conversion of the 64 bit MATLAB double to the 32 bit number in the ADWIN memory is done by the command "set_data_double"².

The magnetic transport can not be implemented using the matrices described above. We define the magnetic transport parameters such as the endpoint and the acceleration profile in a file. Using this, the pre-calculated currents $I_{(x)}$ (see chapter 8) are transformed into time dependent currents $I_{(t)}$. These waveforms are divided in 16 sections and each section

²The exact conversion is unclear, there seems to be an incompatibility with newer MATLAB versions. We use a trick suggested by JÄGER, the interested reader is referred to the script "testloop.m" and the comments therein.

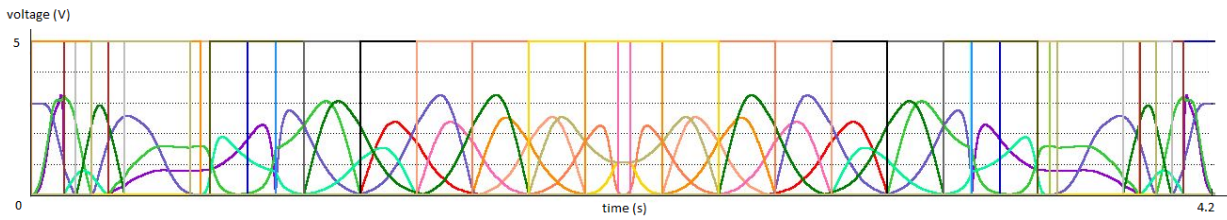


Figure 10.2.: This graph shows the current source control voltages used for a full transport sequence into the cryostat and back. The digital signals, used to control the switchboxes and the switches are also shown. A detailed legend is omitted for clarity.

is interpolated using a third order polynomial. Before sending the data vector to ADWIN, the corresponding transport channels are updated using the calculated polynomials. The complexity of the transport sequence is illustrated in figure 10.2.

Each time a variable is changed or the start button is pressed, the MATLAB program will recalculate the data vector and send it to ADWIN. It also starts the processes on the ADWIN system to initiate the output. The settings of each experimental cycle are stored in a file. ADWIN reports the status of the output process, such that the controller program knows when a cycle is over. A cycle can be interrupted at any time by pressing stop. This stops the output process on the ADWIN system and all voltages return to zero immediately, This has to be considered as switching off highly inductive coils abruptly can be dangerous.

The MATLAB program also communicates with other programs. The camera control software and the data acquisition programs receive the number of the current sequence, to name the image files accordingly. Other devices such as the RF sources receive their settings from the control program through UDP messages. If the temperature or the pressure in the cryostat exceed a predefined value, a stop command is sent to the controller and the cycle is stopped.

The limitations of the control software described here are mainly due to the fact that the number of time steps per experimental cycle is limited. This becomes relevant when trying to recombine several atomic clouds in the cryostat as explained in chapter 13. Another issue is the fact that more complex waveforms can only be realized by concatenating polynomials programmatically, not through the user interface.

10.3. QiController

A completely new control program for ADWIN has been developed by Qi Liang, a complete description of this complex software will be given in his thesis [130]. Here, I will just review the basic concepts of this software. Instead of compacting the desired output to a data vector and calculating the output sequence on the ADWIN CPU, the new control program performs the entire calculation for each timestep and each channel on the PC. This means less work load for the ADWIN processor, thus allowing better time resolution. The only limiting factor is the bandwidth of the data transfer between the PC and the ADWIN system, in our case around 10 MB/s (new modules are equipped with 1000 MBit LAN interfaces). The data is streamed to the memory of the ADWIN unit and output directly by a very lightweight

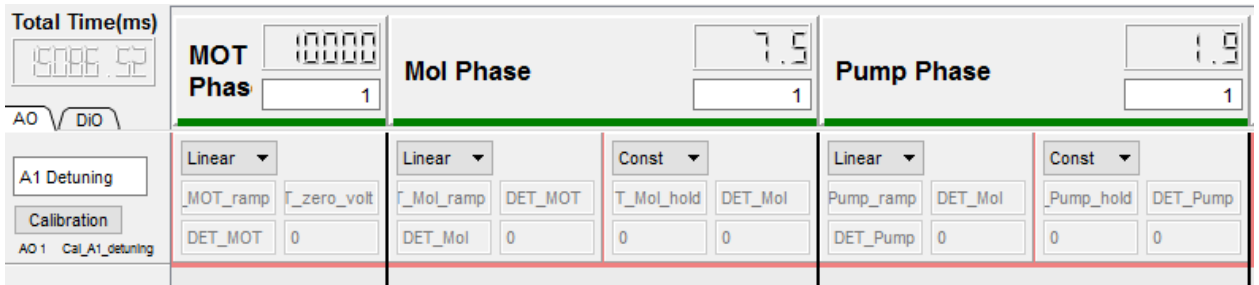


Figure 10.3.: Screenshot of a few sequences of analog channel 1 in the QiController. On top, the names of the first three section are shown. An experimental cycle can simply be created by dragging predefined sections in the channel editor.

ADBASIC program.

Apart from a paradigm change "under the hood", the user interface is also quite different from the old system. The smallest building block of an analog channel is called a "sequence", shown in figure 10.3. Like in the old software, there are predefined functions such as constant and linear ramps, but also exponential, sine wave and other functions. The real flexibility of the new system comes from the fact that the variables can be precalculated files which are output line by line. This allows a very natural implementation of the magnetic transport for example. The digital sequences can also contain files, meaning that one sequence can describe more than one switching event, which is again very useful when implementing the switching times for the transport coils.

A number of sequences can be combined to a so called "section" and saved. Different sections can be combined in the channel editor to a complete experimental cycle using "drag-and-drop". This means a very efficient method to vary an existing cycle. As an example: after optimizing the transfer to the chip trap, the trapping frequencies on the different axis can now be measured by simply adding the predefined section. After the measurement, the section can be removed again and further sections added. Changing from one measurement type to the other can be performed with a few clicks. In the old controller, the workflow is much more complex: the individual channels have to be manually changed. A given experimental cycle consists of the entries in the analog- and digital matrices and can only be saved as a whole. This means a large number of save files is created. When optimizing different stages of the experiment, it is virtually impossible to make sure that all changes are applied to all saved files. A typical example is the MOT detuning: the optimal value changes slightly from day to day³. With the old controller, the "MOT GUI" (the save file) has to be loaded, the optimal value found. Then, these new values have to be applied manually to the "Cryo GUI".

Despite some extremely useful new features such as the concept of the "sections" explained above, the QiController is still in the development phase. All issues leading to unexpected output have been solved, now updates focus on cosmetic changes to the user interface, advanced new features and general stability improvements. As of now, the calculation of a complex cycle can take several minutes even on a fast PC. This is a limiting factor, since in a scan the entire cycle has to be recalculated for every step of the scan, leading to unacceptably long waiting times. Several options are investigated - apart from using better CPUs. For

³Due to a ground issue with the electronics, which is fixed by now.

example, scans could be precalculated on other computers.

10.4. Data acquisition

We use three different cameras for absorption imaging: the MOT camera, the main cryo camera (Pixelfly) and the Ioffe imaging camera. Each camera has a control program where the device settings can be changed. The Pixelfly camera has its own PCI board⁴ and is controlled with a MATLAB program, the two other USB cameras run on Visual Basic programs as there are no MATLAB drivers provided. These programs receive network messages from the control program to set the file names and to wait for TTL trigger signals to make the images. Once the three images for a cycle are taken, the camera programs notify the corresponding acquisition program.

The acquisition program is the same for all cameras. After receiving the network message that the camera program is done, it reads the three images and calculates the absorption picture. The user can select a region of interest (ROI) and a region of background correction (RBC) in the absorption image. This is used to create a zoomed and corrected version of the absorption image. The resulting picture is integrated horizontally and vertically, these profiles are used to calculate the relevant data. Currently, the camera programs and the acquisition program are adapted to increase their stability. Additionally, with the implementation of the QiController, file naming and storage will be reorganized.

10.5. Auxiliary programs

A number of additional devices are controlled by small LABVIEW programs. The architecture of all these programs is the same and depicted in figure 10.4. When started, the program executes all functions in the initialization loop. A while loop keeps listening for incoming network messages. The upper event structure is responsible to react to user or network input and does all data manipulation like saving and plotting. It runs independently of the device under control. The lower event structure is handling all device related activities. This simple structure can be adapted to any new device quickly.

A big issue with all computer controlled devices is the connection. All devices are now connected using long USB cables going from the lab to the control room. Long USB connections are very unreliable and sensitive to electronic noise⁵, we therefore plan to place some PCs below the optical table to significantly shorten the required USB cable lengths.

10.5.1. Temperature and pressure measurement

The four temperature sensors in the cryostat are connected to a temperature controller⁶. This device is connected with USB to the PC. The program reads and displays the values of all sensors every three seconds. If the running mean of one of the sensors exceeds a certain threshold, a network message is sent to the alert program. The running mean is necessary to

⁴PCI board 540SC PCO AG, www.pco.de

⁵If the neighboring experiment switches their coils rapidly, our USB device connections crash.

⁶Model 336, Lakeshore Cryotronics

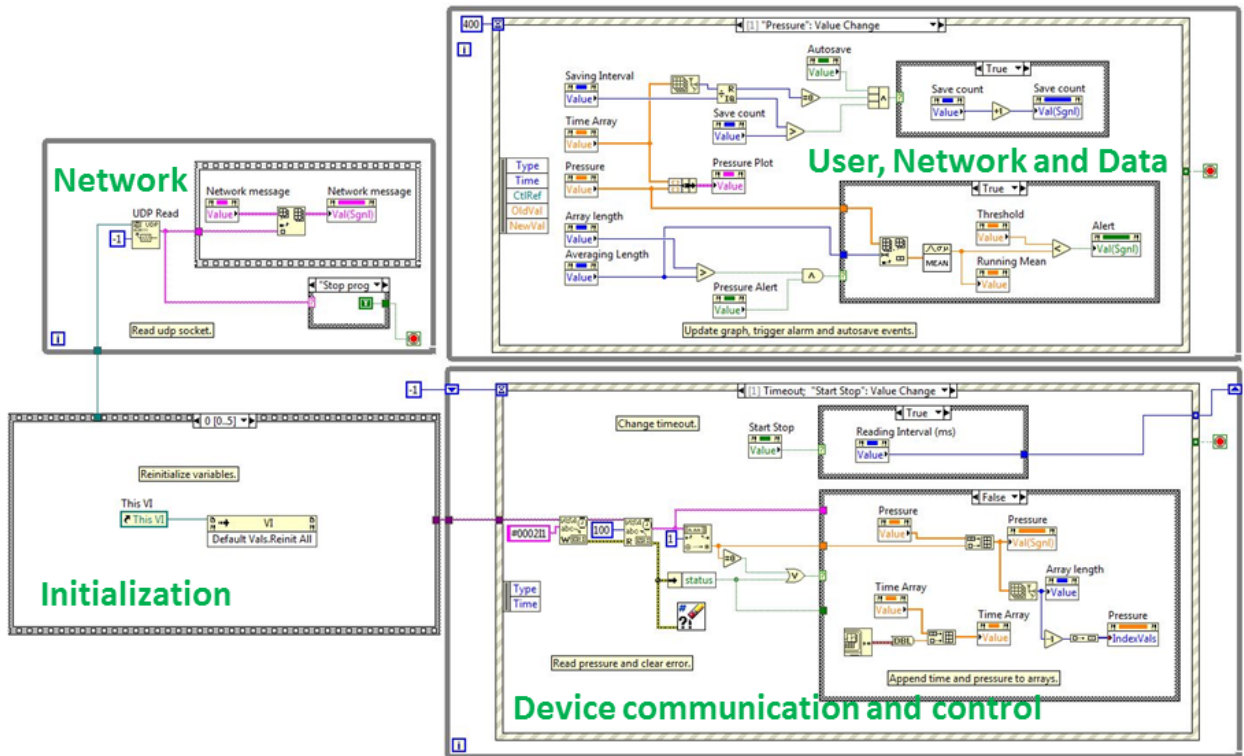


Figure 10.4.: General architecture of all our LABVIEW programs. The initialization loop is executed once at program startup. It initializes all variables to their default values, creates a network socket for incoming UDP messages and establishes the connection to the device. The network loop is a while loop continuously waiting for incoming network messages. A new message is written to the network message array, which triggers an event. The upper event structure handles all user, network and data related events. The timeout event of this structure regularly updates the front panel controls. Incoming network messages and fresh instrument data are also handled by this event structure. This structure can create events for the device structure below, such as the press of the start/stop button or some change of device settings. The device structure handles the full communication with the instrument. Data received from a measurement triggers in turn the upper event structure. Sticking to this program layout makes the programs readable, adaptable and reusable.

avoid false alarms because the temperature sensor readings are sensitive to RF and magnetic fields, showing spikes during magnetic transport and RF cooling.

The pressure gauge in the cryostat is controlled by a Varian XGS 600 gauge controller. This device has a RS232 serial port and is connected to the PC with a serial to USB adapter. The LABVIEW program is basically identical to the temperature control program, including the alarm function. All temperature- and pressure readings are saved to a text file automatically.

10.5.2. Message collection program

This program listens to incoming UDP messages. It collects the messages from all other auxiliary programs. Different messages trigger different acoustic signals to notify the user, for example if an acquisition program fails to take a picture. In case of a temperature or pressure alert, a stop command is sent to the ADWIN control program and the cycle is interrupted.

10.5.3. RF sources

For evaporative cooling in the QUIC trap and the chip trap we use several RF sources⁷, controlled through LABVIEW programs. The ADWIN control program sends a network command containing the start and stop frequency, the amplitude and the ramp time for a linear frequency sweep. The sweeps are triggered with a TTL signal from a digital ADWIN channel. The Agilent RF sources can also be configured to analog frequency modulation using an analog ADWIN channel.

10.5.4. DC power supplies

The MOT bias coils in vertical and in transport direction are supplied with an Agilent 6623A power supply. The third output of this device is used for analog control of the Rubidium dispenser power supply. The LABVIEW program again has the same architecture, network commands from the controller can set the appropriate output voltages. The power supply is operated in CV mode, to get the desired current in the coils the resistance has to be entered correctly. The dispenser control can be turned on at a predefined date and time, reducing the waiting time until sufficient Rubidium is in the chamber.

10.5.5. NI DAQ

The complexity of the experimental sequence calls for a real time monitoring of the transport currents. The currents for the superconducting coils and the chip are measured with ten magnetoresistive current senses⁸ located in the breakout box. These sensors have a bandwidth of 200 kHz, are galvanically isolated from the current and show no drift or hysteresis. We use a NI DAQ card⁹ to monitor the sensor outputs in real time. For a noise free measurement, it is important to keep track of the grounding of the signals. The current senses are grounded at one point on the optical table. The NI DAQ card is set to "referenced single

⁷One SRS DS345 and up to three Agilent 33220

⁸Sensitec CMS2005

⁹NI USB 6218 BNC

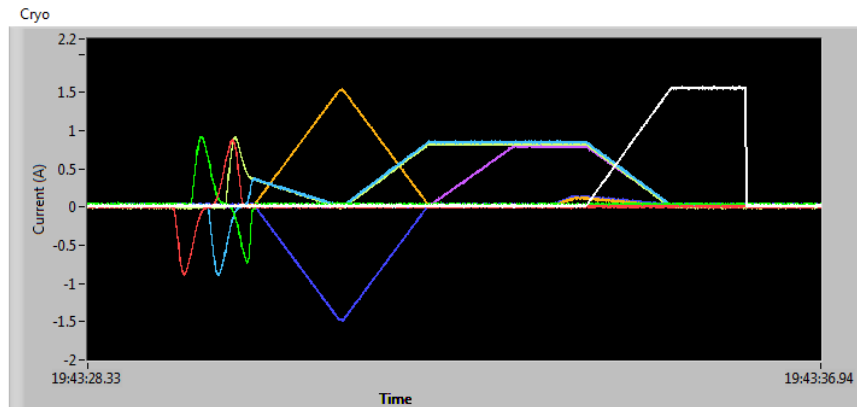


Figure 10.5.: Screenshot of the live current display for the superconducting coils. This sequence shows the end of the magnetic transport, the buffer trap, the QUIC trap and the chip current. The cycle is shortened for clarity, the currents of the chip bias coils are barely visible as they are only a few mA.

ended”, measuring the signal relative to the analog input ground of the device, which is also attached to the same ground connection. The theoretical total sampling rate is 250 kS/s, for reliable operation we use 120 kS/s, 12 kS/s per channel. Accurate measurements of fast transients are therefore not possible, unless the user deactivates some of the channels. Higher sampling rates should be possible with a shorter USB cable. A screenshot of an experimental sequence is shown in figure 10.5.

The output of the Delta power supplies is monitored with another NI DAQ card¹⁰. The power supplies have monitor outputs for the current and the voltage they supply, with the installation of the new switchboxes we will also use magnetoresistive current senses instead.

10.6. Upgrades to the IT

As mentioned in several of the above sections, there are some important upgrades to our hard- and software on the way that should make operation more reliable and user friendly:

- Avoiding long USB cables by putting several PCs in the lab, close to the devices they control. One PC for the NI DAQ cards, one for all other LABVIEW controlled devices, and one computer for all three cameras.
- Several monitors in the lab, where current sequences or camera images can be displayed, will be very helpful during alignment or other tasks in the lab.
- All data transfer is done using LAN, which is fast and reliable.
- A data server with a RAID system, storing all data from the cameras, the controller but also from the monitoring and analysis programs.
- The organization of all data in a flat folder hierarchy (and keeping it in order).

¹⁰NI USB 6229 BNC



Figure 10.6.: Picture of the control room. Not one screen to many.

- Automatizing the Benchmark routine. To test the status of the setup, we perform the same scans (MOT temperature, transport efficiency, QUIC lifetime etc.) every couple of days. The new controller allows to completely automatize this
- Automatizing the analysis. When starting a standard scan (lifetime, temperature, trap frequency etc.), the analysis program should trigger once the scans are done, output results to a PDF file and print it, which can be put in the lab book directly. Avoiding these repetitive manual tasks frees time for more important tasks.
- Overhaul of the acquisition programs to increase stability and make it more user friendly.

Part III.

Results, discussion and outlook

11. Transport of ultracold atoms in a cryogenic environment

The key feature of this experiment is the magnetic conveyor belt to transport ultracold atoms from the room temperature MOT chamber into the cryogenic science chamber. In this chapter I will review the performance of the setup at each steps of an experimental cycle until the atoms have reached the superconducting atomchip trap.

11.1. Laser cooling and magnetic trapping

Every experimental sequence starts with the MOT phase, where the cooler and repumper light and the MOT coils are turned on. Atoms are collected for several seconds. After the MOT phase, the magnetic field is briefly turned off and the detuning of the cooler light is shifted. During this optical molasses phase, the temperature of the cloud can be significantly decreased. Following the optical molasses, all atoms are pumped in the $|2, 2\rangle$ state with a short laser pulse and a quantization field. Without this optical pumping, the number of atoms in the final trap would be more than 50% lower. The current in the MOT coils is then quickly ramped up to form a tight magnetic trap with the right gradient for magnetic transport (130 G/cm). A summary of this first phase is given in table 11.1, pictures of the atomic cloud in the MOT, after the molasses and in the magnetic trap are shown in figure 11.1. We are able to trap around 1.3×10^9 atoms at $100 \mu\text{K}$ in the magnetic trap. The lifetime in this initial trap is around 4 s.

Table 11.1.: Initial laser cooling and trapping

Phase	Duration	Lasers	Currents
MOT	10 s	Cooler, Repumper	MOT coils 10 A
Molasses	10 ms	Cooler, Repumper	-
Opt. pumping	1 ms	Pump	Bias coil 350 mA
Trap	ramp up in 100 ms	-	MOT coils 70 A

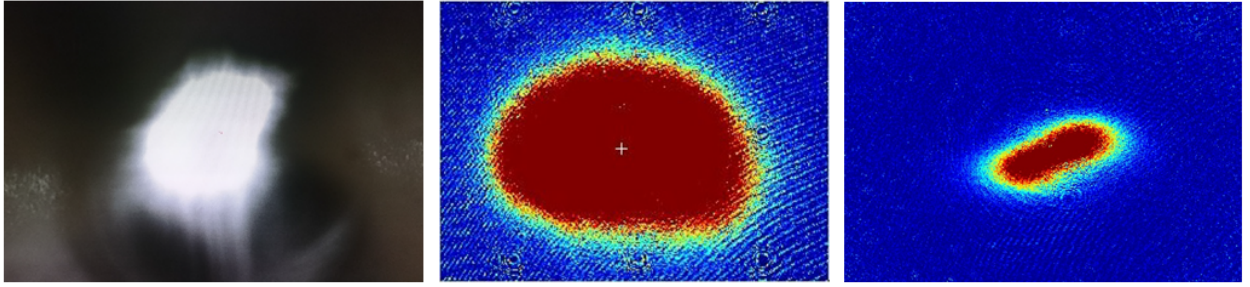


Figure 11.1.: A: The fluorescence of the MOT as seen by the life camera. B: The atom cloud after the molasses phase. The asymmetry is due to slight laser power imbalances. C: The magnetic trap in situ showing the characteristic hour-glass shape of a quadrupole trap (depending on the detuning).

11.2. Magnetic transport

Due to the large number of devices and parameters, and thus possible error sources, debugging of the magnetic transport can only be done in steps. This means that the atoms are transported to an defined endpoint and then brought back into the MOT chamber, where they are imaged. This way any sudden atom loss can be pinpointed to a certain location along the path. For the reverse transport, the $I_{(t)}$ waveforms are just reversed, the atoms experience the exact same accelerations as in the forward run.

The transport efficiencies are shown in the plot 11.2. The drop in horizontal transport efficiency in the region between 80 and 130 mm is due to the small diameter of the vacuum tube in the differential pumping stage and the gate valve as explained in section 5.3. The transport efficiency for longer transport distances increases because the atoms spend less time in the narrow section, where the lifetime is drastically reduced. The vertical transport is very efficient, essentially loss free. As soon as the atoms enter the cryostat, the lifetime goes up from around 6 s in the corner to several tens of seconds because of the reduced background pressure. Overall, the squared transport efficiency approaches 60%, which is around 75% for the single way, assuming the same efficiency on the way back. This means with an initial trap of 1.3×10^9 atoms we get around 9.5×10^8 in the cryostat. The magnetic transport also unavoidably heats the atoms. Directly after transporting back and forth, we the longitudinal temperature fit gives 1 mK, while the transversal fit gives $500 \mu\text{K}$. This is due to trap oscillation. For a proper temperature measurement the atoms have to be held in the trap for around 100 ms, after which both fits show $500 \mu\text{K}$. It should be noted that great care has to be taken when measuring the lifetime of the atoms in the normal conducting part of the transport because of the high power dissipation. Especially the vertical coil mountings get very hot, hold times of more than 10 s are critical. Breaks between the cycles are needed to allow the coils to cool down.

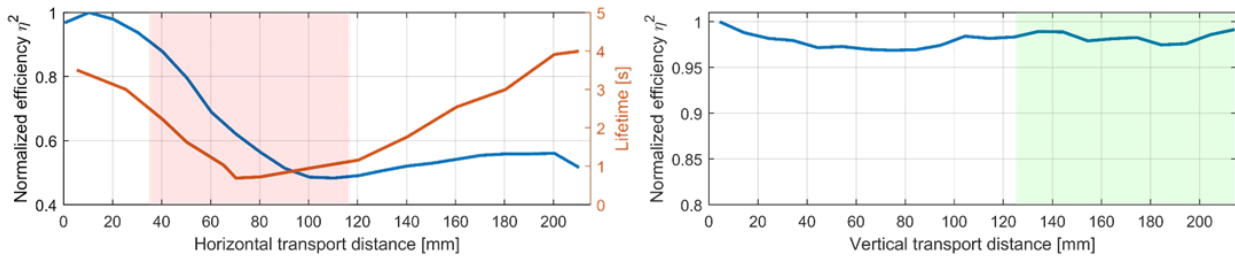


Figure 11.2.: Left: Normalized horizontal transport efficiency and lifetime at different positions. The narrow region of the vacuum tube is shaded in red. Right: Vertical transport efficiency, the region inside the cryostat is shaded in green.

11.3. The quadrupole Ioffe configuration (QUIC) trap

At the end of the magnetic transport the atoms are held by a quadrupole trap formed by the last two transport coils V8 and V9. Quadrupole traps have a zero trap bottom, which means that Majorana spin flip losses occur. At the end of the magnetic transport, the atoms have a temperature of around $500 \mu\text{K}$, where Majorana losses are irrelevant. However, in order to transfer the atoms to a shallow chip trap, the cloud needs to be cooled significantly. The quadrupole-Ioffe configuration features a nonzero trap bottom and a harmonic potential. For this trap, a coil with a smaller radius (the Ioffe coil) is placed between the quadrupole coils, cf. figure 7.5. By ramping up the current in this coil, the magnetic minimum from the original quadrupole trap starts to move towards the Ioffe coil. At a certain current, the trap becomes harmonic and the trap bottom starts to lift, this is illustrated in figure 11.3. The highest trapping frequencies in such a QUIC trap are achieved with a low trap bottom.

Ideally all three coils require the same current for the QUIC trap. This would allow to operate all coils with one current source, which makes the trap much more immune against current noise [48]. Unfortunately the mechanical alignment of the Ioffe coil is not precise enough. The optimal current in our Ioffe coils is about 95 % of the quadrupole current. We can therefore only switch V8 and V9 in series, while the Ioffe coil is driven independently. Switching the coils in series can only be done without current to avoid spikes. We therefore store the atoms with a buffer trap formed by the two vertical bias coils BV8 and BV9, this trap is at the exact same position as the quadrupole trap. Once V8 and V9 are in series, the atoms are transferred back to the initial trap.

The QUIC trap contains several 1×10^8 atoms, we have no reason to doubt a unit transfer efficiency from the quadrupole trap. A proper atom number or temperature measurement by time of flight expansion is not possible, since this would require a rapid switch-off of the fields. Such a rapid change in current creates massive eddy currents in the copper mountings of the coils. The magnetic field produced by the eddy currents violently distort the atom cloud. However, knowing the trapping frequencies and the width of the Gaussian atom distribution we can calculate the temperature according to equation 9.9. The trapping frequencies can be measured by exciting trap oscillations with short magnetic field spikes. After the spike, the entire trap will oscillate around the equilibrium position, this is shown in figure 11.4.

The lifetime in the cryostat in general is very long compared to the room temperature part of the chamber. Since all cold surfaces act as very efficient pumps, the background pressure is greatly reduced, orders of magnitude below the 2×10^{-10} mbar measured with

11. Transport of ultracold atoms in a cryogenic environment

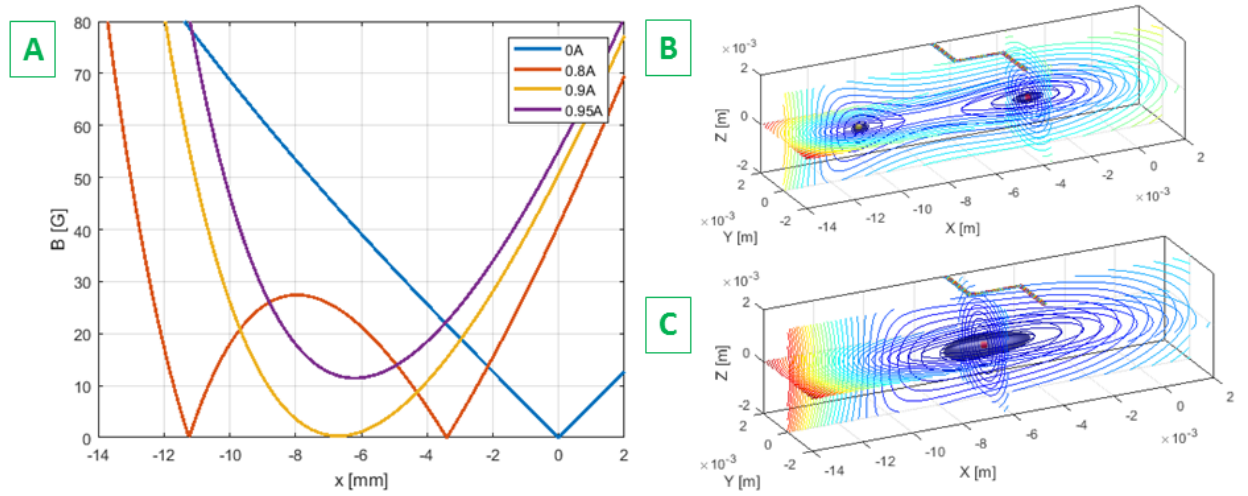


Figure 11.3.: A: The evolution of the magnetic trap as the current in the Ioffe coil is increased, for $I_{quad} = 1$ A. B and C show a 3D simulation of the forming QUIC. The isosurface is drawn 10 G above the minimum.

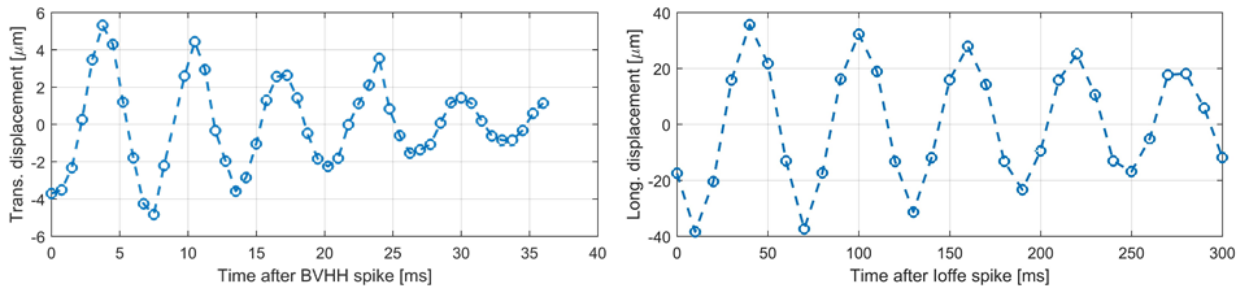


Figure 11.4.: Measurement of the trapping frequencies in the QUIC trap. The longitudinal oscillations are excited with a spike on the Ioffe current, the transversal oscillations with a spike in the vertical bias field. The trapping frequencies are around 16 Hz longitudinally and 160 Hz transversally for a series current of 550 mA and a Ioffe current of 517 mA (94%). This is in good agreement with the simulations.

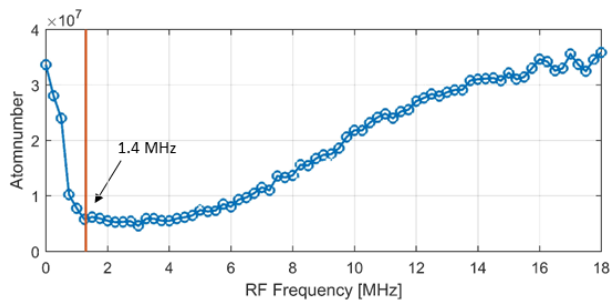


Figure 11.5.: RF trap bottom spectroscopy of the QUIC trap. We apply a constant RF frequency for 30s and then measure the atom number. This is equivalent to creating a hole in the trap at a given height. When the frequency hits the trap bottom, all atoms will "flow" out of the trap. Frequencies below the trap bottom do not affect the atom number.

the pressure gauge. The limiting factor for the lifetime of our QUIC trap is the vicinity of the chip wire, which introduces RF noise. The QUIC lifetime without the chip (and chip mounting) present exceeds 300s. During the QUIC phase, we disconnect the chip wire from the outside electronics using the mechanical relays shown in figure 7.6. Typical lifetimes in the QUIC trap are now around 150s, we expect that our noise filtering efforts described in 7.4 will further increase this number.

As mentioned above, the QUIC trap needs to be cooled significantly from the $500 \mu\text{K}$ before we can transfer the atoms into the shallow atomchip trap. The warm initial cloud and the relatively low trapping frequencies in the QUIC trap call for long evaporation times, which is no problem given the long lifetime. A trap bottom spectroscopy helps to find the frequency range for the cooling ramp and to determine the trap bottom. Figure 11.5 shows the trap bottom of the QUIC trap at around 1.4 MHz which is equivalent to 2 G, as predicted by the simulation. The trap bottom can be lifted by increasing the Ioffe current, however this reduces the trapping frequencies further and affects the transfer efficiency to the chip trap.

RF cooling in the QUIC trap is done by applying a linear RF knife starting at 30 MHz. Trap bottom spectroscopy hints that only frequencies below 20 MHz should have an effect, however a higher starting frequency results in colder and denser clouds. As the QUIC trap is a very deep trap, the long Boltzmann tail of the atomic cloud remains trapped too. The cooling times are quite long, between 30s and 70s. Not only play the collision rate (and thus the trapping frequencies) a role, but also the RF field strength at the location of the atoms. A more effective antenna or an amplified RF signal might help reducing this cooling time in the future. In principle, cooling in the QUIC trap can result in a BEC. The critical temperature for 1×10^5 atoms in our QUIC trap is around 100 nK, the transversal size of this BEC would be on the order of $2 \mu\text{m}$, which is below our imaging resolution. The coldest QUIC traps were about 400 nK, for transfer into the chip trap we only cool down to $\approx 30 \mu\text{K}$. Figure 11.6 shows the atomic cloud for different end frequencies and the corresponding temperatures. The heating rate can be measured by simply waiting: the cooled cloud will warm up and thus its size will grow. We determined the heating rate to be on the order of 25 nK/s .

11. Transport of ultracold atoms in a cryogenic environment

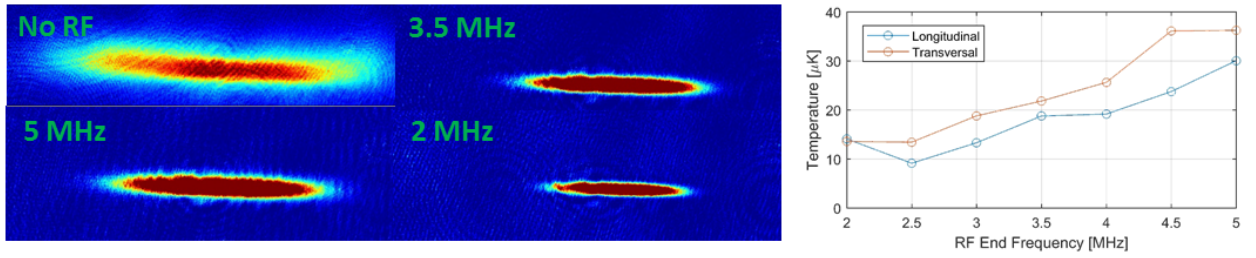


Figure 11.6.: The images show the QUIC trap without cooling and at different RF end frequencies. The temperature calculated from the transversal and longitudinal width agrees, as shown by the plot. The initial temperature directly after transport is around $500 \mu\text{K}$.

11.4. Transfer to the chip trap

Once the QUIC trap is sufficiently cold, the atoms can be transferred into the chip trap. To find the correct current sequence that minimizes atom loss during this procedure, the geometries of the QUIC trap and the chip trap need to be taken into account. A cross sectional view reveals that both traps are quadrupole-like traps, but their magnetic fields are rotated by 45 deg with respect to each other. The naive approach of turning the QUIC trap off while ramping the chip current and the bias field up does not work, all atoms are lost. A full 3D simulation of the magnetic trap was required to find a working sequence. The idea is to first apply the chip bias field in the opposite direction, which moves the QUIC trap to the side and rotates the field. Then a vertical field pulls the atom cloud towards the chip. The last step is to reverse the bias field direction while the chip current is ramped up and the currents for the QUIC trap are ramped down. Optimizing all independent parameters leads to an estimated transfer efficiency of about 60%.

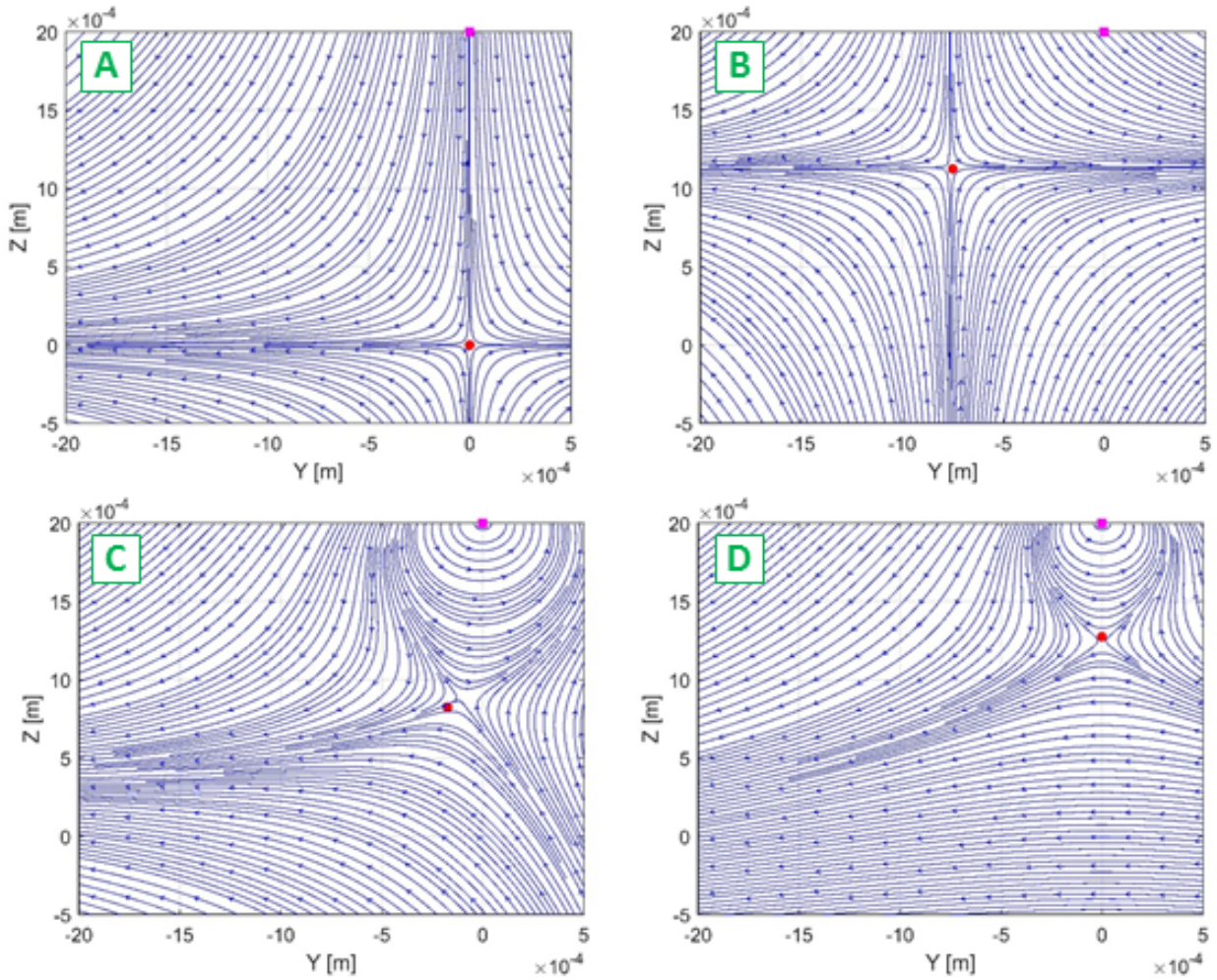


Figure 11.7.: Streamline plots of the magnetic field throughout the reloading sequence. A shows the pure QUIC trap. In B, the cloud is moved up and sideways. C shows the tilting field as the bias field is reversed. D is the final chip trap. The chip wire is marked with a pink square, the trap minimum is indicated by the red dot.

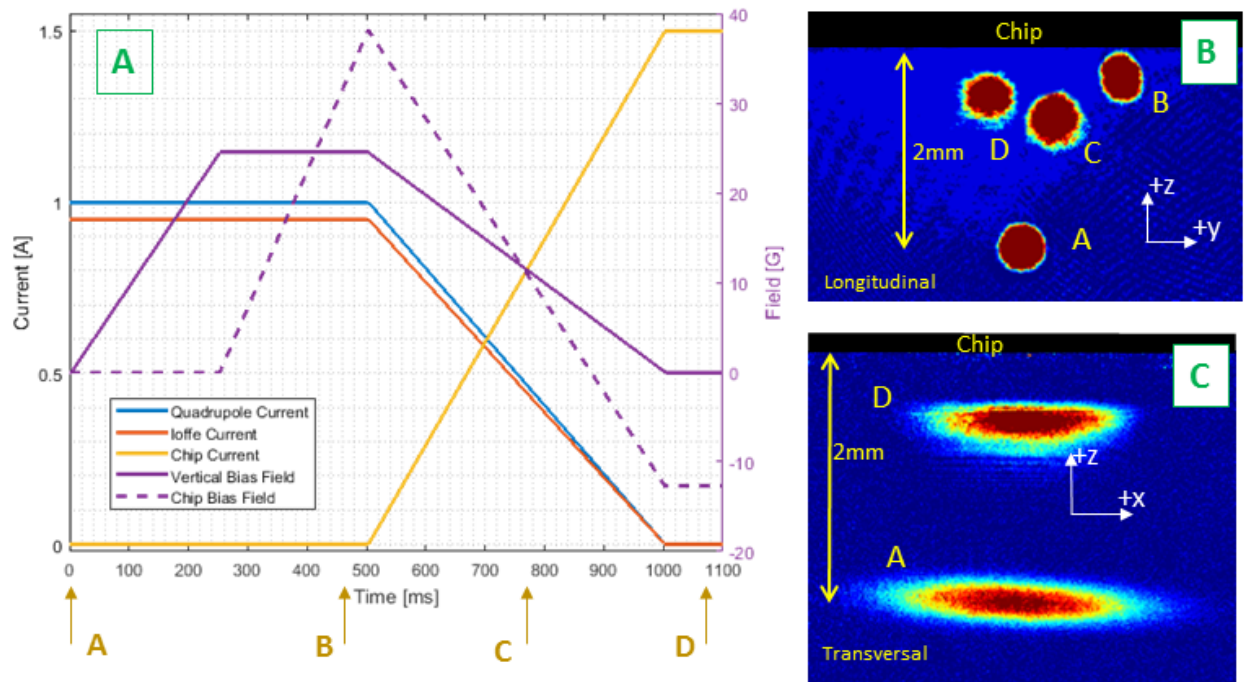


Figure 11.8.: The transfer sequence from the QUIC trap to the chip trap. A shows the currents and fields, B the transfer imaged by the Ioffe camera and C with the main imaging.

12. The superconducting Z trap

A simple way to create a closed magnetic trap on an atomchip is a Z shaped trapping wire in combination with a horizontal bias field perpendicular to the middle part of the Z. The fields of the two long leads of the Z do not cancel completely and create a harmonic longitudinal confinement with a high aspect ratio leading to the typical cigar-shape. Figure 12.1 shows a simulation of an ideal Z trap with the atoms above the middle wire and figure 12.2 shows the trapping potential along different directions. The chip wire used for our measurements has a width of $200\ \mu\text{m}$, the central wire is 2 mm long.

The limited trap depth of the chip trap is the reason why the atoms need to be precooled in the QUIC trap before transfer. We typically cool the QUIC trap to well below $50\ \mu\text{K}$ such that the chip trap with typical trap depths of $\approx 10\ \text{G}$ can accommodate most of the atoms. In contrast to the QUIC trap, the chip trap allows a rapid switch off and thus time of flight measurements. Intuitively one would switch off the chip wire which has basically zero inductance and leave the homogeneous bias field on. In this case however, the atoms get accelerated towards the chip wire, especially for traps relatively close to the chip. Due to the small currents used in the bias coils, rapid switching poses no problem and all TOF measurements are done by switching off the bias field $100\ \mu\text{s}$ before the chip. The temperature can be calculated using equation 9.8, such a fit and the expanding cloud at several TOF values is shown in 12.3. The atom number measurements at positive TOF are more trustworthy as the cloud is not optically dense any more and all atoms experience the same field. Directly after the transfer we have around 2×10^6 atoms at around $50\ \mu\text{K}$ in the chip trap.

For measuring the trapping frequencies, the trap gets a little kick in one direction. This can be done by applying a small current spike on the chip current (or alternatively the bias field), this will change the distance to the wire. The time after this spike is varied and the oscillations of the trap position are measured. For the longitudinal trapping frequencies, we use a spike on the Ioffe coil. The results for the trapping frequency measurements are shown in figure 12.4. If the center of mass oscillation becomes too small, an alternative measurement of the trapping frequency is to use parametric heating. In this method an alternating field applied to the trap will cause heating and thus atom loss, which is maximum on resonance.

The trap bottom of the chip trap can be lifted by applying a homogeneous bias field parallel to the central part of the Z, a so called Ioffe field. Trap bottom spectroscopies for several values of the Ioffe field are shown in figure 12.5.

Without any filtering, the lifetime in the chip trap is only a few seconds, since the chip wire acts as an antenna for electronic noise, especially in the range below 5 MHz. As explained in section 7.4, the long wires connecting the chip pick up all sorts of noise and efficiently couple it to the atoms. Even the lifetime in the QUIC trap, several mm below the chip, is greatly reduced. By decoupling the chip with mechanical relays in the breakout box from the electronics during precooling, the QUIC trap lifetime grows significantly. Using line filters¹

¹Schaffner FN2060-10-06

12. The superconducting Z trap

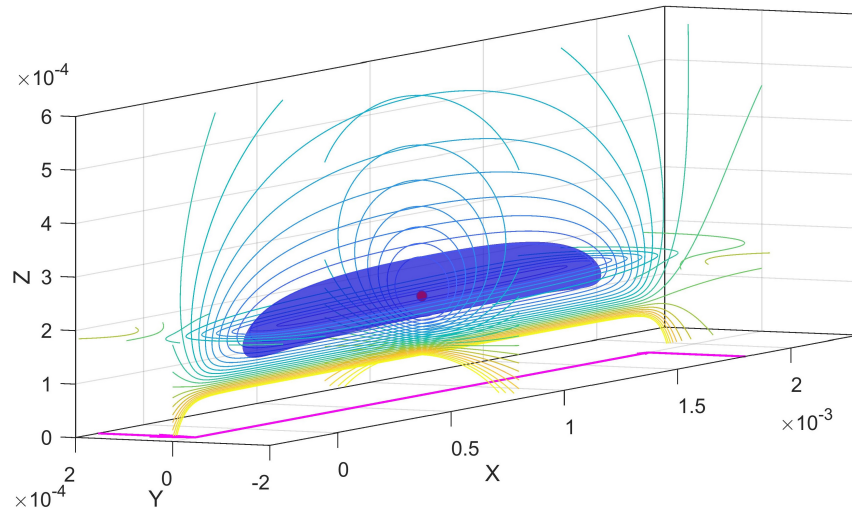


Figure 12.1.: 3D simulation of an ideal Z trap with a chip current of 1.9 A and a horizontal bias field of 20 G. The isosurface is drawn 5 G above the trap bottom, the red dot indicates the trap minimum.

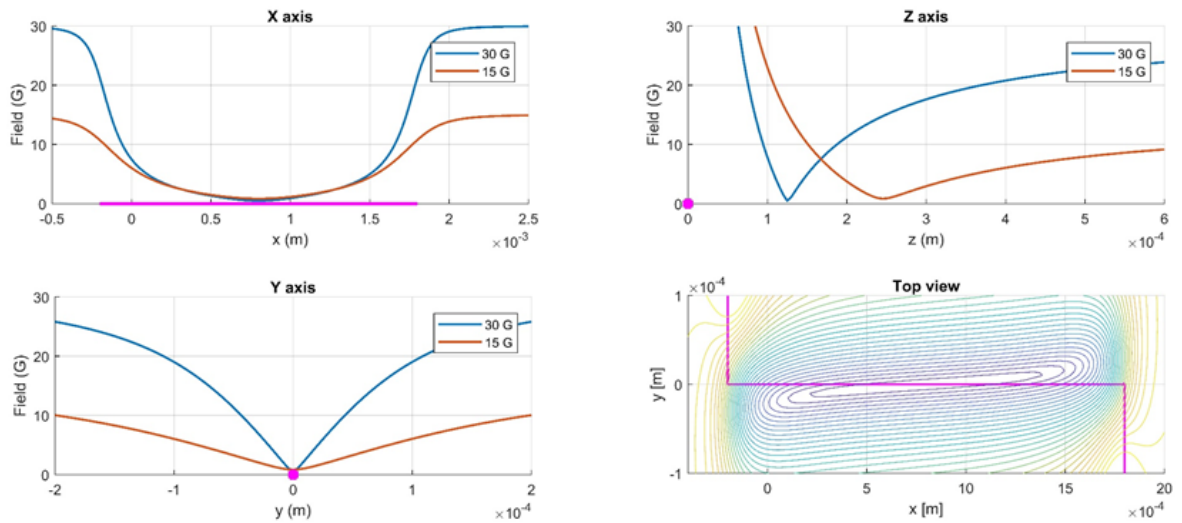


Figure 12.2.: Cuts through the ideal Z trap with a chip current of 1.9 A and two different bias field levels, showing the longitudinal and transverse confinement. The chip wire is marked in magenta. The weakest confinement is in the $-z$ direction, defining the trap depth. The top view shows that the trap is not parallel to the middle wire, but slightly tilted, as a Z is inherently asymmetric.

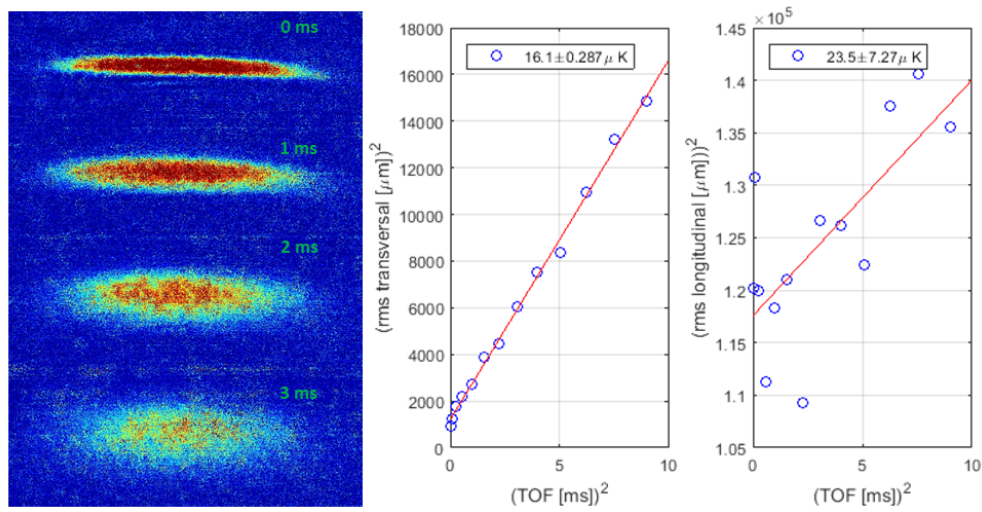


Figure 12.3.: The chip trap during expansion, the TOF values are indicated in the pictures. Gravity points upwards. The cloud width is fit to equation 9.8 to calculate the temperature. Generally, the longitudinal fit is less reliable because the width estimation scatters.

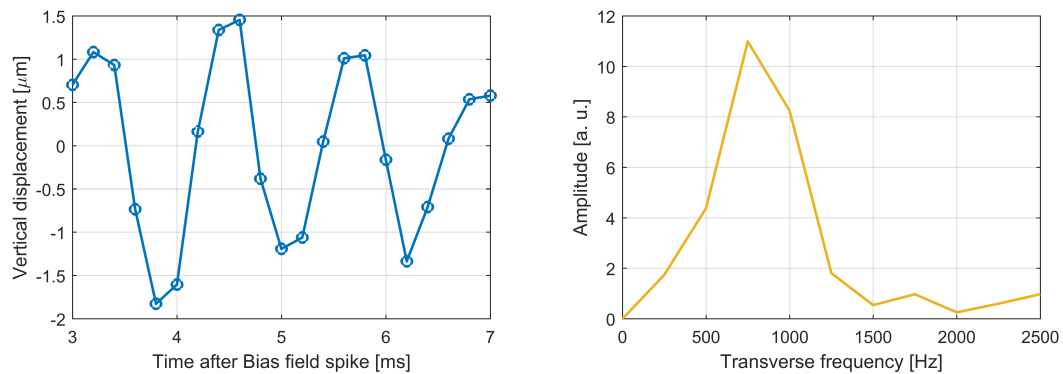


Figure 12.4.: Transverse trapping frequency measurement with a chip current of 1.8 A and a bias field of 25.44 G. The FFT on the right yields a trapping frequency of roughly 730 Hz. The corresponding longitudinal trapping frequency is below 20 Hz (not shown).

12. The superconducting Z trap

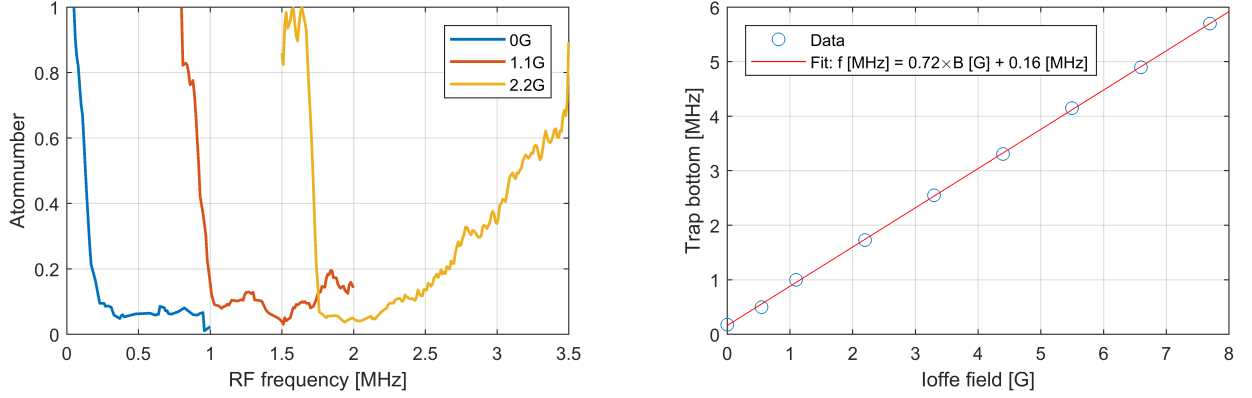


Figure 12.5.: Trap bottom spectroscopy for different values of the Ioffe field with a chip current of 1.9 A and a bias field of 20 G. This method can be used to calibrate the coils producing the Ioffe field (HBIO) as we expect a shift of 0.7 MHz/G.

for the chip current supply as indicated in figure 7.6, the chip lifetime increases to more than 20 s. The remaining noise is brought in mainly through capacitive coupling to the wires inside the cryostat. Additional filtering of all wires entering the cryostat is currently under construction and explained in section B.5. One way to avoid unwanted RF spin flips is to lift the trap bottom above the noise. A lifetime of up to 90 s is reached for a Ioffe field of 5 G.

With a sufficient atom number and a long lifetime, the obvious next step is to cool the atoms in the superconducting atomchip trap to degeneracy. As explained in 2.7, the goal is to increase the phase space density (PSD) $D = n\lambda_{dB}^3$ by several orders of magnitude. The volume of an atomic cloud in a harmonic trap is proportional to \sqrt{T} (cf. equation 2.10), therefore $PSD \propto N/T^3$. Increasing the PSD requires careful optimization of subsequent cooling ramps. Even if the lifetime of the "warm" cloud can seem very long, there can be a heating rate large enough to compete with the cooling. Figure 12.6 summarizes a recent cooling attempt in the superconducting chip trap. We start with slow cooling ramp from 15 MHz to 2.7 MHz in 8 s, followed by 4 s ramp starting from 2.7 MHz. The strategy is to find a cooling ramp that increases the PSD by one order of magnitude, then continue with the next ramp. So far we have not reached a BEC, the reasons for this are not completely clear. A systematic measurement of all trap parameters as a function of the chip current, the bias field and the Ioffe field is required, especially the lifetimes, the trapping frequencies also for colder clouds and the heating rates. These are all standard measurements, however they require a stable experiment for a significant time (weeks) due to the long cycle time of around 70 s.

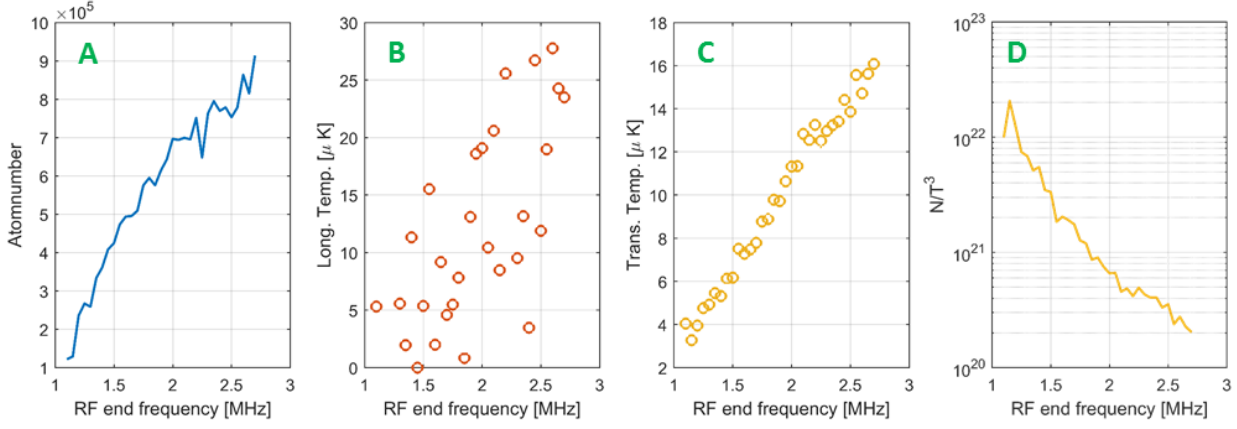


Figure 12.6.: atom number (A), longitudinal- (B) and transversal temperature (C) depending on the RF end frequency for a 4 s cooling ramp in the chip. The phase space density (D) increases by almost two orders of magnitude.

12.1. Magnetic field microscopy

Ultracold atoms can be used as sensitive magnetic field sensors [131, 132]. They have been used to detect small variations on the current flow in the trapping wire of atomchips, the angular distribution of the current flow around defects [133, 134] and the influence of the edge roughness of micro fabricated chip wires [135, 136, 137]. In a Z trap, atoms are sensitive to variations of the longitudinal field component. In an ideal Z trap, this component arises only from the two arms of the Z wire. One can assume that the total trapping potential V can be separated into a longitudinal part $V_l(x)$ and a harmonic part $V_{harm}(y, z)$:

$$V = V_l(x) + V_{harm}(y, z). \quad (12.1)$$

Any additional field in the longitudinal direction will alter the trapping potential and lead to a variation in the atom density. A similar variation in the much steeper transverse harmonic potential would be undetectable. Assuming a thermal cloud, the density along the wire is given by:

$$n(x) \propto \exp^{-V(x)/k_B T}. \quad (12.2)$$

The sensitivity of this method is determined by the smallest atom density fluctuation the imaging system can detect, the spatial resolution and the temperature of the atoms. The relative change in density caused by a variation of the longitudinal field B_x is

$$\frac{\Delta \rho}{\rho} = \frac{\mu_B}{k_B T} \Delta B_x. \quad (12.3)$$

Density variations around 10% are easily visible. For a thermal cloud of 10μ K, this gives a sensitivity of around 14 mG. In the case of a BEC, the magnetic field sensitivity is not determined by the temperature but by the chemical potential and the scattering length. Magnetic field microscopy using BECs reaches sensitivities of below 1 nT and a spatial resolution of 1μ m [138].

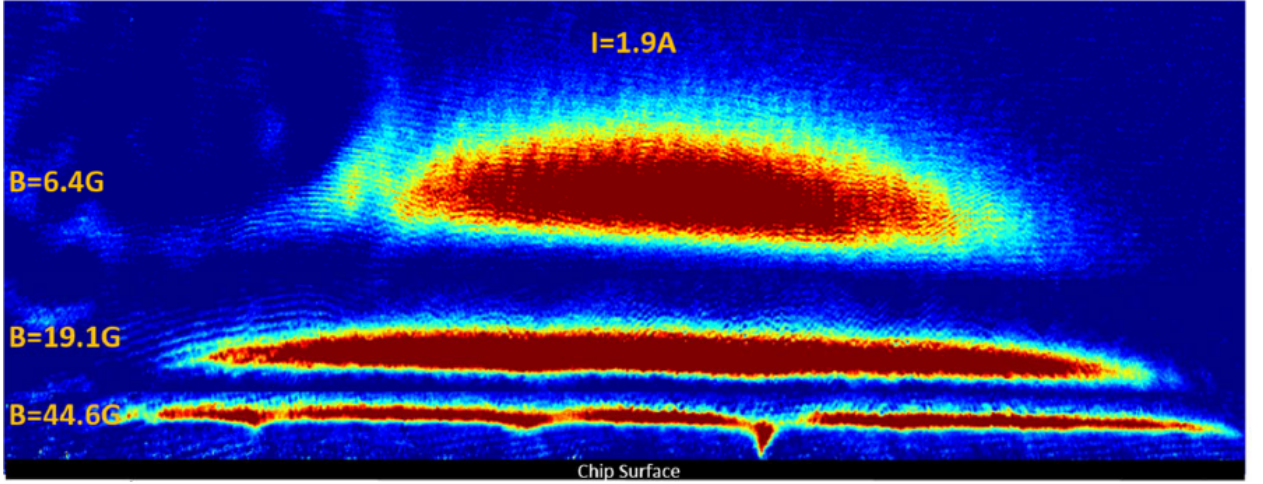


Figure 12.7.: Image of the chip trap for different bias fields. As the atoms get closer to the chip surface, the fragmentation of the trap due to potential variations becomes more obvious.

For our superconducting atomchip, the corrugation of the longitudinal potential becomes obvious when the cloud is brought close to the chip by increasing the bias field. An initially homogeneous-looking cloud starts to fragment and is eventually split in separate clouds, at some points the trap even opens towards the surface, as shown in figure 12.7.

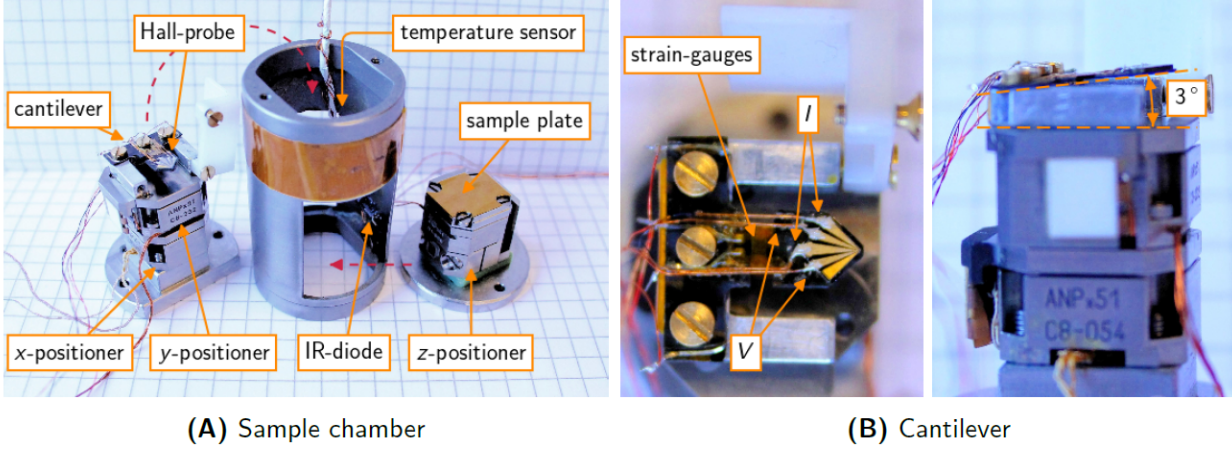
To correlate the observed fragmentation with the material properties of the superconductor, we analyzed the atomchip with a cryogenic μ -Hall scanner² This setup is described in detail in [139]. The sample mount is shown in figure 12.8.

A $400 \times 400\text{nm}^2$ sized Hall sensor is positioned at a fixed distance above the sample. The surface is then scanned using piezo actuators. The entire assembly sits inside a bath cryostat at liquid helium temperatures. As it is not possible to apply a transport current during these measurements, the atomchip is fully magnetized with a field of 5 T prior to the measurement. The results for a fully magnetized sample are equivalent to the transport current case (at I_C), only the direction of the currents has to be reversed on one half. The Hall probe is sensitive to perpendicular magnetic fields B_z , we are interested in the current distribution inside the sample. The magnetic induction B_z at the location of the Hall probe is given (in discretized form) by the sum over the contributions from each volume element with the constant magnetization M :

$$\sum_{k=1}^{nx} \sum_{l=1}^{ny} K_{i,j,k,l} M_{k,l} = B_{i,j}, \quad (12.4)$$

where nx and ny are the grid elements in each direction. We assume that the magnetization only points in z direction. K weighs the contribution of a magnetization at location (k, l) to the magnetic induction at location (i, j) . The above equation can be mapped to one dimension:

²Thanks to Maryaluna Mao, Johannes Hecher, Michael Eisterer and Franz Sauerzopf from the Low Temperature Physics group at the ATI.



(A) Sample chamber

(B) Cantilever

Figure 12.8.: The main components of the scanning stage. On the left is the x-y positioner. On top of this is a cantilever with the Hall probe at the tip. The sample is mounted on the z positioner. Strain gauges detect contact between the sample and the cantilever, allowing to adjust the height of the Hall probe. Picture taken from [139].

$$\sum_{k=1}^{nx} \sum_{l=1}^{ny} K_{i,j,k,l} M_{k,l} = B_{i,j}. \quad (12.5)$$

To get the magnetization M from equation 12.5, one has to invert the matrix K' . It turns out that K' is a highly symmetric block Töplitz matrix, for which efficient inversion algorithms exist³. A detailed derivation of the complete numerical method is given in [140, 141]. Once the magnetization of the sample is known, the local planar current densities can be calculated from:

$$\nabla \times M = J. \quad (12.6)$$

The measurements were performed at 5 K, the Hall probe was kept at a constant distance of $5 \mu\text{m}$ above the sample. The vertical distance is an important factor for the achievable resolution. The stepsize in x- and y-direction was $6 \mu\text{m}$. Taking scans with 400×60 points takes about 48 h. Figure 12.9 shows the results of the Hall scan.

As mentioned above, the currents in one half of the chip wire need to be reversed to recover the transport current case from the measurement on the magnetized chip. A fully magnetized sample carries the critical current density at each slice of the wire. We adjust the critical current such that the lowest slice can carry 2 A, the measured critical current. This leads to a critical current density of 4–5 MA/cm² in parts of the wire, typical values for Niobium.

To calculate the trapping potential from the Hall scan, the current distribution is normalized to the transport current at each slice. This is then used for a full 3D simulation of the magnetic trap. The results are summarized and compared to measured atomic densities

³Toeplitz: A Fast Toolkit for Manipulating Toeplitz Matrices, Copyright (C) 2013 William B. Zhang and John P. Cunningham

12. The superconducting Z trap

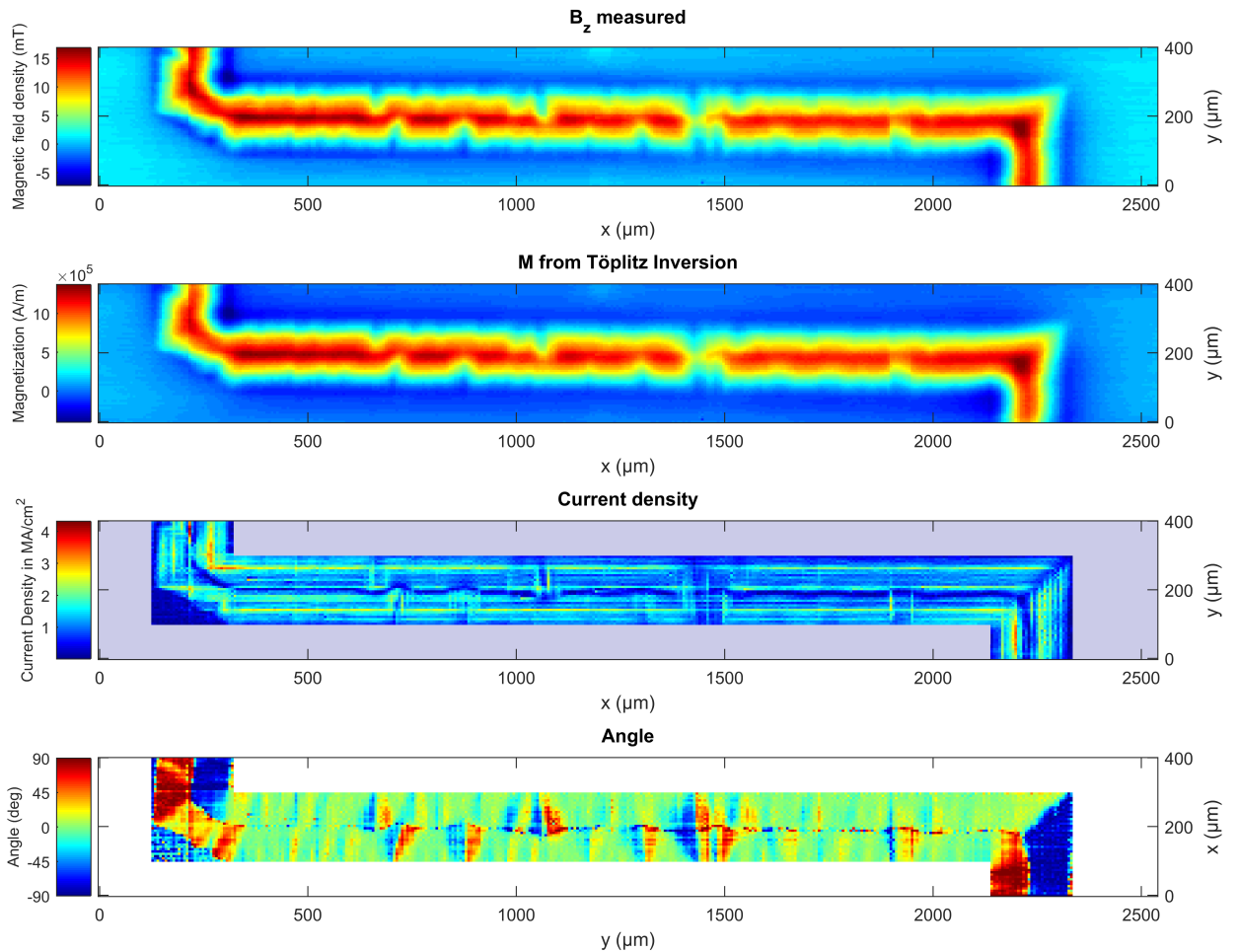


Figure 12.9.: From top to bottom: The measured vertical B field at a height of $5 \mu\text{m}$ above the atomchip. This is the raw data from the μ -Hall scanner. The field reaches around 15 mT. The magnetization can be reconstructed using the numerical method described in the text. Once the magnetization is known, the planar current density can be calculated. The current shows the typical double hat profile for a type-II superconductor after applying a large field (cf. section 12.2). The currents in one half are reversed to recover the transport current case. The last image shows the angular distribution of the currents. There are several locations along the central wire where the current flows almost perpendicular to its normal direction.

in figure 12.10. The Niobium film studied shows massive defects and inhomogeneities. The strong deviations from a straight current flow not only lead to atomic density fluctuations, but also change the trap distance at several locations, at some points the trap even opens towards the surface (cf. figure 12.7). To get higher resolution out of the magnetic field microscopy, colder cloud temperatures and a more sensitive imaging system will be employed in the future. The bias field value at which the fragmentation becomes apparent differs between the simulation and the measurement. We attribute this to the non-uniform current distribution in a real superconducting wire as will be discussed in the next section.

12. The superconducting Z trap

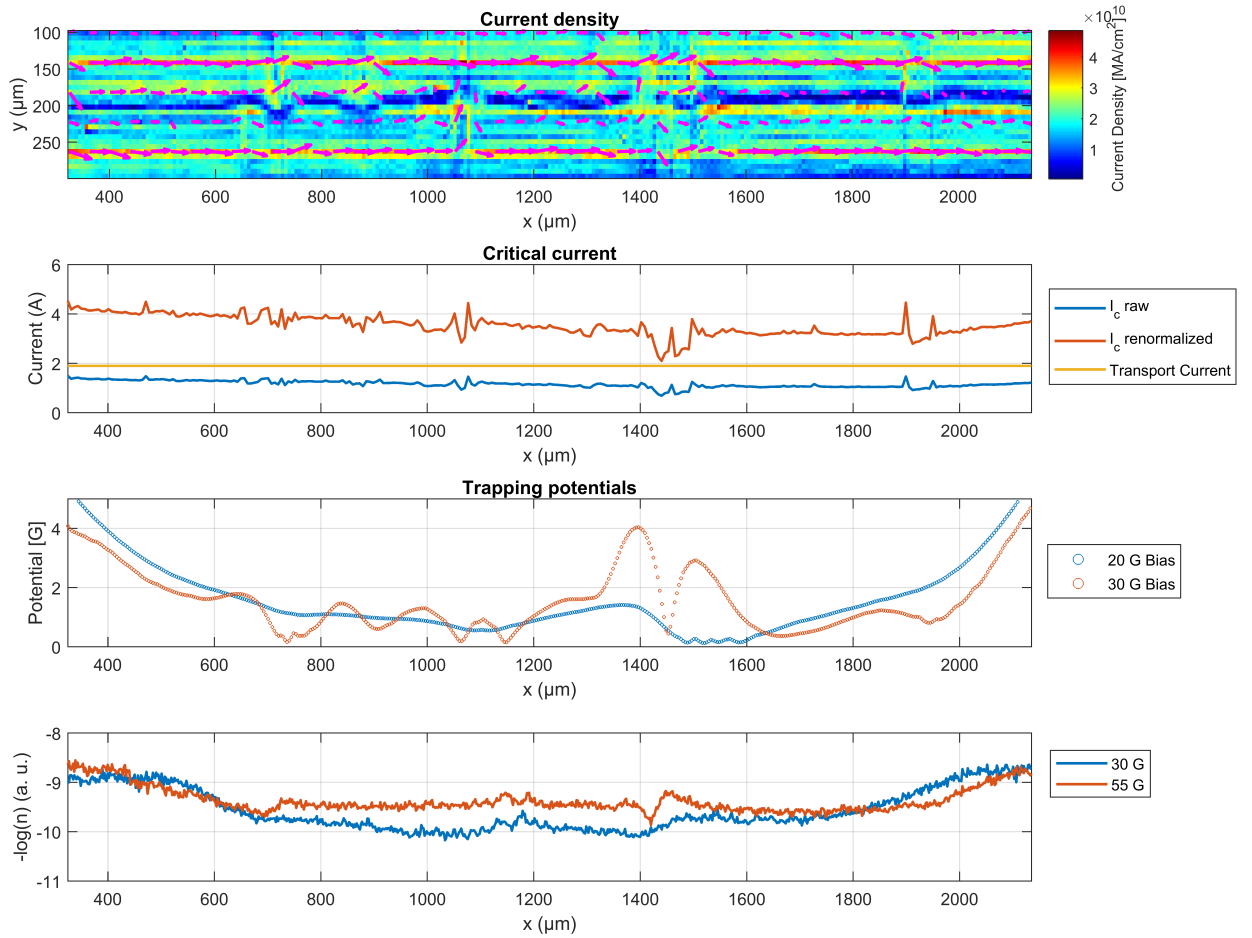


Figure 12.10.: From top to bottom: The first picture shows the corrected current distribution in the central part of the Z wire. Second picture: The integrated current at each slice should be the critical current for this slice, as the sample is fully magnetized. However, this values are below the applied transport current and the critical currents are therefore rescaled such that the weakest slice carries the measured critical current. For the 3D trap simulation, the current at each slice is adjusted to the actual transport current. The third image shows the magnetic potential at two different bias field values from the simulation. For small bias field (=large distances), the fragmentation is less prominent. The last image shows the negative logarithm of the measured atomic density for two different bias fields. This is directly proportional to the magnetic potential. The most prominent feature at around $x = 1400 \mu\text{m}$ is clearly visible, however many other features are not. For a higher sensitivity of the magnetic field microscopy, colder atoms and a more sensitive imaging system are required.

12.2. Current distribution in superconducting atomchips

The DC current distribution in an ideal normal conducting thin film is essentially homogeneous. Geometric effects for example around corners and wire bends can easily be simulated, as can the effect of applied magnetic fields. The situation is completely different in a superconductor where shielding currents form to keep the interior field-free. The situation is additionally complicated in type-II superconductors. Vortices penetrating the sample remain even after the field or current are removed, thus imprinting a memory in the chip (cf. section 3.6). Figure 12.11 shows the current distribution in a superconducting film under several different circumstances, as derived from the expressions given in [85]. It should be noted that these are only valid for an ideal straight type-II superconducting thin film with infinite length. The exact current distribution is additionally dependent on the time derivatives and the order of the applied fields and currents and the exact geometry.

In a regular experimental sequence, our superconducting atomchip is subject to the fields created by the magnetic transport and the QUIC trap and a transport current in the chip trap phase. The macroscopic effect of the current distribution manifests in the distance at which the chip trap forms for a given bias field. For large distances, the details of the current distribution are irrelevant, only the net transport current matters. When the trap distance is comparable to or smaller than the width of the wire, the difference between the different current distributions becomes apparent. We compare the measured distances with several simulated current distributions in figure 12.12, a complete analysis of these measurements is given in [101].

The repeated exposure of the atomchip to the experimental sequence induces a complex and unknown current distribution. To reset the superconductor to the virgin state we use the quenching laser (cf. section 9.4). As the quenching only takes a few milliseconds and the wavelength of the laser is far away from any atomic resonance, quenching can be done just before the transfer into the chip trap, while the atoms are held in the QUIC trap. This opens the possibility to control the current distribution to a certain extent, as the current memory of previous cycles and the magnetic field memory of the latest transport sequence can be erased. Figure 12.13 shows the influence of the current history on the trap.

The non-trivial current distribution in the chip wire allows to create chip traps without any transport current. By magnetizing the chip with a strong perpendicular field, a current distribution similar to the one in figure 12.11 A can be induced. A simplified sketch of the current distribution and the sequence to transfer atoms into such a trap is shown in figure 12.14. Such a trap can be realized without any wire connections to the chip, just like the persistent current traps in [21]. This renders all the electronic noise issues irrelevant and should allow long trapping lifetimes. However, the loading procedure into this trap has yet to be optimized. More details of these kinds of superconducting traps will be presented in [126].

So far we only considered the effect of applied fields and currents on straight superconducting wires. The fact that the real chip wire has two 90 deg turns also affects the current distribution. Forcing the current around the corner creates a current swirl. As it is a superconductor, this swirl persists even after removing the transport current. Numerical simulations on this effect have been published in [142]. We readily observe such zero-current traps, cf. figure 12.15. After loading into the normal chip trap, we simply have to ramp down the chip current.

12. The superconducting Z trap

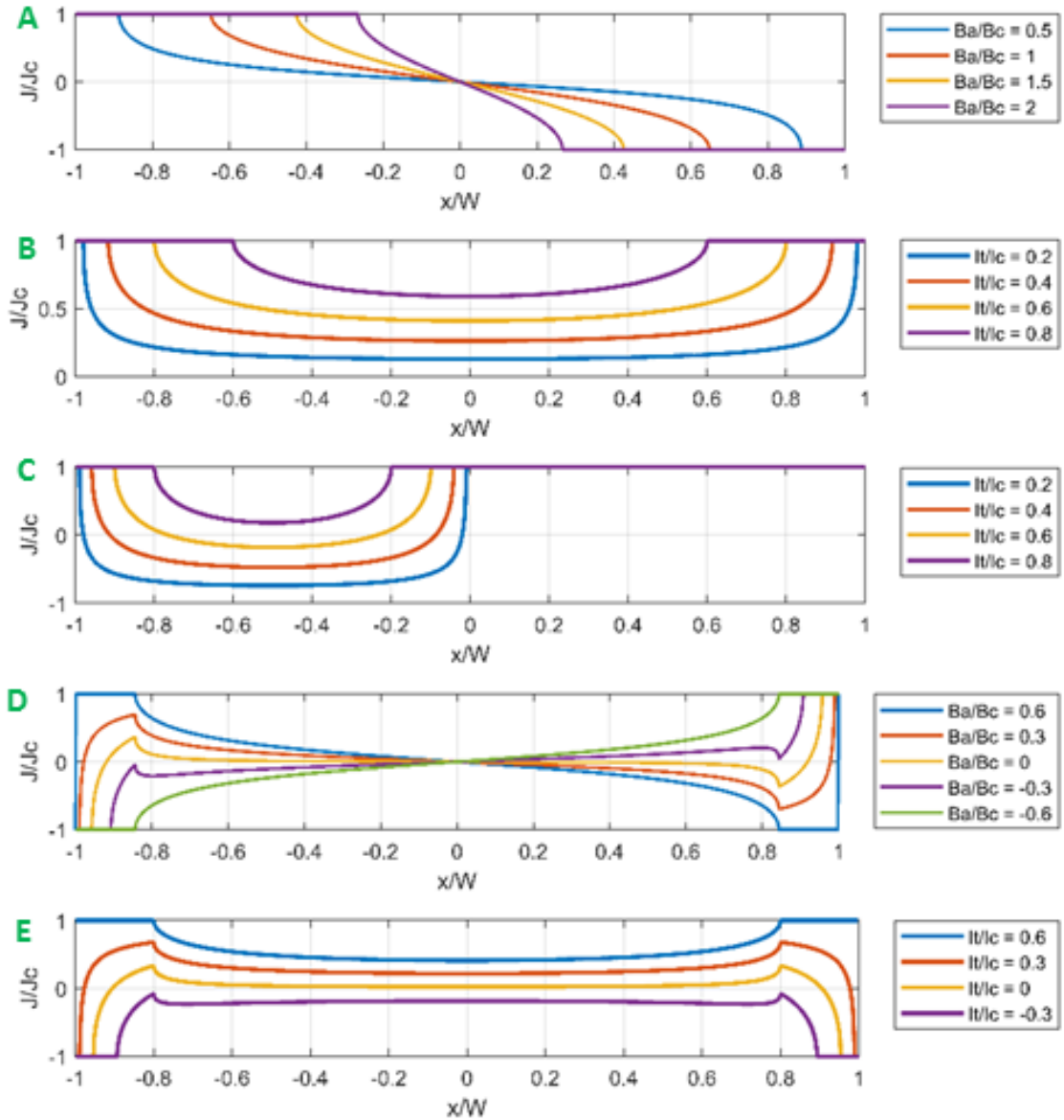


Figure 12.11.: The current distribution in an infinitely long superconducting thin film of width $2W$ as given by [85]. The film has a critical current I_C , vortices reach the center of the film at a field of B_C . A: The response to a perpendicular magnetic field B_A results in opposing currents. B: The current distribution for an applied transport I_t current. For low currents, the current density is concentrated on the sample edges. At I_C , the current distribution becomes homogeneous. C: For a sample in the remanent state, i. e. a fully magnetized sample, a transport current is applied. As one half of the film already carries the critical current density J_c , the transport current only flows in the other half. D: Field memory. The sample is subject to a maximum field $B_{a0} = 0.6B_C$ and then to a lower field B_a . The current distribution shows a memory effect which can only be erased by exceeding $|B_{a0}|$. E: Current memory. A maximum current $I_{t0} = 0.6I_C$ also leads to a memory effect. Note that there are significant parts of the sample carrying a current density opposite of the transport current direction.

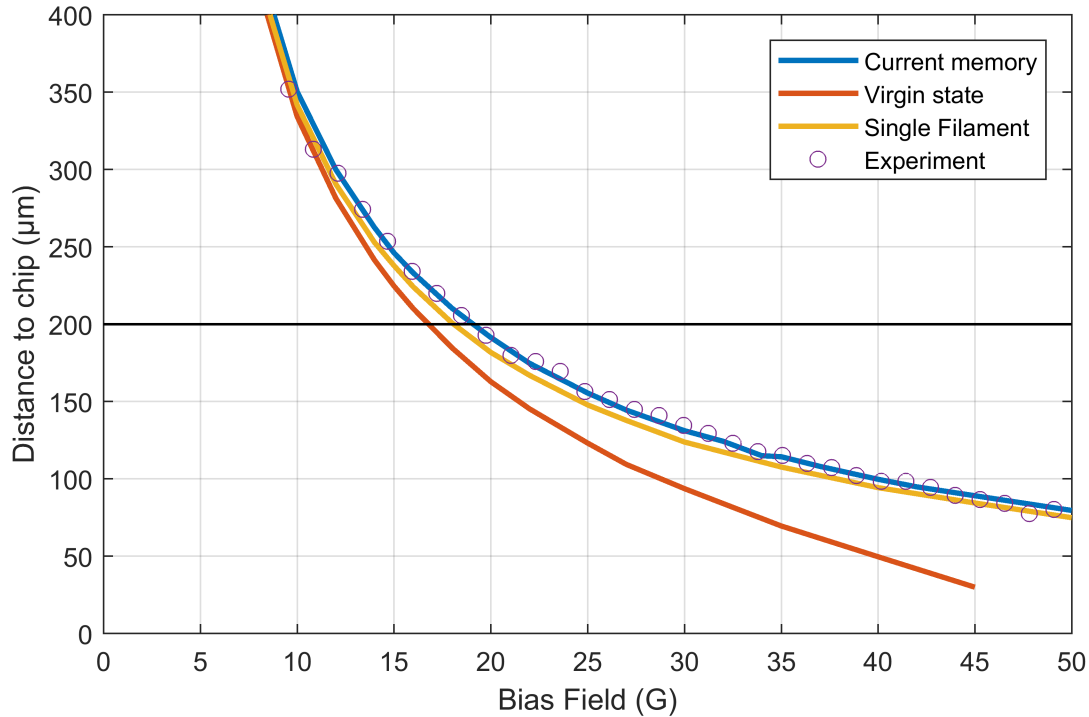


Figure 12.12.: The distance of the chip trap for a transport current of 1.9 A as a function of the applied bias field. The experimental data (circles) is compared to several simulations. The horizontal line at $200 \mu\text{m}$ indicates the width of the wire. For large distances, the current distributions have no influence on the distance. For distances below $2W$ the differences become obvious. The homogeneous current distribution as well as a current history distribution with the expected values for the previous current $I_{t_0} = 2 \text{ A}$ and critical current $I_c = 2.1 \text{ A}$ does not fit the data, neither does the virgin state simulation for realistic values (red curve). We have to assume very high (and unrealistic) $I_{t_0} = 8 \text{ A}$ and $I_c = 8.5 \text{ A}$ to get an agreement with the experiment (blue curve). Surprisingly, the simulation assuming just a single, infinitely thin wire, also fits very well (yellow curve).

12. The superconducting Z trap

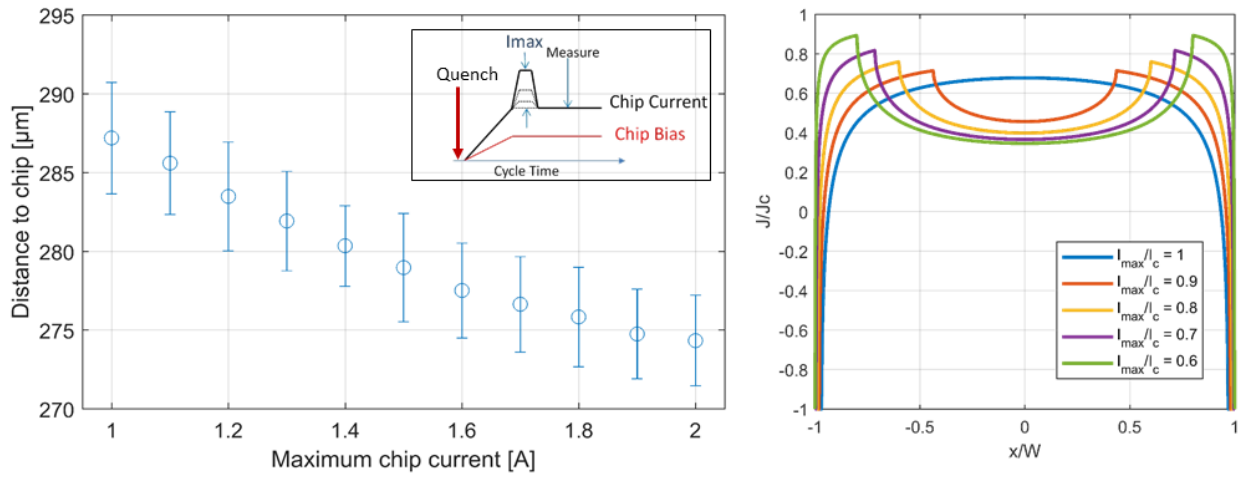


Figure 12.13.: Chip distance as a function of the applied maximum current. The inset shows the experimental sequence, the chip is quenched just before the atoms are transferred. The distance is always measured with the same parameters, the maximum current is applied before. B: The current distribution for different values of I_{max} for a fixed transport current of $0.5I_c$.

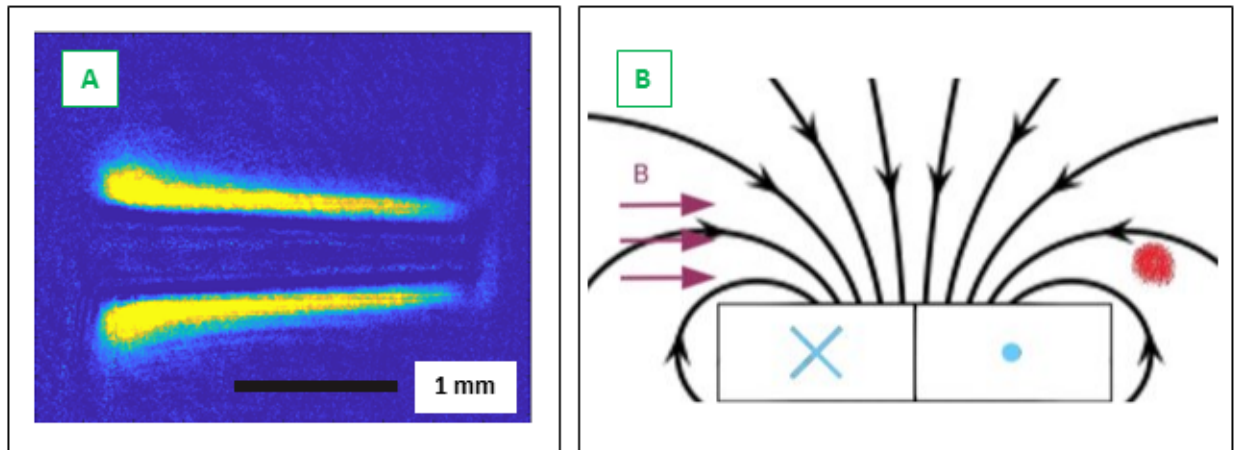


Figure 12.14.: Left: The atomcloud in the magnetized chip trap without transport current in reflection imaging. The asymmetry is probably due to specifics of the transfer sequence. Right: A cut through the magnetized wire with the associated magnetic field. A horizontal bias field creates a trap over one of the wire edges (indicated by the red dot). A vertical bias field would result in a trap above the center of the wire.

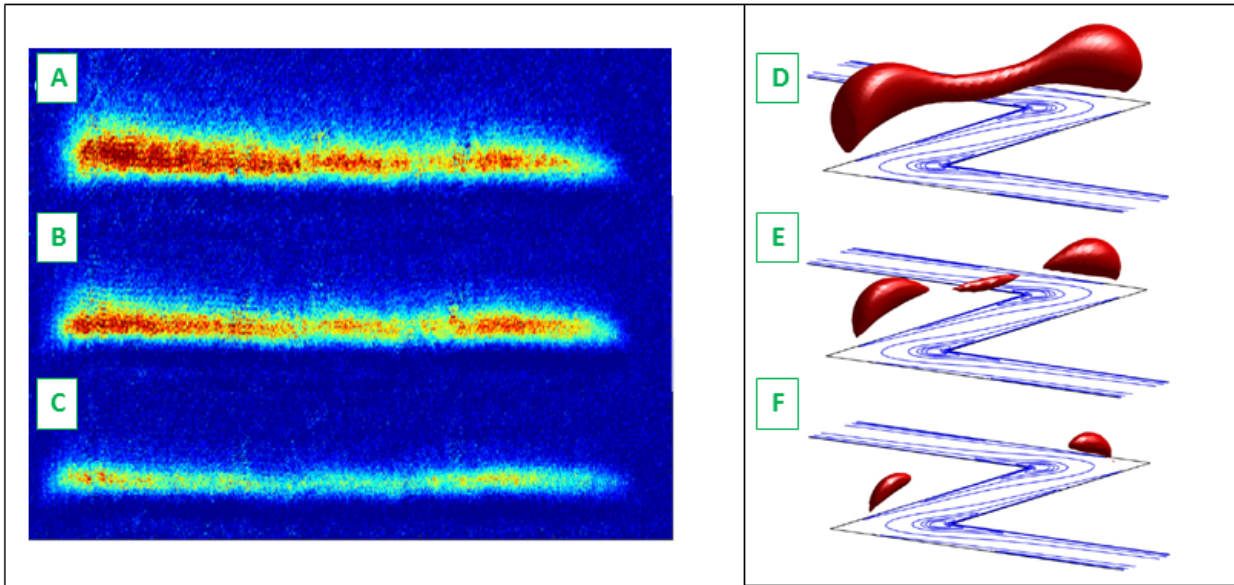


Figure 12.15.: A-C: The zero current trap for different bias field values (6.4 G, 10.1 G, 15.3 G). Note that in contrast to the above figure, the chip has not been subject to a large magnetizing field and the transfer sequence is used. After loading into the normal chiptrap, the chip current is simply ramped to zero. The zero current trap is stable, with lifetimes on the order of seconds. D-F: Simulation of the zero current trap from [142]. For higher bias fields, the simulation and the experiment both show localized traps over the wire bends.

12.2.1. Numerical simulation of supercurrent distributions

To get a more detailed picture of the current distribution in non-straight geometries, we implement a numerical method presented in [143] for a superconducting film in the Meissner state and its extension to type-II superconductors with vortex penetration and remanent magnetization in [144]. I will shortly outline the algorithm described there, the performance of our code and some first results.

Let us assume a planar sample of uniform thickness t which is smaller than the London penetration depth λ and also much smaller than any perpendicular dimension of the superconductor. Additionally we define $\Lambda = \lambda^2/t$. The current density $\mathbf{J}(x, y, z)$ can be assumed to be constant across the thickness of the film and the sheet current density $\mathbf{K}(x, y) \approx \mathbf{J}t$ can be used instead. The scalar stream function $g(x, y)$ is defined such that

$$\mathbf{K}(x, y) = \nabla \times [g(x, y)\hat{\mathbf{z}}]. \quad (12.7)$$

$\hat{\mathbf{z}}$ is the unit vector in z direction. The difference between g at two points is *the net current that crosses any line connecting these points*. The relevant magnetic Gibbs energy of the system subject to a perpendicular external magnetic field $\mathbf{H}_a = H_a \cdot \hat{\mathbf{z}}$ and a feeding current I_a

$$E = E_{kin} + E_{int} + E_{ext} \quad (12.8)$$

consists of the kinetic energy of the charge carriers

$$E_{kin} = \frac{\mu_0 \Lambda}{2} \int_S [\mathbf{K}(\mathbf{r})]^2 dS = \frac{\mu_0 \Lambda}{2} \int_S [\nabla g(\mathbf{r})]^2 dS, \quad (12.9)$$

the internal energy E_{int} due to the magnetic interaction between the currents

$$E_{int} = \frac{1}{2} \int_S \mathbf{K}(\mathbf{r}) \cdot \mathbf{A}_{\mathbf{K}}(\mathbf{r}) dS = \frac{\mu_0}{8\pi} \int_S \int_S \frac{\nabla g(\mathbf{r}) \cdot \nabla' g(\mathbf{r}')}{|\mathbf{r} - \mathbf{r}'|} dS dS' \quad (12.10)$$

and the energy due to the external field:

$$E_{ext} = \int_S \mathbf{K}(\mathbf{r}) \cdot \mathbf{A}_{\mathbf{a}}(\mathbf{r}) dS = \mu_0 H_a \int_S g(\mathbf{r}) dS - \oint_{\delta S} g(\mathbf{r}) \mathbf{A}_{\mathbf{a}}(\mathbf{r}) \cdot d\mathbf{l}. \quad (12.11)$$

$\int_S dS$ is the integral over the surface of the superconducting region, $\oint_{\delta S}$ the line integral along its outer contour. $\mathbf{A}_{\mathbf{a}}(\mathbf{r})$ and $\mathbf{A}_{\mathbf{K}}(\mathbf{r})$ are the vector potentials from the external field and from the induced currents respectively.

The sample is now discretized in C rectangular cells and N nodes. The value of g_n is defined at each node. The gradient of the stream function $(\nabla g)_c$ is calculated from the four values of g at the corners of each cell.

The algorithm tries to find the distribution g_n that minimizes the total energy. At each iteration, g_n is varied by $\pm \Delta g$ and the corresponding change in energy is evaluated. The variation of g_n is applied to the node that causes the largest drop in total energy, then the process is repeated.

To start the optimization, an initial distribution g_n needs to be defined. All values of g on a sample edge without current are set to the same value and $g_n = 0$ on one of these edges. A sample edge with current entering or leaving means that the two end points of that edge

have a fixed difference in g . Holes in the sample are all set to the same g_n , ensuring that there is no current flowing within.

The discretized expressions of the above contributions to the total energy can be found in [143] and especially in [145], equations A1-A7. The concrete implementation in our code is described in [146] and [147]. It turns out that the calculation of the internal energy E_{int} is the by far most time consuming step. To speed up the calculation, several tricks have been implemented. First, the value of the variation Δg starts at a high value and decreases as the energy converges. In the beginning of the procedure, where g_n is random inside the sample, not only the "best" node, but several nodes far from each other, are changed at each iteration. This has to be implemented with great care to avoid oscillating behavior. Parallelization of the code is not helpful, as each step depends on the result of the previous one and the calculation time for one step is relatively short, making the data transfer overhead a limiting factor.

So far the model is only considering the Meissner state of a thin superconducting film. In order to implement the critical state model (CSM, cf. section 3.6), a functional that contains information about the previous magnetic state has to be minimized, it is given in [144], equation 1. An important difference to the Meissner state is that the gradient of the stream function, $|\nabla g|$, has to be smaller than the critical sheet current density K_c . To implement the memory effect, the superposition model described in [148] is employed. The current distribution in a sample subject to a maximum current I_{max} and subsequently a transport current I_t can be calculated by

$$J(x, I_t, I_c) = J(x, I_{max}, I_c) - J(x, I_{max} - I_t, 2I_c). \quad (12.12)$$

The effect of a field history can be implemented by a similar superposition. As of now, the code need about 2×10^4 s for a grid of $N = 10^4$ cells. The code performance still has to be enhanced as the calculation time scales with more than N^2 . However, even with the resolution available now we are able to reproduce the current distribution leading to the zero current trap described in the previous section as shown in figure 12.16. Apart from developing our own simulation tool, we are evaluating the use of 3D-MLSI [149], this software package was designed for inductance calculation of multilayer superconducting circuits.

12. The superconducting Z trap

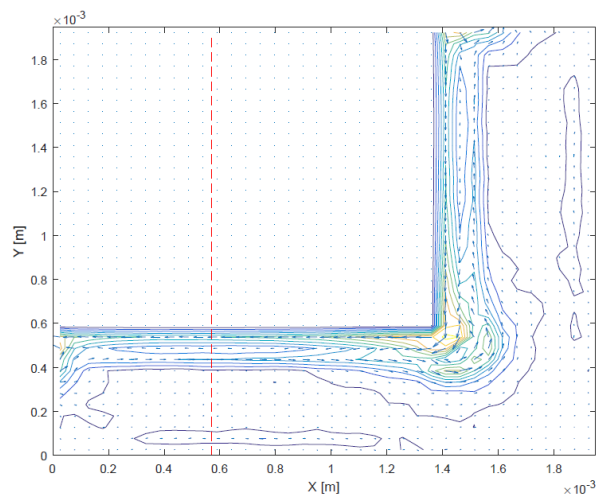


Figure 12.16.: A 40x40 simulation of a superconducting L subject to a current pulse $0 \rightarrow 0.7I_c \rightarrow 0$. The contours are lines of equal current density. At the corner, closed current loops appear. Higher resolution simulations are in progress.

13. Towards trap recombination

A high atom number in the final atomchip trap is important for many of our envisaged experiments. The coupling of the atomic cloud and a microwave resonator scales with \sqrt{N} as will be discussed in chapter 14. A higher atom number at the same initial temperature also means a higher BEC transition temperature and a larger condensate, which will be useful for studying surface effects and for high resolution magnetic field microscopy of superconducting structures.

Of course the first goal is to maximize atom number from the start in the MOT. However, the achievable atom number is limited by the window size, the available laser power and other non adjustable factors. Additionally, the losses throughout transport and subsequent cooling have to be minimized. As of now, we transport about 5×10^8 atoms into the cryostat at a temperature of $500 \mu\text{K}$, most of which we lose during precooling in the QUIC trap.

A possibility to reach higher atom numbers is the combination of several clouds into one. The merger of quadrupole traps has been realized for a cascade of quadrupole like traps on an atomchip in [150]. This experiment also showed that the unification can be done without the loss of phase space density. Another experiment described in [151], two macroscopic quadrupole traps formed by coils were successfully merged. The authors used moving coil pairs and optimized the currents in the two traps to minimize losses during the mixing, they report only 5% loss and a moderate temperature rise from 195 to $310 \mu\text{K}$.

Our setup does not have moving coils, but a large number of transport coils. The idea is to transport the first cloud into the cryostat for storage, load fresh atoms into the MOT and then merge both clouds at some point along the magnetic conveyor belt. The key point that makes this idea so promising is the very long lifetime of the stored cloud inside the cryostat, which is on the order of five minutes. MOT loading plus transport and cloud combination takes less than 15 s, the recombination process can be done repeatedly until the atom number saturates. An increase in atom number by at least one order of magnitude seems feasible. The critical question is how much additional energy we put into the system during the different suggested merger procedures. Increasing the atom number is only advantageous when the temperature rise is limited, thus preserving a certain phase space density.

To realize the recombination we investigate several sequences. The first naive approach is to mix the clouds in the vertical transport section, between coils V7 and V8. The first cloud is stored between V8 and V9, the new cloud is transported to the center of V6 and V7. Ramping down V7 and V8 while increasing the currents the outer coils V6 and V9 will move the traps towards each other. Once the currents in V7 and V8 have reached zero, there is just one new trap formed by V6 and V9. This approach has the advantage that everything happens in the cryogenic environment where the lifetime is long. This sequence is visualized in figure 13.1. Simulation shows that at one point the trap is completely open sideways, while the vertical confinement remains intact all the time. Throughout transport, the orientation of the quadrupole trap the atoms are trapped in never changes. Recombining the traps in the vertical part however means merging traps with different polarities. For geometric

reasons, there has to be a trap with opposite polarity between the old and the new cloud. This poses the main difficulty, the experiments described in [150, 151] did not have to deal with this problem. Since this naive approach to trap recombination can not work without losing all atoms, several alternatives are under investigation.

One way to deal with the loss of lateral confinement is to time the sequence such that the time where the trap is open is short compared to the velocity of the atoms. Only the critical part of the sequence has to happen rapidly. This means that the high inductance coils will be able to follow the (relatively small) current changes, while most of the sequence can be done adiabatically to avoid heating.

Another option is to use gravity to assist in trap merger. In this proposed sequence, the uppermost trap approaches the middle trap. The barrier between these traps is lowered until the atoms flow into the lower trap. The same procedure is repeated with the middle- and lower trap until all atoms are in the lower trap. The critical parameter in this approach is the drop height of the atoms. From $\Delta T = m_{Rb}g\Delta h/k_B = 104 \mu\text{K}/\text{mm}$ it is clear that drop heights exceeding few millimeters have to be avoided, otherwise the heating becomes too much. Optimizing the sequence should also consider using the vertical bias coils BV8 and BV9 as they provide the crucial tuning knobs. Instead of letting the upper cloud fall into the lower cloud, this idea can also be reversed: first we again lower the barrier between the lower and the middle trap. We then accelerate the lower trap upwards and abruptly stop the ramp, such that the inertia of the cloud spills the atoms into the middle trap.

A fourth alternative would be to shoot the lower trap up against gravity and the potential wall of the uppermost trap. The lower cloud would be launched from the corner and accelerated to a final velocity. To provide a lateral confinement to the moving cloud, the transport coils probably have to remain active to a certain extent. This option is certainly tricky to implement, there are many parameters which can be optimized. As a starting point, one would launch a cloud upwards and catch them with V8 and V9, without another trap present. Only then the additional magnetic potential can be added and the sequence modified accordingly. So far no simulations have been done.

All the ideas presented can be implemented by software, no additional hardware is required. The recombination of quadrupole traps was the motivation behind the implementation of the QiController (section 10.3). The old ADWIN control system would not allow so lengthy sequences.

Lastly, if the recombination along the vertical transport axis does not work, it can also be done along the horizontal transport axis. The atoms of the first MOT run would still be stored in the cryostat while the MOT loads again. The both clouds would be transported simultaneously and merged in the horizontal section at the position of H4. The advantage of this is that there is no reversed polarity quadrupole trap and no free fall, thus the trap remains closed at all times and the heating should be moderate. However, to employ this sequence extra power supplies need to be purchased.

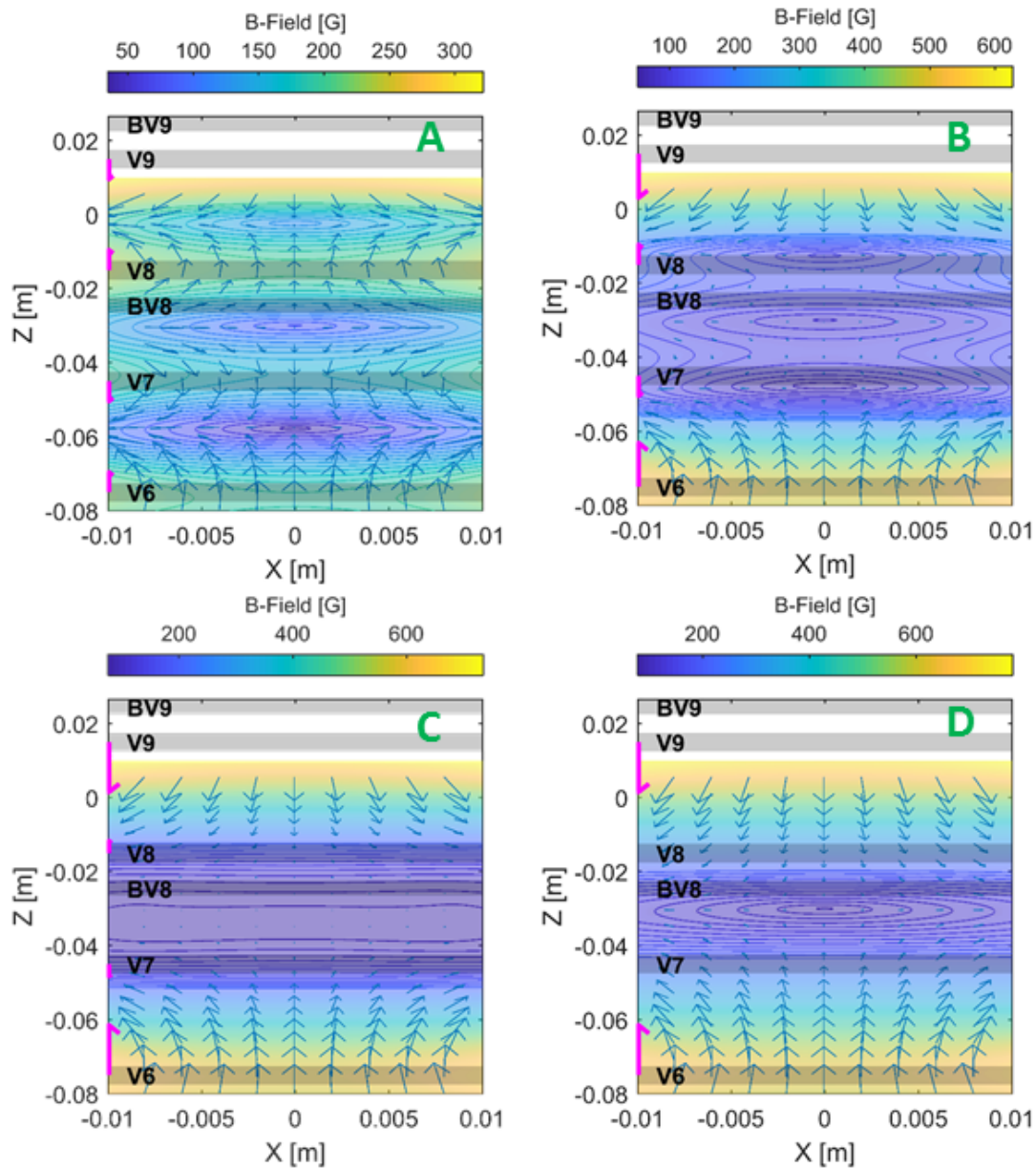


Figure 13.1.: Simulation of the recombination along vertical transport. Gravity is included in this simulation, leading to the asymmetry between the upper and the lower trap. The coils are indicated by gray bars. The pink arrow shows the polarity at which each coil is operated. A: The initial situation with three traps. Note that the (empty) quadrupole trap in the middle has the opposite polarity of the other traps. B: Ramping up the outer coils while decreasing the inner two coils shifts the traps towards each other, but also significantly weakens the tapping potential. C: At one point along the sequence, the sideways barrier vanishes completely. As the field lines of the central trap have to reverse direction, this situation is unavoidable. D: Once the middle traps are off, the outer coils form a tight quadrupole trap with the original polarity again. From here the cloud can be transported upwards as usual.

14. Towards a hybrid quantum system

14.1. Introduction

Implementing quantum information processing is one of the main challenges in applied quantum mechanics. All proposed quantum computers rely on the coherent processing and storage of quantum states. Superconducting electronics provides a rich toolbox of gates and qubits, but the coherence time in these systems is limited to hundreds of microseconds at best [152]. To "protect" the fragile quantum information stored in the superposition of states, a system with much longer coherence times would be required. The coherence times for isolated atoms on the other hand are much longer, on the order of seconds. Creating a hybrid quantum system, using the fast processing and dense integration of superconducting electronics and the long coherence times in atomic ensembles is therefore a promising approach.

A long coherence time also means weak coupling to the environment. This however poses a difficulty for transferring information between the superconducting circuit and the atomic ensemble. The long-term goal of the experiment described here is to achieve strong magnetic coupling of an ultracold cloud of ^{87}Rb using a superconducting microwave resonator, a sketch of the envisaged system is shown in figure 14.1. Reaching strong coupling would constitute a proof-of-principle for such a hybrid quantum system and pave the way for further developments. In this chapter, I will lay out some of the theoretical considerations for such a system and describe the experimental challenges associated with it. The theoretical treatment remains very superficial, several recent theses provide a more in-depth analysis of this subject [153, 154, 155].

The basic model to start our discussion from is the single two-level atom in a single-mode cavity. Such a system is described by the Jaynes-Cummings Hamiltonian [156] as the sum of the individual Hamiltonians for the electromagnetic field H_r , for the atom H_a and their coupling H_{int} :

$$H_{JC} = H_r + H_a + H_{int} = \hbar\omega_r\left(a^\dagger a + \frac{1}{2}\right) + \hbar\omega_a\sigma^+\sigma^- + \hbar g(a\sigma^+ + a^\dagger\sigma^-) \quad (14.1)$$

ω_r and ω_a are the cavity- and the atomic resonance frequencies, a^\dagger and a the photonic annihilation and creation operators, σ^+ and σ^- the raising and lowering operators for the atom. The interaction strength is given by g , one can imagine it as the frequency at which the cavity and the atom exchange their excitation.

If we now consider not one but N atoms in the cavity, the system is described by the Tavis-Cummings Hamiltonian:

$$H_{TC} = H_r + H_a + H_{int} = \hbar\omega_r\left(a^\dagger a + \frac{1}{2}\right) + \hbar\omega_a \sum_{j=1}^N \sigma_j^+ \sigma_j^- + \hbar \sum_{j=1}^N g_j (a\sigma_j^+ + a^\dagger\sigma_j^-) \quad (14.2)$$

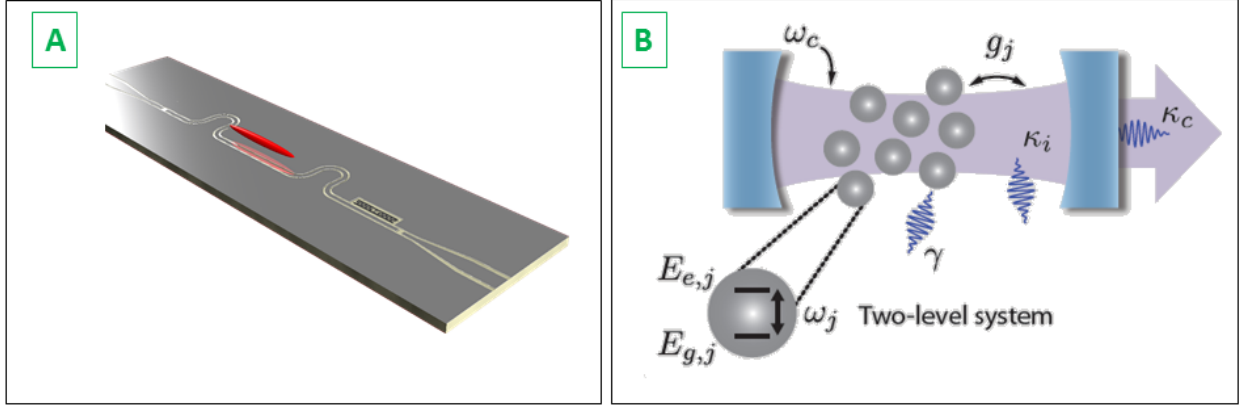


Figure 14.1.: A: Sketch of the hybrid quantum system that bases the main motivation for this thesis. A cloud of ultracold ^{87}Rb atoms is placed close to a coplanar superconducting microwave resonator. From [98]. B: Illustration of an ensemble of two-level atoms with resonance frequency ω_j and a loss rate γ placed in a single mode cavity with frequency ω_c and loss rates κ_i, κ_c . The single atom coupling strength is g_j . From [155].

In case all atoms have the same coupling strength g_0 , the effective coupling of the ensemble to the cavity becomes

$$g_{eff} = g_0 \sqrt{N} \quad (14.3)$$

So far this description does not consider any loss processes. Figure 14.1 B illustrates the cavity loss rate κ and the decoherence of the atoms with rate γ . For a hybrid quantum system with coherent exchange of excitations from the cavity to the atoms, the coupling strength needs to be much stronger than these loss channels such that $g \gg \kappa, \gamma$. This is called the **strong coupling regime**, the long-term goal for our experiment. If atoms and the cavity are on resonance, the cavity transmission will show a characteristic avoided level crossing. The gap between the two normal modes is called the vacuum Rabi splitting, it amounts to $\Omega \approx 2g_{eff}$.

In the **dispersive regime**, the atoms and the cavity are not in resonance but detuned by $\Delta = \omega_a - \omega_r \gg g$. In this regime, the cavity frequency is shifted by $\frac{g_{eff}^2}{\Delta}$. Both regimes are depicted in figure 14.2 A.

Another important parameter characterizing the atom-cavity system is the ensemble cooperativity:

$$C = \frac{g_{eff}^2}{2\gamma\kappa}. \quad (14.4)$$

A cooperativity $C > 1$ does not necessarily mean strong coupling. The system can still feature either a lossy cavity $\kappa > g$ or short atomic coherence time such that $\gamma > g$. Since a long coherence time is the very reason for using atoms, we can safely assume that the cavity losses κ are the limiting factor in our application.

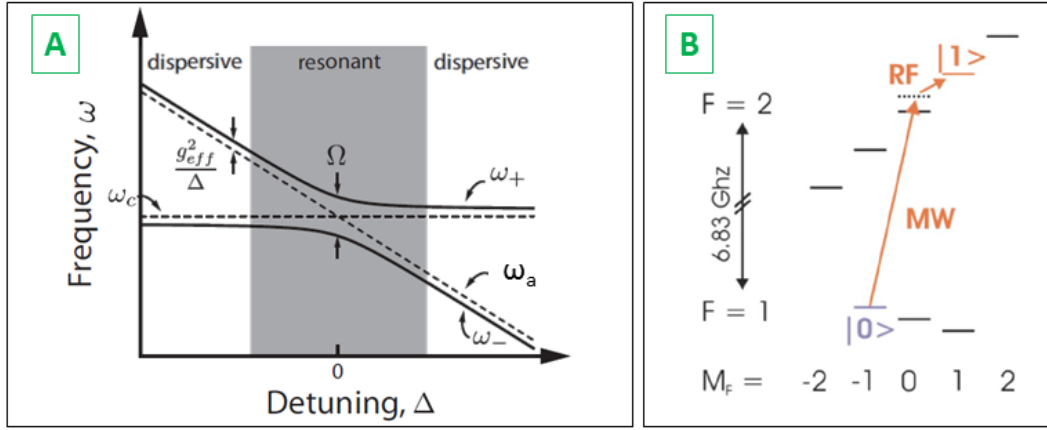


Figure 14.2.: A: The strong coupling- and the dispersive regime. The straight dashed line shows the undisturbed cavity frequency ω_c , the angled dashed line the atomic frequency ω_a . Around zero detuning, the cavity transmission splits into two normal modes spaced by Ω . The dispersive regime far away from resonance is characterized by a small shift in the cavity frequency. From [155]. B: The two photon transition envisaged for the hybrid quantum system, using a microwave photon from the cavity and an RF photon provided by an antenna.

14.1.1. The cavity

We now try to get an estimation of the coupling strength between the atoms and the cavity. The relevant interactions are the magnetic dipole transitions $|F = 1, m_F\rangle \leftrightarrow |F' = 2, m'_F\rangle$. The interaction Hamiltonian is given by

$$H_{int} = \vec{\mu} \cdot \vec{B}. \quad (14.5)$$

If the field \vec{B} of the resonator mode is perpendicular to the quantization axis B_0 , $\Delta m_F = \pm 1$ transitions are induced, for a longitudinal field $\Delta m_F = 0$. To maximize coupling, the magnetic field associated with a cavity photon has to be large at the location of the atoms. The energy in a resonator is given by the volume integral over the magnetic field squared:

$$E = \frac{1}{2\mu_0} \int \vec{B}^2(\vec{r}) dV. \quad (14.6)$$

The exact field distribution $\vec{B}(\vec{r})$ for a specific microwave resonator has to be calculated with numerical simulations, though analytical expressions exist for a few special cases [157]. The "mode volume" describes the spatial extent of the resonator mode and varies significantly between different resonator types. To calculate the field strength caused by a single photon we normalize the energy in equation 14.6 to the energy of a single photon $\hbar\omega$.

The quality-factor (Q-factor) of a cavity with resonance frequency f and FWHM bandwidth Δf is defined as

$$Q = \frac{f}{\Delta f} \approx 2\pi f \frac{\text{energy stored}}{\text{power dissipated}}. \quad (14.7)$$

Both definitions of the Q-factor are nearly equivalent for large enough Q . The second definition relates the maximum stored energy to the energy lost per oscillation cycle. From the second definition of the Q-factor and the (simulated) field distribution $\vec{B}(\vec{r})$, the magnetic field strength at the location of the atomic cloud and thus the expected coupling can be calculated. The Q-factor can also be interpreted as the number of round-trips a cavity photon makes before being lost from the system. The Q-factor is limited by different loss mechanisms:

- The microwaves photons ($E \approx 0.03 \text{ meV}$) can split cooper pairs (with an energy of $\approx 1 \text{ meV}$ at 4 K).
- Dielectric losses dissipate energy in the substrate, this is the reason for choosing sapphire with a loss tangent $\tan \delta < 1 \times 10^{-5}$ [158]
- The motion of vortices in a type-II superconductor like Niobium is a dissipative process, thus limiting the Q-factor [81]. This loss mechanism depends strongly on the material quality but also on the history of applied magnetic fields. We plan to use our quenching laser setup (see section 9.4) to selectively quench the microwave resonator after a transport sequence to restore the Q-factor.
- Another loss channel are so called two-level fluctuators, limiting the Q-factor at millikelvin temperatures [98].
- Radiative losses, as the cavity might emit microwaves into free space.

The resonator at finite temperature will contain an average number \bar{n} of thermal photons given by the Bose-Einstein factor $1/(e^{hf/k_B T} - 1)$. At 4 K $\bar{n} = 10$, to consider the cavity "empty" with $\bar{n} < 0.1$ a temperature below 130 mK is needed, easily achievable with dilution refrigerators. The entire setup presented in this thesis is designed such that it can be upgraded easily to such fridge and its much lower cooling power.

The design goals for the microwave resonators are clear. First we want the highest Q-factor possible, this will increase the field strength and therefore the coupling to the atoms. A high Q-factor is also required to reach the strong coupling regime, where each photon should interact several times with the atomic cloud before being lost. Second we need a small mode volume that coincides with the extent of the cold cloud, ideally with a very homogeneous field such that all atoms experience the same coupling such that equation 14.3 holds. Making a resonator fulfilling these requirements is an art in itself, a detailed discussion of the progress will be presented in the upcoming thesis [103].

14.1.2. The atoms

Two internal hyperfine states of the neutral ^87Rb atoms serve as our qubit ground state $|0\rangle$ and excited state $|1\rangle$. Both states need to be low field seeking such that the atoms remains trapped, they should have the same magnetic moment such that the transition is symmetric. This requirements are met for $|0\rangle \equiv |F = 1, m_F = -1\rangle$ and $|1\rangle \equiv |F = 2, m_F = 1\rangle$ (cf. figure A.1). These two states additionally have the advantage that their first order Zeeman shift

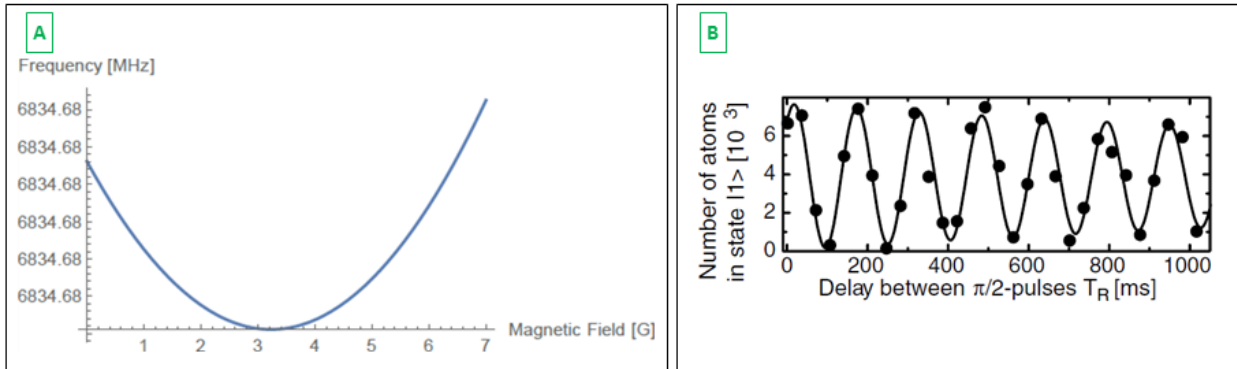


Figure 14.3.: A: Calculated transition frequency between the two clock states as a function of the magnetic field. For the "magic field" of 3.23 G both states experience the same Zeeman shift. B: Ramsey spectroscopy of a trapped atomic ensemble from [159]. Here the population of the upper qubit state $|1\rangle$ varies with the Ramsey time T_R . The coherence time of the ensemble is calculated from the damping of these oscillations.

vanishes at a magnetic field of 3.23 G (the "magic field"), this makes the transition insensitive to small variations of the magnetic field, cf. figure 14.3 A. Using these so called clock states at the magic field therefore reduces the inhomogeneous broadening due to variations in the trapping potential [159].

The transition between the two states is shown in 14.2 B. As $\Delta m_F = 2$, two photons are required, one microwave photon from the resonator and a second photon in the radiofrequency range provided by an external antenna, the same as for evaporative cooling. This second frequency loosens the precision with which the resonator has to hit the right frequency. The RF field should be large such that the limiting factor for the transition are the microwave photons from the cavity.

Measuring the the coherence time of the qubit states can be done with Ramsey spectroscopy. In this method, a $\pi/2$ pulse is applied to the ensemble. Then we wait a variable time T_R , the so called Ramsey time. Finally a second $\pi/2$ pulse is applied and the populations of the two states are probed. The atoms oscillate between the two states, the damping time constant of these oscillations (the so called Ramsey fringes) gives the coherence time of the ensemble. Experiments on room-temperature atomchips have reported coherence times of around 3 s for traps as close as $9 \mu\text{m}$ to the chip surface [159]. First measurements of the coherence time using a superconducting atomchip and an external microwave antenna are presented in [160]. Even at a distance of just $14 \mu\text{m}$ above the gap of an (off-resonant) coplanar waveguide resonator, the coherence time exceeds 3 s. Newer measurements of this group use the on-chip resonators as a microwave source, strong inhomogeneities of the microwave field however prohibit coherence time measurements [16]. We recently built in a microwave antenna into our science chamber (cf. figure 6.7), coherent state manipulation and Ramsey spectroscopy measurements will be presented in [103]. To summarize the requirements on the atomic ensemble and its trap:

- We want as many atoms as possible as this increases the coupling by \sqrt{N} .
- Variations in the magnetic trapping field change the level splitting due to the Zeeman

effect. This can be circumvented to a certain extent by applying an Ioffe field such that the trap bottom is equal to the "magic field" of 3.23 G. Colder and therefore smaller clouds will experience smaller field variations.

- Variations of the microwave/RF intensities across the ensemble lead to spatially varying Rabi frequencies and thus decoherence. Again, colder, smaller clouds are less sensitive to this problem.
- A BEC is not necessarily helpful, as the density dependent collisional shift would increase [161]. Also, a BEC contains less atoms than the initial thermal cloud, reducing the collective coupling.
- To increase the magnetic field strength at the location of the atoms, they should be as close as possible to the resonator. Bringing atoms close to the chip however comes with some difficulties such as trap fragmentation and higher sensitivity to electronic noise, but these are technical problems that can be solved. For very small distances ($< 2.5 \mu\text{m}$) however, the trap depth is reduced by the attractive Casimir-Polder potential [162].

14.1.3. System requirements

The original proposal in [8] made very optimistic assumptions for the relevant parameters: a BEC with 1×10^6 atoms at a distance of $1 \mu\text{m}$ from a coplanar waveguide $\lambda/2$ resonator with a Q-factor of 1×10^6 . This would result in a collective coupling strength of 40 kHz. Out of these numbers, the atom number is the easiest to reach. With an improved transport setup and a working trap recombination, we consider 1×10^7 atoms at $1 \mu\text{K}$ in the QUIC trap realistic. Reducing the distance between the atom cloud and the resonator is not so straightforward. As mentioned before, the trap depth will be reduced due to the Casimir-Polder interaction and atoms will be highly sensitive to any electronic noise present on the chip. Furthermore, the magnetic trap will be deformed by any superconducting surface, such as the ground planes of the resonator. This means that we need a very detailed understanding of the current distribution. A distance of $10 \mu\text{m}$ seems more realistic. A Q-factor of 1×10^6 has been achieved in our group using $\lambda/2$ resonators, this was however measured at millikelvin temperatures. In our setup, the resonator will not be placed in a metal box, the ground planes have to be small to allow for a magnetic trap. The chip will be subject to varying perpendicular fields during transport and, depending on the design, it will also contain a trapping wire. All these factors have some negative influence on the Q-factor. With the controlled annealing of the resonator after the transport sequence and several optimization iterations, a conservative estimation for the achievable Q-factor is 1×10^5 .

Microwave engineering is a vast field filling entire books, for example [157]. In the following sections, I will briefly review the current status of our resonator development, omitting any basic microwave theory as this would go beyond the scope of this thesis. The design, simulation, fabrication and testing of resonators is an iterative and time consuming process, a comprehensive description of our efforts will be given in the upcoming master thesis [103]. For high frequency simulation, we use the commercial software Sonnet¹. The fabricated chips are

¹<https://www.sonnetsoftware.com/>

tested in a bath cryostat². This cryostat has a very precise temperature control and allows the application of large perpendicular fields of several Tesla, where we can fully characterize the temperature and field dependence of the Q-factor and the resonance frequency.

14.2. Lambda half resonators

A coplanar waveguide (CPW) can be imagined as a two-dimensional coaxial cable, where a central conductor is separated from the ground planes by with a certain distance. This is the standard transmission line design for printed circuit boards. A capacitively coupled $\lambda/2$ resonator is directly derived from a CPW transmission line by simply interrupting the central conductor at two locations. Such a resonator is shown in figure 14.4. The length of the resonator (taking into account the refractive index of the substrate material), defines the wavelength of the first order resonance. A standing half-wave between the two coupling capacitors has its maximum of the electrical current (and magnetic field) in the middle of the resonator. The geometry of these resonators makes the combination with a Z-trap very unfavorable. The typical central Z-wire has a length of 2 mm, while a resonator for 6.834 GHz is about 10 mm long and would have to be bent to fit the chip.

A more natural approach is to use the $\lambda/2$ resonators in conjunction with the QUIC trap. A cold cloud with a length of a few hundred μm can be easily placed below the central part of the resonator, ensuring a homogeneous field strength along the cloud. To realize close trap distances, the ground plane of the resonator needs to be narrow such that the trapping field remains intact.

²Thanks to the low temperature physics group at the Atominstitut.

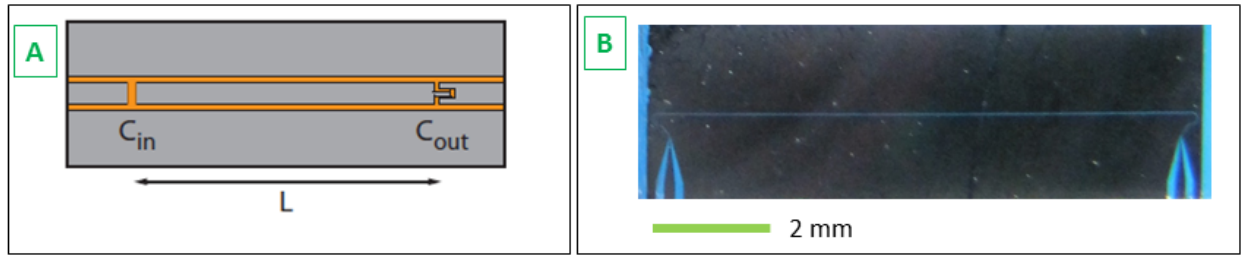


Figure 14.4.: A: Sketch of a $\lambda/2$ resonator. A coplanar waveguide is interrupted by two cuts in the central conductor. The two coupling capacities are labeled C_{in} and C_{out} . To increase the coupling capacity an interdigitated design like in C_{out} can be used. B: Image of one of our $\lambda/2$ resonators directly after dicing, the blue protective layer is still on the chip. The microwaves are launched on the chip on the two connection pads in the bottom. The gaps between the central conductor and the ground planes are barely visible. This resonator has a full ground plane, a test series with reduced ground planes is being tested at the time of writing.

14.3. Lumped element resonators

Another type of resonator is the so called lumped element resonator (LER). As the name suggests, it consists of discrete circuit elements for the capacity C and the inductance L , forming a LC circuit with the resonance frequency $f_0 = 1/(2\pi\sqrt{LC})$. This resonator type has several advantages for our application. Most importantly, the mode volume is very small, leading to high field strengths. The compact design makes it straightforward to include a LER on an atomchip with a Z-trap. Two exemplary designs are shown in figure 14.5.

All LERs shown here are capacitively coupled, in principle also inductive coupling to a feedline is possible. We use designs with two feedlines such that we are able to measure the properties of the resonators in reflection and in transmission, but this is not necessary, freeing even more space on the chip.

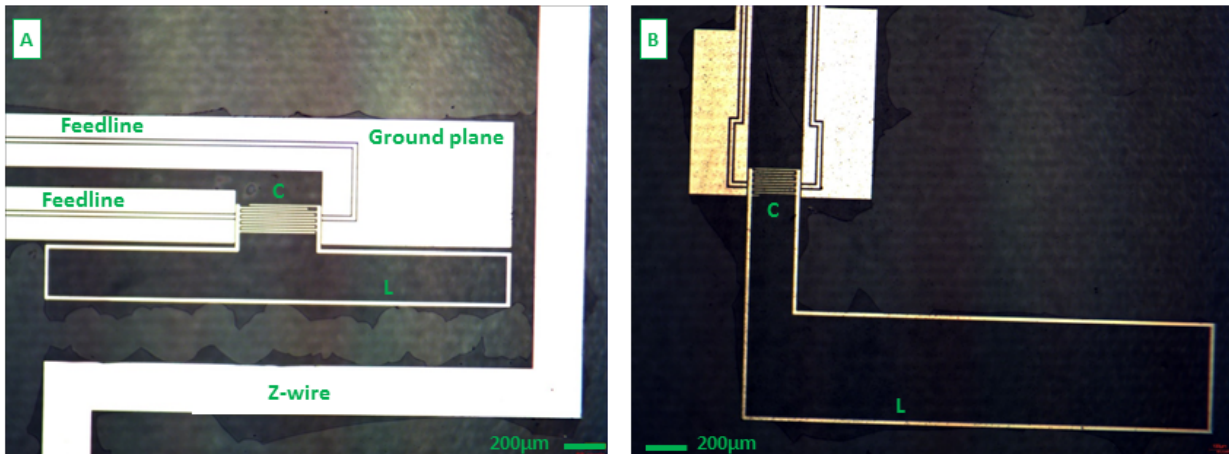


Figure 14.5.: Two lumped element resonator designs. In A, the length of the inductance is matched to the length of the Z-wire. B shows a design without Z wire. Metal surfaces are white. The capacity is formed by the interdigitated structure, the inductive element is essentially just a piece of wire.

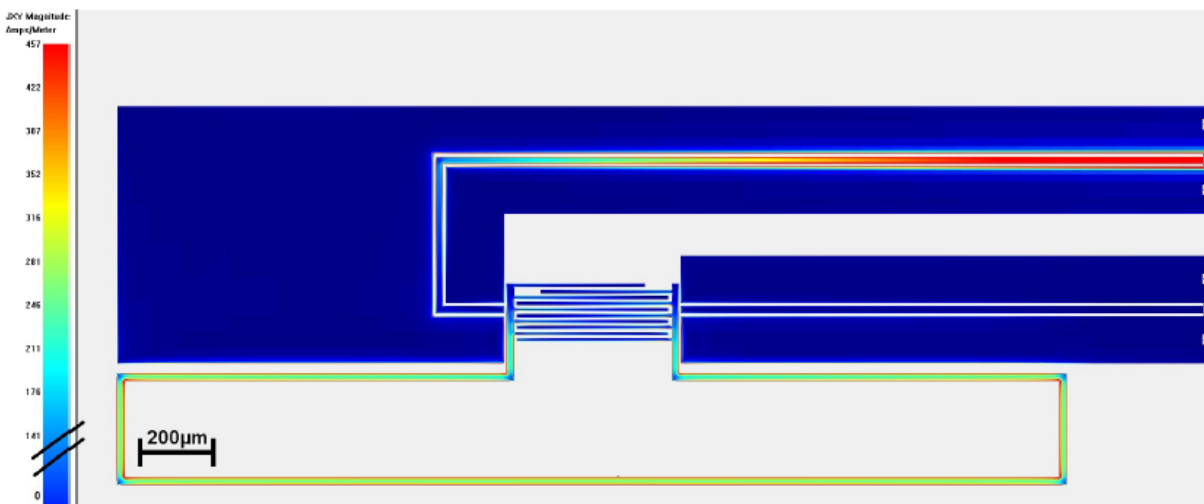


Figure 14.6.: Simulation of the sheet current density in the lumped element resonator in figure 14.5 A using Sonnet Microwave Studio. As expected, there is no current in the capacitive part of the circuit while the inductive part has a rather homogeneous current density along the horizontal part where the atoms will be positioned.

14.4. Three dimensional resonators

A recent study in our group showed how 3D lumped element microwave resonators can be used to get a homogeneous coupling strength to the NV-centers in diamond [163]. This resonator type is shown in figure 14.7. The key point is that it exhibits a very homogeneous magnetic field distribution in the gap between the two ears. We investigate how this design might also be used for coupling ultracold atoms.

We need to make several modifications to the original design. First of all, the resonance frequency has to match the 6.83 GHz for the Rb hyperfine transition, thus reducing the dimensions compared to the 3 GHz design. The other modification is that we need to be able to transport the cold atomic cloud into the resonator. A hole in the side wall with sufficient diameter has no detrimental effect on the Q-factor.

The resonators were designed using COMSOL. Very good agreement between the simulated and the real resonance frequency was achieved. A crucial step in the construction of these resonators is the polishing of the material. Details on the design, simulation and testing are presented in [164].

First tests on the resonators showed Q-factors of up to 1000 at liquid nitrogen temperatures. This relatively low value and the large mode volume leads to very small single-atom coupling strengths, making strong coupling rather unrealistic. We can not fabricate the resonator out of a superconductor, as the Meissner effect would not allow the magnetic trap to enter the resonator.

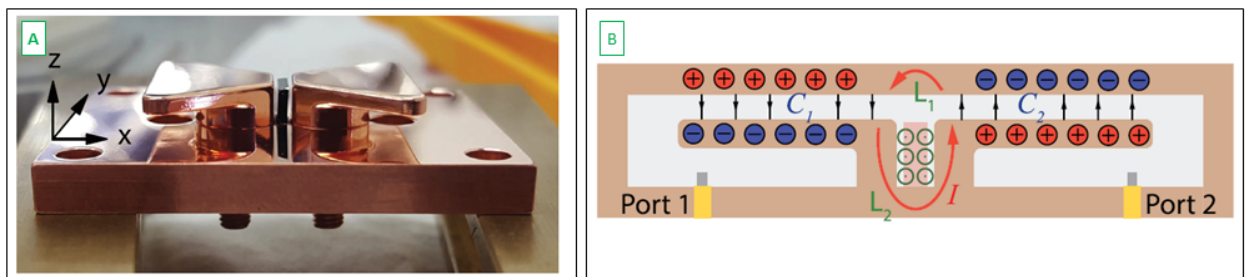


Figure 14.7.: A: A picture of the 3D resonator (without top lid) with the Diamond placed between the "ears". B: Schematic of this resonator type. The capacitive part is formed by the top lid and the top surface of the ears. The current flows from one ear to the other, producing a homogeneous magnetic field. Both taken from [163].

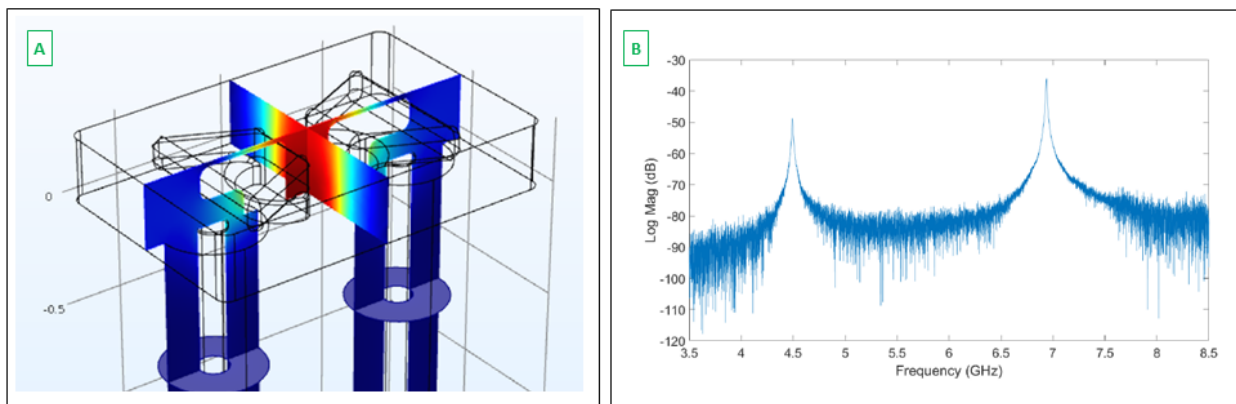


Figure 14.8.: A: Simulation of the magnetic field distribution in the 3D resonator. (Red=high field, blue=low field). In the gap between the ears the field is very homogeneous. B: Room-temperature measurement of our first 3D-resonator. The resonance at 6.94 GHz has a Q-factor of 750.

15. Towards superconducting vortex trap lattices

Arrays of magnetic microtraps have been suggested for applications in quantum information science [165] and quantum simulation of Bose-Hubbard systems [166]. One- and two-dimensional arrays of permanent magnetic microtraps have been realized with lattice spacings down to $10\ \mu\text{m}$ [167] (cf. figure 15.1). These experiments use atomchips with patterned permanent magnetic materials, typically FePt. Further miniaturization of permanent magnetic lattices with sufficient magnetization is a challenging task. Furthermore, the decoherence rate due to Johnson noise is significant close to the normal conducting, room-temperature surfaces.

A recent proposal [169] investigates the possibility of using superconducting vortex lattices for trapping ultracold atoms. Figure 15.2 visualizes the basic idea. Such trap arrays could have several favorable properties for the simulation of Bose-Hubbard Hamiltonians. First, the lattice spacing can be significantly reduced when compared to optical lattices. In a typical type-II superconducting thin film, the inter-vortex spacing can be as low as a few ten nanometers. A small lattice constant leads to a higher recoil energy and to less stringent requirements on the entropy of the simulator. Second, vortices can be pinned to nanofabricated artificial pinning sites such as holes. Therefore, arbitrary trap patterns are possible, in contrast to optical lattices. The decoherence rate due to Johnson noise close to a superconducting surface should be significantly reduced compared to normal conducting materials as suggested by several publications [59, 170], which makes very small trapping distances are possible.

The experimental realization of a vortex trap lattice is challenging in several aspects. First, the nano-patterned atomchip needs to be magnetized such that each antidot carries one single flux quantum. Using our optical quenching setup, this could be done directly before loading the lattice with atoms. Second, a transfer procedure needs to be found that allows to fill the traps with ultracold atoms without destroying the vortex lattice through perpendicular magnetic fields. The biggest challenge however is the detection of the atoms with sub-wavelength spacing. One vague idea would be a site selective trap release and subsequent fluorescence imaging.

As first step towards the realization of a vortex trap lattice, we propose to start with larger magnetized superconducting structures. Magnetic traps created by single magnetized superconducting disks or squares have been studied in [19] and [171] and it has been shown experimentally that a superconducting ring with a single magnetic flux quantum Φ_0 inside causes detectable modifications to a superconducting Z trap [172]. Arrays of rings or disks in the $10\ \mu\text{m}$ range can be used to find and optimize the experimental sequences necessary. We designed several superconducting atomchips featuring rings and other structures, one example is shown in figure 15.3, however at the time of writing they are yet to be tested.

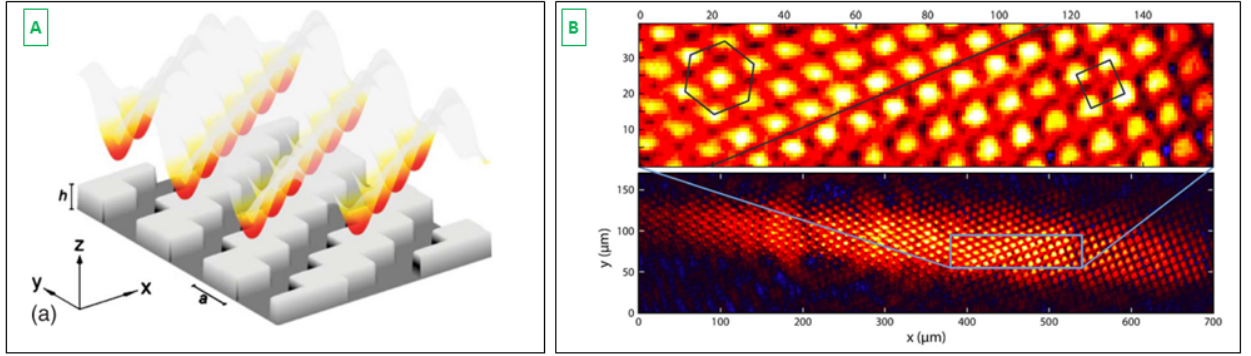


Figure 15.1.: A: Illustration of the potential formed by a material (light gray) uniformly magnetized along z in combination with a bias field along y . From [168]. B: Absorption image of Rubidium atoms loaded in a potential similar to A. Each trap contains around 400 atoms. Both hexagonal and square lattices are realized on the same chip. From [167].

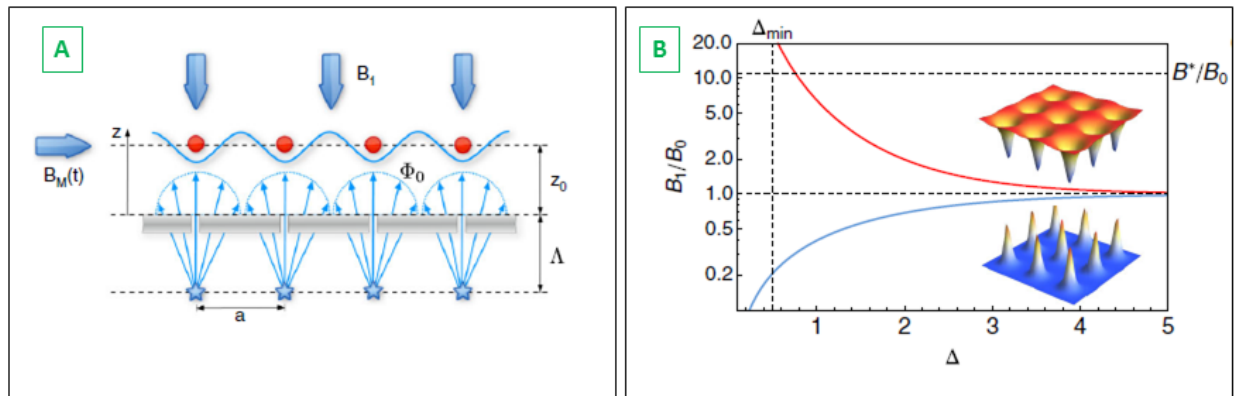


Figure 15.2.: A: Schematic illustration of the superconducting vortex lattice. A type-II superconducting thin film with thickness d and London penetration depth λ is penetrated by vortices. Each vortex contains a single flux quantum Φ_0 , the spacing between the vortices is given by a . The magnetic field can be modeled by magnetic point charges at a distance $\Lambda = \lambda^2/d$ below the film. Λ is called the effective penetration depth. Applying a vertical bias field B_1 creates magnetic traps at a height z above each vortex core. An additional time-orbiting magnetic field $B_M(t)$ avoids Majorana losses. B: The vertical bias field B_1 in units of the average magnetic field at the surface $B_0 = \Phi_0/a^2$ as a function of the trap distance $\Delta = 2\pi/a(z + \Lambda)$. For fields stronger than B_0 , a lattice of traps above each vortex forms (upper inset). For $B_1 < B_0$, a flat trapping landscape with sharp peaks forms (lower inset). Both taken from [169].

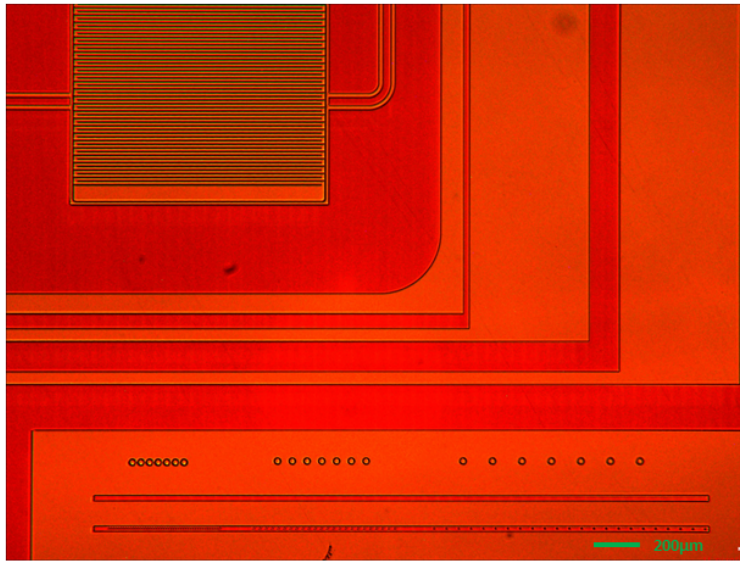


Figure 15.3.: Design of a complex Niobium atomchip. It features (from top to bottom) a lumped element resonator, three Z wires with varying wire width, rings with varying distance, a stripe and a strip with holes.

16. Conclusion and outlook

During the last years, we have overcome many technical challenges and now have a unique setup loading ultracold atoms on superconducting atomchips. For a successful future of the experiment, it is paramount to decrease the time spent bug fixing. The time we spent for actual measurements with atoms on the superconducting atomchip was very limited, never longer than a couple of weeks before some component, either a laser, the cryostat, a power supply etc. broke. (A subjective estimation would be 90% down time.) The complexity of this experiment requires a different approach as with other setups, where typically each device is designed once, built once and then used, even when small design flaws become apparent. In our case, simply because of the much larger number of elements (be reminded of 39 coils!), these small flaws become a problem - there is always something that breaks. Instead of adding another floor to the "house of cards", it is useful to fix the foundation properly. We have identified many of these small improvements and the imminent move to the new lab is a perfect opportunity to implement them. In the long run, the increased reliability will quickly pay off the time "lost" during these rather mundane works. Once the superconducting chip trap is "stable" in the sense that it is recovered within days after closing the cryostat and that it remains there indefinitely, many of the intended measurements can be performed carefully. The BEC, a long standing intermediate goal of our experiment, is only a matter of further optimization and I am convinced that it is just a few weeks (of uninterrupted measurements!) away.

Once the setup has reached a reliable state (with 90% up time, instead of 10%), there are many ideas what can be done with this new experimental platform. One of its unique features is (theoretically) the fast turnaround time after chip replacement. This would allow to perform the magnetic field microscopy and current distribution measurements on a variety of superconducting atomchips.

A long standing question is the lifetime of atomic clouds near superconducting surfaces. A drastic increase in lifetime compared to normal conducting materials has been theoretically suggested due to the reduced Johnson-Nyquist noise [59, 170]. First measurements indicating lifetimes below the Johnson-Nyquist noise limit are not yet conclusive [173]. Another interesting idea is to study the vortex noise from superconducting films [174]. To perform these experiments on our setup, all technical noise sources must be eliminated, and the lifetime of atoms in the chip trap should only be limited by the (very low) background pressure. Apart from the noise filtering efforts, the use of inherently noise free persistent currents in the atomchip and in the bias coils seems to be a promising idea, now possible with the quenching laser setup.

Of course the hybrid quantum system as a long term goal remains intact. We are working on the detailed understanding of the current distribution in the atomchips, a sufficient atom number, a low enough temperature and resonators with acceptable resonance frequencies and Q factors. With these ingredients ready, there is a realistic chance to realize the worlds first coupled system between microwave resonators and ultracold atoms.

16. *Conclusion and outlook*

Using the properties of superconductors to create novel magnetic traps is another promising prospect. The ultimate goal in this direction is of course magnetic trapping by single superconducting vortices, this could be a supplementary method to optical lattices [169]. This goal can only be approached step by step, starting with macro- and mesoscopic superconducting structures and subsequent miniaturization.

Bibliography

- [1] Tim Langen, Remi Geiger, and Jörg Schmiedmayer. “Ultracold Atoms Out of Equilibrium”. In: *Annual Review of Condensed Matter Physics* 6.1 (2015), pp. 201–217. arXiv: 1408.6377.
- [2] Michael Gring et al. “Relaxation and Prethermalization in an Isolated Quantum System”. In: *Science* 337.6100 (2012), pp. 1318–1322. arXiv: 1112.0013.
- [3] Robert Bücke. “Twin-atom beam generation in a one-dimensional Bose gas”. PhD thesis. TU Wien, 2013.
- [4] M. D. Lukin. “Colloquium: Trapping and manipulating photon states in atomic ensembles”. In: *Reviews of Modern Physics* 75.2 (2003), pp. 457–472.
- [5] R J Schoelkopf and S M Girvin. “Wiring up quantum systems.” In: *Nature* 451.7179 (2008), pp. 664–669.
- [6] R. Amsüss et al. “Cavity QED with magnetically coupled collective spin states”. In: *Physical Review Letters* 107.6 (2011), pp. 1–5. arXiv: 1103.1045.
- [7] T. Frey et al. “Dipole coupling of a double quantum dot to a microwave resonator”. In: *Physical Review Letters* 108.4 (2012), pp. 1–5. arXiv: 1108.5378.
- [8] J. Verdú et al. “Strong magnetic coupling of an ultracold gas to a superconducting waveguide cavity”. In: *Physical Review Letters* 103.4 (2009), pp. 1–4. arXiv: 0809.2552.
- [9] Stefan Minniberger et al. “Magnetic conveyor belt transport of ultracold atoms to a superconducting atomchip”. In: *Applied Physics B* (2014), pp. 1017–1021. arXiv: 1311.3155.
- [10] T. Nirrengarten et al. “Realization of a superconducting atom chip”. In: *Physical Review Letters* 97.20 (2006), pp. 1–4. arXiv: 0610019 [quant-ph].
- [11] C. Roux et al. “Bose-Einstein condensation on a superconducting atom chip”. In: 56004 (2008), p. 4. arXiv: 0801.3538.
- [12] A. Emmert et al. “Measurement of the trapping lifetime close to a cold metallic surface on a cryogenic atom-chip”. In: *European Physical Journal D* 51.2 (2009), pp. 173–177. arXiv: 0901.4331.
- [13] C. Hermann-Avigliano et al. “Long coherence times for Rydberg qubits on a superconducting atom chip”. In: *Physical Review A* 90.4 (2014), pp. 1–5.
- [14] Thanh Long Nguyen et al. “Towards quantum simulation with circular Rydberg atoms”. In: (2017), pp. 1–25. arXiv: 1707.04397.
- [15] D. Cano et al. “Experimental system for research on ultracold atomic gases near superconducting microstructures”. In: *European Physical Journal D* 63.1 (2011), pp. 17–23.

- [16] H. Hattermann et al. “Coupling ultracold atoms to a superconducting coplanar waveguide resonator”. In: 1 (2017), pp. 1–16. arXiv: 1707.02730.
- [17] F. Jessen et al. “Trapping of ultracold atoms in a $^3\text{He}/^4\text{He}$ dilution refrigerator”. In: *Applied Physics B: Lasers and Optics* (2013), pp. 1–7. arXiv: 1309.2548.
- [18] Fan Yang et al. “A Scanning Quantum Cryogenic Atom Microscope”. In: *arXiv preprint* 94305.1 (2016), pp. 1–16. arXiv: 1608.06922.
- [19] M. Siercke et al. “Reconfigurable self-sufficient traps for ultracold atoms based on a superconducting square”. In: *Physical Review A - Atomic, Molecular, and Optical Physics* 85.4 (2012), pp. 1–5. arXiv: 1204.2891.
- [20] T. Müller et al. “Programmable trap geometries with superconducting atom chips”. In: *Physical Review A - Atomic, Molecular, and Optical Physics* 81.5 (2010), pp. 1–4. arXiv: 1003.5417.
- [21] Christoph Hufnagel, Tetsuya Mukai, and Fujio Shimizu. “Stability of a superconductive atom chip with persistent current”. In: *Physical Review A - Atomic, Molecular, and Optical Physics* 79.5 (2009), pp. 1–5.
- [22] Hiromitsu Imai et al. “Bose-Einstein condensate on a persistent-supercurrent atom chip”. In: *Applied Physics B: Lasers and Optics* (2014), pp. 1–9.
- [23] Max Planck. “Zur Theorie des Gesetzes der Energieverteilung im Normalspectrum”. In: *Verhandlungen der Deutschen physikalischen Gesellschaft* 2.17 (1900), p. 245.
- [24] Albert Einstein. “Zur Quantentheorie der Strahlung”. In: *Mitteilungen der Physikalischen Gesellschaft Zürich* 16 (1916), pp. 47–62.
- [25] Arthur H Compton. “A Quantum Theory of the Scattering of X-rays by Light Elements”. In: *Phys. Rev.* 21.5 (1923), pp. 483–502.
- [26] O. R. Frisch. “Experimenteller Nachweis des Einsteinschen Strahlungsrückstoßes”. In: *Zeitschrift für Physik* 86.1 (1933), pp. 42–48.
- [27] Louis De Broglie. “The wave nature of the electron”. In: *Nobel lectures, Physics 1922-1941* (1929), pp. 244–256.
- [28] C Davisson and L H Germer. “Diffraction of Electrons by a Crystal of Nickel”. In: *Phys. Rev.* 30.6 (1927), pp. 705–740.
- [29] E Schrödinger. “Quantisierung als Eigenwertproblem”. In: *Annalen der Physik* 386 (1926), pp. 109–139.
- [30] A Einstein. “Strahlungs-Emission und -Absorption nach der Quantentheorie”. In: *Deutsche Physikalische Gesellschaft* 18 (1916).
- [31] T. H. Maiman. “Stimulated Optical Radiation in Ruby”. In: *Nature* 187.4736 (1960), pp. 493–494.
- [32] T W Hänsch and A L Schawlow. “Cooling of Gases by LASER Radiation”. In: *Optics Communications* 13.I (1975), pp. 68–69.
- [33] John Prodan et al. “Stopping atoms with laser light”. In: *Physical Review Letters* 54.10 (1985), pp. 992–995.

- [34] Alan L. Migdall et al. “First observation of magnetically trapped neutral atoms”. In: *Physical Review Letters* 54.24 (1985), pp. 2596–2599.
- [35] Bose. “Plancks Gesetz und Lichtquantenhypothese”. In: *Zeitschrift für Physik* 26.1 (1924), pp. 178–181.
- [36] Albert Einstein. “Quantentheorie des einatomigen idealen Gases”. In: *Sitzungsberichte der Preussischen Akademie der Wissenschaften* 1 (1925).
- [37] M H Anderson et al. “Observation of Bose-Einstein Condensation in a Dilute Atomic Vapor”. In: *Science* 269.5221 (1995), pp. 198–201. arXiv: arXiv:1011.1669v3.
- [38] Harold J. Metcalf and Peter van der Straten. *Laser Cooling and Trapping*. Graduate Texts in Contemporary Physics. New York, NY: Springer New York, 1999.
- [39] Daniel Steck. *Rubidium 87 D line data*. Tech. rep. 2001.
- [40] P. D. Lett et al. “Optical molasses”. In: *Journal of the Optical Society of America B* 6.11 (1989), p. 2084.
- [41] J. Dalibard and C. Cohen-Tannoudji. “Laser cooling below the Doppler limit by polarization gradients: simple theoretical models”. In: *Journal of the Optical Society of America B* 6.11 (1989), p. 2023.
- [42] Stephan Schneider. “Bose-Einstein Kondensation in einer magnetischen Z-Falle”. PhD thesis. Universität Heidelberg, 2003.
- [43] A. Ashkin and J. P. Gordon. “Stability of radiation-pressure particle traps: an optical Earnshaw theorem”. In: *Optics letters* 8.10 (1983), pp. 511–513.
- [44] E. L. Raab et al. “Trapping of Neutral Sodium Atoms with Radiation Pressure”. In: *Physical Review Letters* 59.23 (1987), pp. 2631–2634. arXiv: arXiv:1009.2475v1.
- [45] S. Earnshaw. *On the Nature of the Molecular Forces which Regulate the Constitution of the Luminiferous Ether*. 1842. arXiv: t92818w00 [13960].
- [46] William H Wing. “On neutral particle trapping in quasistatic electromagnetic fields”. In: *Progress in Quantum Electronics* 8.3 (1984), pp. 181–199.
- [47] Jörg Schmiedmayer. “Guiding and trapping a neutral atom on a wire”. In: *Physical Review A* 52.1 (1995).
- [48] Tilman Esslinger, Immanuel Bloch, and Theodor W Hänsch. “Bose-Einstein condensation in a quadrupole-Ioffe-configuration trap”. In: *Physical Review A* 58.4 (1998), R2664–R2667.
- [49] Markus Bartenstein et al. “Atoms and wires: Toward atom chips”. In: *IEEE Journal of Quantum Electronics* 36.12 (2000), pp. 1364–1376.
- [50] Ron Folman et al. “Controlling Cold Atoms using Nanofabricated Surfaces: Atom Chips”. In: *Physical Review Letters* 84.20 (2000), pp. 4749–4752. arXiv: 9912106 [quant-ph].
- [51] Ettore Majorana. “Atomi orientati in campo magnetico variabile”. In: *Il Nuovo Cimento (1924-1942)* 9.2 (1932), pp. 43–50.
- [52] C. Sukumar and D. Brink. “Spin-flip transitions in a magnetic trap”. In: *Physical Review A* 56.3 (1997), pp. 2451–2454.

- [53] T Arpornthip, C Sackett, and K. J. Hughes. “Vacuum-pressure measurement using a magneto-optical trap”. In: *Physical Review A* 85.3 (2012), p. 033420. arXiv: 1203.0189.
- [54] H. Boesten, A. Moerdijk, and B. Verhaar. “Dipolar decay in two recent Bose-Einstein condensation experiments”. In: *Physical Review A* 54.1 (1996), R29–R32.
- [55] Wolfgang Ketterle and N.J. Van Druten. “Evaporative cooling of trapped atoms”. In: *Advances In Atomic, Molecular, and Optical Physics* 37 (1996), pp. 181–236.
- [56] C. Henkel et al. “Fundamental limits for coherent manipulation on atom chips”. In: *Applied Physics B: Lasers and Optics* 76.2 (2003), pp. 173–182. arXiv: 0208165 [quant-ph].
- [57] Alexander Kasper. “Bose-Einstein condensation in a robust microtrap – the combination of wire traps and atom chips”. PhD thesis. Universität Heidelberg, 2003.
- [58] M. Gehm et al. “Dynamics of noise-induced heating in atom traps”. In: *Physical Review A* 58.5 (1998), pp. 3914–3921.
- [59] Ulrich Hohenester et al. “Spin-flip lifetimes in superconducting atom chips: Bardeen-Cooper-Schrieffer versus Eliashberg theory”. In: *Physical Review A - Atomic, Molecular, and Optical Physics* 76.3 (2007), pp. 1–9. arXiv: 0707.0238.
- [60] Kendall B Davis et al. “Evaporative cooling of sodium atoms”. In: *Physical Review Letters* 75.26 (1995), p. 2909.
- [61] G Cook and R. H. Dickerson. “Understanding the chemical potential”. In: *Am. J. Phys.* 63.8 (1995), pp. 737–742.
- [62] J. Ensher et al. “Bose-Einstein Condensation in a Dilute Gas: Measurement of Energy and Ground-State Occupation”. In: *Physical Review Letters* 77.25 (1996), pp. 4984–4987.
- [63] Dirk Van Delft and Peter Kes. “The discovery of superconductivity”. In: *Physics Today* 63.9 (2010), pp. 38–43.
- [64] W Meissner and R Ochsenfeld. “Ein neuer Effekt bei Eintritt der Supraleitfähigkeit”. In: *Naturwissenschaften* 21.44 (1933), pp. 787–788.
- [65] F London and H London. “The Electromagnetic Equations of the Supraconductor”. In: *Proceedings of the Royal Society of London A: Mathematical, Physical and Engineering Sciences* 149.866 (1935), pp. 71–88.
- [66] Anatoly Shepelev. “The Discovery of Type II Superconductors (Shubnikov Phase)”. In: *Superconductor*. Sciyo, 2010.
- [67] Vitalii L Ginzburg and Lev D Landau. “On the theory of superconductivity”. In: *Zh. eksp. teor. Fiz* 20.1064-1082 (1950), p. 35.
- [68] Alexei Abrikosov. “Nobel lecture: Type-II superconductors and the vortex lattice”. In: *Reviews of modern physics* 76.3 (2003), pp. 975–979.
- [69] J. Bardeen, L. N. Cooper, and J. R. Schrieffer. “Theory of superconductivity”. In: *Physical Review* 108.5 (1957), pp. 1175–1204.

- [70] Lev Gor'kov. "Microscopic derivation of the Ginzburg-Landau equations in the theory of superconductivity". In: *Sov-Phys JETP* 9 (1959), p. 1364.
- [71] J. G. Bednorz and K. A. Müller. "Possible highT_c superconductivity in the Ba La Cu O system". In: *Zeitschrift für Physik B Condensed Matter* 64.2 (1986), pp. 189–193.
- [72] Leon N. Cooper. "Bound electron pairs in a degenerate fermi gas". In: *Physical Review* 104.4 (1956), pp. 1189–1190. arXiv: 1506.05455.
- [73] URL: <https://dc.edu.au/wp-content/uploads/cooper-pair-phonon.png> (visited on 11/10/2017).
- [74] URL: <https://de.wikipedia.org/wiki/BCS-Theorie> (visited on 11/10/2017).
- [75] L. D. Landau. "On the theory of phase transitions". In: *Zh. Eks. Teor. Fiz.* 7.1937 (1937), pp. 19–32.
- [76] Werner Buckel and Reinhold Kleiner, eds. *Superconductivity*. Weinheim, Germany: Wiley-VCH Verlag GmbH, 2004.
- [77] URL: <http://www.supraconductivite.fr/en/index.php?p=supra-levitation-phase-more> (visited on 11/10/2017).
- [78] U. Essmann and H. Träuble. "The direct observation of individual flux lines in type II superconductors". In: *Physics Letters A* 24.10 (1967), pp. 526–527.
- [79] URL: <http://scienceblogs.com/startswithabang/2011/10/22/weekend-diversion-lift-me-up-q/> (visited on 11/10/2017).
- [80] URL: https://commons.wikimedia.org/wiki/File:Magnetisation_and_superconductors.png (visited on 11/10/2017).
- [81] Rene Flükiger. "Overview of Superconductivity and Challenges in Applications". In: *Reviews of Accelerator Science and Technology* 05.April (2012), pp. 1–23.
- [82] C. M. Rey and A. P. Malozemoff. *Fundamentals of superconductivity*. Elsevier Ltd, 2015, pp. 29–73.
- [83] C. P. Bean. "Magnetization of hard superconductors". In: *Physical Review Letters* 8.6 (1962), pp. 250–253. arXiv: arXiv:1011.1669v3.
- [84] Charles P. Bean. "Magnetization of high-field superconductors". In: *Reviews of Modern Physics* 36.1 (1964), pp. 31–39.
- [85] E. Zeldov et al. "Magnetization and transport current in thin superconducting films". In: *Physical Review B* 49.14 (1994).
- [86] D. X. Chen et al. "Transverse demagnetizing factors of long rectangular bars: I. Analytical expressions for extreme values of susceptibility". In: *Journal of Applied Physics* 91.8 (2002), pp. 5254–5259.
- [87] R.A. French. "Intrinsic type-2 superconductivity in pure niobium". In: *Cryogenics* 8.5 (1968), pp. 301–308.
- [88] R. P. Huebener et al. "Critical current density in superconducting niobium films". In: *Journal of Low Temperature Physics* 19.3-4 (1975), pp. 247–258.
- [89] B. W. Maxfield and W. L. McLean. "Superconducting penetration depth of niobium". In: *Physical Review* 139.5A (1965).

- [90] V. R. Karasik and I. Y. Shebalin. “Superconducting properties of pure niobium”. In: *Sov-Phys JETP* 30.6 (1970), pp. 1068–1076.
- [91] Markus Greiner et al. “Magnetic transport of trapped cold atoms over a large distance”. In: *Physical Review A - Atomic, Molecular, and Optical Physics* 63.3 (2001), pp. 1–4.
- [92] T. L. Gustavson et al. “Transport of Bose-Einstein condensates with optical tweezers”. In: *Physical Review Letters* 88.2 (2002), pp. 204011–204014. arXiv: 0108496 [cond-mat].
- [93] S. Haslinger et al. “Electron beam driven alkali metal atom source for loading a magneto-optical trap in a cryogenic environment”. In: *Applied Physics B: Lasers and Optics* 102.4 (2011), pp. 819–823. arXiv: 1003.5144.
- [94] Patrick Sieberer. “Title TBA”. Bachelor Thesis. TU Wien, Dec. 2017.
- [95] Michael Bauer. “Title TBA”. Bachelor Thesis. TU Wien, Dec. 2017.
- [96] R. W. Fast et al. “Electrical and mechanical properties of lead/tin solders and splices for superconducting cables”. In: *Cryogenics* 28.1 (1988), pp. 7–9.
- [97] S. Groth et al. “Atom chips: Fabrication and thermal properties”. In: *Applied Physics Letters* 85.14 (2004), pp. 2980–2982. arXiv: 0404141 [cond-mat].
- [98] Christian Koller. “Towards the realization of hybrid quantum systems”. PhD thesis. TU Wien, 2012.
- [99] T. Müller et al. “Towards a guided atom interferometer based on a superconducting atom chip”. In: *New Journal of Physics* 10 (2008). arXiv: 0806.1789.
- [100] T. Mukai et al. “Persistent supercurrent atom chip”. In: *Physical Review Letters* 98.26 (2007), pp. 1–4. arXiv: 0702142 [cond-mat].
- [101] Fritz Randulf S Diorico. “Novel Atomchip Technologies with Superconductors”. PhD thesis. TU Wien, 2016.
- [102] Peter Gerges. “Towards a hybrid quantum system - design and test of superconducting microwave resonators”. Bachelor Thesis. TU Wien, May 2017.
- [103] Lukas Cvitkovich. “Title TBA”. Master Thesis. TU Wien, Oct. 2018.
- [104] Stefan Haslinger. “Cold Atoms in a Cryogenic Environment”. PhD thesis. TU Wien, 2011.
- [105] Lukas Aschatz; Dominik Ilk. “Magnetic coupling of ultracold atoms with an superconducting atomchip”. Bachelor Thesis. TU Wien, Aug. 2015.
- [106] Bill Whitlock. *MIT CEDIA Class EST016 : UNDERSTANDING, FINDING and ELIMINATING GROUND LOOPS*. URL: http://web.mit.edu/jhawk/tmp/p/EST016_Ground_Loops_handout.pdf. Last visited on 2017-11-15.
- [107] James Simpson et al. “Simple Analytic Expressions for the Magnetic Field of a Circular Current Loop”. In: *NASA Technical Report* (2001), pp. 1–3.
- [108] Stefan Reuter. “Magnetic transport and recombination of an atom cloud”. Bachelor Thesis. TU Wien, Feb. 2017.

- [109] James D. Hanson and Steven P. Hirshman. “Compact expressions for the Biot-Savart fields of a filamentary segment”. In: *Physics of Plasmas* 9.10 (2002), p. 4410.
- [110] A. L. Schawlow and C. H. Townes. “Infrared and optical masers”. In: *Physical Review* 112.6 (1958), pp. 1940–1949.
- [111] Charles H. Henry. “Theory of the Linewidth of Semiconductor Lasers”. In: *IEEE Journal of Quantum Electronics* 18.2 (1982), pp. 259–264.
- [112] Robert Amsüss. “Development of a Source of Ultracold Atoms for Cryogenic Environments”. In: *Diplomarbeit, Technische Universität Wien* (2008).
- [113] URL: https://www.thorlabs.com/newgrouppage9.cfm?objectgroup_id=7573 (visited on 11/10/2017).
- [114] URL: <http://www.dilas.com/marcom/2016/the-perfect-beam/web.html> (visited on 11/10/2017).
- [115] Carl E. Wieman and Leo Hollberg. “Using diode lasers for atomic physics”. In: *Review of Scientific Instruments* 62.1 (1991), pp. 1–20.
- [116] Thomas Angerler. “A robust system for a DFB- and an ECDL laser setup”. Bachelor Thesis. TU Wien, Sept. 2017.
- [117] Daryl W. Preston. “Doppler-free saturated absorption: Laser spectroscopy”. In: *American Journal of Physics* 64.11 (1996), pp. 1432–1436.
- [118] Benedikt Gerstenecker. “Tailoring trap current distributions in superconducting atom-chips”. In: *Diplomarbeit, Technische Universität Wien* (2017).
- [119] M. Pappa et al. “Ultra-sensitive atom imaging for matter-wave optics”. In: *New Journal of Physics* 13 (2011).
- [120] Robert Bückler. “Fluorescence Imaging of Ultracold Atoms”. In: *Diplomarbeit, Technische Universität Wien* (2007).
- [121] G. Reinaudi et al. “Strong saturation absorption imaging of dense clouds of ultracold atoms”. In: *Optics Letters* 32.21 (2007), pp. 3143–3145. arXiv: 0707.2930.
- [122] Klaus Hueck et al. “Calibrating High Intensity Absorption Imaging of Ultracold Atoms”. In: 3145.2007 (2017), pp. 3143–3145. arXiv: 1702.01943.
- [123] Michael Gring. “Prethermalization in an isolated many body system”. PhD thesis. TU Wien, 2012.
- [124] Tadas Pyragius. “Developing and building an absorption imaging system for Ultracold Atoms”. In: *arXiv preprint arXiv:1209.3408* (2012), p. 28. arXiv: 1209.3408.
- [125] David A Smith et al. “Absorption imaging of ultracold atoms on atom chips.” In: *Optics express* 19.9 (2011), pp. 8471–8485. arXiv: 1101.4206.
- [126] Naz Shokrani. “Title TBA”. Master Thesis. TU Wien, Mar. 2018.
- [127] Clemens Heistracher. “Vertical Imaging of the QUIC and calibration of a current source”. Bachelor Thesis. TU Wien, Aug. 2017.
- [128] Christoph Hufnagel. “Superconducting microtraps for ultracold atoms”. PhD thesis. TU Wien, 2011.

- [129] M Brajdic. “Entwicklung einer Computersteuerung und ihre Anwendung in einem Experiment zur vereinfachten Bose-Einstein Kondensation in einer Oberflächenfalle”. In: *Diploma Thesis, University of Heidleberg* (2003).
- [130] Qi Liang. “PHD Thesis, in preparation”. PhD thesis. TU Wien, 2018.
- [131] Stephan Wildermuth et al. “Bose-Einstein condensates: microscopic magnetic-field imaging.” In: *Nature* 435.7041 (2005), p. 440.
- [132] S. Wildermuth et al. “Sensing electric and magnetic fields with Bose-Einstein condensates”. In: *Applied Physics Letters* 88.26 (2006), pp. 26–29.
- [133] Simon Aigner. “Magnetic Field Microscopy using Ultracold Atoms”. PhD thesis. Universität Heidelberg, 2007.
- [134] S Aigner et al. “Long-range order in electronic transport through disordered metal films.” In: *Science (New York, N.Y.)* 319.5867 (2008), pp. 1226–1229.
- [135] J. Estève et al. “Role of wire imperfections in micromagnetic traps for atoms”. In: *Physical Review A - Atomic, Molecular, and Optical Physics* 70.4 (2004), pp. 2–5. arXiv: 0403020 [physics].
- [136] T. Schumm et al. “Atom chips in the real world: The effects of wire corrugation”. In: *European Physical Journal D* 32.2 (2005), pp. 171–180. arXiv: 0407094 [physics].
- [137] P. Krüger et al. “Potential roughness near lithographically fabricated atom chips”. In: *Physical Review A - Atomic, Molecular, and Optical Physics* 76.6 (2007), pp. 1–8. arXiv: 0504686 [cond-mat].
- [138] Stephan Wildermuth. “One-dimensional Bose-Einstein condensates in micro-traps”. PhD thesis. Universität Heidelberg, 2005.
- [139] Johannes Matthias Hecher. “Current Transport in Polycrystalline Iron Based Superconductors”. PhD thesis. TU Wien, 2016.
- [140] Johann Emhofer et al. “Current and field distribution in meandered coated conductors for roebel cables”. In: *IEEE Transactions on Applied Superconductivity* 21.3 PART 3 (2011), pp. 3389–3392.
- [141] F Hengstberger et al. “Assessing the spatial and field dependence of the critical current density in YBCO bulk superconductors by scanning Hall probes”. In: *Superconductor Science and Technology* 22.2 (2009), p. 025011. arXiv: arXiv:0811.4279v1.
- [142] Vladimir Sokolovsky, Leonid Prigozhin, and John W Barrett. “3D modeling of magnetic atom traps on type-II superconductor chips”. In: 124004 (2014), pp. 1–18.
- [143] Guillem Via, Carles Navau, and Alvaro Sanchez. “Magnetic and transport currents in thin film superconductors of arbitrary shape within the London approximation”. In: *Journal of Applied Physics* 113.9 (2013), p. 093905.
- [144] Guillem Via et al. “Simultaneous magnetic and transport currents in thin film superconductors within the critical-state approximation”. In: *Superconductor Science and Technology* 28.1 (2014), p. 14003.
- [145] C. Navau et al. “Alternating current susceptibility calculations for thin-film superconductors with regions of different critical-current densities”. In: *Journal of Applied Physics* 103.11 (2008).

- [146] Alexander Rabensteiner; Klara Schernthaner. “Implementation of a numerical method for superconducting current distributions”. Bachelor Thesis. TU Wien, Dec. 2017.
- [147] Felix Wagner. “Simulation of superconducting current distributions”. Bachelor Thesis. TU Wien, Dec. 2017.
- [148] Ernst Helmut Brandt and Mikhail Indenbom. “Type-II-superconductor strip with current in a perpendicular magnetic field”. In: *Physical Review B* 48.17 (1993).
- [149] Mikhail M. Khapaev et al. “3D-MLSI: Software package for inductance calculation in multilayer superconducting integrated circuits”. In: *IEEE Transactions on Applied Superconductivity* 11.1 I (2001), pp. 1090–1093.
- [150] W. Hänsel et al. “Magnetic conveyor belt for transporting and merging trapped atom clouds”. In: *Physical Review Letters* 86.4 (2001), pp. 608–611.
- [151] Jesper Fevre Bertelsen et al. “Mixing of ultracold atomic clouds by merging of two magnetic traps”. In: *Physical Review A - Atomic, Molecular, and Optical Physics* 75.1 (2007), pp. 1–11. arXiv: 0606416 [cond-mat].
- [152] G. Wendin. “Quantum information processing with superconducting circuits: a review”. In: *Reports on Progress in Physics* 80.10 (2017), p. 106001. arXiv: 1610.02208.
- [153] Stefan Putz. “Circuit Cavity QED with Macroscopic Solid-State Spin Ensembles”. PhD thesis. TU Wien, 2016.
- [154] Florian Steiner. “Nanofiber based Cavity Quantum Electrodynamics (CQED) Interface for Atomchips”. PhD thesis. TU Wien, 2017.
- [155] Robert Amsüss. “Strong coupling of an NV- spin ensemble to a superconducting resonator”. PhD thesis. TU Wien, 2013.
- [156] E. T. Jaynes and F. W. Cummings. “Comparison of Quantum and Semiclassical Radiation Theories with Application to the Beam Maser”. In: *Proceedings of the IEEE* 51.1 (1963), pp. 89–109.
- [157] D. Pozar. *Microwave Engineering Fourth Edition*. 2005, pp. 1–756.
- [158] Yufang Zhang and Zhenqing Wang. “Measurement of dielectric loss tangent at cryogenic temperature using superconducting film resonator”. In: *Journal of Theoretical and Applied Physics* 10.1 (2016), pp. 27–32.
- [159] Philipp Treutlein et al. “Coherence in microchip traps”. In: *Physical Review Letters* 92.20 (2004), pp. 8–11. arXiv: 0311197 [quant-ph].
- [160] Simon Bernon et al. “Manipulation and coherence of ultra-cold atoms on a superconducting atom chip.” In: *Nature communications* 4 (2013), p. 2380. arXiv: 1302.6610.
- [161] D. M. Harber et al. “Effect of cold collisions on spin coherence and resonance shifts in a magnetically trapped ultra-cold gas”. In: (2002), pp. 1–6. arXiv: 0208294 [cond-mat].
- [162] Yu-ju Lin et al. “Impact of the Casimir-Polder Potential and Johnson Noise on Bose-Einstein Condensate Stability Near Surfaces”. In: *Physical Review Letters* 92.5 (2004), p. 050404. arXiv: 0308457 [cond-mat].
- [163] Andreas Angerer et al. “Collective strong coupling with homogeneous Rabi frequencies using a 3D lumped element microwave resonator”. In: *Applied Physics Letters* 109.3 (July 2016), p. 033508. arXiv: 1605.05554.

- [164] Vito Pecile; Carina Killian. “A hybrid quantum system with a 3d cavity and ultracold atoms”. Bachelor Thesis. TU Wien, Oct. 2016.
- [165] V. Y F Leung et al. “Microtrap arrays on magnetic film atom chips for quantum information science”. In: *Quantum Information Processing* 10.6 (2011), pp. 955–974. arXiv: 1104.3067.
- [166] Saeed Ghanbari et al. “Superfluid to Mott insulator quantum phase transition in a 2D permanent magnetic lattice”. In: *European Physical Journal B* 70.3 (2009), pp. 305–310.
- [167] V Y F Leung et al. “Magnetic-film atom chip with 10 μm period lattices of microtraps for quantum information science with Rydberg atoms.” In: *The Review of scientific instruments* 85.May (2014), p. 053102. arXiv: 1311.4512.
- [168] R. Gerritsma et al. “Lattice of microtraps for ultracold atoms based on patterned magnetic films”. In: *Physical Review A - Atomic, Molecular, and Optical Physics* 76.3 (2007), pp. 1–6. arXiv: 0706.1170.
- [169] O. Romero-Isart et al. “Superconducting vortex lattices for ultracold atoms”. In: *Physical Review Letters* 111.14 (2013), pp. 1–5. arXiv: 1302.3504.
- [170] S Scheel et al. “Atomic spin relaxation and spatial decoherence near metallic and superconducting surfaces”. In: *Journal of Physics: Conference Series* 36 (2006), pp. 188–193.
- [171] Fujio Shimizu, Christoph Hufnagel, and Tetsuya Mukai. “Stable neutral atom trap with a thin superconducting disc”. In: *Physical Review Letters* 103.25 (2009), pp. 5–8.
- [172] P. Weiss et al. “Sensitivity of ultracold atoms to quantized flux in a superconducting ring”. In: *arXiv* (2015), pp. 1–5. arXiv: 1502.0185.
- [173] B. Kasch et al. “Cold atoms near superconductors: Atomic spin coherence beyond the Johnson noise limit”. In: *New Journal of Physics* 12 (2010). arXiv: 0906.1369.
- [174] Stefan Scheel, Rachele Fermani, and E. a. Hinds. “Feasibility of studying vortex noise in two-dimensional superconductors with cold atoms”. In: *Physical Review A - Atomic, Molecular, and Optical Physics* 75.6 (2007), pp. 1–4. arXiv: 0702566 [cond-mat].
- [175] Alexander Bodenseher. “Implementing a robust I/O system for a bilateral current source”. Bachelor Thesis. TU Wien, Dec. 2017.

Appendices

A. Properties of Rubidium 87

Table A.1.: Physical properties of Rubidium 87. Mostly from [39].

Atomic Number	37
Relative Natural Abundance	27.83 %
Atomic Mass	1.443×10^{-25} kg
Density at 25 °C	1.53 g/cm ³
Melting Point	39.3 °C
Boiling Point	688 °C
Vapor Pressure at 25 °C	5.22×10^{-5} Pa
Nuclear Spin	3/2

Table A.2.: D2 line properties.

Frequency	384.230 48 THz
Energy	1.589 eV
Wavelength (Vacuum)	780.241 nm
Wavelength (Air)	780.0333 nm
Lifetime	26.23 ns
Natural Line Width	6.066 MHz
Recoil Velocity	5.884 mm/s
Recoil Energy	3.77 kHz
Recoil Temperature	361.96 nK
Doppler Shift at recoil velocity	7.519 kHz
Doppler Temperature	145.57 μ K
Saturation Intensity for σ^{\pm} pol. light	1.669 mW/cm ²
Scattering cross section	2.906×10^{-9} cm ²

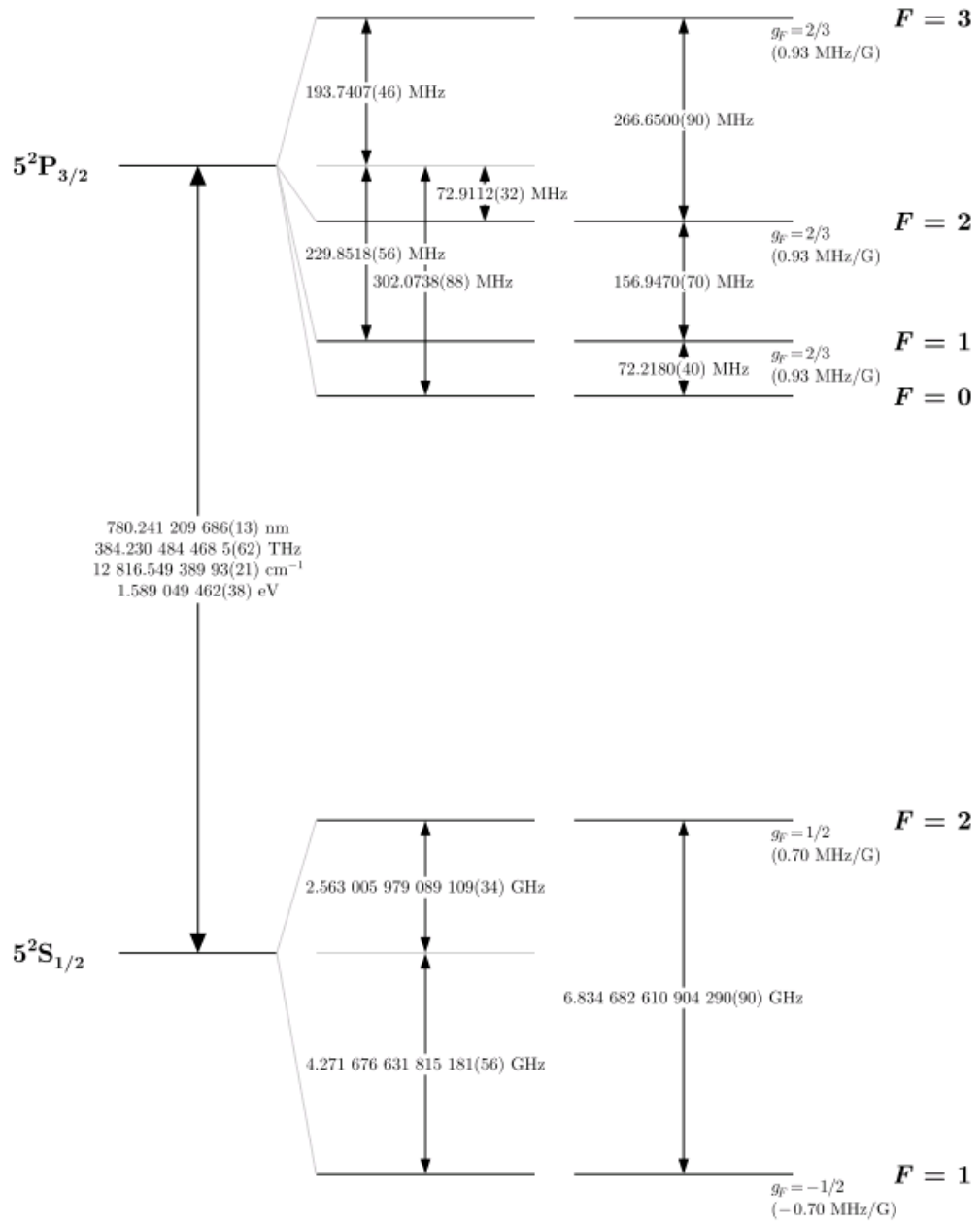


Figure A.1.: Rubidium 87 $D2$ transition hyperfine structure, taken from [39]. The shifts are not necessarily to scale. The factors g_F are given for the low field case, the frequency shift between adjacent levels is shown in parenthesis.

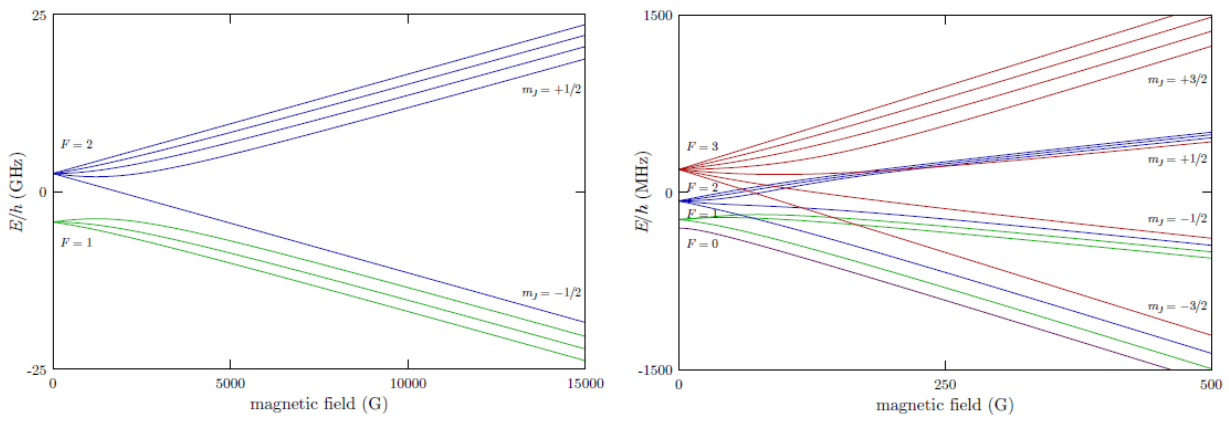


Figure A.2.: Hyperfine level structure in an external field for the $5^2S_{1/2}$ (left) and the relevant excited state $5^2P_{3/2}$ (right). Note that the scales for the level shift and the field are very different in both plots. For magnetic trapping, i. e. fields close to $0G$, the levels of the ground state can be assumed to shift linearly according to $\Delta E = g_F m_F \mu_B |B|$. Both plots taken from [39].

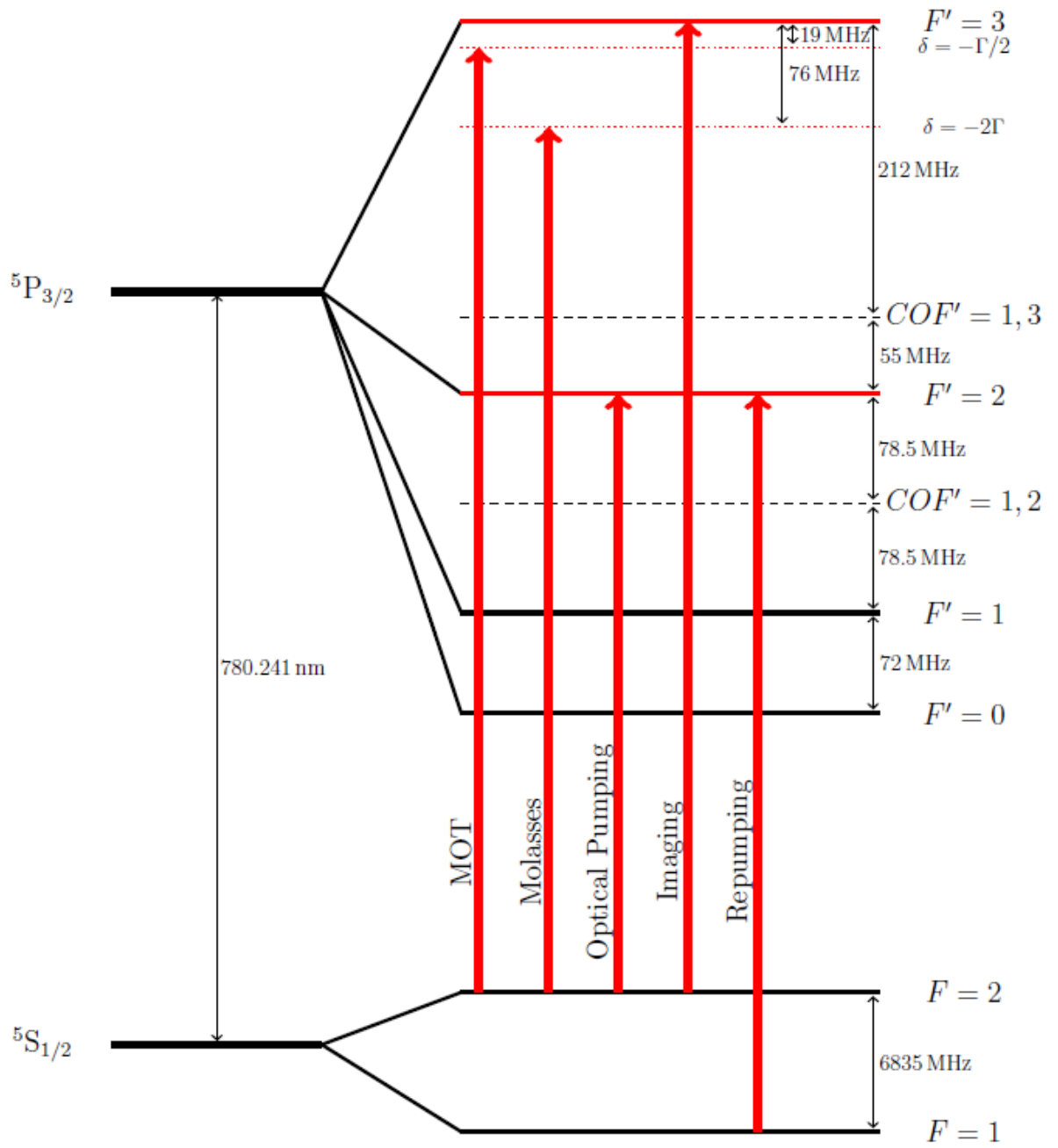


Figure A.3.: Used laser frequencies. Taken from [118]

B. Electronics

B.1. The switchbox

The purpose of the switchboxes is to divert the current from the delta power supplies to different coils and to reverse the polarity of the currents for the vertical transport coils. It consists of a power supply board, a logic board and the high current side, as is shown in figure B.1. The power supply board stores energy in several capacitors and ensures a safe shutdown of the unit in case of external power loss. The logic board, shown in figure B.2, works as follows: Each logic board has four digital inputs for TTL signals from ADWIN. A demultiplexer circuit¹ decodes these binary inputs into one of 16 mutually exclusive outputs. An inverter² negates the output of the demultiplexer such that one channel is high and all others low (refer to the datasheet of the demultiplexer for details). In total, 4 cases are distinguished: two unipolar outputs and two cases for bipolar output. For unipolar switching, the logic signal from the inverter is fed into a MOSFET driver chip³, which acts on two parallel MOSFETS⁴ which switch the current. For the H-bridge, the corresponding logic signal is fed into two half-bridge driver ICs⁵, on the high side input of one and the low side input of the other driver and vice versa. Each output of the half-bridge drivers is connected to the gate terminals of two parallel MOSFETS. For the H-bridge, the current passes through two MOSFET banks. The high current part of the circuit is built with massive copper rods, connections inside the box are made with a flexible 25 mm² cable. The old switchbox design had the cables screwed inside the box, making it virtually impossible to service the unit without dismantling the whole switchbox. The new design uses high current plugs, allowing to unplug the power supply and the coils and take out the switchbox. Each output contains a magnetoresistive current sense⁶. The signal outputs of this current senses are available at the front panel. Having the possibility to monitor the current through all coils simultaneously is invaluable for debugging.

¹Texas Instruments SN74154N

²NXP Semiconductor 74HC04

³International rectifier IR4426

⁴Vishay SUP75N06

⁵International rectifier IR2304

⁶CMS2050, Sensitec

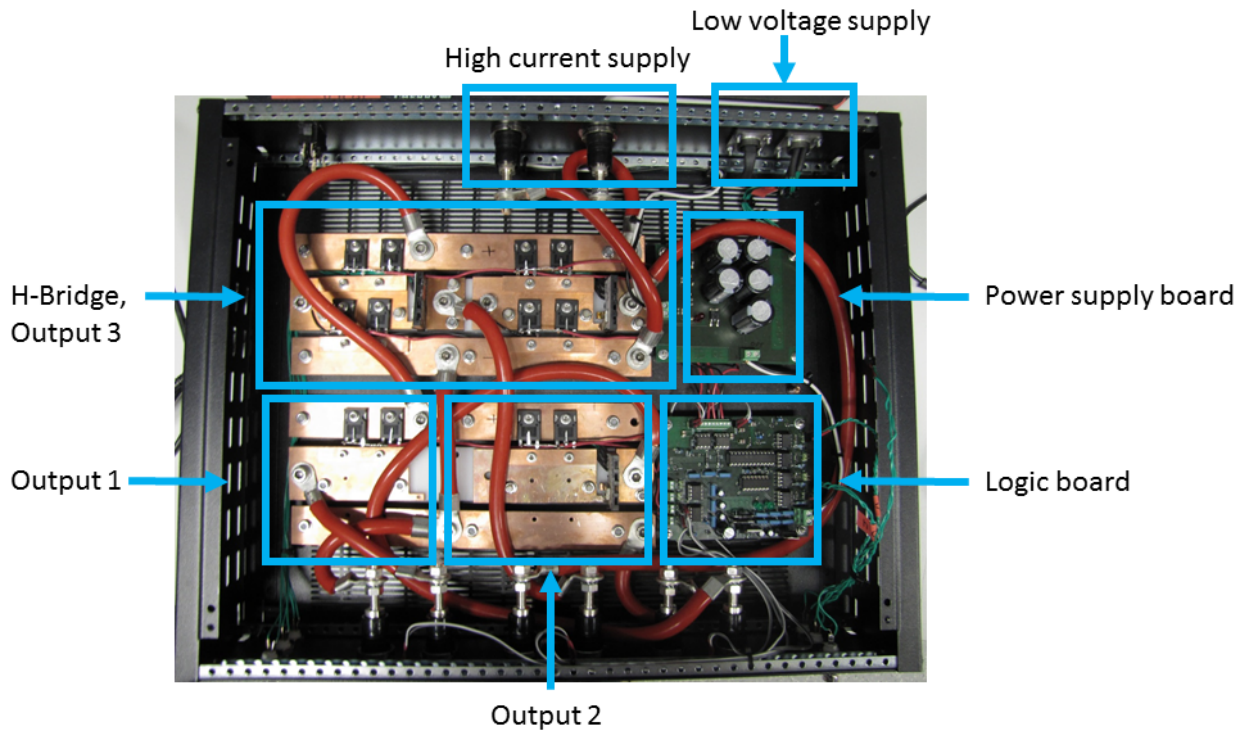


Figure B.1.: The new switchbox design. The Delta power supply is connected on the back-side, along with the DC voltage for the logic board. The power supply board ensures safe operation in case of power loss. The MOSFETS are mounted on massive copper rails. The front panel

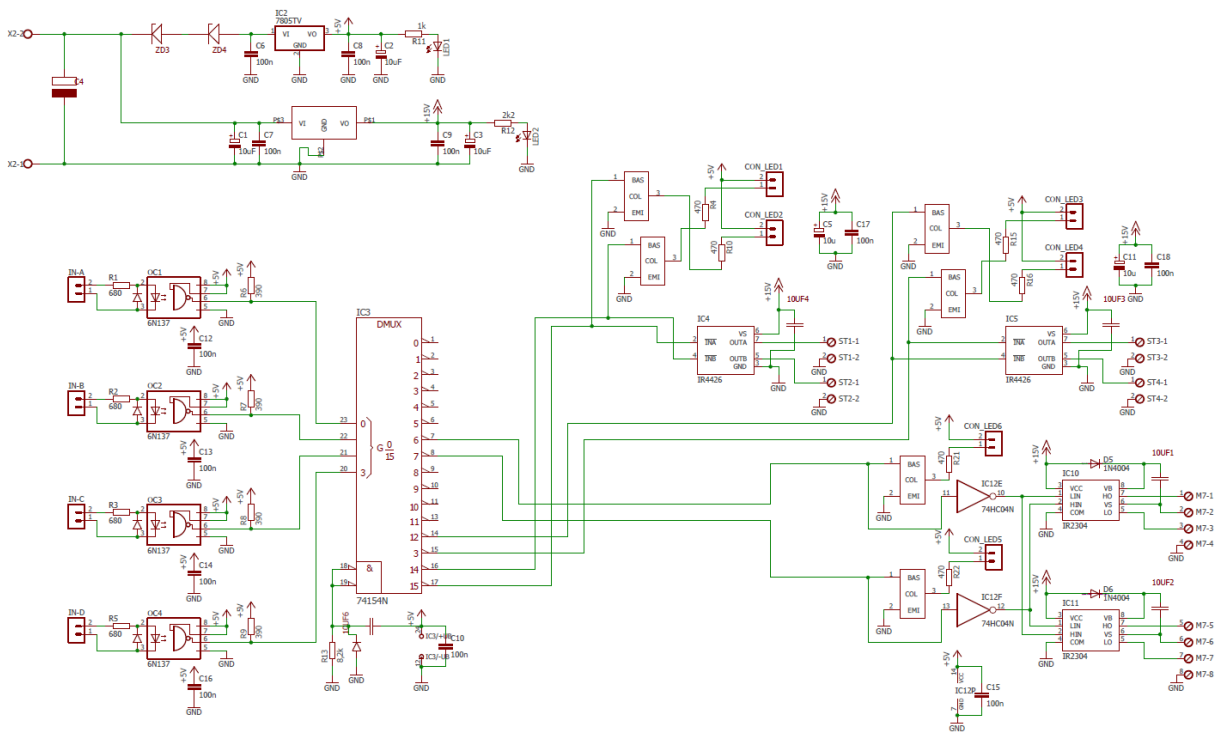


Figure B.2.: Schematics of the new switchbox design. The function is explained in the text.

B.2. The Heidelberg current source

This is the standard chip driver current source in our group. It was developed by the electronic workshop in Heidelberg in 2002 [57]. The emphasis in this design was ultra-low noise. The circuit diagram is shown in figure B.3, the working principle is as follows: An analog control voltage (1) is fed to an ultra-low noise operational amplifier⁷ (2). A large compensation capacitor (3) reduces the slew rate and the gain at high frequencies. This helps to reduce high frequency noise, but also slows down the response time of the current source and limits the switching speed. The output of the low noise op-amp is amplified by another transistor (4), which controls the base current of two npn bipolar transistors (5). The load current load also passes through a resistor network (6). The voltage in the middle of this network provides the feedback to the inverting input of the operational amplifier. The output of the current source depends on the temperature of the resistor network, limiting its stability under changing load. We observe a drop in current of up to several percent within a few tens of seconds at high currents (2 A). The diode (7) across the load has to be removed when powering the high inductance superconducting coils. Otherwise the coils will not follow the desired current ramps.

In principle the current source needs a -12 V , a $+12\text{ V}$ and a $+15\text{ V}$ supply. We use the same source for the two positive inputs. To reach a higher output current (more than 2 A), voltages up to $+18\text{ V}$ can be used.

To avoid introducing noise, car batteries instead of regular power supplies are used. We designed a box for simultaneously charging up to 12 batteries while making sure they remain completely galvanically isolated when in operation.

The noise level achieved with this current source is excellent, owing to the low noise amplifier, the reduced bandwidth, proper filtering of the supply voltages and the total lack of digital components, which typically produce some noise at their clock frequency. However, the current drift remains a problem, especially for higher currents. A temperature stabilization of the resistor network, or an external stable current sense (many commercial power supplies have this feature) could mitigate this issue.

⁷LT1028, Linear technology

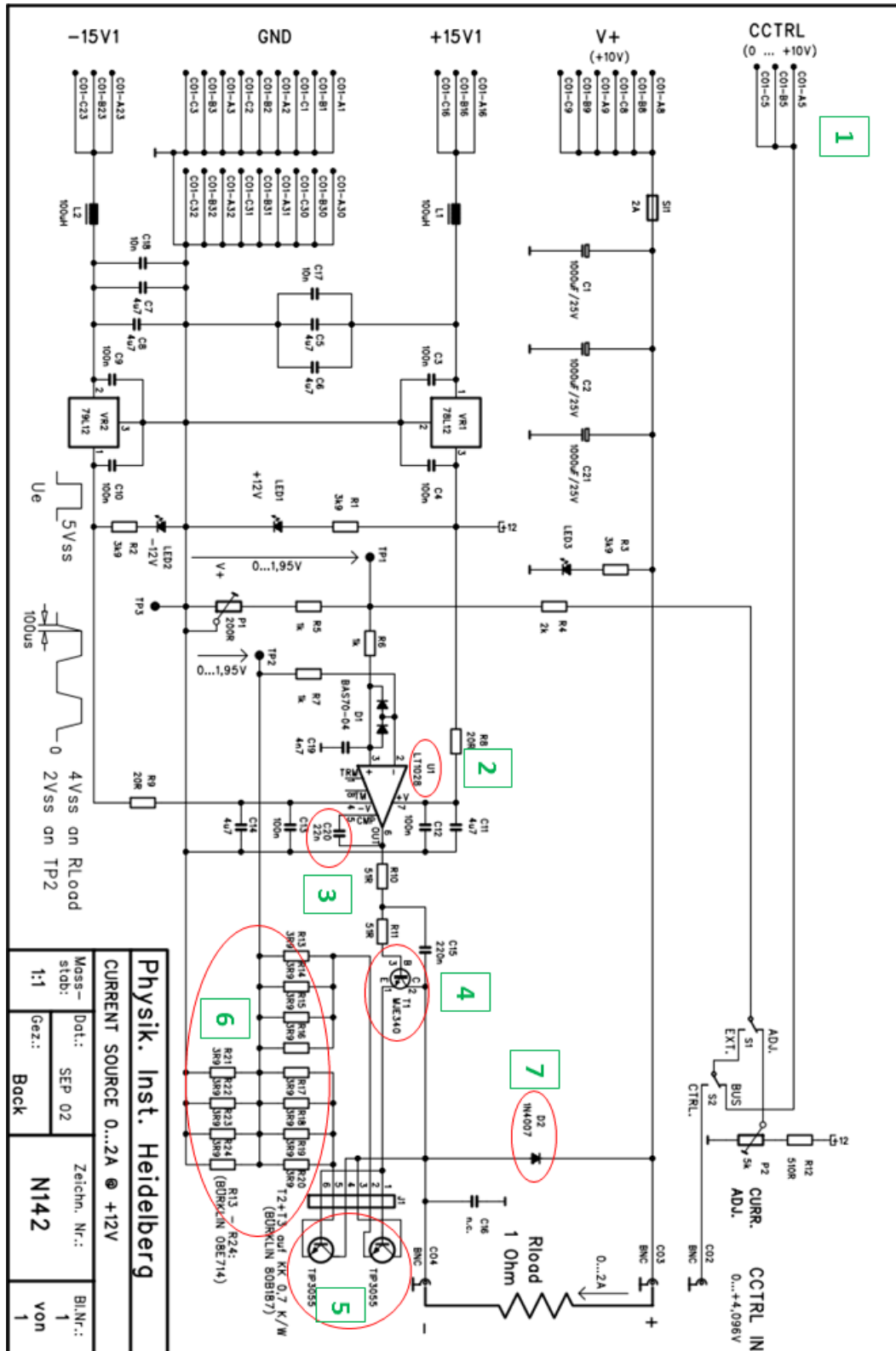


Figure B.3.: Circuit diagram of the chip driver current source. Details are given in the text.

B.3. The Bilateral Current Source

Andrew Pelczar from the electronic workshop of the Atominstitut has developed a new bilateral current source. It can output two unipolar currents or one bipolar current in the range of ± 3 A with a total power of 75 W. The design goal for this current source was extreme precision (better than 1×10^{-4}) and low drift, surpassing all commercially available products. Furthermore, this current source offers high flexibility in operation. It can be controlled by an analog input voltage but also output internally stored arbitrary current waveforms. The fact that it is bipolar helps in reducing the number of devices needed for the magnetic transport. In chapter 4 I listed as an example the number of devices and channels involved in controlling the coil V6. With the new current source this will come down to just one current source and one digital channel triggering the output. Also the circuits described in the next section B.4 will profit from this massive simplification.

The current source is fully digitally controlled by a 32 bit microcontroller⁸. Analog input voltages are converted by an 18 bit ADC⁹, digital waveforms and device calibration data are stored in a nonvolatile 1 Mbit F-RAM chip¹⁰. The digital current control signal from the microcontroller is converted by an ultra-stable 16 bit DAC chip¹¹. After converting the voltage level by a low-noise op-amp¹², a power op-amp¹³ controls the actual output current. To achieve the desired current stability, sensing resistors¹⁴ with extremely low temperature coefficient and low long term drift are used. To further increase current stability, the heat sink for the power op-amps and the sensing resistors is kept at a constant temperature. The current source is designed to keep the internal power dissipation constant, independent of the output current. This sophisticated temperature management system includes an internal water cooling cycle and software controlled fans. There are numerous sensors for temperatures, output currents, voltages, water pressure etc. reporting to the microcontroller, making the software a key component. Proper integration into the experimental control system promises highly reliable operation. As a first step, a MATLAB interface to upload arbitrary waveforms has already been programmed and tested [175]. The frontpanel of the current source is shown in figure B.4. Figure B.6 shows a small part of the circuit diagram with the DACs and the power op-amps. For a complete description of the circuit and comprehensive test reports under various conditions, refer to the manual, which will be written by the electronic workshop as soon as the first production batch is done).

Due to the large number of components, the noise level of this current source is above the N142 described in the previous section. Any digital component also produces some noise at its clock frequency, the worst noise source is however the active cooling by the electric fan and water pump. Careful arrangement of these devices in the housing as well as shielding with copper foil reduces the noise significantly, but can not eliminate it entirely. A comparison of the noise levels is shown in figure B.5.

⁸PIC32MX695F512H, Microchip

⁹LTC 2338-18, Linear Technology

¹⁰FM24V10, Cypress

¹¹AD5760BCPZ, Analog Devices

¹²AD8675ARZ, Analog Devices

¹³OPA549T, Texas Instruments

¹⁴UNR 4-3425, Powertron



Figure B.4.: The front panel of the new current source. Programming the waveforms is done through the RS 435 socket. DAQ out and Hall out allow analog monitoring of the current setting, all other parameters can be read through the programming interface.

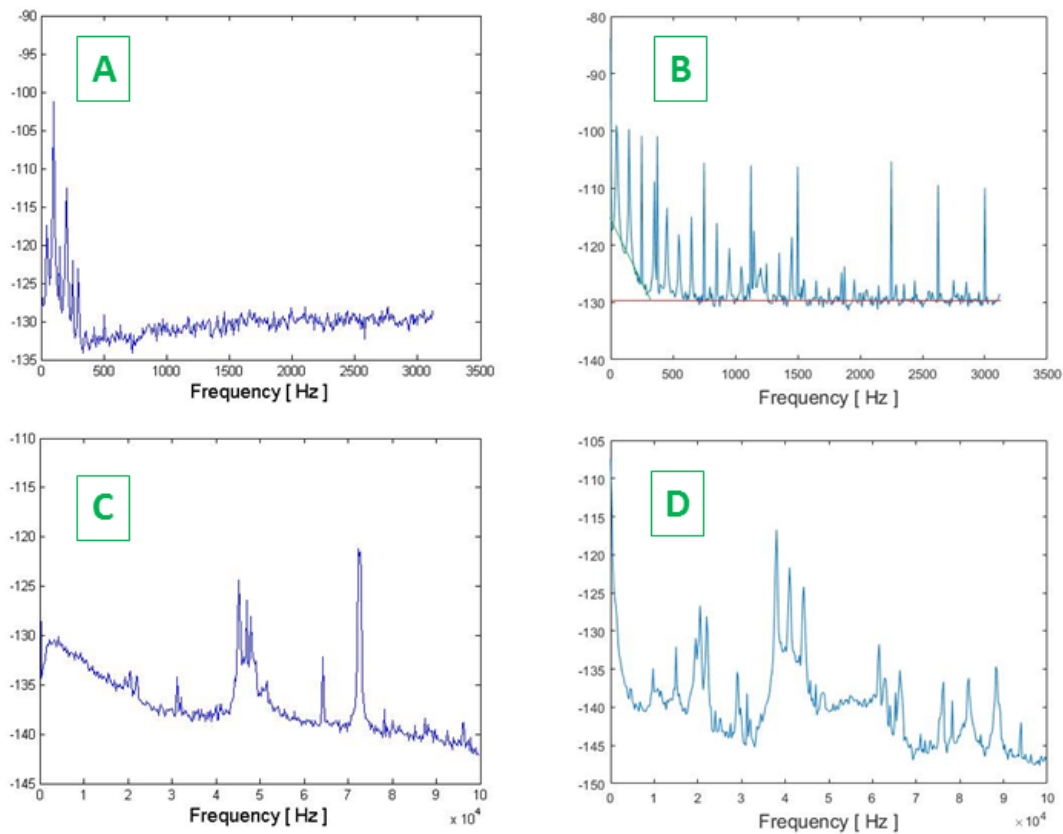


Figure B.5.: Comparison of the noise from the N142 current source (left, A and C) and the new bilateral current source (right, B and D). The N142 current source was measured in the Rb-II lab with their actual chip driver current source. Test current was 1 A. The y-axis of all plots is in units of dBV. All measurements were done using the SR770 Spectrum analyzer. Generally, the new current source shows more features in the spectrum, even if the noise floor is comparable to the N142.

B.4. Coil configurations

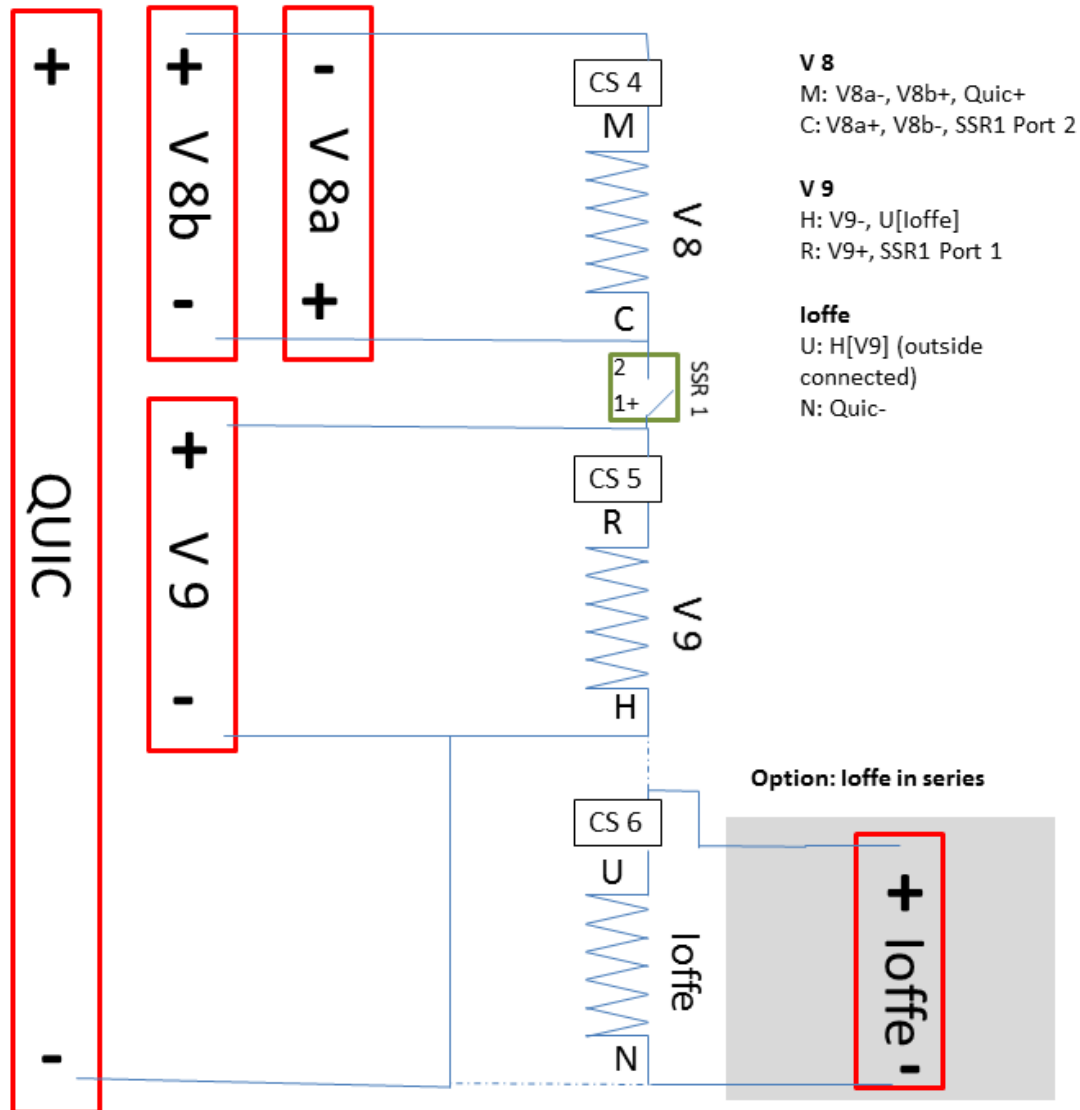


Figure B.7.: QUIC circuit. Current sources and switches are not shown separately for clarity. The letters on both ends of each coil are the corresponding labels on the breakout box. CS stands for current sense. At the time of writing, the Ioffe coil was powered independently.

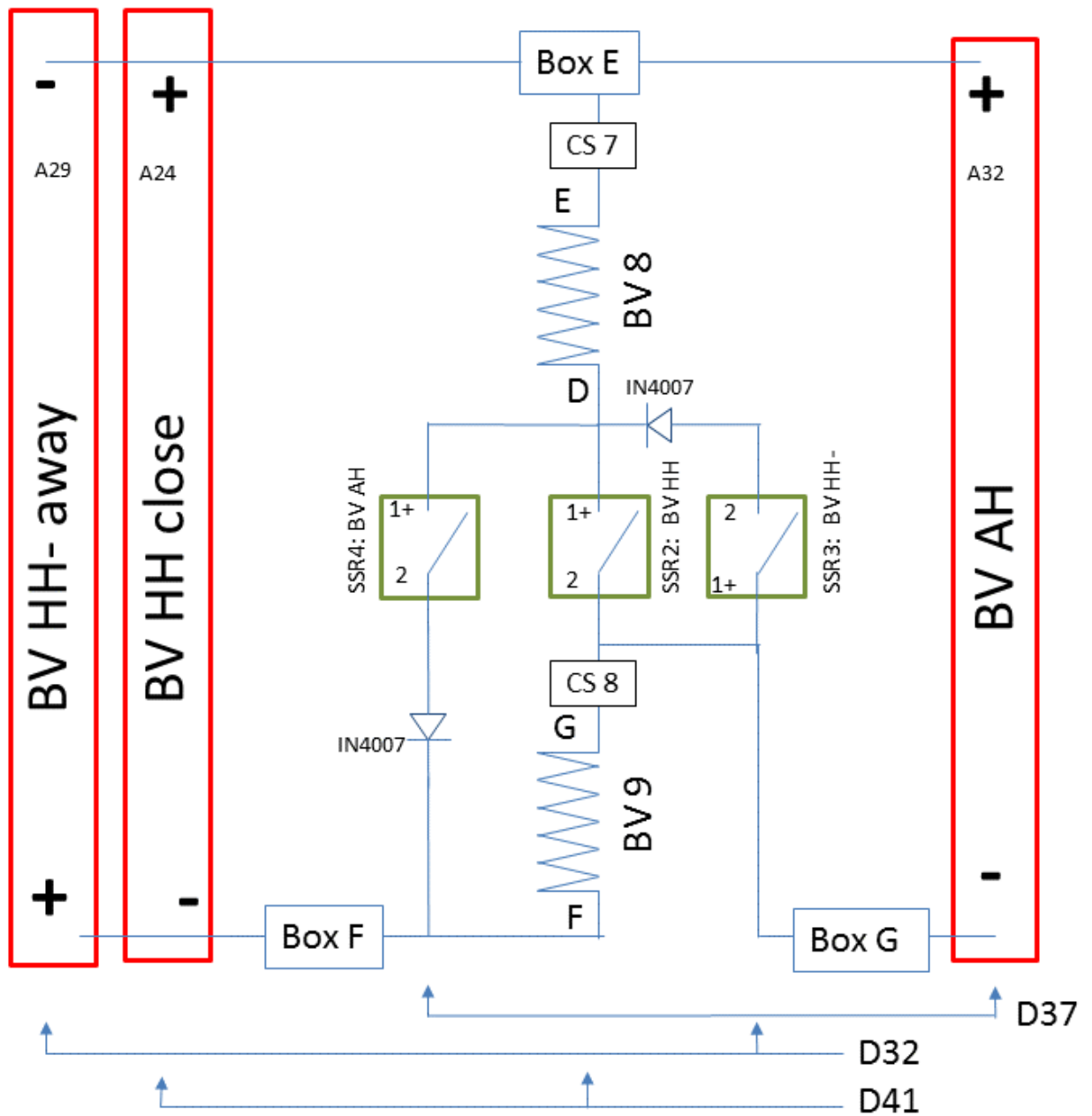


Figure B.8.: Connection diagram for the coils BV8 and BV9. They can be switched in anti-Helmholtz mode for the buffer trap or in Helmholtz mode to provide a homogeneous vertical bias field.

B.5. Breakout box

The purpose of the breakout box is to provide access to the wires entering the cryostat through the three electrical feedthroughs. The first version of this box bundles all 50 wires. These includes all temperature sensors. The box contains ten magnetoresistive current senses, several solid state relays and two mechanical relays for the chip wires. The connections inside this box are realized with short wire strands, leading to a very chaotic arrangement as can be seen in figure B.9. This construction is not only difficult to repair as it is hard to find the right wire, it is also a major noise source. The wires are crossing each other in an undefined fashion, allowing high frequency noise to couple between them.

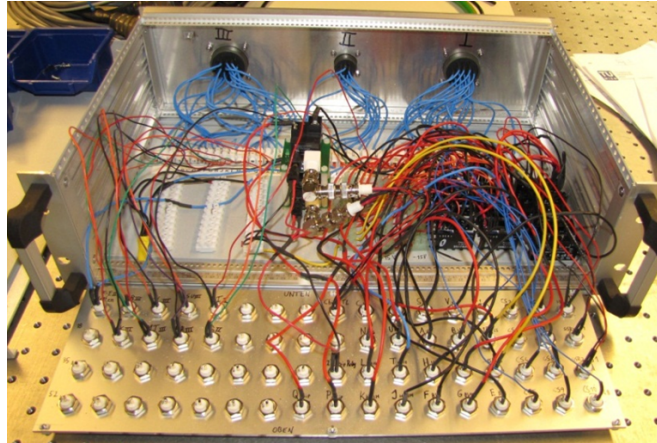


Figure B.9.: The chaotic wiring of the old breakout box.

We are designing a new separate breakout box for the current carrying wires. This box will not only route the wires on a PCB board to minimize crosstalk, but also feature a noise filtering stage. After entering the box through the front panel, all wires are immediately connected to the first PCB board, where the current senses are located. They connected with the appropriate power supply filtering (as given by the datasheet) to provide maximum bandwidth (200 kHz) and a better signal to noise level.

The second PCB board is responsible for the noise filtering. For this purpose, each wire pair gets its own long, thin PCB board, where several ferrite cores as the one shown in figure B.10 can be slipped on. These ferrites efficiently absorb high frequency components of the noise. Several capacitors between the ground plane on the back side of the PCB and the wire provide an additional path for noise elimination. A metal wall between the first and second board provides additional protection from interference.

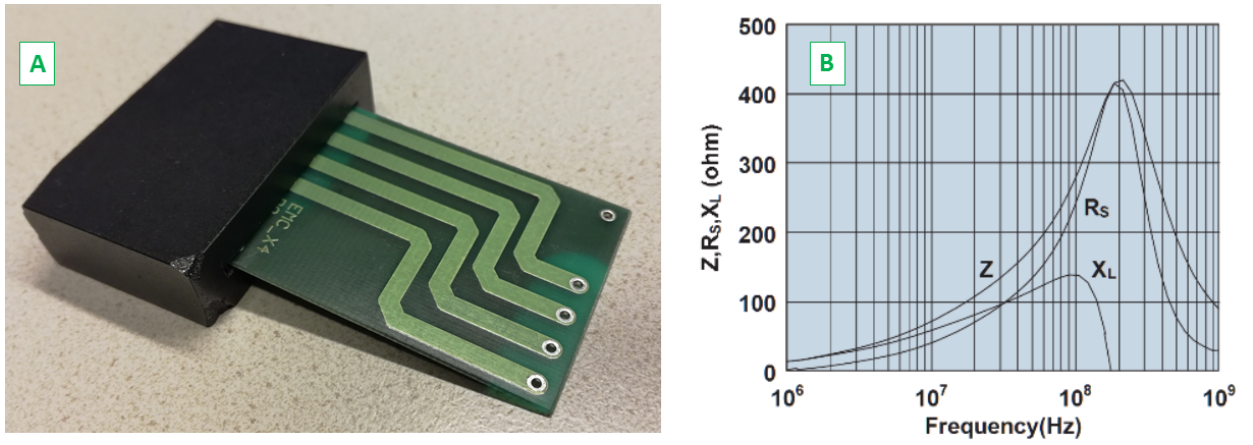


Figure B.10.: A: A slip on ferrite. B: Impedance (Z), reactance (X) and resistance (R) vs. frequency. High frequencies get efficiently absorbed.

Acknowledgments

First and foremost I have to thank my supervisor Jörg Schmiedmayer for the opportunity to work on this challenging project.

I am thankful to my dear colleague Fritz Diorico for countless hours in- and outside the lab, it was a great pleasure working with you!

Our Masterstudents, Benedikt Gertenecker, Thomas Weigner, Naz Shokrani, Lukas Cvitkovitch and (briefly) Zaneta Kurpias showed a lot of courage to join us in taming the beast.

In the last 2.5 years, we have been sharing a lab with the Lithium experiment, with Rugway Wu, Qi Liang and Pradyumna Paranjape (who will hopefully be allowed to stay!). Thank you and all other members of your team for an enjoyable cooperation in a sometimes overcrowded laboratory. I am looking forward to see your BEC!

I thank all former and current members of the Atomchip group for many, many interesting evenings in the coffee corner and the occasional cold beverage. The spirit in this group is remarkable and highly enjoyable - I hope it stays that way!

I am grateful to Thorsten Schumm for his continued advice and for proofreading this thesis.

Finally I have to thank Hartmut Häffner for the opportunity to work in his group during my COQUS-secondment.